Light-induced electronic and structural dynamics in layered transition-metal dichalcogenides

Takumi Fukuda

February 2024

Light-induced electronic and structural dynamics in layered transition-metal dichalcogenides

Takumi Fukuda

Doctral Program in Engineering Sciences
Subprogram in Applied Physics

Submitted to the
Degree Programs in Pure and Applied Sciences of the
Graduate School of Science and Technology,
in Partial Fulfillment of the Requirements
for the Degree of Doctor of Philosophy in
Engineering

at the
University of Tsukuba

Contents

Acknowledgement

Throughout my doctoral program and the research included in this dissertation, I have received invaluable support from numerous individuals, both in the academic and personal aspects of my life. It might be hard to complete my Ph.D. without their assistance during the wide spread of COVID-19.

First and foremost, I would like to thank my supervisor, Prof. Muneaki Hase, for his dedicated mentorship and support over the six years I started my research as an undergraduate student to my Ph.D. at the University of Tsukuba. I really enjoyed my Ph.D. journey with him, as he gave me so much freedom and infinite inspiration without putting any pressure on me. He has an extraordinarily gentle personality that can heal everything, and he is always passionate and curious about research. I learned a great deal from him about living as a researcher. It was not just about the exceptional experimental skills in handling femtosecond lasers and measuring coherent phonons but also about engaging in discussions, developing a keen eye for research, writing meaningful papers, securing research funding, and planning a career path after obtaining a PhD. Furthermore, he provided me with numerous valuable opportunities: collaborating with many researchers, actively participating in domestic and international conferences, and writing papers as a corresponding author. These experiences enhanced my research skills and contributed significantly to my personal and mental growth. Additionally, I implicitly learned crucial aspects of being an educator from him. Despite his busy schedule, he was always kind and never showed irritability. He was an ideal educator, always willing to advise and support students while respecting their independence. I always wonder how he manages to juggle research, education, and administrative tasks without secretarial staff. I deeply cherish the philosophy of research and education I learned from him as my own origin. I earnestly desire to continue improving my skills as a researcher, guided by these principles.

I would like to express my gratitude to Associate Prof. Masaki Hada for his sincere research and personal support, going beyond the role of an assistant supervisor. He often visited my office almost daily to chat with me, check on my health and research progress, and then always talk. He especially shared his extensive academic experience with me. His stories have helped me a lot in planning my career after I finish my PhD. He appreciated my research accurately and proposed a collaborative study using ultrafast electron diffraction experiments complementary to coherent phonon spectroscopy. It was an awe-inspiring experience for me since I could learn how to figure out "what exactly we are looking at", like assembling a puzzle, through comprehensive time-resolved measurements and various experiments. I'm very grateful to Hada-sensei for always inspiring me and expanding my view on my research.

Outside our lab, I would like to thank close collaborations with National Institute of Advanced Industrial Science and Technology (AIST) members. I am very grateful to Kotaro Makino, a former member of Hase Lab, for always kindly taking the time to discuss the data and analysis based on an accurate understanding of coherent phonons.

I'm thankful to Yuta Saito (now a Professor at Tohoku University) for always cheering me up and helping me with sample and device fabrications. I would like to express my gratitude to Paul J. Fons (now a Professor at Keio University) for conducting the first-principles calculations of TMD materials and for constantly refining my rudimentary English into beautiful expressions. I also thank Alexander V. Kolobov (now a Professor at Herzen State Pedagogical University, Russia) and Atsushi Ando for supporting my research.

I am very grateful to Prof. Keiji Ueno and Assistant Prof. Ryo Ishikawa at Saitama University, who have provided me with high-quality TMD single crystals and allowed me to measure their low-frequency Raman spectra, which are essential for my studies.

In the same department at Univ. Tsukuba, I am very thankful to Associate Prof. Shoji Yoshida, Assistant Prof. Yusuke Arashida, and Assistant Prof. Hiroyuki Mogi for taking time to kindly teach me the TMD exfoliation and transferring techniques, daily enjoyable discussions on ultrafast topics and taking beautiful STM images of the TMD samples, respectively. They always inspired me, and I could learn a lot from them, who are incredibly professional in everything and have infinite curiosity to build extraordinary time-resolved instruments (e.g., THz-/MIR-STM and SEM) that look like a "forest" of optics and explore new localized non-equilibrium physics.

I am grateful to Assistant Prof. Shunsuke A. Sato (Center for Computational Sciences, Univ. Tsukuba) for fruitful discussions on the theoretical perspectives of my studies and for kindly giving me helpful advice for my academic career. I am very thankful to Naoki Ichiji (formerly Kubo Group at Univ. Tsukuba, now a Postdoc at Univ. Tokyo) for providing me with exciting and practical tips for ultrafast lasers and opportunities to participate in the community of younger Japanese PhDs who are professionals in optics and relevant fields.

I would like to express my gratitude to all the members of my office, "3D314", who have shared their dedication to research and enjoyable discussions. In particular, I am incredibly thankful to Aika Watabe and Yu Mizukoshi, who accompanied me for breakfast, lunch, and dinner and guided me to various beautiful places. I hope Mizukoshi can enjoy his Ph.D. journey and will have a good harvest for his research. To former member Yuta Komori, I sincerely appreciate your support as a discussion partner and companion throughout my academic journey, from my time as a student until now. I also extend my thanks to a former member, Takara Suzuki. His efficiency in experiments, analysis, and paper writing, which I witnessed even before joining Hase Lab, significantly impacted my research style. I would also like to express my gratitude to the current group members, including Guo Junjie, Takuto Ichikawa, Senmi Takamizawa, Kazuhiro Kikuchi, Daisuke Sato, Chiho Yamada, Mizuki Akei, Yuta Kimura, Koei Yanagisawa, Ranka Isshiki, as well as former members Jessica Afalla, Richarj Mondal, Aizitiaili Abulikemu, Tomohito Nakayama, Mari Motojima, Ryosuke Sakurai, Toshiki Sakai, Ryota Kaburauchi, Ritsuko Fujiwara, Ryuya Matsumoto, and Satoshi Ogane. I hope all of you maintain the lively and harmonious atmosphere of office 3D314 and enjoy a fruitful research journey. I would also like to express my gratitude to the members of the Hada Lab: Yuri Saida for everyday conversations and information sharing

and Uta Ozaki for the collaborative research on TMD materials.

I'm honored to have met Buhin-san (@tjmlab), a renowned figure in condensed matter physics, on Twitter (now X). Checking the latest arXiv papers he always shares and summarizes on his timeline has continuously enriched my knowledge.

I was also mentally supported by various communities beyond research. First, I am deeply grateful to Associate Prof. Emi Morita (International Institute for Integrative Sleep Medicine, IIIS, Univ. Tsukuba) for allowing me to participate in data analysis and management tasks in the entirely different field of sleep epidemiology research. I also want to thank her for her constant support of my research life and for providing me with numerous valuable advice regarding my career path. I also thank Sumi Hasegawa and Kanako Imaizumi, my colleagues at the same workplace, for always encouraging me. I would like to extend my special thanks to Ryuya Komuro and Ayaka Fujisaki (both from the Department of Humanities and Social Sciences, Tsukuba University) for overcoming PhD life together. Although our research fields differed, having someone to share the unique worries and frustrations of Ph.D. students over drinks and to celebrate the good news with may have been the most important thing for my mental well-being. I hope to maintain our long-lasting relationship. Special thanks also go to my board game buddies, Ryo Watabe (University of Tokyo), Takuya Mushano (Department of Physics, University of Tsukuba), and Takushi Mizoguchi (formerly of the Suemasu/Toko group). Playing intellectually challenging games like Catan and "Momo-Tetsu" (on Switch) with them has broadened my thinking. To my "Splatoon" (on Switch) friends, Ko-Munchkin, Towa, Naka, Oreo13, Ringo, and Fubo (handle names), thank you for playing with me every day through voice chat. Chatting about various things and screaming during play sessions were great ways to relieve stress. I would also like to thank Takamitsu Ishiyama and the other Suemasu/Toko group members for kindly inviting me to exercise at Tsukuba Wellness Park. Additionally, I owe a special thanks to Ryoichi Sasaki (formerly Terada Lab), Michiru Kajiwara (formerly Terada Lab), Shinzui Jo (formerly N. Kobayashi Lab), Kohei Tsukahara (formerly Sano Lab), Yusuke Fukami (formerly Sasaki/Yamada Lab), Kei Higashijima, Shu Murasaki, and Rema Komatsubara, who often spent time with me and always cheered me up on a personal level.

I am grateful to the Japan Society for the Promotion of Science Research Fellowship for Young Scientists (DC1) for supporting my life and research expenses throughout my three-year doctoral course.

Finally, I extend my greatest gratitude to my parents and family, who have always respected my way of life and supported me with their unconditional love. Also, to my beloved dogs Hana (a Shetland Sheepdog who passed away at the age of 15 in 2022), Rin (a 12-year-old Toy Poodle), and Ramu (a 1-year-old Border Collie).

University of Tsukuba,
Tsukuba, Ibaraki, Japan

Takumi Fukuda

The List of Publications

■ First- and/or Corresponding-Author Publications

*: corresponding author(s)

1. **T. Fukuda***, K. Makino, Y. Saito, P. Fons, A. V. Kolobov, K. Ueno, M. Hase, "Ultrafast dynamics of the low frequency shear phonon in 1T'−$MoTe_2$ ", *Appl. Phys. Lett.* **116**, 093103 (2020). [Peer-Reviewed], Chapter 5

2. **T. Fukuda***, R. Kaburauchi, Y. Saito, K. Makino, P. Fons, K. Ueno, M. Hase, "Photo-Induced Tellurium Segregation in $MoTe_2$", *Phys. Status Solidi RRL.* **16**, 2100633 (2022). [Peer-Reviewed], Chapter 4

3. **T. Fukuda***, U. Ozaki, S. Jeong, Y. Arashida, K. En-ya, S. Yoshida, P. Fons, J. Fujita, K. Ueno, M. Hase, M. Hada*, "Photoinduced Structural Dynamics of 2H − $MoTe_2$ Under Extermely High-Density Excitation Conditions", *J. Phys. Chem.* **127**, 13149-13156 (2023). [Peer-Reviewed], Chapter 7

4. Y. Iwasaki†, **T. Fukuda**†, G. Noyama, M. Akei, H. Shigekawa, M. Hase, Y. Arashida*, M. Hada*, "Electronic intraband scattering in a transition-metal dichalcogenide observed by double-excitation ultrafast electron diffraction", *Appl. Phys. Lett.* **123**, 181901 (2023). [Peer-Reviewed], †: equally contributed.

5. **T. Fukuda***, K. Makino, Y. Saito, P. Fons, A. Ando, R. Ishikawa, T. Mori, K. Ueno, J. Afalla, M. Hase, "Coherent optical response driven by non-equilibrium electron-phonon dynamics in a layered transition-metal dichalcogenide", *APL Mater.* **12** 021102 (2024). [Peer-Reviewed], Chapter 6

■ Co-Author Publications

1. A. Abulikemu, **T. Fukuda**, M. Hase*, "Ultrafast dynamics of coherent phonons and phonon-polaritons in lithium niobate crystals", *Appl. Phys. Exp.* **15**, 092005

(2022). [Peer-Reviewed]

2. J. Afalla*, J. Muldera, S. Takamizawa, **T. Fukuda**, K. Ueno, M. Tani, M. Hase, "Terahertz emission from transient currents and coherent phonons in layered $MoSe_2$ and WSe_2", *J. Appl. Phys.* **133**, 165103 (2023). [Peer-Reviewed]

3. Y. Mizukoshi, **T. Fukuda**, Y. Komori, R. Ishikawa, K. Ueno, M. Hase*, "Ultrafast melting of charge-density wave fluctuations at room temperature in $1T - TiSe2$ monitored under non-equilibrium conditions", *Appl. Phys. Lett.* **122**, 243101 (2023). [Peer-Reviewed]

■ Major Presentations (International)

1. **T. Fukuda**, P. Fons, K. Makino, Y. Saito, K. Ueno, J. Afalla, M. Hase, "The initial time-delay response of reflectivity changes in photoexcited two-dimensional layered semiconductor $2H - MoTe_2$ ", CLEO/Europe-EQEC 2023, Munich, Poster presentation. [Peer-Reviewed]

2. **T. Fukuda**, Ryota Kaburauchi, Y. Saito, K. Makino, P. Fons, K. Ueno, M. Hase, "Femtosecond -laser induced Tellurium segregation in polymorphic two-dimensional layered $MoTe_2$", 22-th Internatinal Vacuum Congress (IVC-22), Sapporo, Poster presentation. [Peer-Reviewed]

3. **T. Fukuda**, K. Makino, Y. Saito, P. Fons, A. V. Kolobov, A. Ando, T. Mori, R. Ishikawa, K. Ueno, J. Afalla, M. Hase, "Non-equilibrium steady states periodically driven by a long-lived coherent phonon in $2H - MoTe_2$ ", The International Conference on Ultrafast Phenomena (UP) 2022, Online, Poster presentation. [Peer-Reviewed]

4. **T. Fukuda**, R. Kaburauchi, Y. Saito, K. Makino, P. Fons, K. Ueno, M. Hase, "Photo-Induced Tellurium Segregation in $MoTe_2$", European Phase-Change Ovonic Symposium (E/PCOS) 2021, Online, Poster presentation. [Peer-Reviewed]

5. **T. Fukuda**, K. Makino, Y. Saito, P. Fons, A. V. Kolobov, K. Ueno, M. Hase, "Ultrafast coherent lattice vibration in 1T'−$MoTe_2$ bulk crystal", Material Research Society (MRS) 2019 Fall Meeting, Boston, Massachusetts, Poster presentation. [Peer-Reviewed]

Chapter 1

Introduction

"Plus ultra."

– the national motto of Spain and/or the school motto of Yu-ei high school in a comic "My Hero Academia" written and illustrated by Kohei Horikoshi.

Humans have grown significantly by overcoming various barriers and limitations. The practical knowledge and technologies accumulated during this growth process have been passed on to the next generation, contributing to developing the world's culture we live in today. The core of cultural development has relied on science and technology. Especially in research fields related to light and matter, the development has been achieved by overcoming limits with the aim of "faster and smaller". My research is also on the extension of such goals. This chapter provides historical background on the development of lasers, ultrafast spectroscopy, and two-dimensional layered materials, focusing on the position of my Ph.D. research.

1.1 Ultrafast Laser Sciences

1.1.1 Developments of Laser Technologies

LASER (Light Amplification by Stimulated Emission of Radiation) is a coherent light source known for its excellent directionality and convergence. The history of lasers began with the quantum theory of stimulated emission described by Einstein in 1917.[1] Following this, advancements in theory and technology [2, 3] led to the successful operation of the first laser emission by Maiman in 1960, using ruby as a media to produce 694.3 nm light.[4] This breakthrough significantly influenced the field of photonics, leading to rapid advancements and widespread applications, transforming human lifestyles.

After the development of the Kerr effect and Q-switch techniques, the late 1960s saw the start of ultrafast pulse lasers with the creation of mode-locked nanosecond pulse lasers using ruby and Nd:Glass. The 1970s introduced high-repetition-rate picosecond pulse lasers using Nd:YAG and dye media. The development of optical parametric oscillators (OPOs) expanded the range of light wavelengths, encouraging spectroscopic studies of ultrafast physical and chemical processes in materials. The 1980s saw the development of femtosecond pulse lasers through colliding pulse mode-locking (CPM). Various pulse compression and mode-locking techniques advanced, achieving pulse widths as short as 6 fs by 1987.[5] The 1990s saw the widespread use of self-mode-locked Ti:Sapphire femtosecond lasers, which were more stable and more accessible to produce than dye lasers. Advancements in chirped pulse amplification (CPA) enabled high-intensity amplification wavelength conversion and phase control of femtosecond pulses.[6] The 2000s were notable for the generation of attosecond pulse trains (250 as) [7] and single attosecond pulses (650 as) [8] using high-harmonic generation (HHG) in noble gases by applying intense long-wavelength femtosecond pulses.

In just 40 years since the invention of lasers, ultrafast pulse lasers have reduced pulse widths by over ten orders of magnitude. This rapid progress has significantly propelled fundamental research and applications across various fields, including molec-

ular dynamics, chemical reactions, lattice vibrations, electronic transitions, biological imaging, medical applications, and laser fabrication. It is worth noting that I have spent a significant period in the history of ultrafast science during my Ph.D. life. The contributions of Mourou and Strickland in developing CPA technology and increasing the intensity of ultrafast pulses were recognized with the Nobel Prize in Physics in 2018. Additionally, Agostini, Krausz, and L'Huiller, central to advancing HHG and attosecond science, were awarded the Nobel Prize in Physics in 2023. My research journey began in 2018, aligning with my final year as a doctoral student in 2024. During this period, it has been striking to see Nobel Prizes awarded for femtosecond to attosecond science, reflecting the rapid advancements in this field.

1.1.2 Time-Resolved Spectroscopy

Chemical reactions and the movement of electrons and atoms in molecules and solids happen quickly, ranging from nanoseconds to femtoseconds. The development of ultrashort pulse light sources is directly linked to the progress of spectroscopic methods that can visualize these fast physical and chemical processes. Ultrafast time-domain spectroscopy, based on the pump-probe method explained in Chapter 2, captures the dynamics of materials by using a pump pulse for excitation and a probe pulse to record the state after excitation. Since the time delay between pump and probe pulses determines the intrinsic time resolution, the pulse widths become shorter, and more detailed time-resolved measurements are possible.

Time-domain spectroscopy started to grow with the introduction of picosecond pulse lasers in the 1970s. By the late 1970s, techniques like time-domain fluorescence measurements and transient grating spectroscopy were developed, enabling studies of intramolecular energy transport dynamics on picosecond to nanosecond scales.[9, 10]

With the introduction of femtosecond lasers in the early 1980s, it became possible to observe the dissociation process of isolated molecules in a vacuum (such as ICN, NaI, HgI) and molecular vibrations with precise timing of oscillations.[11] In 1999, Zewail was

awarded the Nobel Prize in Chemistry as a pioneer of those femtochemistry studies. In the 1990s, developments of Ti:Sapphire femtosecond lasers and regenerative amplifiers boosted fundamental research into the ultrafast motion of carriers and optical phonons. In particular, lattice vibrations of solids (coherent phonons, as detailed in Chapter 3) such as semiconductors and semimetals were observed, and discussions on the ultrafast changes in structural phase transitions became common.

Until then, studies into ultrafast dynamics mainly used methods to measure temporal changes in optical constants like reflectivity and transmissivity of probe light. From the late 1990s to the 2000s, time-resolved crystal diffraction methods using X-ray and electron beam pulses as probes became available, allowing direct tracking of structural changes. Around the same time, time-resolved two-photon photoelectron spectroscopy using near-ultraviolet light as a probe and time-resolved angle-resolved photoelectron spectroscopy was developed, enabling direct observation of the changes over time in electronic states and band structures in photoexcited states. Since the 1990s, time-domain scanning tunneling microscopy techniques have also advanced, allowing the observation of temporal local dynamics of atomic structures and electron wave functions on scales from nanometers to picometers, from nanoseconds to femtoseconds. From the 2000s onwards, there have been advancements in more stable and intense fiber ultra-short pulse light sources, the growth of large-scale free-electron lasers, efficient generation methods for high-intensity sub-cycle THz waves, and improvements in detector performance. These advancements have enabled highly flexible time-domain measurements, allowing observation of various light-induced non-equilibrium states (such as quasiparticle generation, Floquet states, and photo-induced phase transitions) caused by light-matter interaction with very high precision in time, energy, and spatial resolution.

1.2 Transition-Metal Dichalcogenides

1.2.1 Fundamental

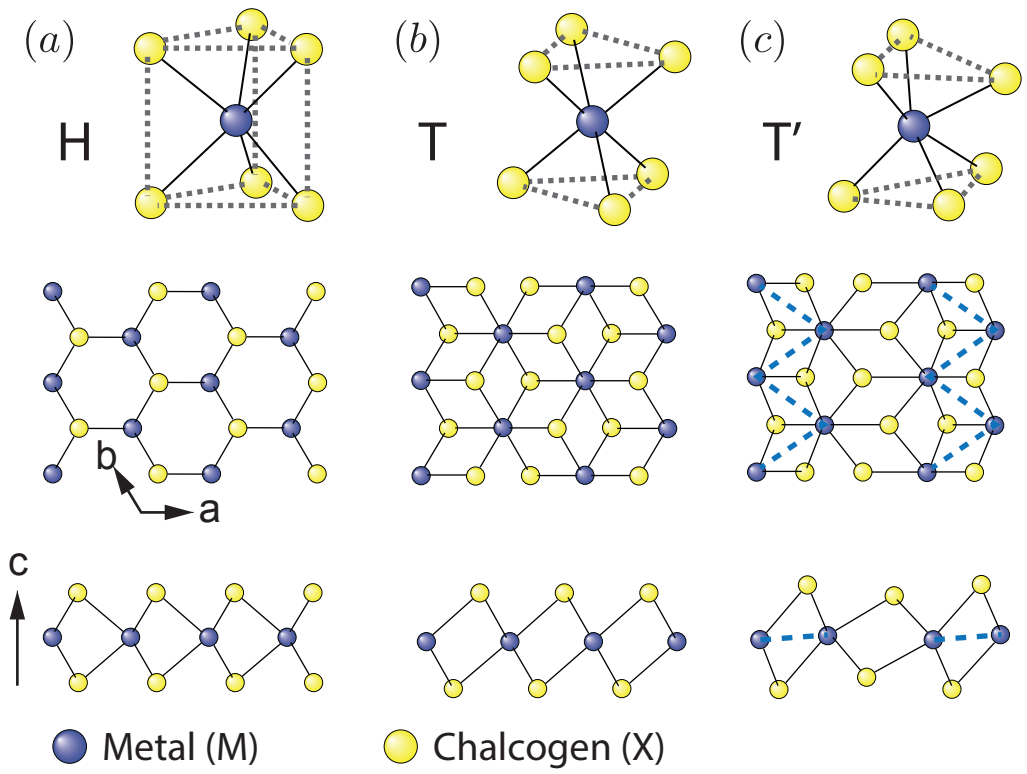

Figure 1.1: Possible lattice structures of TMDs: (a) hexagonal (H), (b) tetragonal (T), and (c) distorted tetragonal (T') structures.

Overviews and History: The extensive physical properties inherent in two-dimensional (2D) atomic layer materials and their potential in engineering applications propel research in physics, engineering, and other academic fields. This growth in interdisciplinary research was initiated by Geim and Novoselov, who exfoliated large-area monolayer graphene from layered graphite and discovered unique electronic transport phenomena, leading to the Nobel Prize in Physics 2010 awarded.[12, 13, 14] In addition, the stacking degree of freedom, such as twisted bi-layer graphene stacked at a specific "magic angle" of around 1.1°, can surprisingly alter its electronic properties, leading to

unconventional superconductivity and Mott insulator states, phenomena not present in monolayer graphene or bulk graphite.[15]

Research interest in 2D layered systems has increasingly shifted towards layered transition-metal dichalcogenides (TMDs), as shown in Fig. 1.1. TMDs are a family of 2D layered materials, represented by the chemical composition MX_2, where M is a transition metal (such as Mo or W), and X is a chalcogen (S, Se, or Te). Due to their diverse chemical compositions, crystal structures, and stacking orders, which vary from monolayer to bulk or artificial stacks, TMDs display a range of electronic phases involving semiconductor, a semimetal, superconductor, charge-density-wave (CDW) state, and topologically nontrivial phases. This versatility in electronic and structural states is promising for developing the next generation of atomically thin electronic, spintronic, and optoelectronic applications.[16]

Initially, research on layered TMDs was prominent from the 1960s to the 1980s.[17, 18, 19, 20, 21] This field saw a revival in the 2010s, driven by the discovery of exotic electronic phases in the monolayer limit. A significant finding in 2010 was that the bandgap MoS_2 shifts from indirect to direct when reduced from multiple layers to a monolayer.[22] The band gap of semiconductor TMDs varies with chemical composition and layer number, spanning from about 1 to 2 eV, covering the near-infrared to visible light regions. Moreover, various monolayer hexagonal TMD semiconductors, including MoS_2, WS_2, $MoSe_2$, and WSe_2, exhibited valley-selective spin polarization [23, 24, 25] and excitons with large binding energy over 100 meV.[26, 27] This is attributed to the spatial inversion symmetry breaking and weak screening of Coulomb interactions by strong confinement effects within the atomic layer.

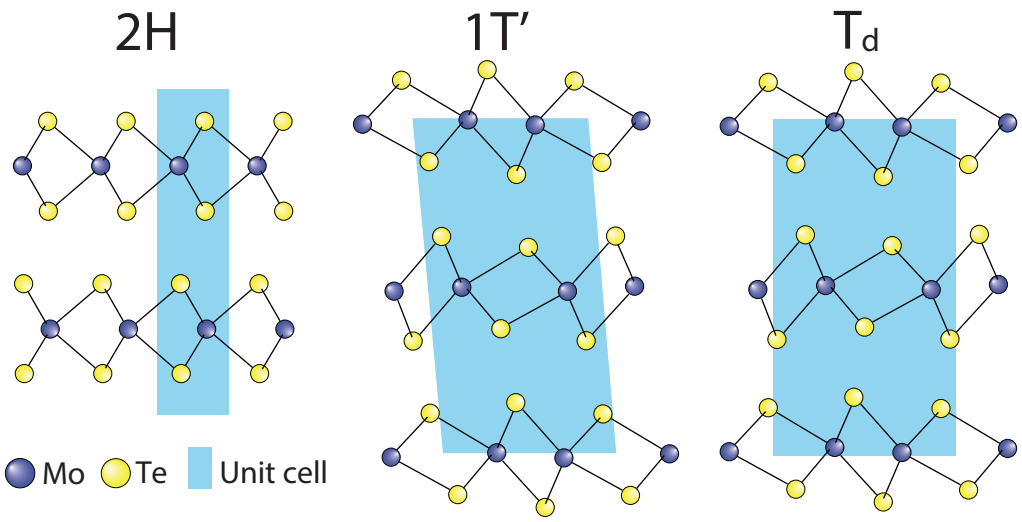

Figure 1.2: Lattice structure of $MoTe_2$ polymorphs: (a) Semiconductor 2H phase (hexagonal), (b) Semimetal 1T' phase (distorted tetragonal, centrosymmetric monoclinic structure), and (c) Weyl semimetal T_d (distorted tetragonal, non-centrosymmetric orthorhombic structure).

$MoTe_2$ Polymorphs: Generally, research on the fundamental properties and applications of sulfur and selenium-based TMDs is prominent. However, $MoTe_2$, which includes tellurium as a constituent element, is particularly notable for its unique polymorphic layered structures not seen in other compositions. $MoTe_2$ is characterized by having three different crystallographic phases: 2H (hexagonal), 1T' (distorted tetragonal: monoclinic), and T_d (distorted tetragonal: orthorhombic), as shown in Fig. 1.3. The 2H phase is a semiconductor with a bandgap of about 1 eV. The 1T' phase is a semimetal at room temperature. However, it undergoes a structural phase transition to a ferroelectric semimetal when cooled below 250 K due to a change in the interlayer stacking order. At room temperature, the 2H phase is the most stable structure, and the 1T' phase is the metastable structure. When grown in a quartz ampoule in solid-vapor equilibrium during Chemical Vapor Transport (CVT), a 2H structure forms at around 600 °C. A 1T' structure can be obtained by growing at about 800 °C followed by rapid cooling. In contrast, the same telluride compound WTe_2 is in the T_d phase at room temperature, and the 2H phase is unstable. Therefore, $MoTe_2$ is a composition with dis-

tinctive features in its crystal structure and phonon degrees of freedom. If it is possible to control the semiconductor and semimetal structures spatially through external stimuli, applications in atomically thin phase-change memory are anticipated. The concept of "Phase Patterning" using light to alter the spatial structure of $MoTe_2$ originated from a 2015 study.[28] Subsequently, structural control between the semiconductor 2H phase and the semimetal 1T phase has been attempted through various external forces such as strain, gate voltage-induced electron doping, and electric fields.[29, 30, 31] Moreover, around the same time, it was theoretically or experimentally shown that the T_d phase of $MoTe_2$ and WTe_2 is a Weyl semimetal, a topologically nontrivial phase, leading to active research into topological phase transitions between the semimetal 1T' phase and the Weyl semimetal T_d phase.[32, 33, 34, 35] Thus, $MoTe_2$ not only exhibits interesting physical properties due to its structure but has also garnered attention for the possibility of two types of structural phase transitions: the semiconductor-semimetal transition between the 2H and 1T' phases and the topological transition between the 1T' and T_d phases.

1.2.2 Light-Induced Phenomena

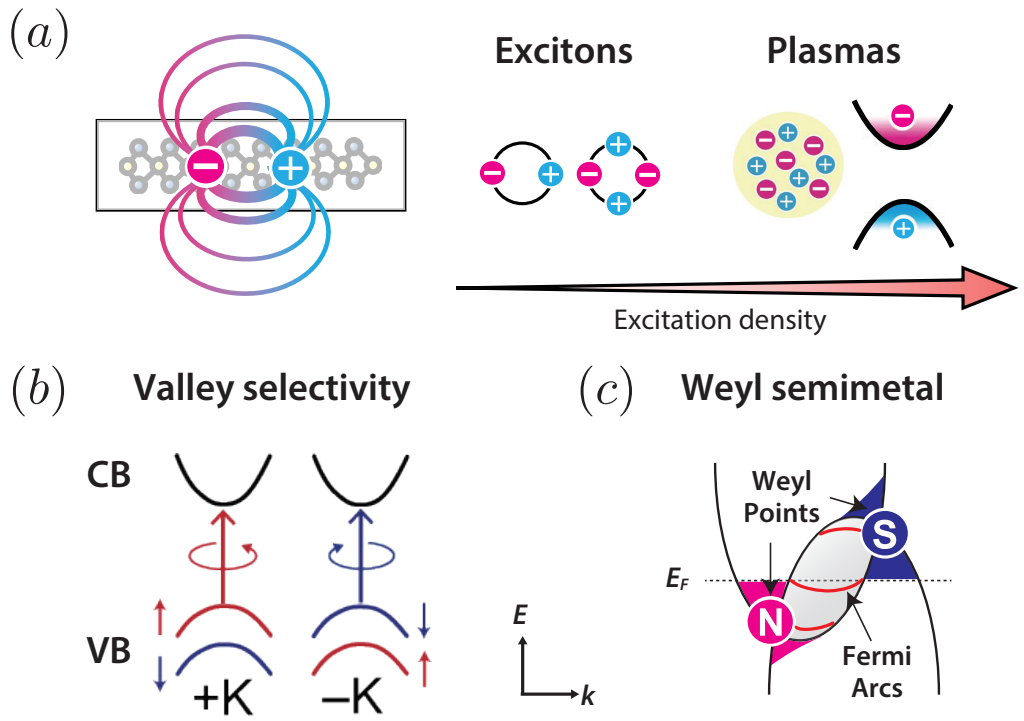

Figure 1.3: (a) Characteristic electron-hole interactions and quasiparticle generations in layered TMD system. Strong confinement of electrons in an atomic layer leads to suppression of screening effect, giving rise to large binding excitons. Increasing excitation density dissociate excitons into electron-hole plasma, exhibiting large band-gap renormalization. (b) Valley selective spin excitations at K/K' valleys in a hexagonal structure by circularly polarized light. (c) Weyl semimetal phase, one of the topological phases, in the presence of Weyl points (monopoles) and Fermi arcs in the momentum space.

One of the primary research directions concerning TMDs involves investigating the ultrafast formation of exotic hybridization states between a coherent light source and various degrees of freedom, such as valley selectivity, excitons, and lattice structures, depending on the photoexcitation levels. In the late 2010s, a particularly prominent research area in light-matter interactions within TMDs focused on the ultrafast valley-selective manipulation of exciton energy levels [Fig. 1.3]. This manipulation is achieved through the valley-selective optical Stark effect and the valley-exclusive

Bloch-Siegert shift at the K/K' valleys in momentum space of monolayer (1H) semiconductors in the presence of photon-dressed Floquet states, driven by circularly polarized light.[36, 37, 38, 39] As well as large binding intralayer excitons, different types of exciton formations, including interlayer excitons [40, 41, 42], momentum-forbidden dark excitons [43, 44], and moiré excitons [45, 46], have been identified through optical response and in momentum space upon photoexcitation. These exciton formations depend on the layer stacking order, encompassing monolayers, bulk structures, hetero structures, and twisted configurations. Under intense photoexcitation conditions, exciton dissociations into electron-hole plasmas (a Mott transition) have been observed, leading to the disappearance of exciton levels accompanied by giant band-gap renormalization, which significantly alters the optical response.[47, 48]

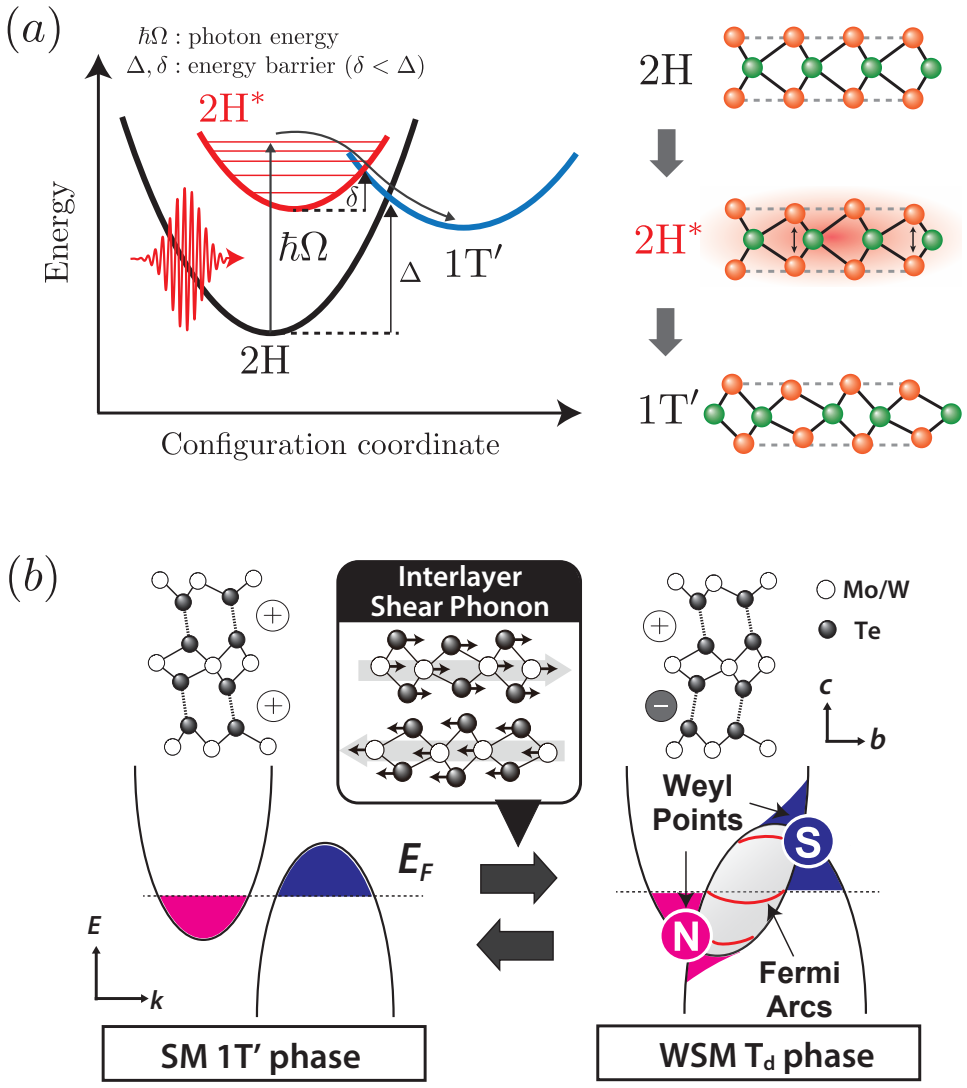

Figure 1.4: Structural phase transition in TMDs between (a) 2H and 1T' phases: form semiconductor to semimetal ($MoTe_2$) and (b) T_d and 1T' phases: Weyl semimetal (WSM) and normal semimetal (1T').

Concurrently, theoretical investigations into the anticipated photo-induced semiconductor-semimetal phase transition in $MoTe_2$ were developing. In 2016, a pioneering theoretical calculation study by Kolobov et al. [49] predicted that the excitation of several % of valence electrons to the conduction band could induce a structural phase transition in $MoTe_2$ from semiconductor 2H phase to semimetal 1T' phase via transient formation of

metallic 2H* phase with significant lattice distortion [Fig. 1.4(a)]. Following this pioneering work, multiple theoretical studies have corroborated similar results.[50, 51, 52] Despite active discussions in theoretical studies on the structural phase transition processes in TMDs, including $MoTe_2$, experimental studies verifying the ultrafast structural dynamics of TMDs upon ultrashort-pulse excitation by ultrashort pulse were limited, at least when I started my research activities as an undergraduate student in 2018. It should be noted that, in 2019, one year after I started my research, the ultrafast structural phase transition from T_d to $1T'$ phases of WTe_2 and $MoTe_2$, as shown in Fig. 1.4(b) was demonstrated through time-resolved electron diffraction and optical spectroscopy.[53, 54] It was just when the importance of the structure of TMD was beginning to be recognized.

Therefore, it is crucial to gain insight into the TMD system into what kind of lattice vibrations are excited, how the crystal structure changes, and how changes in the lattice system are coupled with the characteristic electronic or quasiparticle states. This could pave the way for new physical properties related to phonons and structural phase transitions in TMDs and the discovery of universal and novel physical phenomena resulting from electron-phonon interactions.

The Hase Group at the University of Tsukuba, where I joined as a Ph.D. student, has a significant experimental instrument to investigate the time-domain dynamics of coherent phonons in solids by high-time resolution and has reported numerous light-induced phase transition phenomena. Additionally, collaboration with the Hada Group in the same department allows for direct evaluation of structural changes by utilizing ultrafast electron diffraction instruments. By making the most of such an environment, I began my long research journey as an undergraduate/graduate student to discover new non-equilibrium physical phenomena involving structural phase transitions and phonons in TMDs.

1.3 Motivation and Structure of This Thesis

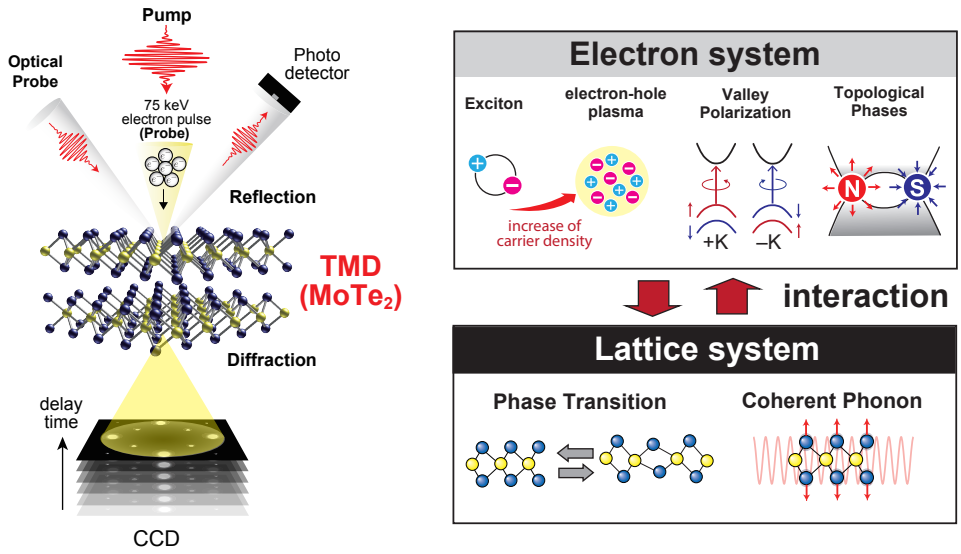

Figure 1.5: Schematic description of the aim of this thesis. Left panel shows experimental pump-probe methods conceived in this thesis: transient reflectivity change and ultrafast electron diffraction measurements. Right panel represents the interaction between electron and lattice systems of $MoTe_2$ upon photoexcitation.

In this thesis, I am pursuing to gain insight into the photo-excited electron-lattice system in polymorphic $MoTe_2$ from the perspectives of coherent phonons via reflective-type optical pump-probe spectroscopy [Fig. 1.5]. In particular, my research aims to clarify the role of electron-phonon interactions upon photoexcitation: how the presence of photoexcited carriers involves structural phase transitions and how the coherent lattice motions can modify the electronic and optical properties of materials.

Chapter 2 shows the fundamentals of femtosecond pulsed lasers, experimental methods, and optical layouts to characterize the coherent phonons and structural dynamics: transient reflectivity-change and ultrafast electron diffraction measurements.

In Chapter 3, I will detail comprehensively how the coherent phonons in solids are generated and detected from the perspectives of history, theory, and experiment. In this thesis, time-domain observation of coherent phonon and its interpretation is essential to figure out structural changes upon photoexcitation and electronic modulations via

electron-phonon interactions.

In Chapter 4, I present the comprehensive investigation of photo-induced Tellurium segregation and how much excitation density can be applied to $MoTe_2$ polymorphs: a semiconductor 2H phase and the semimetal 1T' phase under various incident laser conditions to further explore the light-induced structural phase transition in $MoTe_2$ under high-density electronic excitation conditions.

In Chapter 5, I will show the ultrafast coherent interlayer shear lattice vibration dynamics of $1T' - MoTe_2$ at room temperature.

In Chapter 6, I will show how many-body phenomena, such as electron-hole and electron-phonon interactions in the non-equilibrium regime, can change the electronic and optical properties of a layered semiconductor $2H - MoTe_2$ in the presence of an extremely long-lived coherent optical phonon.

In Chapter 7, by making use of the knowledge obtained from the study in Chapter 4, the investigation of ultrafast structural dynamics in $2H - MoTe_2$ under 400-nm photoexcitation and high-density excitation density ($1 \sim 30$ mJ/cm^2) below damage threshold has been demonstrated by complementary methods combining the coherent phonon spectroscopy and ultrafast electron diffraction measurements.

Lastly, I will summarize this thesis in chapter 8. In addition, I suggest the future outlook from my point of view, where more investigations are expected following this thesis.

Chapter 2

Experimental Methods

This chapter introduces the technical descriptions on femtosecond pulsed lasers and ultrafast methodologies. The first part of this introduction includes the femtosecond oscillator, regenerative amplifier, and optical parametric amplification (OPA). The second part describes the principles of pump-probe measurements used in my studies, such as transient reflectivity and ultrafast electron diffraction measurements. Finally, I'll detail the short-time Fourier transform (STFT) analysis process for time-frequency-domain data evaluation.

2.1 Femtosecond Laser Sources

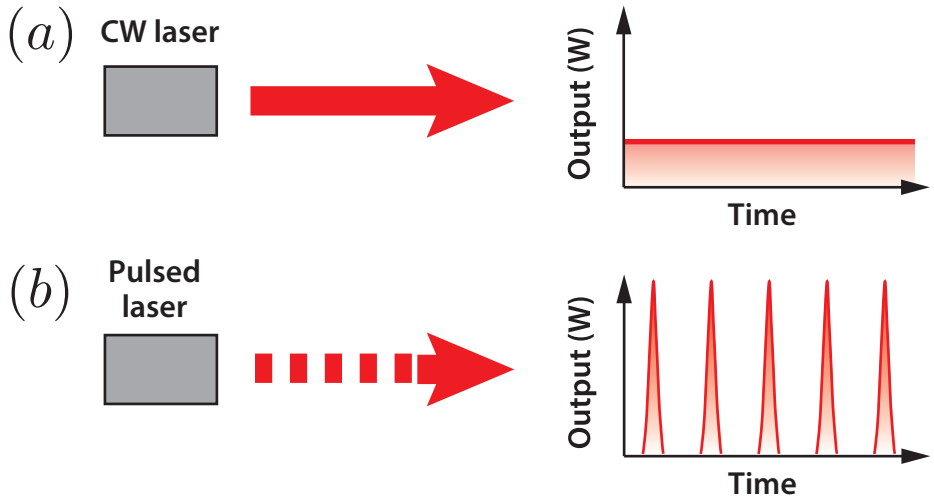

Figure 2.1: Schematic illustration of continuous wave (CW) laser (a) and pulsed laser (b) and their time evolution of light intensity.

There are currently two main kinds of laser sources: continuous wave (CW) lasers and pulsed lasers, as shown in Fig. 2.1. CW lasers contain only a single frequency and have a constant intensity over time. On the other hand, pulsed lasers can emit light with significantly high intensity in an extremely short time like the flash of a camera. The use of high-intensity femtosecond lasers is essential for facilitating wavelength conversion via nonlinear optical effects and for the temporal investigation of ultrafast dynamics in the electrons and structures of solids, employing pump-probe experiments. In this section, I will describe the processes involved in generating, amplifying, and altering the wavelength of femtosecond lasers.

2.1.1 Oscillator System

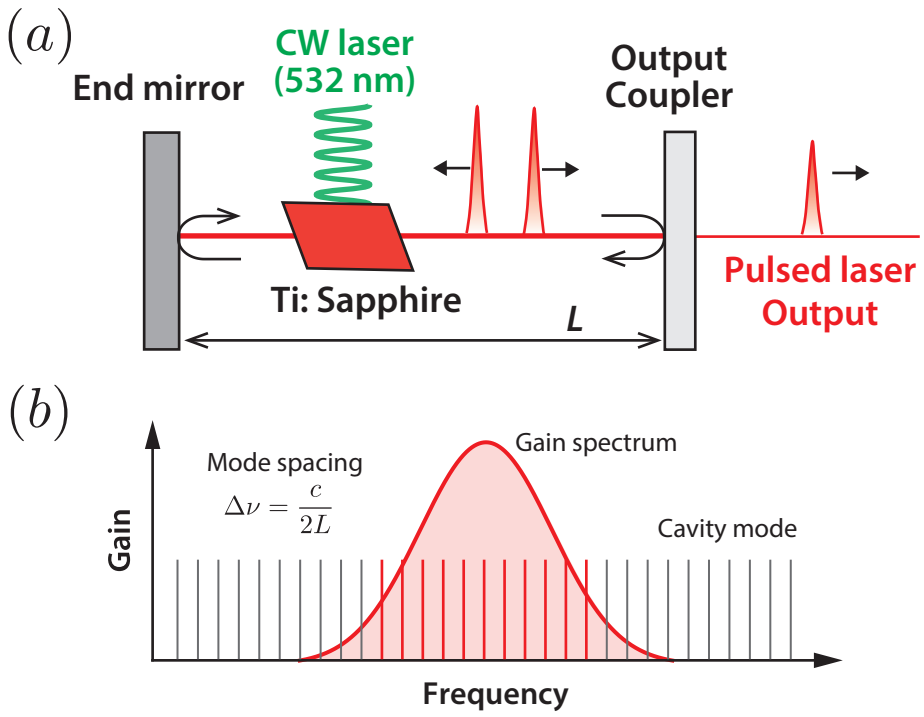

Figure 2.2: (a) Schematic configuration of the cavity structure of a Ti:Sapphire femtosecond-laser oscillator. (b) Gain spectrum produced by a Ti:Sapphire crystal when excited by a CW laser and longitudinal cavity modes formed into a comb-like structure, the spacing of which is determined by the cavity length L.

In a Ti:Sapphire crystal laser source, broad gain-spectrum light emitted from the crystal excited by a CW laser is confined within a cavity structure by two pairs of mirrors. When the temporal phases of each light electric field align in the laser cavity, femtosecond pulsed laser can be output. Such a femtosecond laser source are referred to as a "femtosecond oscillator". The properties of the oscillator can be understood using the Fabry-Perot cavity model. Inside the cavity length L, enclosed by two pairs of mirrors — one being a fully reflective end mirror and the other a partially transmitting output coupler — under the resonance conditions, the output light spectrum has a comb-like

longitudinal cavity modes with mode spacing $\Delta\nu$ as follows:

$$\Delta\nu = \frac{c}{2L}. \tag{2.1}$$

where c is the light speed. This $\Delta\nu$ is also known as the repetition rate of pulsed-laser output, determined by only L. Furthermore, the light waves of the cavity modes within the gain spectrum are involved in pulse generation. The more cavity modes included (smaller intervals between modes, or the longer L), the stronger and shorter the ultra-short pulses that can be generated.

The operation of aligning the temporal phases of such laser cavity modes is called "Mode locking (ML)". There are two types of ML: passive and active. Passive ML automatically aligns the phases of laser cavity modes without any external operations within the laser cavity. In contract, active ML involves directly controlling the phase of light operating devices like acoustic-optic modulators (AOMs) within the laser cavity. Currently, the most commonly used is passive ML, as is referred to as Kerr-lens mode locking (KLM). In KLM, the refractive index of the medium changes due to the Kerr effect when a high-intensity light electric field passes through the medium. The Kerr effect is a third-order nonlinear optical effect, where the refractive index n of the medium changes linearly with the light intensity I:

$$n(I) \approx n_0 + n_2 I, \tag{2.2}$$

where n_0 is the intrinsic refractive index and n_2 is the nonlinear coefficient. Therefore, a strong electric field causes self-focusing in the medium, reducing the beam diameter. This property ensures that only strong pulses with reduced beam diameters due to the Kerr effect can pass through a slit with small diameter, while the portion of CW laser, which have weaker intensity and larger beam diameters, cannot. While traveling back and forth several times within the laser cavity, only the strong light is selectively enhanced, and the phase of the light is automatically fixed. It should be noted that

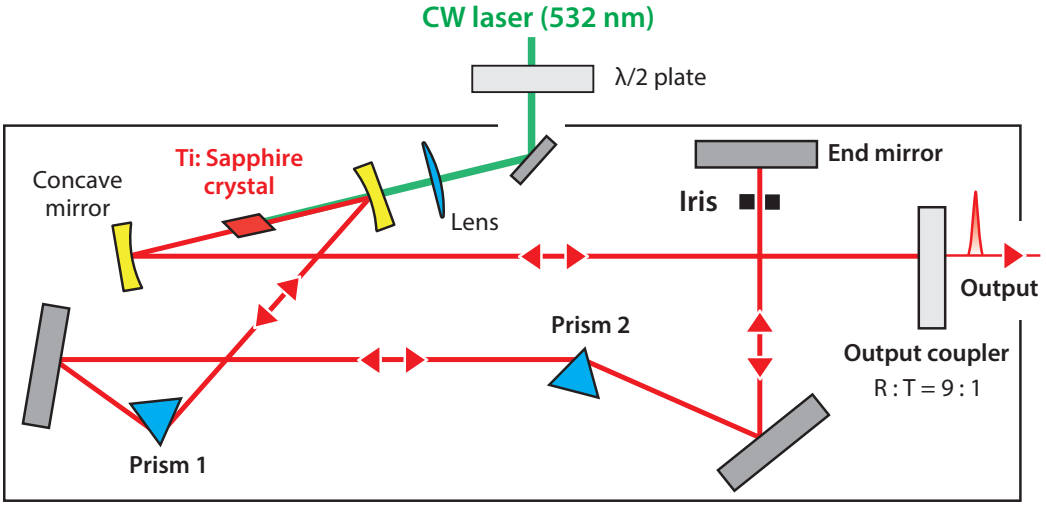

Figure 2.3: Optical layout of a typical femtosecond oscillator using in this study (KMLabs Chinook-875 Ti:Sapphire oscillator).

it's necessary to include dispersion compensation systems, such as a pair of prisms to compensate for pulse width broadening due to group velocity dispersion when passing through optical elements.

A typical example for optical layout of Ti:Sapphire femtosecond oscillator, KMLabs Chinook-875 (*Kapteyn-Muranane Laboratories*), mainly used in this study is depicted in Fig. 2.3. It generates a broad-spectrum when the Ti:Sapphire crystal is excited by a CW laser, Millenia eV (*Spectra-Physics*), output of 4.8 W $Nd : YVO_4$ laser at 1064 nm, which is converted to the second harmonic at 532 nm. The Kerr effect occurring in the Ti:Sapphire crystal plays a role in KLM. A prism pair is placed for dispersion compensation. By adjusting Prism 2, the pulse width can be adjusted. This oscillator can produce femtosecond pulses with a central wavelength of 830 nm, pulse width of $\sim$ 30 fs, and repetition rate of 80 MHz. Between Prism 2 and the end mirror, the wavelengths of light are spatially dispersed. Thus, by placing an iris in this space, the central wavelength can be varied from approximately 820 nm to 880 nm. However, this narrows the range of wavelengths in the pulse, broadening the pulse width to 40-60 fs.

2.1.2 Regenerative Amplifier System

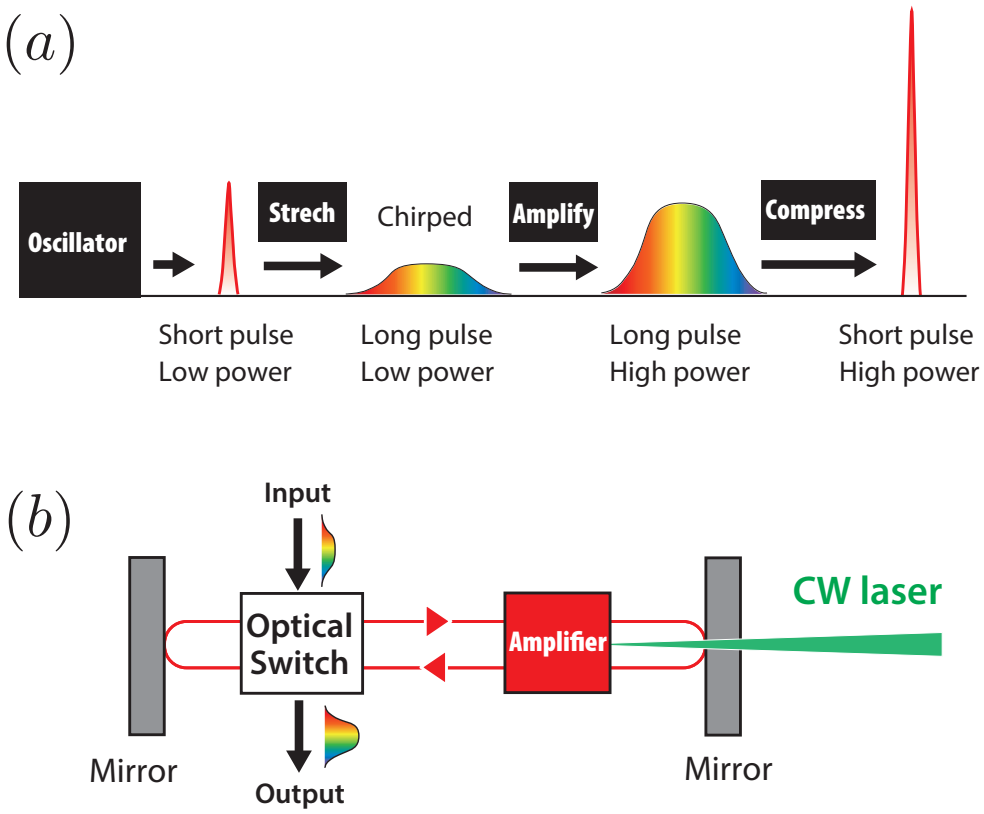

Figure 2.4: (a) Schematic illustration of the general procedure of chirped-pulse amplification (CPA) method. Grating pairs are used for the stretching and compression of pulsed light. (b) Schematic configuration of regenerative amplifier system. Generally, Pockels cells are used for optical switch.

The femtosecond pulses generated by the oscillator system described in the previous chapter are not strong enough per pulse to cause wavelength conversion through nonlinear optical effects or high-density excitation phenomena, posing a problem for practical applications. Here, I will briefly introduce chirped pulse amplification (CPA) and regenerative amplifiers.

CPA is the most widely used scheme for amplification of ultrashort pulses. The process of CPA can be described in Fig. 2.4(a). First, the low-peak intensity ultrashort pulse output from the oscillator is used as seed light. Next, the pulse is temporally

stretched using a pair of diffraction gratings, reducing its peak intensity. This process is called "chirping" of pulses. Then, the intensity of chirped pulse is amplified. Finally, the pulse width is compressed again using the diffraction gratings, producing ultra-short pulses with huge-peak intensities. The key feature of CPA is that it allows the amplification of light intensity without damaging optical elements by lowering the peak intensity with chirped pulses. This groundbreaking method of pulse amplification through CPA contributes to the understanding and development of various high-intensity light properties and spectroscopy techniques, including nonlinear optical phenomena and THz generation and its applications. As a result of such ripple effects, as introduced in Chapter 1, Mourou and Strickland, who developed this technique, were awarded the Nobel Prize in Physics in 2018.

A regenerative amplifier is one of the methods in CPA to amplify chirped pulses. The amplification process is simply described in Fig. 2.4(b). First, from a series of pulses ranging from tens to 100 MHz, just one pulse is selected and trapped inside the cavity containing the gain medium. Then, right after the gain energy stored in the medium reaches saturation from the pulse traveling back and forth, the amplified pulse is extracted from outside the cavity. By temporally modulating the voltage applied to a Pockels cell and controlling the polarization characteristics, it is possible to switch the beam path between trapping the pulse inside the resonator and extracting it outside. This process allows the energy of a single pulse to be amplified by about 10^3 to 10^6 times. By using such highly amplified femtosecond pulse lasers, wavelength conversion processes, such as second-harmonic generation (SHG) and optical parametric amplifier (OPA) can be carried out efficiently.

2.1.3 Optical Parametric Amplifier (OPA)

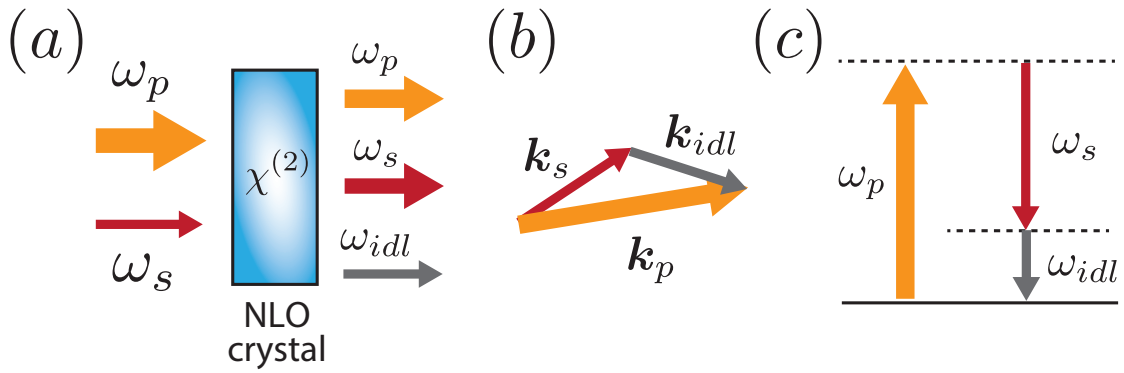

Figure 2.5: (a) Schematic illustration of wavelength conversion process by optical parametric amplification (OPA) through a nonlinear optical (NLO) crystal. ω_p and ω_s denotes pump light and lower-frequency seed light (signal light after the NLO crystal), respectively. ω_{idl} is the idler light. (b) Light-momentum conservation diagram of OPA process. (c) Energy conservation diagram of OPA process.

Using high-intensity femtosecond pulsed lasers dramatically enhances the efficiency of nonlinear optical effects in materials. Consequently, various wavelength conversions can be efficiently performed. OPA is one such method of wavelength conversion, a second-order nonlinear optical process that generates two photon energies from one photon energy, as depicted in Fig. 2.5(a). In this process, intense pump light (photon energy ω_p) and weak seed light (ω_s) are spatially and temporally overlapped and focused at incident angles that meet the phase matching condition (Fig. 2.5(b)) in a nonlinear optical crystal (NLO) with broken spatial inversion symmetry. Due to the $\chi^{(2)}$ process of NLO, the seed light is amplified as a signal light. Furthermore, long-wavelength idler light ($\omega_{idl} = \omega_p - \omega_s$) is also generated, as shown in Fig. 2.5(c). Typically, broadband near-infrared white light ($1.1 \sim 1.6$ μm) is used as seed light. When using 800 nm (1.55 eV) from a Ti:Sapphire source as pump light, signal light with a variable central wavelength of $1.1 \sim 1.6$ μm ($0.78 \sim 1.1$ eV) and idler light of $1.6 \sim 2.8$ μm ($0.45 \sim 0.77$ eV) can be obtained through OPA, as well as residual of the pump light. Such output can be used for further wavelength conversions, such as second-harmonic

generation (SHG) or difference-frequency generation (DFG). Therefore, OPA enables the investigation of excitation and optical responses in broad ranges of photon energy.

2.2 Principle of Pump-Probe Methods

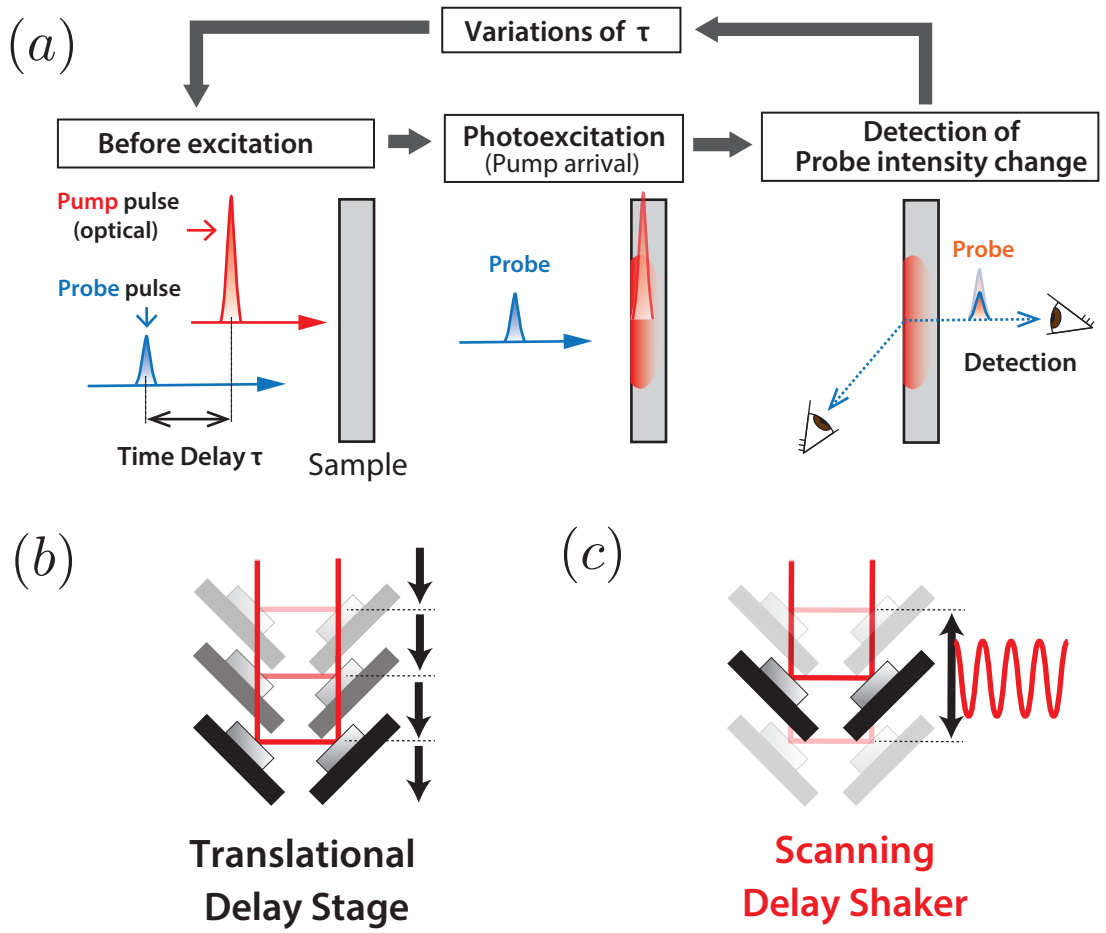

Figure 2.6: (a) Schematic procedure of general pump-probe method. Variation of pump-probe time delay τ facilitated by (b) translational delay stage and (c) scanning delay shaker (oscillating mirrors).

The pump-probe experiments are the most widely used and powerful strategies for investigating ultrafast phenomena of matter by tracking changes in various physical quantities in the time domain. Intense ultrashort laser pulses having a time duration

from nanosecond (ns: 10^{-9} s) to femtosecond(fs: 10^{-15} s) or sub-fs are used for the pump-probe measurements. In principle, the pump-probe experiments are carried out in the following process (Fig. 2.7(a)): at first, an optical pump pulse excites electrons and lattice on the sample surface; subsequently, a time-delayed probe pulse after the arrival of the pump pulse passes through the photoexcited sample surface, leading to the probe intensity change in each time delay. Usually, the time delay in pump-probe experiments is adjusted by altering the optical path of the pump pulse, using either a translational delay stage or a modulated delay shaker, as depicted in Fig. 2.7(b). Finally, a transient time response can be obtained as a series of the acquired probe intensity changes depending on pump-probe time delays. This involves non-equilibrium properties of matters under impulsive excitation. It should be noted that the time resolution of the pump-probe measurement is determined by the duration of the laser pulse or auto-correlation time of the pump and probe pulses, which can be evaluated by nonlinear correlation using SHG, frequency-resolved optical gating (FROG) methods, and so on. Shorter laser pulses allow time-resolved tracking of fast physical phenomena, such as coherent phonon having fine temporal periodicity (e.g., $10^0 \sim 10^2$ fs). Various pump-probe experiments depend on what kinds of pump and probe sources are used and how to detect them. The most straightforward scheme is an optical pump-probe experiment. This scheme uses the pulsed light for both pump and probe with transmission and reflection geometries. The observed transient transmission and reflectivity changes involve the dynamics of photoexcited electron and phonon generations and relaxations.

To date, various advanced pump-probe experiments have been developed to investigate more specific physical quantities than that obtained in optical measurements, such as time-resolved diffraction methods based on electron (UED) and X-ray (tr-XRD) probe pulses, angle-resolved photoemission spectroscopy (tr-ARPES), scanning-tunneling microscopy(THz/MIR-STM), and so on.

2.3 Transient Reflectivity Measurement (Coherent Phonon Spectroscopy)

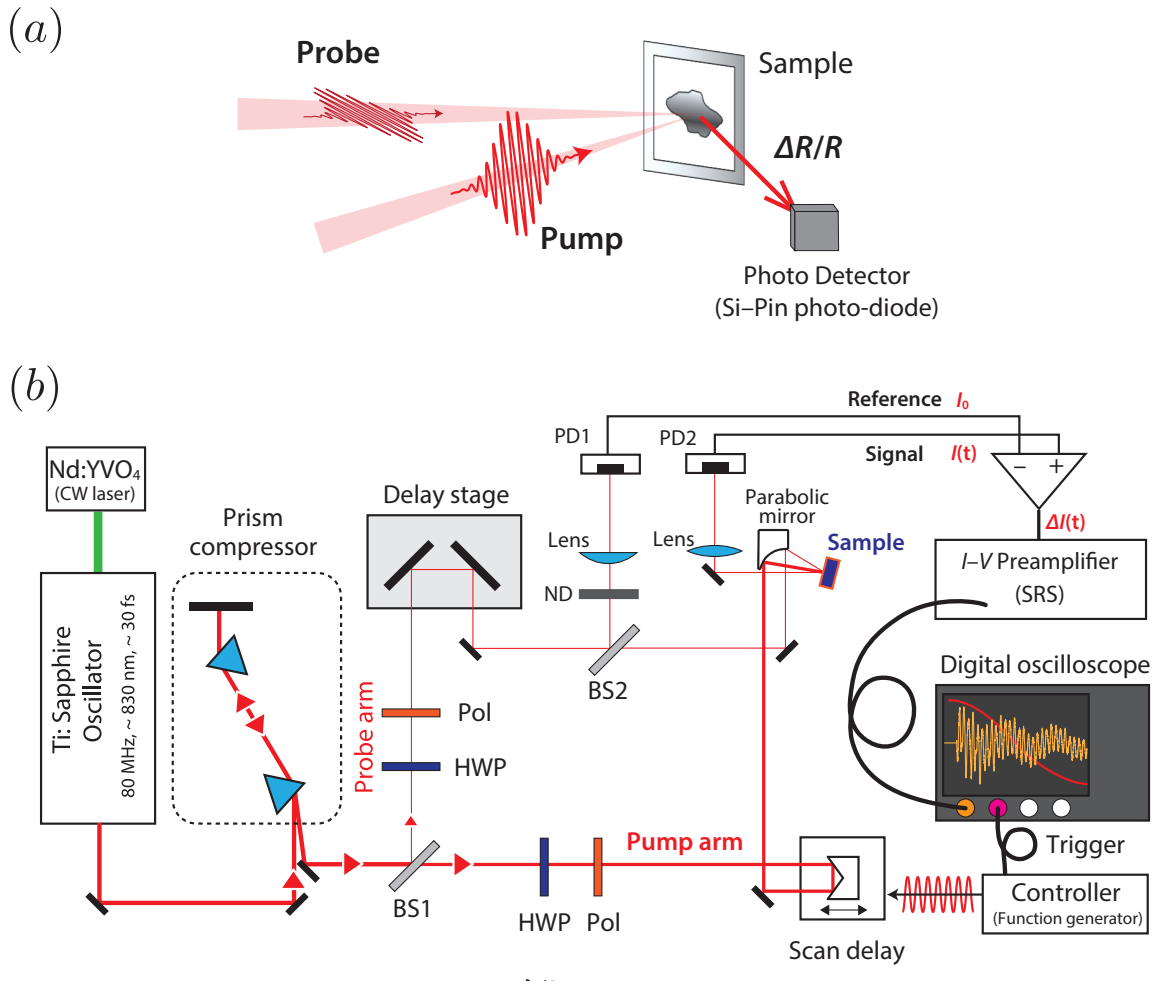

Figure 2.7: (a) Schematic configuration of time-resolved reflectivity change ($\Delta R/R$) measurement. (b) Optical layout of $\Delta R/R$ measurement using 80 MHz femtosecond-laser oscillator, where HWP is the $\lambda/2$ wave plat, Pol is the polarizer, BS is the beam splitter, ND is the neutral-density filter, PD is the Si-Pin photo-detector.

2.3.1 Fundamental

The transient reflectivity measurement is one of the most fundamental optical pump-probe experiments to investigate ultrafast phenomena of solids such as electron and

phonon dynamics. The transient reflectivity measurement is a special case for the probe pulse using light with a reflection geometry, as shown in Fig. 2.7(a). Figure 2.7(b) shows an optical layout of transient reflectivity-change measurement operated at an 80-MHz Ti:Sapphire laser source (wavelength $\sim$ 830 nm and pulse duration $\sim$ 30 fs), demonstrated in my study. In the present optical layout, the group velocity dispersion given by optical elements is first compensated by a prism pair, then the light is split into pump and probe path. The light intensity is adjusted using a combination of half-wave plate (HWP) and polarizer (Pol), making the pump light s-polarized and the probe light p-polarized. The optical-path length of the pump arm is modulated by a delay shaker (Scan Delay, *APE-Berlin*), and then the light is focused on the sample using a parabolic mirror. The probe light is split from the light for the reference signal and then focused on the sample. Where the pump and probe lights overlap temporally and spatially, the reflected probe light is focused onto a Si-Pin photo-detector (PD1) with a +18 V bias. The photocurrent from PD1 ($I(t)$) is subtracted from the photocurrent (I_0) of the reference light on PD2, which has a -18 V bias, taking the difference $\Delta I(t) = I(t) - I_0$. To adjust the average value of the differential current being zero, the reference photocurrent is adjusted by the ND filter. Then, $\Delta I(t)$ is amplified to a large voltage signal by an I-V preamplifier (SRS) and connected to an oscilloscope. Using the driving AC signal applying to the delay shaker as a trigger signal, the synchronized time-resolved signal of $\Delta I(t)$ is displayed in real-time on the oscilloscope. Finally, $\Delta R(t)/R$ is given by

$$\frac{\Delta R(t)}{R} = \frac{\Delta I(t)}{I_0} = \frac{I(t) - I_0}{I_0}. \tag{2.3}$$

In general, the measured transient reflectivity change $\Delta R/R$ in time domain involves following physical processes:(i) transient electronic response upon photoexcitation; (ii) electronic relaxation due to various scattering processes in the form of an exponential decay function; (iii) coherent phonon oscillation in the form of damped sinusoidal functions. The process of (i) can be seen within sub-picosecond, which is time duration of optical pulses. The process of (ii) and (iii) can be generally observed for time

period from several to several hundred picoseconds after photoexcitation. The coherent phonon oscillation can be extracted by subtracting the contributions from (i) and (ii) from the $\Delta R/R$ signal. By fitting the data with a damped oscillation function or Fourier transform analysis, we can calculate the initial amplitude, frequency, and decay constant of the coherent phonon signal. The frequency spectrum obtained from the Fourier transform can be compared with the static Raman spectrum. This comparison allows us to identify the vibration patterns and symmetries (e.g., A_g mode or E_g mode) of the phonons or other quasi-particle mode. Varying laser parameters for pump and probe light, such as fluence (pump-light intensity), wavelength, or polarization, enables a deeper understanding of the characteristics of various involved lattice dynamics and interactions. These include structural phase transitions, electron-phonon interactions, phonon-phonon interactions, and scattering mechanisms.

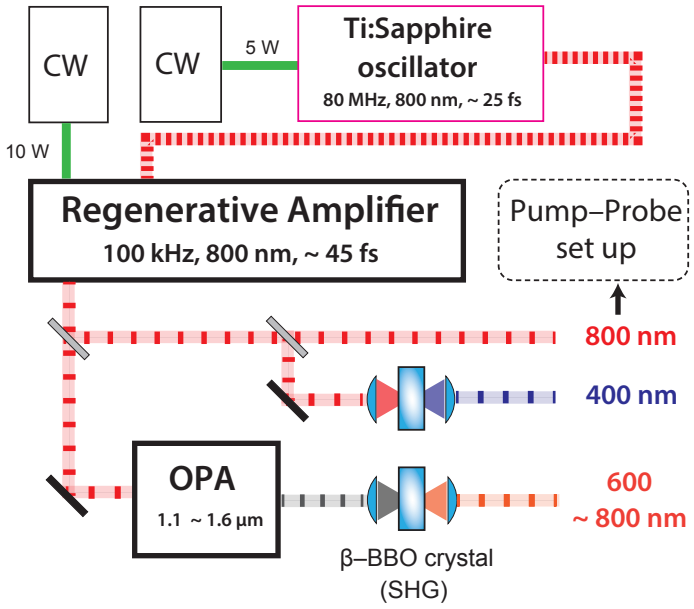

Figure 2.8: Schematic configuration of the layout for an optical experiment using a 100kHz regenerative amplifier and a wavelength conversion process (OPA and SHG).

For comprehensive investigations under high-density excitation and varying wavelength conditions, the regenerative amplifier, complemented by wavelength conversion techniques such as SHG and OPA, is utilized as a laser source, as illustrated in Fig.

2.8. In the optical layout, a femtosecond oscillator (Mantis, *Coherent*), serves as the seed light source for amplification. This oscillator provides an output with a repetition frequency of 80 MHz, a wavelength of 800 nm, and a pulse duration of $\sim$ 20 fs. A 10-W 532-nm CW light source (Verdi12, *Coherent*), pumps a regenerative amplifier. The seed pulse is amplified through the regenerative amplifier (RegA 9000, *Coherent*) and a stretcher/compressor (RegA 9840, *Coherent*). Consequently, an amplified pulse with a repetition rate of 100 kHz, the central wavelength at 800 nm, the pulse duration of $\sim$ 45 fs, the pulse energy $>$ 6 μJ is output. By utilizing a β-BBO (Beta Barium Borate) crystal, a 400 nm is generated via SHG with a pulse width of about 60 fs. Additionally, an OPA (*Coherent* model 9850) facilitates the generation of near-infrared (NIR) light in the variable wavelength range of 1.1 $\sim$ 1.6 μm. The NIR light output from OPA can be further converted into the wavelength range of 600 $\sim$ 800 nm (a pulse duration of $\sim$ 60 fs) through SHG facilitated by the BBO crystal. Both the 800 nm pulses from the regenerative amplifier and those obtained through wavelength conversion are then introduced into a pump-probe optical system, as depicted in Fig. 2.7(b).

2.3.2 Fast Scanning System

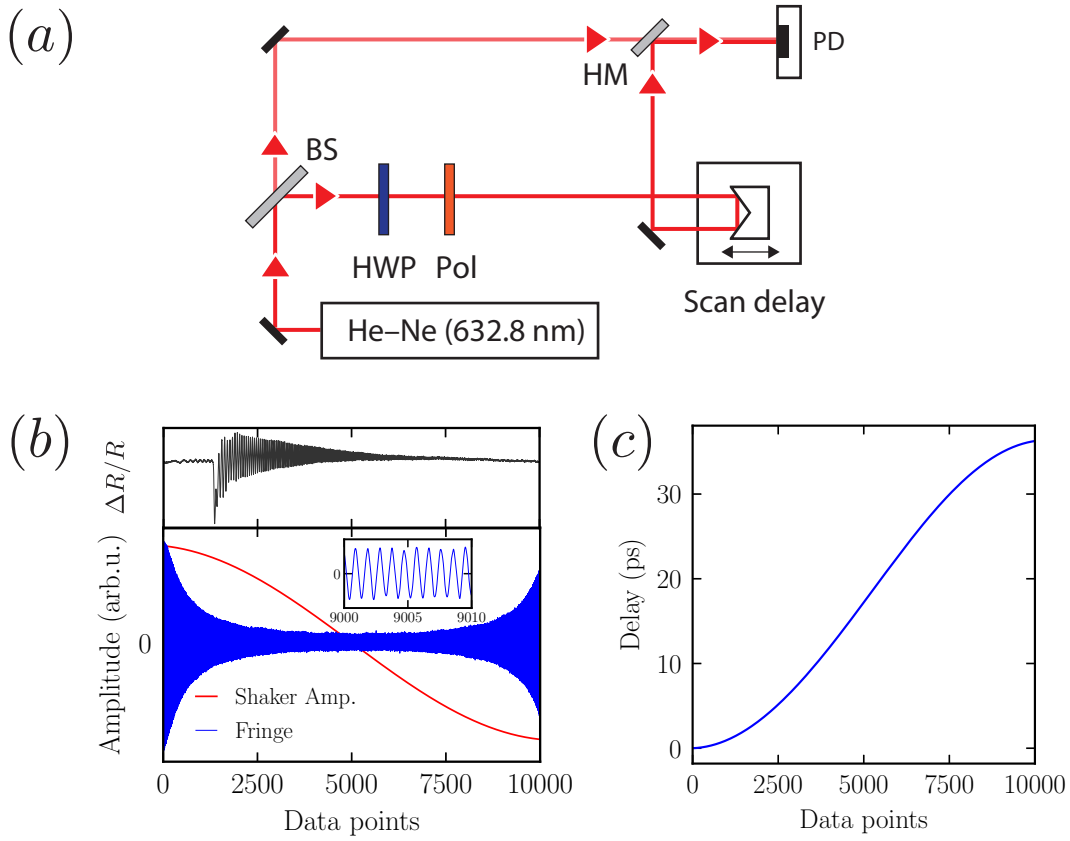

Figure 2.9: (a) An optical layout for a Michelson interferometer, designed to calibrate the time axis of acquired time-domain data. (b) Acquired raw time-domain data (displayed in the upper panel) and the interferometric fringe pattern of a He-Ne laser (with a wavelength of 632.8 nm) observed during the half cycle of mirror modulation. The inset exhibit a fine temporal periodic pattern of the fringe, whose periodicity corresponds to ~ 2.11 fs based on the wavelength of the He-Ne laser. (c) Calibrating data points into time delay based on the interferometric fringe.

The fast-scanning method is a technique for acquiring time-resolved signals by automatically generating optical delays using a mechanical oscillator, commonly referred to as a delay shaker. This method synchronizes changes in the probe light current ($\Delta I(t)$) from Si-Pin photo-detector with the temporal delay modulation caused by the delay shaker oscillating at around 10Hz, displaying the time-domain signal in real-time on

an oscilloscope. By accumulating data on the oscilloscope for about 5 minutes, it is possible to obtain time-domain signals with an exceptionally high signal-to-noise (S/N) ratio that can reflect changes as small as 10^{-7}. Another significant advantage of this method is the ease of adjusting the temporal and spatial overlap of the pump and probe lights while monitoring the time-domain signal on the oscilloscope, a benefit not available with the traditional translation of the delay stage.

In the transient reflectivity change measurements, the delay shaker scans approximately 30 ps of time delay with a 9.5 Hz sine wave. Due to the slow scan speed near the endpoints in the sine wave oscillation, the measured time-domain signals become temporally distorted [see upper panel of Fig. 2.9(b)]. Therefore, it is necessary to calibrate the time axis. Fig. 2.9(a) illustrates a Michelson interferometer incorporated into the optical system for this purpose, using a He-Ne laser as the light source. The 632.8 nm light from the source is split into two paths by a beam splitter (BS). One path passes through the delay shaker, and the other is the reference light. These two beams recombine at a half-mirror (HF) and interfere on a photo-detector, maintaining their spatial overlap. The movement of the delay shaker causes a change in the temporal phase of light, resulting in a temporally varying interference pattern observed on the oscilloscope as shown in the lower panel of Fig. 2.9(b). One cycle of the observed interference pattern corresponds to approximately 2.11 fs, equivalent to the time period of 634.2 nm. This relationship is used to calibrate the time delay for each data point as shown in Fig. 2.9(c).

It should be noted that while the fast-scanning method is specialized for efficiently acquiring one-dimensional time-domain data, including coherent phonon signals, it is not a universal technique applicable to all time-domain spectroscopy methods. For instance, time-domain measurements using two-dimensional data from CCDs are not suitable for this method due to the inability of data transfer speeds to keep up with the modulation frequency of the delay shaker.

2.4 Ultrafast Electron Diffraction Measurement

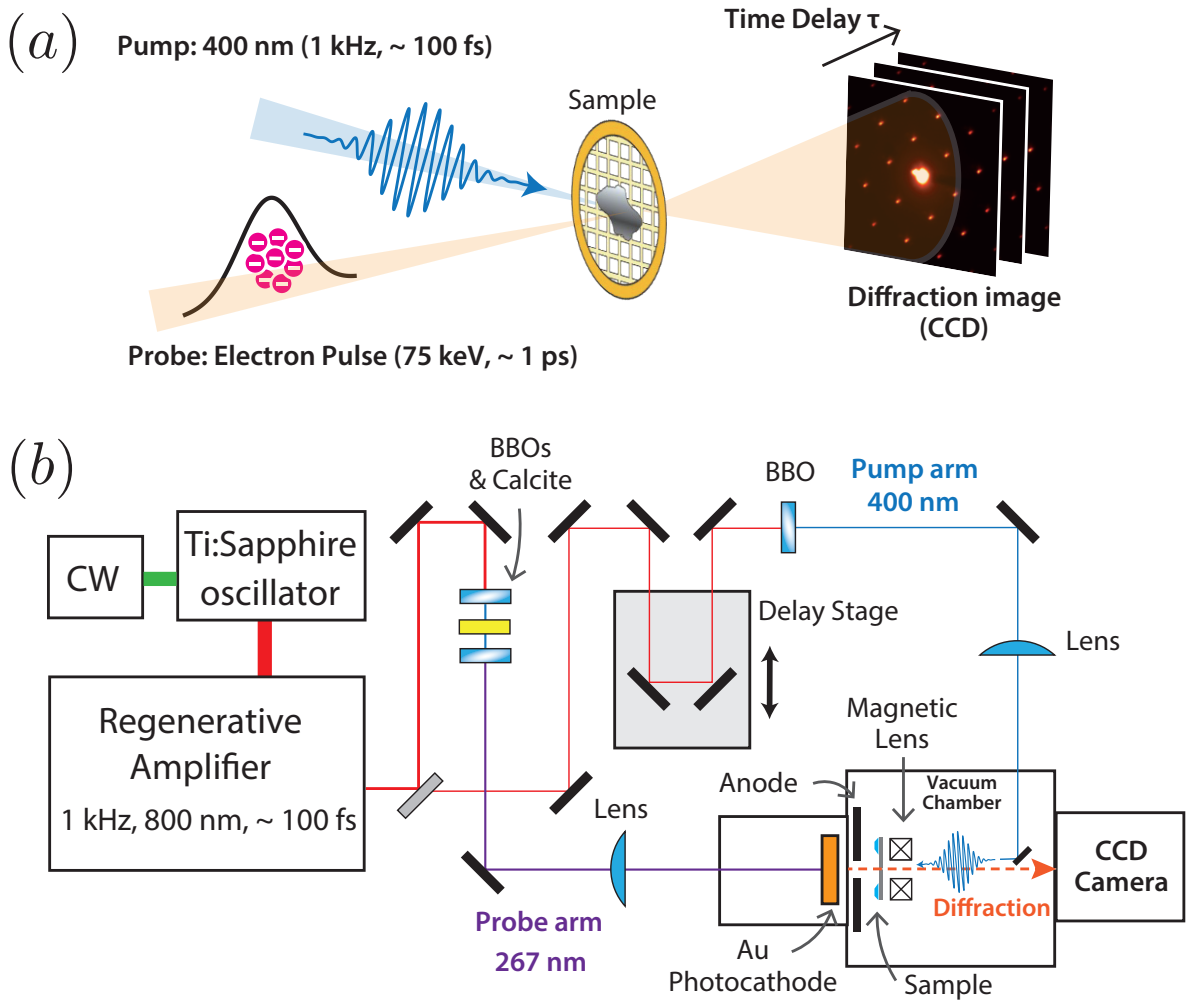

Figure 2.10: (a) Schematic configuration of pump-probe time-resolved ultrafast electron diffraction (UED) measurement.(b) Optical layout of the UED measurement.

2.4.1 Fundamental

Ultrafast electron diffraction is a method where a ultrashort pulse light is used as a pump to excite a sample, and an electron pulse is used as a probe to be incident on the sample. This method measures diffraction images that correspond to the symmetry of the crystal structure. Therefore, it is a significantly powerful tool for direct observation

and evaluation of temporal evolution of crystal structure deformations.

In principle, when X-rays or electron beams with wavelengths (or energies) equal to or less than the spatially periodic lattice planes in a crystal are directed onto the crystal, scattered waves with an intensity distribution corresponding to that periodicity are produced, giving rise to a constructive interference. This is referred to as crystal diffraction, often described by Bragg's law:

$$2d \sin\theta = n\lambda, \tag{2.4}$$

where d is the spacing of lattice plane, θ is the glancing angle, n is the integer, and λ is the wavelength. When an incident ray with wave vector $\boldsymbol{k}$ is scattered by a scattering body from k_0, the scattering factor (structure factor) $F(\boldsymbol{K})$ is defined as follows:

$$F(\boldsymbol{K}) = \int_V dv\ \rho(\boldsymbol{r}) \exp\left(-2\pi i \boldsymbol{K}\cdot\boldsymbol{r}\right), \tag{2.5}$$

where $\rho(\boldsymbol{r})$ is electron density in the scattering body , $\boldsymbol{K} = \boldsymbol{k} - \boldsymbol{k}_0$ is the scattering vector of rays, and V is the volume of the crystal. When $\boldsymbol{K}\cdot\boldsymbol{r}$ is an integer, $F(\boldsymbol{K})$ is significantly enhanced. In the case of the spatially periodic crystal, the axes of a unit cell can be defined as $\boldsymbol{a}_1$, $\boldsymbol{a}_2$, and $\boldsymbol{a}_3$. When an atom located in the average position $\langle\boldsymbol{r}_j\rangle$ in a unit cell, the average position in the entire crystal can be written as follows:

$$\boldsymbol{r}_{uvw,j} = \langle\boldsymbol{r}_j\rangle + u\boldsymbol{a}_1 + v\boldsymbol{a}_2 + w\boldsymbol{a}_3, \tag{2.6}$$

where u, v, and w are the integers. Since the spatial electron-density distribution around $\boldsymbol{r}_{uvw,j}$ is defined as $\rho_j(\boldsymbol{r} - \boldsymbol{r}_{uvw,j})$ in a unit cell, the electron density in the entire

crystal can be written as follows:

$$\begin{aligned}\rho_{\mathrm{tot}}(\boldsymbol{r}) &= \sum_{u,v,w}\sum_{j}\rho_j(\boldsymbol{r}-\boldsymbol{r}_{uvw,j}) \\ &= \sum_{u,v,w}\sum_{j}\rho_j(\boldsymbol{r}-\langle\boldsymbol{r}_j\rangle-u\boldsymbol{a}_1-v\boldsymbol{a}_2-w\boldsymbol{a}_3)\end{aligned} \tag{2.7}$$

By substituting Eq. (2.7) into Eq. (2.5), scattering factor from the crystal can be derived as follows:

$$\begin{aligned}F_{\mathrm{tot}}(\boldsymbol{K}) &= \int_V dv\ \rho_{\mathrm{tot}}(\boldsymbol{r})\exp\left(-2\pi i\boldsymbol{K}\cdot\boldsymbol{r}\right) \\ &= \sum_{u,v,w}\exp\left[-2\pi i\boldsymbol{K}\cdot(u\boldsymbol{a}_1+v\boldsymbol{a}_2+w\boldsymbol{a}_3)\right] \\ &\quad\times\sum_{j}\exp\left[-2\pi i\boldsymbol{K}\cdot\langle\boldsymbol{r}_j\rangle\right]\int_V dv\ \rho_j(\boldsymbol{r})\exp\left(-2\pi i\boldsymbol{K}\cdot\boldsymbol{r}\right) \\ &= G(\boldsymbol{K})\sum_{j}f_j(\boldsymbol{K})\exp\left[-2\pi i\boldsymbol{K}\cdot\langle\boldsymbol{r}_j\rangle\right].\end{aligned} \tag{2.8}$$

$G(\boldsymbol{K})$ denotes Laue's function, which determines the Bragg's angle of diffraction in crystallography. More specifically, when $\boldsymbol{K}$ is the reciprocal vector $\boldsymbol{q}$ for the lattice vectors $\boldsymbol{a}_1$, $\boldsymbol{a}_2$, and $\boldsymbol{a}_3$: i.e., $\boldsymbol{q}_{hkl}=h\boldsymbol{b}_1+k\boldsymbol{b}_2+l\boldsymbol{b}_3$, where h, k, and l are integers, and b_n is a reciplocal vector for each axes satisfying $\boldsymbol{a_n}\cdot\boldsymbol{b_n}=2\pi$, then $G(\boldsymbol{q}_{hkl})$ becomes a large value. Consequently, when the scattering vector coincides with a reciprocal lattice vector of the crystal, the total structure factor F_{tot} is significantly enhanced, leading to observable diffraction patterns. The diffraction intensity depends on $\sum_j f_j(\boldsymbol{K})\exp\left[-2\pi i\boldsymbol{K}\cdot\langle\boldsymbol{r}_j\rangle\right]$.

2.4.2 Set Up

The optical layout used for the UED measurement is illustrated in Fig. 2.10. The laser sources consist of a 532-nm CW laser (Millennia eV, Nd:YVO4, *Spectra-Physics*), an actively mode-locked Ti:Sapphire laser (Tsunami, *Spectra-Physics*) with an Acousto-optic modulator (AOM), a 527-nm Q-switched solid-state laser (Empower, Nd:YLF,

Spectra-Physics), and a regenerative amplifier (Spitfire Pro XP, *Spectra-Physics*s).

Initially, the Tsunami is excited by a 532-nm, 5-W CW laser, producing output at a central wavelength of 800 nm, with a pulse width of 100 fs and a repetition rate of 82 MHz. Femtosecond pulses are then input into the Spitfire Pro XP regenerative amplifier, which is excited by a 527-nm, 20-W laser. This results in output with a central wavelength of 800 nm, a pulse width of 100 fs, a repetition frequency of 1 kHz, and a pulse energy of 3.5 mJ.

Subsequently, the beam is split by a beam splitter into pump and probe lights. The pump light is converted to a wavelength of 400 nm using a BBO crystal and then focused on the sample placed inside a vacuum chamber. The probe light is first focused through one BBO crystal, and its dispersion caused inside the BBO is compensated using the birefringence of Calcite. A second BBO crystal generates near-ultraviolet light at 267 nm, the sum frequency of the fundamental 800 nm and second harmonic 400 nm lights. During reflection off the mirrors, wavelengths other than 267 nm are eliminated, and the light is focused onto an Au photocathode inside the vacuum chamber, generating electrons through the photoelectric effect. Electrons are accelerated by the electrostatic field generated between the photocathode, to which a voltage of -75 kV is applied, and anode, and then directed towards the sample. Electrons diffracted through the sample are focused onto a CCD camera by the magnetic lens. The CCD finally captures the images of diffraction patterns. By moving the translational delay stage and repeating measurements at each time delay, time-resolved diffraction images are acquired, providing insights into the dynamic structural changes of the sample.

2.5 Short-Time Fourier Transform (STFT) Analysis

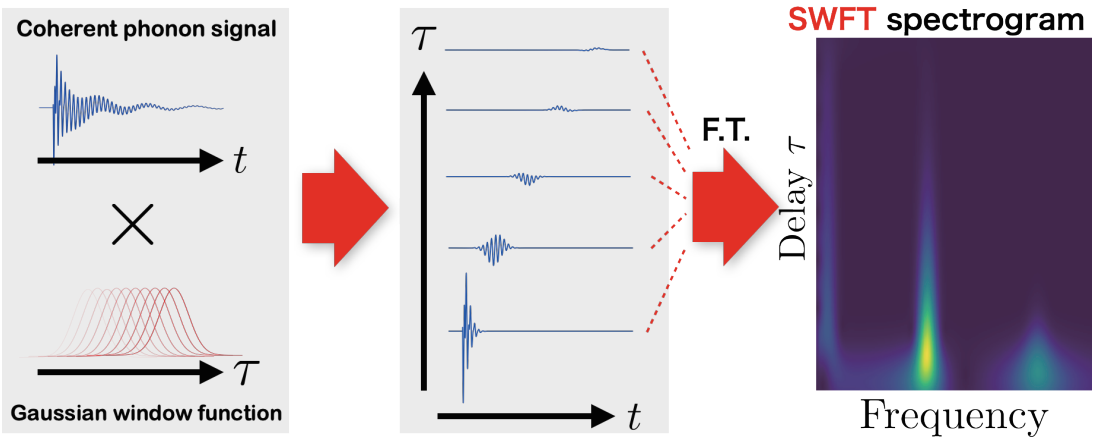

Figure 2.11: Schematic procedure of short-time Fourier transform (STFT) method.

In comparison to frequency-domain Raman scattering spectroscopy, coherent phonon spectroscopy excels in assessing the temporal characteristics of phonon frequency spectrum in the time domain. To underscore this advantage, we introduce a method known as the Short-time Fourier Transform (STFT), as the schematic procedure depicted in Fig. 2.11. In contrast to that the conventional Fourier transform (FT) outputs the frequency spectrum across the entire time-domain signal, the STFT can approach facilitates the real-time tracking of the frequency spectrum of oscillating coherent phonon signals in the time domain. This capability allows for the evaluation of transient phenomena, including the generation and relaxation of quasiparticles or structural phase transitions occurring at extremely early time delays upon photoexcitation.

Here, I will provide an explanation of the Short-time Fourier Transform (STFT) method used in this study. The FT and inverse FT are mathematical operations applied to any function f, defined by the following equations:

$$f(\omega) = \int_{-\infty}^{\infty} dt\ f(t)e^{-i\omega t}, \quad f(t) = \frac{1}{2\pi}\int_{-\infty}^{\infty} d\omega\ f(\omega)e^{i\omega t}. \tag{2.9}$$

According to the equations above, $f(\omega)$ does not depend on time t, and $f(t)$ does not depend on frequency ω. Consequently, in the conventional FT, it is impossible to simultaneously reconcile information in both the time and frequency domains.

To gain insights into the time evolution of phonon spectra, the STFT is carried out based on the following equation, and we can obtain time-frequency 2D spectrograms of coherent phonon.

$$I(\omega,\tau) = \left| \int_{-\infty}^{\infty} dt\ g(t-\tau) f(t) e^{-i\omega t} \right|, \quad g(t-\tau) \propto e^{-\frac{(t-\tau)^2}{\sigma^2}},\ \sigma = \frac{w}{2\sqrt{\log 2}}, \tag{2.10}$$

where $g(t-\tau)$ is a Gaussian function used as a window function, and w is a full-width half maximum (FWHM) of the window function. Figure 2.10 shows the schematic procedure of STFT analysis. We repeat the Fourier transform (FT) of $g(t-\tau) \times (\Delta R(t)/R)$ having the same data points as $\Delta R(t)/R$ in each delay time τ. The SWFT analysis method shares similarities with the "wavelet transform". However, it is essential to highlight key distinctions among them. Wavelet transform utilizes localized orthogonal basis functions known as "mother wavelets" (such as the Mexican hat function) to acquire time-frequency domain information of a signal. In contrast, STFT employs non-localized plane waves (simple FT) as its basis functions. Therefore, strictly speaking, wavelet transform and STFT are distinct methodologies.

Chapter 3

Coherent Phonons

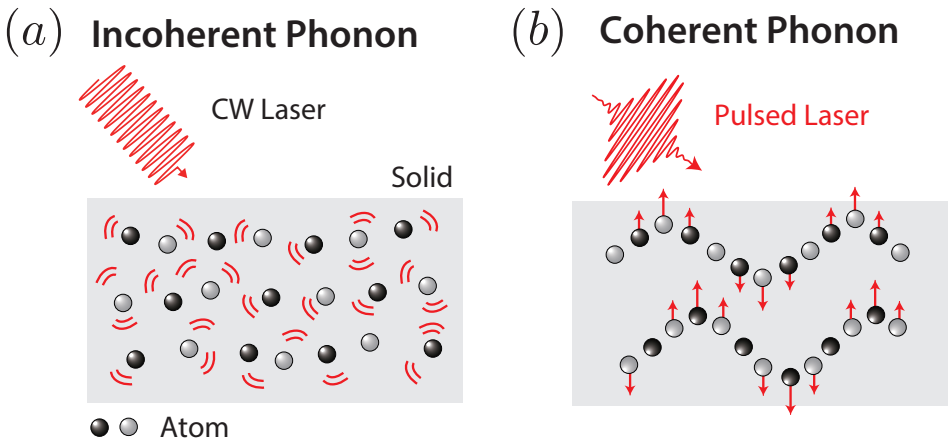

Figure 3.1: Schematic illustration of incoherent (thermal) phonon (a) and coherent phonon motions (b) in solids.

3.1 Fundamental

Overview Phonons, quantized picture of lattice vibrations, serve as quasiparticles embodying the spatial translational symmetry of a crystal structure. In general, phonons manifest as thermal vibrations, resulting in the average atomic positions to randomly (incoherently) fluctuate. This fluctuation leads to increase the electron scattering rate, leading to increase of electrical resistance and linewidth broadening of optical or diffraction peaks. Therefore, the presence of thermal phonons in a equilibrium state hinder the fundamental characterization of electronic states and the improvement of device performance. In contrast to incoherent thermal phonons, coherent phonons represent lattice vibrations that are excited in both time and phase coherently. They can only be observed in a non-equilibrium state immediately after photoexcitation by an ultra-short

pulse laser. In particular, Raman-active optical phonon modes at the zone center are excited, and their spatiotemporal vibrations modulate various physical quantities such as electronic states and optical constants over time. This modulation often appears as damped oscillations with amplitude, frequency, and phase within the pump-probe signal. The frequency of the time-domain coherent phonon oscillations is consistent with that detected through frequency-domain Raman spectroscopy. Coherent phonons, having distinct non-thermal and temporal-evolution features, are expected to induce ultrafast structural changes or non-equilibrium quasiparticle states driven by transient atomic displacements. Furthermore, induced coherent atomic displacements are expected to cause ultrafast structural changes. Additionally, the variation in lattice vibration patterns allows for assessing the time evolution of lattice symmetry changes associated with photoexcitation. This is an advantage over Raman spectroscopy, which does not provide information in the time domain.[55]

History To achieve time resolution of optical phonons with terahertz (THz) frequencies, femtosecond time resolution became essential. The development of femtosecond colliding pulse mode-locked (CPM) dye lasers in the 1980s played a key role to experimentally observe optical-phonon oscillations in time domain.

The foundational research for measuring coherent phonons, referred to as "laser-induced phonons", was conducted from the late 1970s to the early 1980s using picosecond lasers for transient grating measurements.[9, 10, 56, 57] Then, acoustic phonons in the GHz range were measured in the time domain with sub-nanosecond temporal resolution.

In 1985, a pioneering observation of optical phonons was conducted by a research group at MIT, USA, using the transient grating method on the molecular crystal perylene.[58] This milestone event contributed to the proposal and theoretical foundation of coherent phonon generation via the Impulsive Stimulated Raman Scattering (ISRS) process.[59, 60] In the beginning of the 1990s, time-resolved measurements of coherent optical phonon dynamics expanded to include general solid-state crystals, such as

semiconductors and semimetals, in addition to molecular crystals. Notably, researchers at RWTH Aachen University in Germany observed the generation of coherent longitudinal optical (LO) phonons in a doped polar semiconductor GaAs.[61], attributed to impulsive screening of surface electric field (ISSEF) or depolarization effects of surface-space-charge depletion layer in the presence of photoexcited carriers that drive a polar LO coherent phonon.[62, 63] Concurrently, researchers at MIT identified the mechanism of displacive excitation of coherent phonon (DECP) excitation in semimetals like Bi and Sb through time-resolved reflectivity change experiments.[64, 65] By the mid-1990s to early 2000s, there was vigorous debate over the microscopic theory of coherent phonon generation mechanisms, leading to the understanding that DECP could be explained within the resonant ISRS framework.[66, 67, 68] In the 2000s, advancements of stable Ti:Sapphire lasers and regenerative amplifiers, as well as advanced measurement methods such as time-resolved X-ray diffraction, lead to further understanding of coherent lattice dynamics. These techniques enabled detailed studies of structural phase transitions under conditions of high-density photoexcitation.[69, 70, 71] During the 2000s, optical measurement techniques for coherent phonons had matured, enabling the elucidation of phonon dynamics and underlying physical mechanisms in various materials, including phase-change materials [72] and carbon-based materials: e.g., carbon nanotubes [73, 74, 75, 76], graphite [77], and diamond [78]. Furthermore, researchers extensively conducted experiments to control coherent phonon amplitude using multiple excitation pulses for photo-induced structural phase transitions [79, 80, 81] and the relationship with the Raman tensor [82, 83] for further understanding and applications related to coherent phonon generation. Additionally, unique physical phenomena in the time domain, such as the mechanism of quasiparticles like the LO-phonon-plasmon coupled (LOPC) mode [84, 85, 86, 87, 88] and phonon-polariton in ferroelectrics [89], as well as the collapse-revival dynamics of coherent phonons under high-density electronic excitation [90, 91], were discussed. Entering the 2010s, a new mechanism emerged known as ionic Raman scattering (IRS), driven by high-intensity mid-infrared light.[92] IRS uniquely excites specific infrared phonon levels of tens of meV without exciting

the electronic system, thereby efficiently driving Raman-active phonons. The discovery of IRS, where phonons themselves excite other phonons, marked a significant breakthrough, leading to establishment of "Nonlinear Phononics". The advancement of computational resources has facilitated research that corroborates the coherent phonon generation processes through first-principles calculations, employing time-dependent density functional theory (TDDFT).[93, 94] In 2018, another notable development was the discovery of sum-frequency excitation (SFE) of coherent optical phonon, driven by a high-intensity THz electric field.[95] Since the electronic excitation are absent here, the IRS and SFE mechanisms are expected to a possible route that enables ultrafast control of material properties in the absence of sample damage by heat accumulation.

The history of coherent phonons has thus been a journey of continuous discovery over the past 40 years. A better understanding of their generation mechanisms is anticipated to lead to the realization and application of new non-equilibrium states of matter with extended coherence times. However, those generation mechanisms remains to be systematically compiled and explained. The following section aims to comprehensively classify and introduce the generation and detection mechanisms of coherent phonons. In writing this chapter, I referred to the following review papers written by respected predecessors.

- Dhar, *et al.* [96]: This comprehensive review covers time-resolved vibrational spectroscopy from theoretical and experimental perspectives, including discussions on non-resonant and resonant ISRS mechanisms triggered by photoexcitation with ultrashort pulses in molecules and solids.

- Merlin, *et al.* [97]: This advanced review provides a theoretical description of coherent phonon generation and detection, underpinned by experimental results.

- Kutt, *et al.* [98]; Dekorsy, *et al.* [99]; Först, *et al.* [100]; Ishioka, *et al.* [101]: These fundamental reviews focus on the generation and detection of coherent phonons investigated prior to 2010. They comprehensively introduce various technical approaches and experimental studies on measuring coherent phonons.

- Hase [102]: This review paper summarizes the various scattering mechanisms and interactions that contribute to the damping of coherent phonons.

- Subedi [103]; Mankowsky, *et al.* [104]: These review papers discuss nonlinear phononics driven by the IRS process.

- Caruso, *et al.* [105]: This comprehensive review theoretically systematizes nearly all known processes of coherent phonon generation identified up to 2023.

3.2 Driving Forces of Coherent Phonons

In contrast to thermal phonons, coherent phonons are "phase-locked" oscillations of atomic or lattice vibrations among individual phonon modes. Therefore, the coherent phonon amplitude $Q(t)$ can be phenomenologically represented by well-known classical equations of motion under forced driving conditions as follows:

$$\frac{\partial^2 Q^{(j)}(t)}{\partial t^2} + 2\gamma \frac{\partial Q^{(j)}(t)}{\partial t} + \Omega_j^2 Q^{(j)}(t) = \frac{F^{Q^{(j)}}(t)}{\mu^*}, \tag{3.1}$$

where μ^* is the reduced lattice mass, $Q^{(j)}(t)$ is a phonon displacement among several phonons, γ is the dephasing (decoherence) rate of the coherent phonon, Ω_j is the phonon frequency, $F^{Q^{(j)}}(t)$ is the driving force. It should be noted that γ includes various scattering factors, such as electron-phonon, phonon-phonon, and phonon-impurity scatterings.[106, 107, 108]; the force time of charge-density fluctuations.[109] In general, dephasing time of coherent phonon is much longer than its period that $\gamma < \Omega_j$ is always satisfied. According to Eq. (3.1), the solution for $Q^{(j)}(t)$ comprises both a general solution in the absence of $F^{Q^{(j)}}$ and a specific solution in the presence of $F^{Q^{(j)}}$. The general solution of Eq. (3.1) is represented as follows in the case of $\gamma < \Omega_j$:

$$Q_{\mathrm{gs}}^{(j)}(t) = A\mathrm{e}^{-\gamma t} \cos\left(\tilde{\Omega}_j t - \phi_0\right), \tag{3.2}$$

where $\tilde{\Omega}_j = \sqrt{\Omega_j^2 - \gamma^2}$, A and ϕ_0 are arbitrary constants of a phonon amplitude and an oscillatory phase, respectively.

The special solutions in the presence of $F^{Q^{(j)}}$ would be rather essential to characterize coherent phonon generations. To drive coherent phonons, it is expected to be necessary to either induce forced oscillation with an external field at frequencies close to that of the phonons or to apply a slowly varying external or internal field. Based on the fundamental mechanics, the driving force $F^{Q^{(j)}}(t)$ is defined as follows:

$$F^{Q^{(j)}}(t) = -\frac{\partial U}{\partial Q^{(j)}}, \tag{3.3}$$

where U is the arbitrary energy depending on phonon $Q^{(j)}(t)$ related to the light-matter interaction, electron-phonon interaction, lattice potentials, and so on. For example, an energy induced by light-matter interaction U_{LM} can be defined as follows:

$$U_{\mathrm{LM}} = -P(t) \cdot E(t), \tag{3.4}$$

where $P(t)$ is a time-varing polarization of matter under photoexcitation, and $E(t)$ is external electric field of light. $P(t)$ generally depends on $Q(t)$. An energy induced by electron-phonon interaction, especially deformation potential interaction, U_{DP} can be defined as follows:

$$U_{\mathrm{DP}} = -\sum_i \Xi_i \cdot Q^{(i)}(t), \tag{3.5}$$

where Ξ is a constant derived from deformation-potential electron-phonon interaction. By incorporating physical elements corresponding to each generation mechanism of coherent phonons into the driving force $F^{Q^{(j)}}$, one can efficiently categorize them.

3.3 Generation Mechanisms

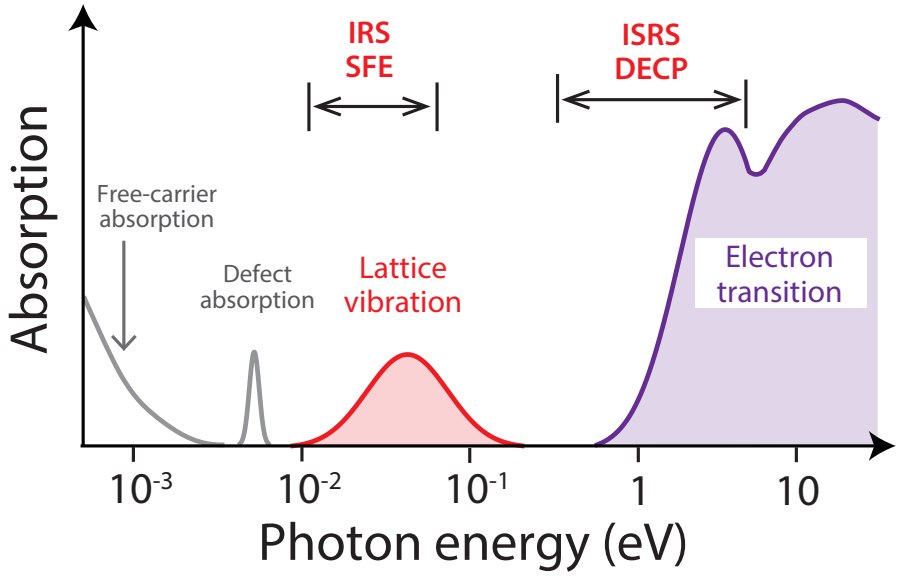

Figure 3.2: Schematic graph describing excited phenomena depending on photon energy.

The generation of coherent phonons is conventionally described by the following processes: impulsive stimulated Raman scattering (ISRS), displacive excitation of coherent phonons (DECP), impulsive screening of the surface electric field (ISSEF), ionic Raman scattering (IRS), and sum-frequency excitation (SFE). Figure 3.2 classifies excitation phenomena within solids by energy regions and illustrates the correspondence between the excitation energy of light used for each coherent phonon generation mechanism. In cases of photoexcitation where the photon energy is significantly higher than the phonon energy, the ISRS or DECP processes are generally applicable. It should be noted that the ISRS process relates to non-resonant electronic excitation, while the DECP process is a resonant case of ISRS. Conversely, when the photon energy of photoexcitation is close to that of the phonon energy, the IRS or SFE processes are applicable. In the subsequent sections, I will elaborate on each of these generation processes.

3.3.1 ISRS: Impulsive Stimulated Raman Scattering

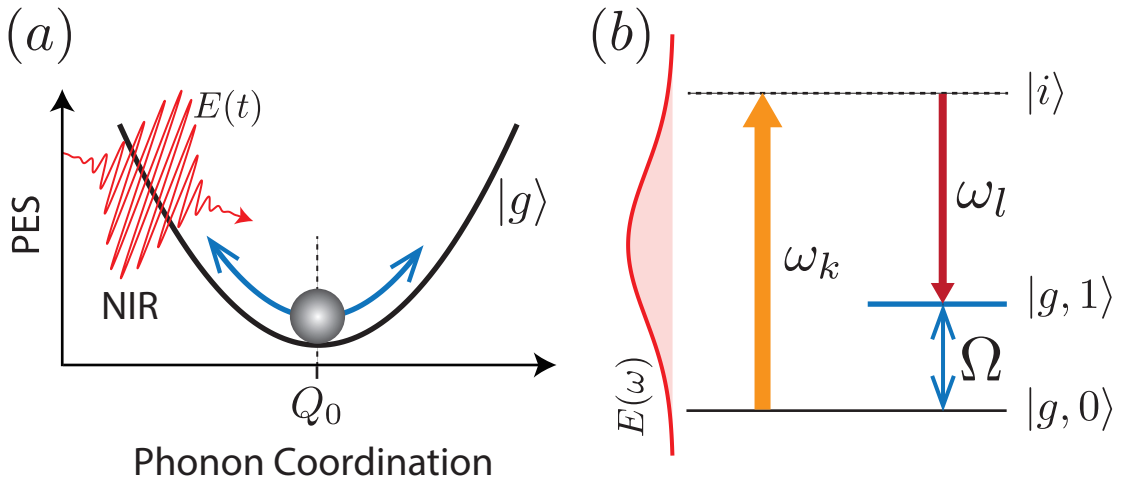

Figure 3.3: Schematic illustration of ISRS process. (a) Potential energy surface (PES) depending on phonon coordination. Q_0 is equilibrium position of the phonon. $E(t)$ is the light field of a pulse. $|g\rangle$ denotes electronic ground state. (b) Energy diagram. $E(\omega)$ is the broad spectrum of $E(t)$. $|g, n\rangle$ denotes the n-th excitation state of phonon in the absence of electronic excitation. $|i\rangle$ is the intermediate state. Ω is the phonon frequency.

General Description: The ISRS is characterized as a Raman scattering process that instantaneously generates optical phonons under femtosecond pulsed laser irradiation. This model is particularly valid when the media is transparent to light in the absence of electronic excitation: i.e., $E_g > \hbar\omega$, where E_g is the transition energy or band gap, and $\hbar\omega$ is the photon energy. The combinations of two photon energies (e.g., ω_k and ω_l present in the broad spectrum of an ultrashort pulse) are the driving forces of coherent phonon generations in ISRS. As shown in Fig. 3.7, it is expected to induce sinusoidal lattice vibrations ($Q(t) \propto \sin\Omega t$), whose frequencies satisfy the energy conservation law $|\omega_k - \omega_l| \approx \Omega_{\text{phonon}}$ and the momentum conservation law $\boldsymbol{q}_k - \boldsymbol{q}_l \approx \boldsymbol{q}_{\text{phonon}}$ can be excited, where $\boldsymbol{k}_k$ and $\boldsymbol{k}_l$ denote momentum of light. Here, in principle, Raman-active optical phonon modes like isotropic A_g modes or anisotropic E_g modes) can be excited.

Driving Force of ISRS: More specifically, deriving the driving force for the ISRS provides a clearer understanding of the aforementioned description. For the ISRS is facilitated by light-matter interaction, the driving force for ISRS can be defined based on Eq. (3.3) and Eq. (3.4). In the case of nonlinear optics under the use of strong electric field, the induced polarization $P(t)$ can be expressed in the form of a power series in the field strength $E(t)$ [110]:

$$P(t) = P_0 + \epsilon_0 \left[\chi^{(1)} E(t) + \chi^{(2)} E^2(t) + \chi^{(3)} E^3(t) + \cdots \right], \tag{3.6}$$

where P_0 is the spontaneous polarization, ϵ_0 is the vacuum permittivity, $\chi^{(n)}$ is the nth-order nonlinear susceptibility. The photon energy of $E(t)$, assumed here, is in mid- or near-infrared ($> 10^2$ meV), which is substantially larger than phonon energy ($\sim 10^1$ meV). Given that the $P(t)$ and each term of Eq. (3.6) depend on a phonon displacement $Q^{(j)}$, both P_0 and $\chi^{(n)}$ can be expanded in terms of $Q^{(j)}$ as follows:

$$P_0(Q^{(j)}) = P_0(0) + \left. \frac{\partial P_0}{\partial Q^{(j)}} \right|_{Q^{(j)}=0} Q^{(j)} + \cdots, \tag{3.7}$$

$$\chi^{(n)}(Q^{(j)}) = \chi^{(n)}(0) + \left. \frac{\partial \chi^{(n)}}{\partial Q^{(j)}} \right|_{Q^{(j)}=0} Q^{(j)} + \cdots. \tag{3.8}$$

By substituting Eq. (3.7) and Eq. (3.8) into Eq. (3.6), the induced polarization $P(t)$ can be rewritten as follows:

$$\begin{aligned} P(t) = & \left(P_0(0) + \left. \frac{\partial P_0}{\partial Q^{(j)}} \right|_{Q^{(j)}=0} Q^{(j)} + \cdots \right) E(t) \\ & + \epsilon_0 \left(\chi^{(1)}(0) + \left. \frac{\partial \chi^{(1)}}{\partial Q^{(j)}} \right|_{Q^{(j)}=0} Q^{(j)} + \cdots. \right) E^2(t) + \cdots \end{aligned} \tag{3.9}$$

For simplicity, we will only consider the terms proportional to $Q^{(j)}(t)$ and $E(t)$ in the subsequent discussion. By substituting Eq. (3.9) into Eq. (3.3), the driving force can

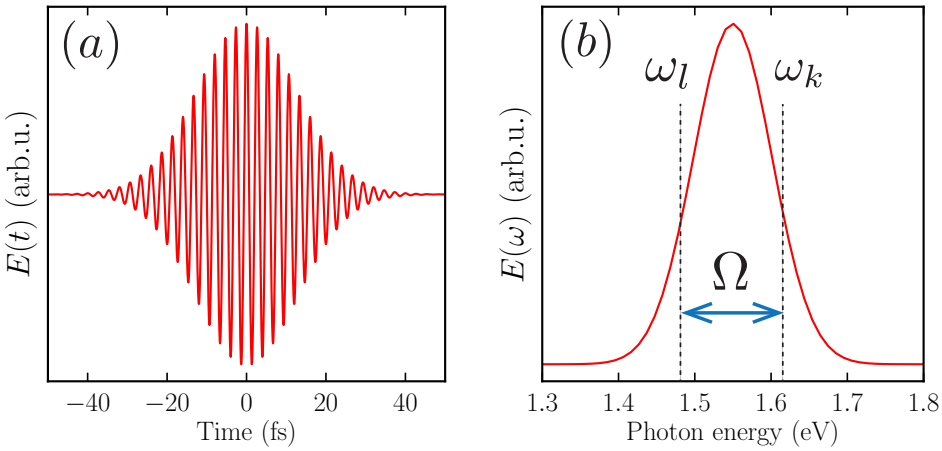

Figure 3.4: (a) Simulated femtosecond pulsed light field $E(t)$ based on Eq. (3.11). (b) $E(\omega)$ obtained by Fourier transform of $E(t)$.

be derived as follows:

$$F^{Q^{(j)}}(t) \approx \left.\frac{\partial P_0}{\partial Q^{(j)}}\right|_{Q^{(j)}=0} E(t) + \epsilon_0 \left.\frac{\partial \chi^{(1)}}{\partial Q^{(j)}}\right|_{Q^{(j)}=0} E^2(t). \tag{3.10}$$

It is essential to consider which components of the driving force expression, derived in Eq. (3.10), are responsible for driving the phonons. Here, $E(t)$ is assumed to be a gaussian-shaped electric field as follows:

$$E(t) = E_0 \exp(-t^2/\tau^2) \cos \omega_0 t, \tag{3.11}$$

where E_0 is the maximum amplitude of electric field, τ is associated with pulse duration, $\hbar\omega_0$ is the central photon energy, and $\hbar$ is the Dirac's constant. For simplicity, the momentum of light is not considered in $E(t)$ here. The waveform of $E(t)$ based on Eq. (3.11) is output in Fig. 3.4(a), where $\tau = 20$ fs and $\hbar\omega_0 = 1.5$ eV. Given that we are considering photon energy in the mid-to the near-infrared range, which is significantly higher than the phonon energy range, driving phonons with the first term linear to $E(t)$ in Eq. (3.10) is quite challenging. Therefore, the first term can be neglected in the ISRS process. It should be noted that the first term, referred to as "infrared absorption",

plays a pivotal role when a light electric field is close to the phonon energy, as described later in the sections on IRS and SFE processes.

In regard to the second term of Eq. (3.10), I will proceed to organize the expression of $E^2(t)$. The spectral components $E(\omega)$ is given by the Fourier transform of the $E(t)$ as follows:

$$E(\omega) = \frac{1}{\sqrt{2\pi}} \int_{-\infty}^{+\infty} \mathrm{d}t \; E(t) \exp(-i\omega t) \approx \frac{E_0 \tau}{\sqrt{2}} \exp\left[-\frac{(\omega - \omega_0)^2}{(2/\tau)^2} \right], \text{ when } \omega > 0. \quad (3.12)$$

This Eq. (3.12) indicates that the shorter the pulse duration τ, the broader the spectrum of $E(\omega)$ around the photon energy $\hbar\omega_0$. The Fourier spectrum of $E(t)$ is shown in Fig. 3.4(b). Based on Eq. (3.12), for simplicity, $E(t)$ can be approximately expressed as a superposition of cosine oscillations corresponding to each spectral component of the pulse as follows:

$$E(t) \sim \sum_{k=-\infty}^{\infty} E_k \cos \omega_k t, \quad (3.13)$$

where k is an integer, $\omega_k = \omega_0 - k\Delta$, Δ is a small amount, $E_k = E(\omega_k)$. By using the expression of Eq. (3.13), $E^2(t)$ can be represented as follows:

$$\begin{aligned} E^2(t) &\sim \left(\sum_k E_k \cos \omega_k t \right) \left(\sum_l E_l \cos \omega_l t \right) \\ &= \frac{1}{2} \sum_{k,l} E_k E_l \left[\cos(\omega_k - \omega_l)t + \cos(\omega_k + \omega_l)t \right]. \end{aligned} \quad (3.14)$$

The high-frequency terms in Eq. (3.14), specifically $\cos(\omega_k + \omega_l)t$, can be disregarded as they do not correspond to the phonon frequency. In contrast, the low-frequency terms $\cos(\omega_k - \omega_l)t$ that correspond to the phonon frequency: i.e., $|\omega_k - \omega_l| = \Omega_j$ illustrated in Fig. 3.4(b), become the driving force for the coherent phonon.

For the initially derived driving force in Eq. (3.10), considering that the first term linear to $E(t)$ and high-frequency term can be neglected, the driving force for ISRS is

derived as follows:

$$F_{\mathrm{ISRS}}^{Q^{(j)}}(t) = \frac{\epsilon_0}{2}\frac{\partial\chi^{(1)}}{\partial Q^{(j)}}\bigg|_{Q^{(j)}=0}\sum_{k,l}E_kE_l\cos(\omega_k-\omega_l)t = \sum_{k,l}\mathcal{R}_{kl}^{(j)}E_kE_l\cos\tilde{\omega}_{kl}t, \tag{3.15}$$

where $\tilde{\omega}_{kl}=\omega_k-\omega_l$, and the summation is applied only to combinations of k and l that satisfy $|\tilde{\omega}_{kl}|=\Omega_j$. The $\mathcal{R}_{kl}^{(j)}\propto\partial\chi/\partial Q$ is referred to as a Raman tensor. The special solution of Eq. (3.1) for $F_{\mathrm{ISRS}}^{Q^{(j)}}(t)$ can be expressed as follows:

$$Q_{j,s}^{\mathrm{ISRS}}(t) = \sum_{k,l}\underbrace{\frac{\mathcal{R}_{kl}^{(j)}E_kE_l}{\mu^*\sqrt{\left(\Omega_j^2-\tilde{\omega}_{kl}^2\right)^2+4\gamma^2\tilde{\omega}_{kl}^2}}}_{\mathcal{F}_{kl}}\cos(\tilde{\omega}_{kl}t-\phi_{s,kl}),\ \tan\phi_{s,kl}=\frac{2\gamma\tilde{\omega}_{kl}}{\Omega_j^2-\tilde{\omega}_{kl}^2}. \tag{3.16}$$

The solution of the differential equation is given by summation of the general solution Eq. (3.2) and special solution Eq. (3.16): i.e., $Q^{(j)}(t)=Q_{\mathrm{gs}}^{(j)}(t)+Q_{j,s}^{\mathrm{ISRS}}(t)$. By assuming initial conditions: i.e., $Q^{(j)}(0)=0$ and $\dot{Q}_j(0)=0$, the exact solution is obtained as follows:

$$Q^{(j)}(t) = \sum_{k,l}\mathcal{F}_{k,l}\left[\cos(\tilde{\omega}_{kl}t-\phi_{s,kl})-\mathrm{e}^{-\gamma\mathrm{t}}\cos\phi_{s,kl}\left(\cos\tilde{\Omega}_jt+\tan\phi_0\sin\tilde{\Omega}_jt\right)\right], \tag{3.17}$$

$$\tan\phi_0 = \frac{\sum_{k,l}\mathcal{F}_{kl}\left(\tilde{\omega}_{kl}\sin\phi_{s,kl}-\gamma\cos\phi_{s,kl}\right)}{\tilde{\Omega}_j\sum_{k,l}\mathcal{F}_{kl}\cos\phi_{s,kl}}. \tag{3.18}$$

In this case, among the terms in Eq. (3.17), specific combinations of k and l that satisfy $|\tilde{\omega}_{kl}|\approx\Omega_j$ significantly enhance the values of $\mathcal{F}_{kl}$ and mainly contribute to the induced phonon displacement $Q^{(j)}(t)$. Therefore, the combinations that satisfy $|\tilde{\omega}_{kl}|=\Omega_j$ are only taken into account for simplicity. In the limit of $\tilde{\omega}_{jk}\to\Omega_j$, $\phi_{s,kl}$ converges as follows.

$$\lim_{\Omega_j-\tilde{\omega}_{kl}\to\pm0}\tan\phi_{s,kl}=\pm\infty,\ \ \therefore\phi_{s,kl}\to\pm\frac{\pi}{2},\ \cos\phi_{s,kl}\to0. \tag{3.19}$$

By combining Eq. (3.17) and Eq. (3.19), $Q(t)$ can be approximated in the following

representation:

$$|Q^{(j)}(t)| \sim \sum_{k,l} \frac{\mathcal{R}_{kl}^{(j)} E_k E_l}{2\mu^* \gamma \Omega_j} \sin(\Omega_j t). \tag{3.20}$$

Therefore, in the ISRS model, a coherent phonon oscillation follow a sinusoidal wave: i.e., $Q(t) \propto \sin \Omega t$ after the arrival of the light pulse at $t = 0$. In addition, as indicated by the expressions in Eq. (3.15) and Eq. (3.20), the magnitude of phonon displacement depends on $\mathcal{R}_{kl}^{(j)}$ or $\sum_{k,l} E_k E_l$, both of which are components of the driving force $F_{\mathrm{ISRS}}^{Q^{(j)}}$. This fact suggests that the use of laser pulse with a shorter pulse duration or a broader spectrum leads to an enhancement of the induced phonon amplitude proportional to the intensity of light $I(t) \sim |E(t)|^2$.

Limitation of ISRS: It is worth noted that there is a limitation of coherent phonon excitations in the ISRS process, as reported by Uchida and co-workers.[111]

According to Eq. (3.20), the phonon displacement in the ISRS model is linear to the light intensity. Therefore, increasing the light intensity can infinitely increase the phonon displacement. However, the results shown in Ref. [111] indicate that under conditions of high-intensity non-resonant excitation, the phonon amplitude exhibits saturating behavior. The saturation of coherent phonon generation can be well described by considering dressed adiabatic potentials based on Floquet theory. That modified potential energy surfaces give finite impulsive driving force and upper limit of possible phonon displacement.

3.3.2 DECP: Displacive Excitation of Coherent Phonons

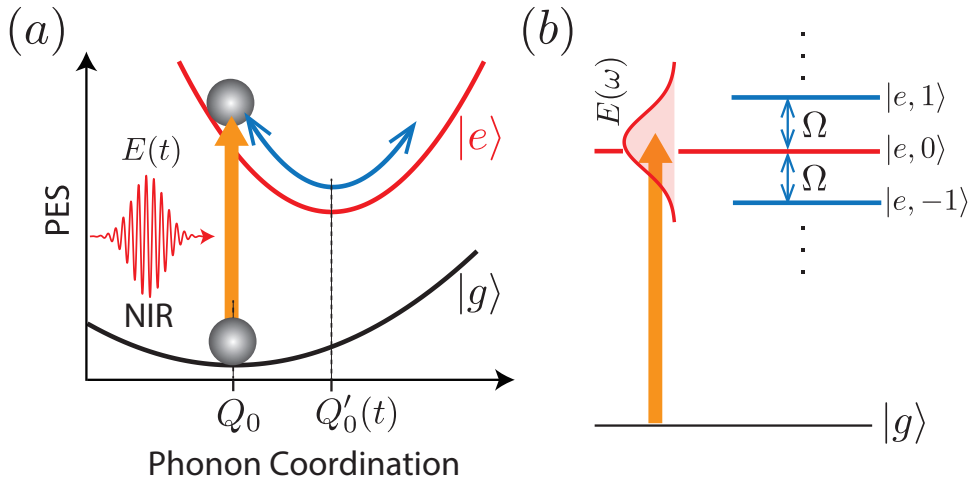

Figure 3.5: Schematic illustration of DECP process. (a) PES depending on phonon coordination. Q_0' is displaced equilibrium position in the presence of electronic excitation. $|e\rangle$ denotes electronic excited state. (b) Energy diagram. $|e, n\rangle$ denotes the n-th excitation state of phonon in the presence of electronic excitation. $|i\rangle$ is the intermediate state.

General Description: The DECP model describes how coherent phonons are generated when a material that absorbs light or is opaque to it undergoes ultrafast electronic excitation (i.e., $E_g < \hbar\omega$) from the valence to conduction bands. This model, which is a resonant case of the ISRS process, was actively developed in the beginning of the 1990s.[64, 65] Briefly and specifically, the DECP model describes photoexcited carrier-driven coherent phonon generation. When carriers are photoexcited by an ultrashort light pulse, they immediately influence the lattice potential, caused by the decrease in valence electrons or changes in spatial charge distributions. Subsequently, as shown in Fig. 3.5, the equilibrium position of phonon coordination $Q_0 = Q(t \leq 0)$ immediately shift to a new quasi-equilibrium position Q_0' that linearly depends on photoexcited carrier density $n(t)$:

$$Q_0'(t) = \kappa n(t), \tag{3.21}$$

where κ is a constant that is associated with some physical quantities, such as electron-phonon coupling. Since photoexcitation typically induces uniform carrier generation in space, phonon displacement should manifest isotropically. Consequently, this leads to the excitation of coherent phonons, which do not contribute to the reduction of lattice symmetry, such as lattice vibration modes assigned as A modes. Finally, the displacement of equilibrium position drives coherent phonons with cosine-like vibrations, characterized by an amplitude of $|Q_0 - Q_0'|$.

Driving Force of DECP: Phenomenologically, the equation of motion when the equilibrium position of phonon coordination shifts due to the photoexcited carriers can be expressed as follows:

$$\frac{\partial^2 Q^{(j)}(t)}{\partial t^2} + 2\gamma \frac{\partial Q^{(j)}(t)}{\partial t} + \Omega_j^2 \left[Q^{(j)}(t) - Q_0'(t) \right] = 0. \tag{3.22}$$

After organizing Eq. (3.22), the following expression can be obtained as follows:

$$\frac{\partial^2 Q^{(j)}(t)}{\partial t^2} + 2\gamma \frac{\partial Q^{(j)}(t)}{\partial t} + \Omega_j^2 Q^{(j)}(t) = \Omega_j^2 Q_0'(t). \tag{3.23}$$

By comparing Eq. (3.1) and Eq. (3.22), the driving force of DECP can be expressed as follows:

$$F_{\mathrm{DECP}}^{Q^{(j)}} = \mu^* \Omega_j^2 Q_0'(t) = W n(t), \tag{3.24}$$

where $W = \mu^* \Omega_j^2 \kappa$ associated with deformation-potential electron-phonon interaction Ξ, as will be explained in detail later. Consequently, the driving force of DECP is proportional to the density of photoexcited carriers $n(t)$.

It should be noted that $F_{\mathrm{DECP}}^{Q^{(j)}}$ can also be written based on the energy of Eq. 3.5 [67, 68]:

$$\tilde{F}_{\mathrm{DECP}}^{Q^{(j)}} = -\frac{\partial U_{\mathrm{DP}}}{\partial Q^{(j)}} = \Xi_j. \tag{3.25}$$

Photoexcited carriers are generated by pulsed laser field. Therefore, time-evolution of $n(t)$ should be given by the generation-and-scattering rate equation driven by laser

intensity $I(t)$:

$$\frac{\mathrm{d}n(t)}{\mathrm{d}t} + \alpha n(t) = aI(t), \tag{3.26}$$

where α denotes a decay rate of carriers, and a is related to optical response of materials, such as dielectric functions. When $I(t \to -\infty) = 0$ is satisfied, the solution of Eq. (3.26) can be written as follows:

$$n(t) = a\exp(-\alpha t)\int_{-\infty}^{t} \mathrm{d}t'\ I(t')\exp(+\alpha t'). \tag{3.27}$$

Assuming the impusive limit, $I(t) = \delta(t)$, the carrier scattering can be expressed by $n(t) = n_0\mathrm{e}^{-\alpha t}$, where $n_0 = n(t = 0)$. Therefore, the special solution of Eq. (3.1) based on the driving force Eq. (3.24) can be simply derived as follows:

$$Q_s^{\mathrm{DECP}}(t) = \frac{Wn_0}{\mu^*(\alpha^2 - 2\alpha\gamma + \Omega_j^2)}\mathrm{e}^{-\alpha t}. \tag{3.28}$$

In the same as the procedure being done in the following ISRS section, the solution of the differential equation is given by summation of the general solution (Eq. (3.2)) and special solution Eq. (3.28): i.e., $Q^{(j)}(t) = Q_{\mathrm{gs}}^{(j)}(t) + Q_s^{\mathrm{DECP}}(t)$. By assuming initial conditions: i.e., $Q^{(j)}(0) = 0$ and $\dot{Q}_j(0) = 0$, the exact solution is obtained as follows:

$$Q^{(j)}(t) = \frac{Wn_0}{\mu^*(\alpha^2 - 2\alpha\gamma + \Omega^2)}\left[e^{-\alpha t} - e^{-\gamma t}\left(\cos\tilde{\Omega}_j t + \frac{\gamma - \alpha}{\tilde{\Omega}_j}\sin\tilde{\Omega}_j t\right)\right]. \tag{3.29}$$

Given that $\gamma,\ \alpha \ll \Omega_j$, $Q^{(j)}(t)$ is approximated to be following expression:

$$Q^{(j)}(t) \sim \frac{Wn_0}{\mu^*(\alpha^2 - 2\alpha\gamma + \Omega^2)}\left(e^{-\alpha t} - e^{-\gamma t}\cos\Omega_j t\right). \tag{3.30}$$

The $Q^{(j)}(t)$ in Eq. (3.30) clearly shows the changes in equilibrium position in the first term and cosine-like oscillation around the new equilibrium position. Furthermore, the oscillation amplitude linearly depends on photoexcited carrier density.

Microscopic Theory: In contrast to the phenomenological description above, the microscopic theory of DECP based on the quantum mechanical approach has been developed by Kuznetsov and Stanton, here referred to as *KS model*.[66] This theoretical framework successfully describes that the photoexcited carriers drive only optical phonons with zero momentum. Furthermore, this model makes it clear that W in Eq. (3.24) is associated with the deformation potential. The detailed explanation is omitted here, but in the KS model, a Hamiltonian is started by assuming a two-level system, where the electron system and the phonon system are combined:

$$\hat{H} = \hat{H}_{\mathrm{el}} + \hat{H}_{\mathrm{ph}} + \hat{H}_{\mathrm{el-ph}}, \tag{3.31}$$

and each term is represented as follows:

$$\begin{aligned}
\hat{H}_{\mathrm{el}} &= \sum_{\alpha,\boldsymbol{k}} \varepsilon_{\alpha\boldsymbol{k}} c^{\dagger}_{\alpha\boldsymbol{k}} c_{\alpha\boldsymbol{k}} \\
\hat{H}_{\mathrm{ph}} &= \sum_{\boldsymbol{q}} \hbar\Omega_{\boldsymbol{q}} b^{\dagger}_{\boldsymbol{q}} b_{\boldsymbol{q}} \\
\hat{H}_{\mathrm{el-ph}} &= \sum_{\alpha,\boldsymbol{k},\boldsymbol{q}} \mathcal{M}^{\alpha}_{\boldsymbol{kq}} (b^{\dagger}_{\boldsymbol{q}} + b_{-\boldsymbol{q}}) c^{\dagger}_{\alpha\boldsymbol{k}} c_{\alpha\boldsymbol{k}+\boldsymbol{q}} \\
&= V^{-\frac{1}{2}} \sum_{\alpha,\boldsymbol{k},\boldsymbol{q}} \xi^{\alpha}_{\boldsymbol{kq}} (b^{\dagger}_{\boldsymbol{q}} + b_{-\boldsymbol{q}}) c^{\dagger}_{\alpha\boldsymbol{k}} c_{\alpha\boldsymbol{k}+\boldsymbol{q}},
\end{aligned} \tag{3.32}$$

where $\varepsilon_{\alpha\boldsymbol{k}}$ denotes energy dispersion of Bloch electrons in $\boldsymbol{k}$ space; $\Omega_{\boldsymbol{q}}$ is the phonon frequency having a momentum $\boldsymbol{q}$; $\alpha = \{c,\ v\}$ denotes conduction and valence bands, respectively; $c^{\dagger}$ and c are creation and annihilation operators of electrons, respectively; $b^{\dagger}_{\boldsymbol{q}}$ and $b_{\boldsymbol{q}}$ are phonon creation and annihilation operators, respectively; $\mathcal{M}^{\alpha}_{\boldsymbol{kq}}$ and $\xi^{\alpha}_{\boldsymbol{kq}}$ are associated with matrix elements associated with deformation-potential electron-phonon coupling; V is the volume of the system. The phonon operator can be written as following well-known formalism [112]:

$$\hat{u}(\boldsymbol{r}) = \sum_{q} \sqrt{\frac{\hbar}{2\rho V\Omega_{\boldsymbol{q}}}} \left\{ \hat{b}_{\boldsymbol{q}} \mathrm{e}^{+i\boldsymbol{q}\cdot\boldsymbol{r}} + \hat{b}^{\dagger}_{-\boldsymbol{q}} \mathrm{e}^{-i\boldsymbol{q}\cdot\boldsymbol{r}} \right\}, \tag{3.33}$$

where ρ is the reduced mass density and V is the volume of the system. The expectation value of displacement for phonon mode having a momentum $\boldsymbol{q}$ can be represented as follows:

$$\langle u_{\boldsymbol{q}} \rangle = \left\langle \frac{1}{V} \int \mathrm{d}^3\boldsymbol{r}\ \hat{u}(\boldsymbol{r}) \mathrm{e}^{-i\boldsymbol{q}\cdot\boldsymbol{r}} \right\rangle = \sqrt{\frac{\hbar}{2\rho V \Omega_{\boldsymbol{q}}}} D_{\boldsymbol{q}}, \tag{3.34}$$

where $D_{\boldsymbol{q}}$ is coherent amplitude, satisfying

$$D_{\boldsymbol{q}} = \left\langle \hat{b}_{\boldsymbol{q}} + \hat{b}^{\dagger}_{-\boldsymbol{q}} \right\rangle = \left\langle \hat{b}_{\boldsymbol{q}} \right\rangle + \left\langle \hat{b}^{\dagger}_{-\boldsymbol{q}} \right\rangle. \tag{3.35}$$

By using the commutation relations between the Hamiltonian and phonon operators, it is possible to derive the following equation of motion for $D_{\boldsymbol{q}}$:

$$\frac{\partial^2 D_{\boldsymbol{q}}}{\partial t^2} + \Omega_{\boldsymbol{q}}^2 D_{\boldsymbol{q}} = -2\Omega_{\boldsymbol{q}} \sum_{\alpha,\boldsymbol{k}} \mathcal{M}^{\alpha}_{\boldsymbol{k}\boldsymbol{q}} n^{\alpha}_{\boldsymbol{k},\boldsymbol{k}+\boldsymbol{q}}, \tag{3.36}$$

where $n^{\alpha}_{\boldsymbol{k},\boldsymbol{k}+\boldsymbol{q}} = \langle c^{\dagger}_{\alpha\boldsymbol{k}} c_{\alpha\boldsymbol{k}+\boldsymbol{q}} \rangle$ is associated with spacial charge density. Here, assuming the photoexcitation creates homogeneous carrier distribution, $n^{\alpha}_{\boldsymbol{k},\boldsymbol{k}'}$ should be diagonal: $n^{\alpha}_{\boldsymbol{k},\boldsymbol{k}'} = f^{\alpha}_{\boldsymbol{k}}(t)\delta_{\boldsymbol{k}\boldsymbol{k}'}$. Therefore, only the optical phonon mode ($\boldsymbol{q} = \boldsymbol{0}$) is likely to be excited. Also assuming that the $\mathcal{M}^{\alpha}_{\boldsymbol{k}}$ does not depend on $\boldsymbol{k}$, Eq. (3.36) can be rewritten as follows:

$$\begin{aligned}
\frac{\partial^2 D_0}{\partial t^2} + \Omega_0^2 D_0 &= -2\Omega_0 \sum_{\alpha} \mathcal{M}^{\alpha} \sum_{\boldsymbol{k}} f^{\alpha}_{\boldsymbol{k}}(t) \\
&= -2\Omega_0 V^{-\frac{1}{2}} \left[\xi^v(-N(t)) + \xi^c N(t) \right] \\
&= \underbrace{2\Omega_0 V^{-\frac{1}{2}} \left(\xi^v - \xi^c \right)}_{W} N(t),
\end{aligned} \tag{3.37}$$

where $N(t)$ represents the density of electron-hole pairs, and W is associated with deformation-potential electron-phonon interactions, $\xi^v - \xi^c$. The right-hand side of Eq. (3.37) corresponds to the driving force of DECP, Eq. (3.24), which is phenomenologically derived.

Resonant ISRS and DECP: The ISRS and DECP are models applied respectively to transparent materials without electron excitation and opaque materials with electron excitation. However, by introducing a characteristic tensor that reflects absorption effects, DECP can be explained in an extended manner for the ISRS model. To achieve a unified understanding of the resonant ISRS and DECP, it is effective to consider the Fourier components of the driving force.

First, the differential equation regarding the driving force in the DECP model can be expressed as follows using Eqs. (3.24) and (3.26):

$$\frac{\mathrm{d}F(t)}{\mathrm{d}t} + \alpha F(t) = aWI(t). \tag{3.38}$$

By employing Fourier transform for both-handed sides of equation, Eq. (3.38) can be rewritten as follows:

$$\begin{aligned} i\Omega F(\Omega) + \alpha F(\Omega) &= aWI(\Omega) \\ \therefore \quad F(\Omega) &= \frac{aW}{\alpha + i\Omega} I(\Omega), \end{aligned} \tag{3.39}$$

where Ω is the frequency. The formalization of Eq. (3.39) was developed by Riffe and Sabbah [113], here referred to as *RS formalization*. When the excited charge density has an infinite lifetime ($\alpha = 0$), $F(\Omega) \propto I(\Omega)/i\Omega$ is purely imaginary. Given that inverse Fourier transform of $I(\Omega)/i\Omega$ corresponds to $\int_{-\infty}^{t} \mathrm{d}t'\ I(t')$, $F(t)$ can be reproduced as follows:

$$F(t) \propto \int_{-\infty}^{t} \mathrm{d}t'\ I(t'). \tag{3.40}$$

Since $I(t)$ is the pulsed light intensity, $F(t \to -\infty) = 0$ and $F(t \to +\infty) = const.$ are satisfied. When its Fourier component includes only an imaginary number, $F(t)$ is a step-function-like force that corresponds to to the change in equilibrium position induced by photoexcited carriers with an infinite lifetime ($\alpha \to 0$).

Otherwise, Steven, Kuhl, and Merlin developed an advanced ISRS model that includes virtual and real electronic excitation [68], referred to as *SKM model*. The Fourier

component of driving force derived from the SKM model is represented using the complex dielectric function $\epsilon = \epsilon_1 + i\epsilon_2$, where ϵ_1 and ϵ_2 are real numbers as follows:

$$F(\Omega) \propto \left(\frac{\mathrm{d}\varepsilon_1}{\mathrm{d}\omega} - \frac{2\varepsilon_2}{i\Omega} \right) I(\Omega), \tag{3.41}$$

where ω denotes the photon energy, and ϵ_1 and ϵ_2 are evaluated at the central photon energy of the pulsed light, approximately ω_0. The first term indicates virtual excitation, whereas the second term is associated with photon absorption and subsequent electronic excitation. This relationship explicitly illustrates that $F(t)$ is directly proportional to $I(t)$ as evidenced by the first term. In the context of an opaque material, characterized by the condition $\mathrm{d}\epsilon_1/\mathrm{d}\omega \ll \epsilon_2/\Omega$, the function $F(\Omega)$ is rendered purely imaginary. In this case, $F(t)$ gives a step-function-like force consistent with the RS formalization. Consequently, the SKM model can be successfully applied to the coherent phonon generations in transparent and opaque materials.

Limitation of DECP: According to the DECP model, the displacement of phonons is linear with respect to the density of excited electrons N. Thus, increasing the density of photoexcited carriers through high-density light excitation can infinitely increase the phonon displacement. However, due to the flattening of the potential energy surface accompanying structural phase transitions to different local-minimum metastable states, the change in the equilibrium position of atoms and relevant optical responses with respect to N may saturate.[114, 115, 116]

Furthermore, under photoexcitation conditions close to the damage threshold, the N may become nonlinear with respect to the excitation light intensity, giving rise to saturation of N. This also gives an upper limit on phonon displacement, frequency shift, and decay time constant, as well as relevant optical response. [69, 70, 117, 118] This may be due to nonlinear absorption phenomena in the electronic system, such as saturable absorption or multi-photon absorption. Such phenomena will be discussed in detail in Chapter 7.

3.3.3 ISSEF: Impulsive Screening of the Surface Electric Field

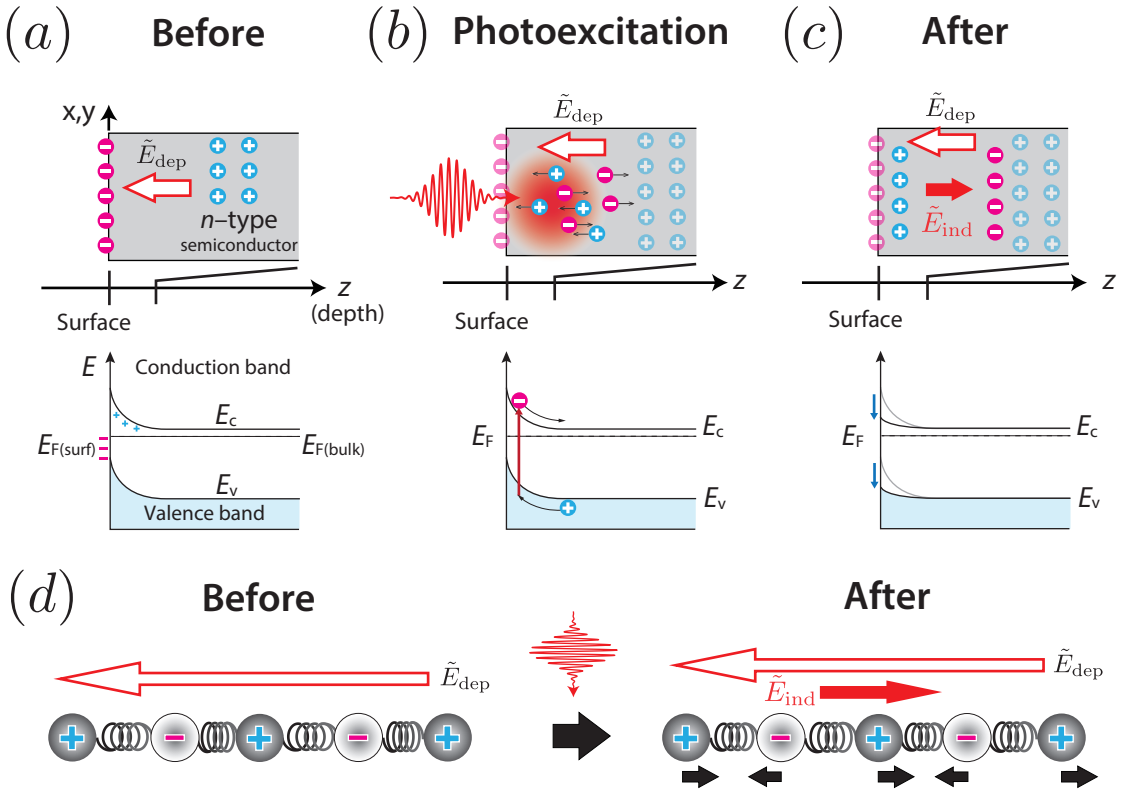

Figure 3.6: Schematic illustration of ISSEF process in space and energy: (a) Before excitation, (b) Upon photoexcitation, and (c) After excitation in a n-type semiconductor. $\tilde{E}_{dep}$ denotes static electric field in surface depletion region induced by surface-charge field. $\tilde{E}_{ind}$ is the screening electric field induced by photoexcited electron-hole plasmas. (d) show the lattice motion before and after the screening electric field is valid.

General Description: The ISSEF model refers to a generation mechanism for coherent phonons, driven by the transient electric fields induced by the non-equilibrium spatial charge distribution on the surface of a material excited by light. This model is primarily applied for the excitation of polar longitudinal optical (LO) phonons in polar semiconductors composed of group III-V elements, such as GaAs, GaN, and InAs. Polar semiconductors are those in which the atomic bonding possesses characteristics of both covalent and ionic bonds. The strength of the ionic bonding increases with the difference in electronegativity between the constituent elements.[112] For example, in a

typical group III-V semiconductor like GaAs crystals, electrons are attracted towards the As atoms, which have higher electronegativity, resulting in Ga atoms carrying a positive charge and As atoms a negative charge. Polar phonons refer to lattice vibrations exhibiting a vibrational pattern where the separation distance between pairs of positively and negatively charged constituent atoms modulates. Such phonons are typically classified into longitudinal optical (LO) phonon modes. In polar semiconductors with a Zinc-blende-type structure like GaAs, LO phonons (high-frequency side) and transverse optical (TO) phonons (low-frequency side) are split at the zone center (Γ point) of crystal momentum. However, TO phonons do not contribute to the change in polarization.

The generation process of coherent LO optical phonons in the ISSEF model can be explained in Figure 3.6. Here, we consider an n-type polar semiconductor where the Fermi level is located close to the conduction band. This kind of semiconductor is composed of two elements: one positively and the other negatively charged. Initially, in the equilibrium state of the n-type semiconductor and near its surface, the Fermi level inside the bulk is pinned due to neutral surface states, as depicted in Fig. 3.6(a). This leads to the formation of a depletion layer, with negative charges at the surface and positive charges inside, creating an electric field $\tilde{E}_{\mathrm{dep}}$ from the bulk toward the surface [Fig. 3.6(a)]. $\tilde{E}_{\mathrm{dep}}$ results in band-bending, determining the equilibrium position of atoms [Fig. 3.6(d)]. When excited with light above the band gap, electron-hole plasmas are generated near the surface [Fig. 3.6(b)]. Following the direction of $\tilde{E}_{\mathrm{dep}}$, the photoexcited electrons and holes drift. This redistributes the charges, with positive charges near the surface and negative ones inside, thus screening the surface charge field. The induced screening field $\tilde{E}_{\mathrm{ind}}$ reduces the depletion layer field $\hat{E}_{\mathrm{dep}}$, altering the equilibrium position of atoms and driving LO phonons [Fig. 3.6(c) and (d)]. This can be understood in a similar way to the DECP model. In DECP, the driving force was the change in equilibrium position due to the excitation of valence electrons to conduction electrons, while in ISSEF, it is the spatial electric field and polarization changes (transient currents, movement of coherent wave packets) induced by inhomogeneously

photoexcited carriers that alter the equilibrium position.

Driving Force of ISSEF: Briefly, the driving force of ISSEF process is known to be written as follows:

$$F^{Q}_{\mathrm{ISSEF}} \sim F^{Q}_{\mathrm{ISRS},r} + \frac{e^*}{\epsilon_0 \epsilon_\infty} P^{\mathrm{NL}}_r, \tag{3.42}$$

where ϵ_∞ is the high-frequency dielectric constant, and P^{NL}_r is the induced nonlinear longitudinal polarization along direction $r \in \{x, y, z\}$. The P^{NL}_r, for example, incorporates several possible physical components, arising from spatial charge gradients and separation in the presence of large number of photoexcited carriers in a surface space-charge field:

$$\begin{aligned} P^{\mathrm{NL}}_r \sim & \chi^{(2)}_{kl,r} E_k E_l + \chi^{(3)}_{klm,r} E_k E_l E_m \\ & + \int_{-\infty}^{t} dt' \; J_r(t') + Ne \int_{-\infty}^{t} dt' \int_{-\infty}^{+\infty} dx_r \; \langle \Psi(x_r, t') | x_r | \Psi(x_r, t') \rangle \,, \end{aligned} \tag{3.43}$$

where $\chi^{(2)}_{kl,r}$ and $\chi^{(3)}_{kl,r}$ are second- and third-order nonlinear susceptibility along direction r, J_r is a current. Therefore, the first two terms denotes nonlinear polarization; the third term represents a longitudinal polarization induced by non-equilibrium surge or drift currents; the fourth term describes the coherent macroscopic motion of electronic wavepacket.

3.3.4 IRS: Ionic Raman Scattering

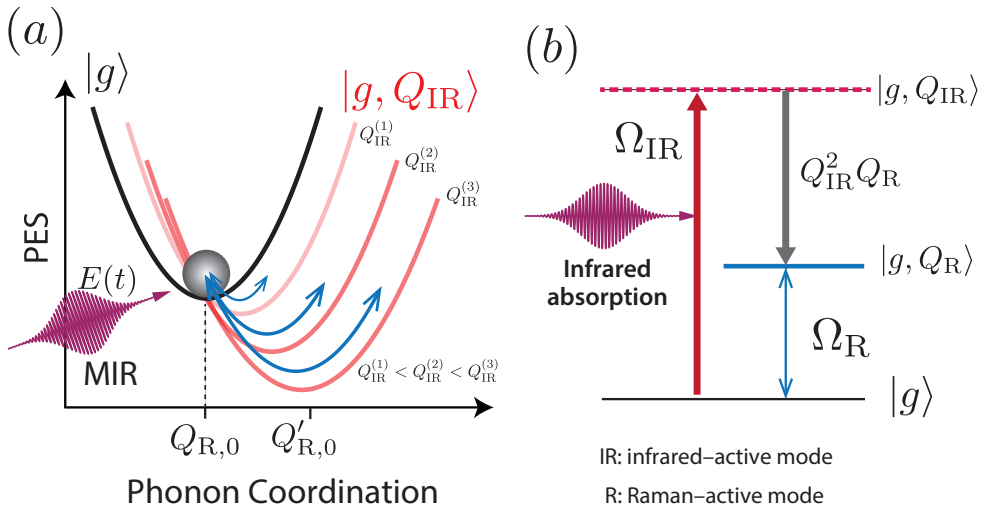

Figure 3.7: Schematic illustration of IRS process. (a) PES depending on Raman-active phonon coordination (Q_{R}). Q_{IR} denotes the coordination of an infrared-active(IR) phonon. (b) Energy diagram. A process of $Q_{\mathrm{IR}}^2 Q_{\mathrm{R}}$ denotes the nonlinear phonon-phonon coupling of IR-active and Raman-active phonon mode.

General Description: IRS is a generation mechanism for coherent phonons driven by the lattice anharmonicity associated with the large amplitude excitation of infrared-active phonons.[92] Unlike previously mentioned mechanisms, IRS employs light close to the energy of the phonons in the absence electronic transitions. The infrared-active phonons can be excited using far-infrared light resonant with the phonon energy, based on the principles of infrared absorption. When the infrared-active phonons are driven by a strong alternative electric field, the lattice undergoes significant distortion and a equilibrium-position displacement of the lattice potential, resulting in driving new Raman-active optical phonons in a manner similar to the DECP process, as illustrated in Fig. 3.7(a). Therefore, the energy level of an infrared-active phonon acts as an intermediate state for Raman scattering, as depicted in Fig. 3.7(b), which is a mechanism predominantly depending on lattice anharmonicity rather on electron-phonon interactions. This is the reason why this process is referred to as "Ionic" Raman scattering or "Nonlinear Phononics" in a way analogous to the nonlinear optics. IRS has been

primarily reported in materials such as perovskite-type transition-metal oxides, which demonstrates interesting electronic and magnetic properties.[119]

Driving Force of IRS: In the IRS model, the process can be divided into two main stages: (i) the excitation of infrared-active phonons due to the absorption of the electric field in the infrared range and (ii) the excitation of Raman-active phonons through a large amplitude infrared phonon via anharmonic potential. Therefore, the driving force for infrared-active phonons is the electric field, while for Raman-active phonons, it is the motion of the infrared-active phonons.

In the case of a cubic structure, the anharmonic lattice potential due to Q_{IR} (infrared-active phonon amplitude) and Q_{R} (Raman-active phonon amplitude) can be defined as follows.

$$V(Q_{\mathrm{IR}}, Q_{\mathrm{R}}) = \frac{1}{2}\Omega_{\mathrm{R}}^2 Q_{\mathrm{R}} + \frac{1}{2}\Omega_{\mathrm{IR}}^2 Q_{\mathrm{IR}} - a_{12} Q_{\mathrm{R}} Q_{\mathrm{IR}}^2 - a_{21} Q_{\mathrm{R}}^2 Q_{\mathrm{IR}} + \cdots , \tag{3.44}$$

where a_{ij} denotes anharmonic coupling constants. In centrosymmetric crystals, IR phonons can be classified as having odd-parity, while Raman phonons have even-parity symmetry. In this case, in Eq. (3.44), only terms with even-parity symmetry have non-zero values, i.e., $Q_{\mathrm{R}} Q_{\mathrm{IR}}^2$. By considering the forces due to the lattice potential ($F = -\partial V / \partial Q_{\mathrm{IR\ or\ R}}$) from Eq. (3.44) and the electric field $F = C_{\mathrm{IR}} E(t) \sim \sin \Omega_{\mathrm{IR}} t$ from Eq. (3.9), the equation of motion in IRS can be expressed as follows.

$$\begin{aligned}
&\text{(i) } \mu_{\mathrm{IR}}^* \left(\frac{\partial^2 Q_{\mathrm{IR}}(t)}{\partial t^2} + 2\gamma \frac{\partial Q_{\mathrm{IR}}(t)}{\partial t} + \Omega_{\mathrm{IR}}^2 Q_{\mathrm{IR}}(t) \right) = a_{12} Q_{\mathrm{R}} Q_{\mathrm{IR}} + C_{\mathrm{IR}} E(t), \\
&\text{(ii) } \mu_{\mathrm{R}}^* \left(\frac{\partial^2 Q_{\mathrm{R}}(t)}{\partial t^2} + 2\gamma \frac{\partial Q_{\mathrm{R}}(t)}{\partial t} + \Omega_{\mathrm{R}}^2 Q_{\mathrm{R}}(t) \right) = a_{12} Q_{\mathrm{IR}}^2 .
\end{aligned} \tag{3.45}$$

3.3.5 SFE: Sum-Frequency Excitation

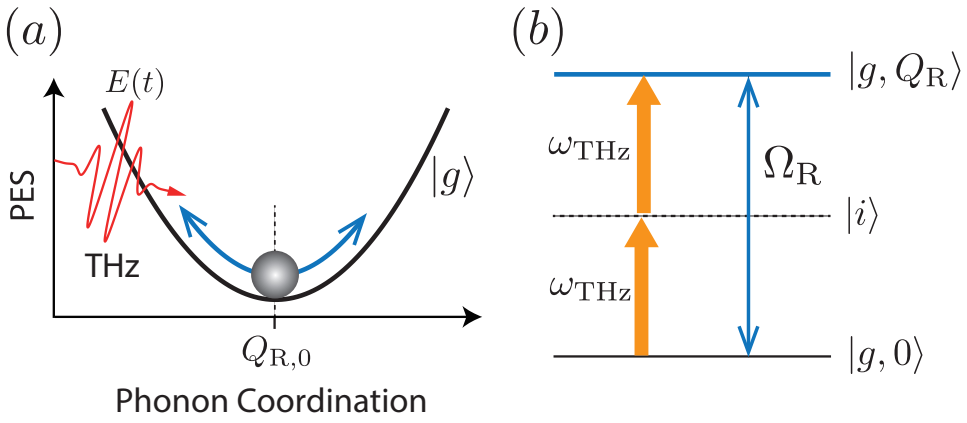

Figure 3.8: Schematic illustration of SFE process. (a) PES depending on Raman-active phonon coordination (Q_{R}) excited by THz pulse. (b) Energy diagram.

General Description: The SFE process involves the excitation of Raman-active lattice vibrations at a frequency double that of the THz electric field.[95] This phenomenon can be conceptualized as a two-photon absorption process concerning phonon levels. In the context of the ISRS model, as detailed in Section 3.3.1, SFE involves a virtual level $|i\rangle$ located between the ground state and the phonon-excited state, as illustrated in Fig. 3.8. The first observation of coherent phonon generation through SFE using a THz pump was in diamonds [95], and similar phenomena have been verified in other solids, such as V_2O_3.[120] Like IRS, SFE involves the excitation of phonons without the accompanying electronic excitation, making it a promising method for manipulating crystal structures by exclusively driving phonons. Furthermore, sum-frequency ionic Raman scattering (SFE-IRS), a hybridized model for IRS and SFE models, has been recently proposed theoretically.[121] SFE-IRS produces Raman-active phonons at twice the frequency of infrared-active phonons generated by infrared absorption.

Driving Force of SFE: The driving force for Raman-active phonons by a terahertz (THz) pulse $E(t) \sim \cos\omega_{\mathrm{THz}}t$, which is close to the phonon frequency, can be expressed

as follows:

$$F_{\mathrm{SFE}}^{Q_{\mathrm{R}}} = \left.\frac{\partial P_0}{\partial Q_{\mathrm{R}}}\right|_{Q_{\mathrm{R}}=0} E(t) + \epsilon_0 \left.\frac{\partial \chi^{(1)}}{\partial Q_{\mathrm{R}}}\right|_{Q_{\mathrm{R}}=0} E^2(t). \tag{3.46}$$

The first term is zero and can therefore be ignored due to $\partial P_0/\partial Q_{\mathrm{R}} = 0$. Consequently, the second term becomes the driving force for SFE model. Since $E(t)^2 \sim (1 + \cos 2\omega_{\mathrm{THz}} t)/2$, coherent phonons are driven when $2\omega_{\mathrm{THz}} \sim \Omega_R$ is satisfied.

3.4 Detection Mechanisms

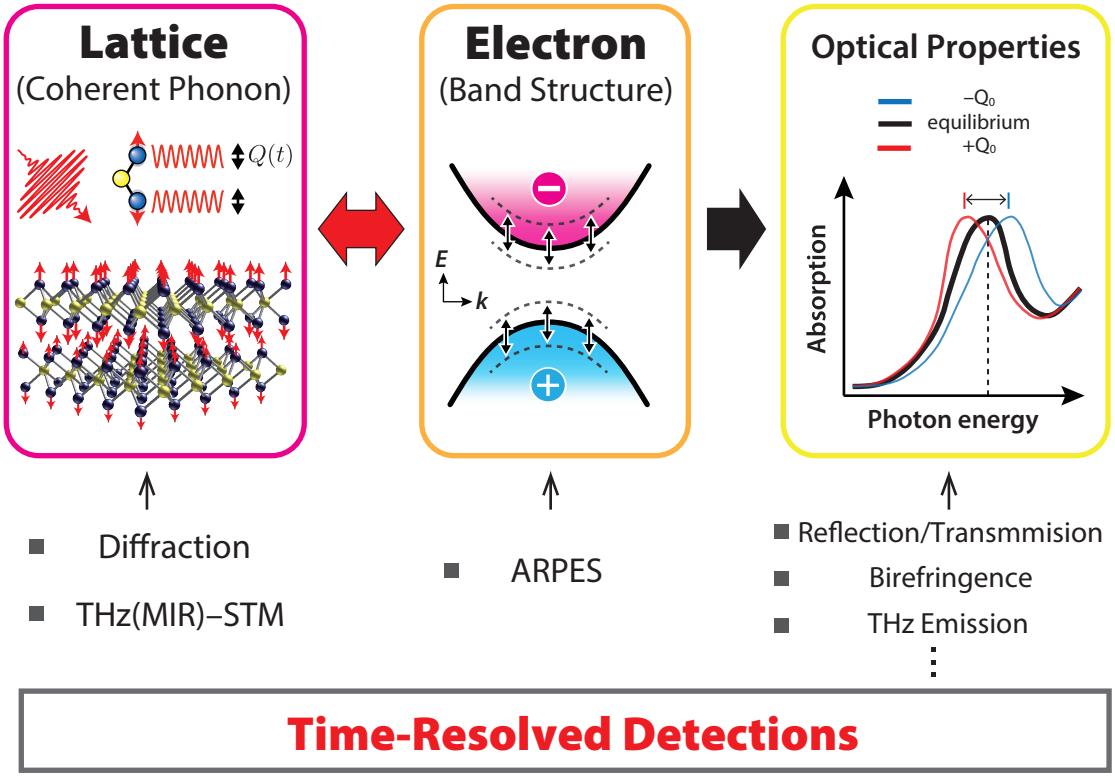

Figure 3.9: An overview for detecting coherent phonons.

It is essential to discuss the detection mechanisms of coherent phonons, often even more than to explore their generation mechanisms. Due to coherent phonon amplitudes being often less than a picometer (pm) [66, 122], it is significantly challenging to directly

capture their temporal spatial modulation. Instead, coherent phonons can be visualized as probe-pulse modulations depending on pump-probe delays, such as changes in light intensity, diffraction intensity, and photoelectron emissions. Therefore, Understanding how the real-space movement of atoms influences those changes in probe pulses is crucial for accurately interpreting experimentally observed coherent phonon signals.

Figure 3.9 present a schematic overview, illustrating how coherent phonons lead to variations in lattice, electronic states, and optical constants; which level of physical quantity changes are captured by each time-resolved measurement technique. When coherent phonons are excited by ultrashort pulses, they result in an immediate shift in the atomic positions within the crystal structure. This shift, in turn, influences the energy of Bloch electrons through deformation potential interactions. If photoexcited carriers are generated, they can inversely impact the lattice system. The modulation of electronic states by phonons contributes to the alteration of the resonance energy, leading to temporal changes in optical constants across the entire light energy spectrum. The following section briefly introduces how each time-resolved detection method can observe coherent phonon signals, focusing on the change in specific physical quantities that they measure.

Optical Detection: The use of light as a probe is the most historically established method for detecting coherent phonons. After the excitation of coherent phonons, the electronic states are modulated through deformation-potential interactions, which in turn are reflected in the optical constants. Thus, the optical susceptibility $\chi(\omega)$, depending on the probe photon energy $\hbar\omega$, is modulated over time by the phonon displacement $Q(t)$, can be expressed in terms of a higher-order expansion as follows [112]:

$$\chi(\omega; Q) = \chi_0(\omega) + \sum_n \frac{1}{n!} \left(\frac{\partial^n \chi}{\partial Q^n} \right)_{Q=0} Q^n(t), \tag{3.47}$$

where $\chi_0(\omega)$ is the optical susceptibility of the material in the absence of any interactions and $\partial^n \chi / \partial Q^n$ represents the n-th order Raman tensor associated with deformation

potential (DP) interactions. $\chi(\omega; Q)$ is dominated by a time-domain oscillation proportional to $Q(t)$.

There are mainly three optical detection methods for observing coherent phonons: (i)reflectivity/transmittivity change measurements ($\Delta R/R$ and $\Delta T/T$), (ii) electro-optic (Kerr-rotation) measurements, and (iii) THz-emission measurements. The method (i) measures isotropic changes in the intensity of the probe light itself. It is particularly effective for observing optical phonons in the isotropic A mode, where the Raman tensor has diagonal components.[83] The method (ii) evaluates the birefringence changes in a medium by measuring changes in the polarization rotation or ellipticity of the probe light. It allows for the observation of anisotropic E-mode optical phonons, where the Raman tensor has non-diagonal components. In the method (iii), THz radiation from a material upon photo excitation is sampled using nonlinear optical crystals or photoconductive antennas (PCA).[123, 124, 125, 126] It has been shown that coherent IR-active phonons play a role in the THz emission.

Diffractions: Crystal diffraction methods, such as x-ray or electron diffraction, are uniquely advantageous for directly evaluating changes in the structural symmetry of materials within their reciprocal space. The investigation by optical responses often includes various physical changes, making it challenging to isolate specific structural variations. In contrast, the crystal diffraction method is beneficial to directly evaluate temporal atomic motions. Coherent phonons cause temporal modulations in the average atomic positions within a crystal structure, leading to modulation of the structure factor F, as evident from Eq. (2.8) introduced in Section 2.4. The use of x-ray or electron pulses, which are shorter in duration than the period of the coherent phonons, enables the direct observation of changes in the diffraction intensity.[127, 53] These changes correlate with the phonon frequency, allowing for an in-depth analysis of their impact on the crystal structure.

Angle-Resolved Photoemission Spectroscopy (ARPES): Time-resolved angle-resolved photoemission spectroscopy (tr-ARPES) is an advanced spectroscopic technique that enables the direct observation of electron energy and momentum dynamics in materials during photoexcitation. The distinctive feature of this approach is not only that it allows for the direct experimental visualization of the band structure, which governs the properties of solids, but also that it enables discussion of the correspondence with theoretical simulations based on first-principles calculations.[128] Notably, the recent advancement of frequency-domain tr-ARPES facilitates the observation of coherent phonons that includes information of electron-phonon-coupling strength directly. To date, energy modulation in the electronic states, synchronized with the coherent phonon frequencies, has been observed in various kinds of quantum materials.[129, 130, 131, 132]

Scanning-Tunneling Microscopy (STM): The time-resolved measurement technique, as discussed above, monitored the motion of coherent phonons by detecting variations in macroscopic physical quantities, employing a probe system with a spot size significantly larger than atomic scale. Recently, a remarkable time-resolved scanning-tunneling microscopy (STM) has been developed, capable of measuring the dynamics of coherent phonons at the nanometer scale through the analysis of probe tunneling currents.[133] Consequently, this innovation enables the exploration of nanoscale coherent phonon physics at an atomic-level spatial resolution, previously observable only at a macroscopic scale.

Chapter 4

Photo-Induced Tellurium Segregation in Polymorphic $MoTe_2$

To elucidate the mechanisms of structural dynamics, particularly photo-induced structural phase transitions, it is crucial to verify (1) how much intense light irradiation $MoTe_2$ can withstand and (2) what kind of structure is produced by irradiation above the damage threshold. This chapter clarified the damage threshold and the structure and nature of the damage area under various light irradiation conditions for the polymorphic structures of $MoTe_2$, namely the 2H and 1T' structures. The results showed that the damage threshold of the sample increases when using high-energy light with a low repetition frequency. Furthermore, coherent phonon oscillations at 3.6 THz, attributed to Te precipitation, were observed in the damaged area. However, the anticipated structural phase transition from the semiconductor 2H phase to the semimetal 1T' phase was not observed within the damaged area.

The descriptions in this chapter are based on the research found in **T. Fukuda**, *et al. Phys. Status Solidi RRL.* **16**, 2100633 (2022). [134]

4.1 Motivation and Introduction

Structural polymorphism of transition-metal dichalcogenides (TMDCs), a class of two-dimensional (2D) layered materials composed of a transition-metal and two chalcogens, has been attractive from a fundamental physics viewpoint for the study of non-equilibrium structural dynamics as well as for memory applications as a phase-change material [135, 136, 137, 53, 54, 138]. $MoTe_2$, a well-known TMDC, is a representative polytype and exhibits three distinct crystal structures: a semiconducting 2H (Fig. 4.1(a)), a semimetallic 1T′ (Fig. 4.1(b)), and a Type-II Weyl semimetallic T_d phase [33, 35]. The 2H phase is stable at room temperature (300 K), the 1T′ phase is metastable at room temperature, and the T_d phase is a low temperature (< 250 K) polymorph of the 1T′ phase. Reversible switching between the semiconducting and metallic phases of $MoTe_2$ by illumination with light is of particular interest for the development of novel device fabrication methods, such as an atomic scale phase-patterning technology with the low-dimensional structures for the fabrication of atomically thin high-performance integrated circuits [28, 139, 140]. Illumination with light also offers an alternative technique to induce phase transitions over other methods such as temperature [141], electronic doping [16], strain [142]. Theoretical studies suggest that high-density electronic excitation of the semiconducting 2H phase by light pulses with photon energy above the band gap can induce a structural phase transition into a metallic $2H^*$ or semimetallic 1T′ phase [49, 50, 51]. However, experimental studies of light-induced structural phase transitions remain controversial. When a strong continuous-wave (CW) laser is used, tellurium segregates from $MoTe_2$ via photo-thermal or heat-accumulation effects [143], as surface oxidation in the presence of elevated temperature even under vacuum conditions [144]. On the other hand, there have been few studies of light-induced structural phase transitions in $MoTe_2$ using femtosecond pulses, for which photo-thermal effects are expected to be significantly less than the case for CW laser irradiation since femtosecond electronic excitation occurs before thermal effects appear [145]. Here, we explore the lattice dynamics of 2H- and 1T'$-MoTe_2$ samples

monitored by coherent phonon spectroscopy under high-intensity irradiation with a 30-45 fs pulsed laser at ambient conditions (300 K) to gain insights into the possibility of controlling the structural polymorphism of $MoTe_2$ by light in the presence of minimal thermal effects.

4.2 Experimental Methods

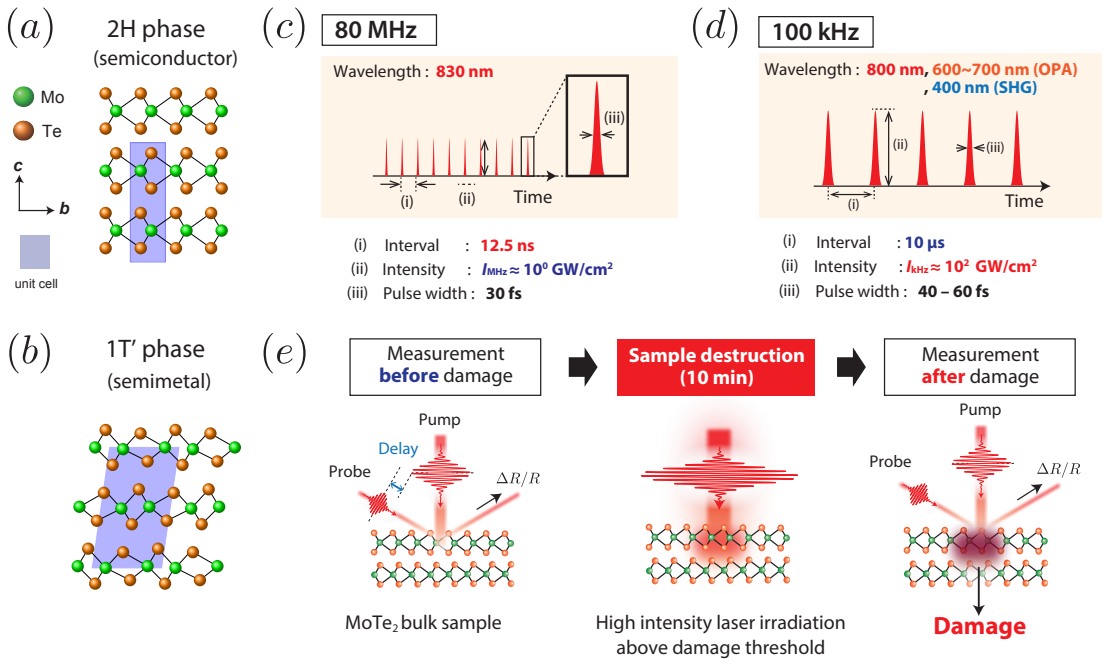

Figure 4.1: (a) and (b) Lattice structures of a $2H - MoTe_2$ and 1T'$-MoTe_2$ crystals, respectively. (c) and (d) Comparison of the experimental conditions between 80MHz and 100 kHz repetition pulsed lasers, respectively. (e) Experimental procedure of the reflective-type pump-probe spectroscopy before and after optical sample damage in the present study. (d) Lattice structure of a 1T'$-MoTe_2$ crystal.

The flake form $MoTe_2$ bulk single crystals used were grown by the flux zone method for the 2H phase (commercially available from *2D Semiconductors*, USA), and chemical vapor transport (CVT) for the 1T' phase [146]. The thickness of the samples used was about 100 μm. Based on density functional theory (DFT) simulations, the optical penetration depth was estimated to be $\approx$ 45 nm for the photon energy of 1.5 eV

($\lambda \approx 800$ nm) and ≈ 25 nm for 2.0 eV ($\lambda \approx 600$ nm) for both the 2H and 1T' phases, which suggests there is negligible photon-energy dependence. Since the sample thickness is much thicker than the optical penetration depth, the effects of the substrate or the sample thickness dependence are negligibly small in our study. Coherent phonons, whose generation process is traditionally described as resonant or non-resonant impulsive stimulated Raman scattering (ISRS) [68] or displacive excitation of coherent phonons (DECP) [65], were detected by a degenerate reflective-type optical pump-probe technique that uses the same wavelength for the pump and probe pulses. As shown in Figs. 4.1(c) and (d), we used two types of femtosecond light sources to evaluate the resulting photo-thermal and heat-accumulation effects as shown in): one is 30-fs pulse duration, 830 nm (= 1.49 eV) central wavelength with an 80-MHz repetition rate from a Ti:Sapphire oscillator, with the other had a duration of 45 fs, 100 kHz repetition rate, a 800-nm (= 1.55-eV) central wavelength generated with a regenerative amplifier and an optical parametric amplifier (OPA) to allow variation of the central wavelength of the light. The OPA generated light between 1200 nm $\sim$ 1600 nm. Both 600 nm (= 1.78 eV) and 700 nm (= 2.06 eV) light is available via second harmonic generation (SHG) using a BBO crystal under phase-matching conditions. The high repetition 80-MHz laser delivers femtosecond pulses with an interval of 12.5 ns and a peak intensity of $I_{\mathrm{MHz}} \approx 1$ GW/cm^2. On the other hand, the low repetitive 100-kHz laser delivers femtosecond pulses with an interval of 10 μs and a peak intensity of $I_{\mathrm{kHz}} \approx 10^2$ GW/cm^2. It is noted that the pump and probe light is refocused to a spot with a diameter estimated to be about 20 μm on the sample surface. Considering that the rise in photo-induced temperature accumulates on a sub-microsecond time scale, photo-thermal effects induced by the high-repetition pulsed laser are more significant than those induced by the low-repetition light source. In contrast, the excitation density per light pulse of the low repetitive one is more significant than that of the high repetitive one. As schematically described in Fig. 4.1(e), we performed measurements of coherent phonon signals to investigate a possible structural phase transition. We took images of sample surfaces by optical microscopy before and after 10 minutes of

laser irradiation above the damage threshold without changing the irradiation spot location. It is noted that the measurements were conducted under an ambient condition, and the pump fluence used for before-and-after measurements was set to an intensity lower than the damage threshold. Photo-induced structural changes can be evaluated by comparing the phonon spectra and the optical contrasts. The figures used in this article were generated using Matplotlib [147].

4.3 80-MHz Excitation

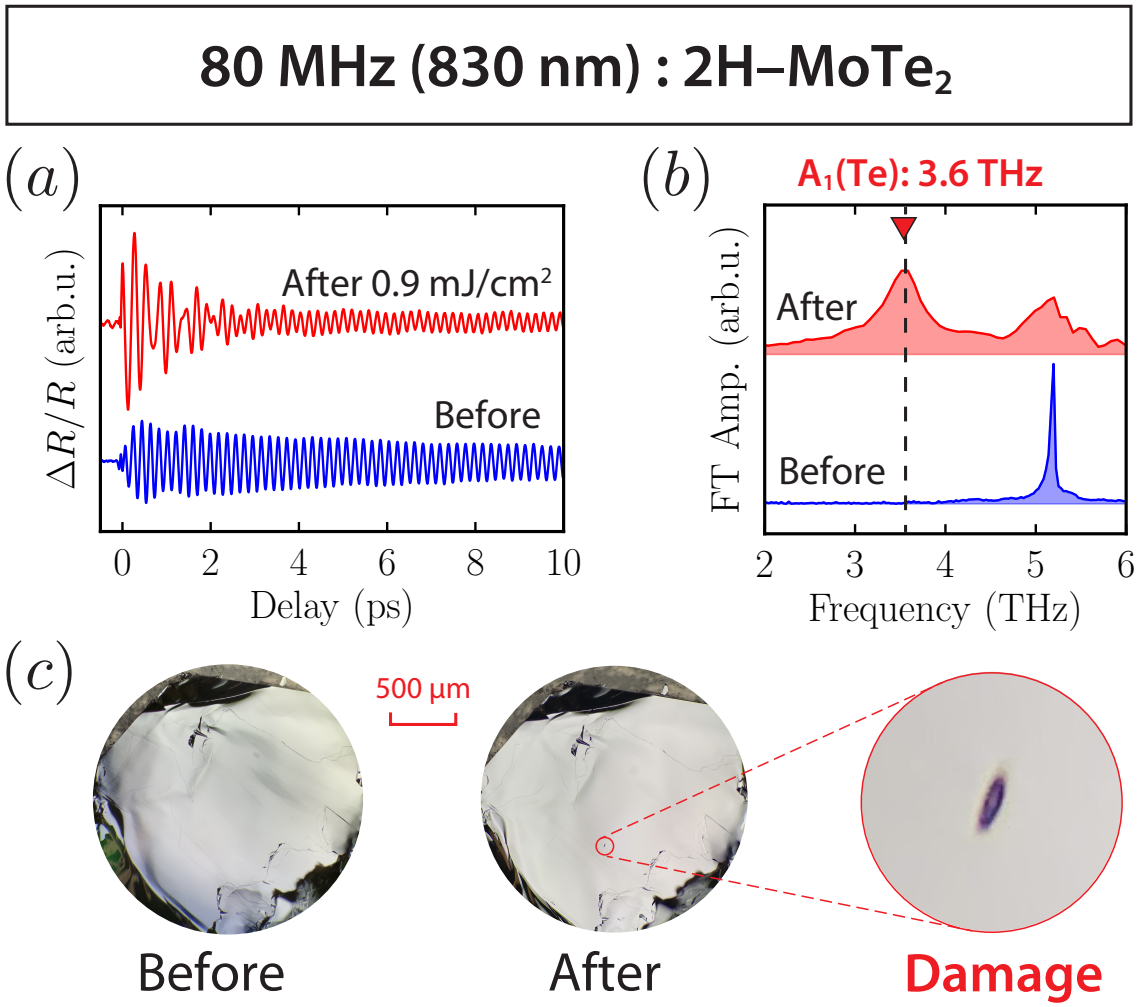

Figure 4.2: 80-MHz Experiment for $2H - MoTe_2$ before and after the damage-threshold irradiation of $F = 0.9$ mJ/cm^2. (a) Experimental coherent phonon signal subtracted from time-domain $\Delta R/R$ data before and after sample damage. (b) FT spectra of (a) (c) Optical microscope image of the sample surface before and after sample damage.

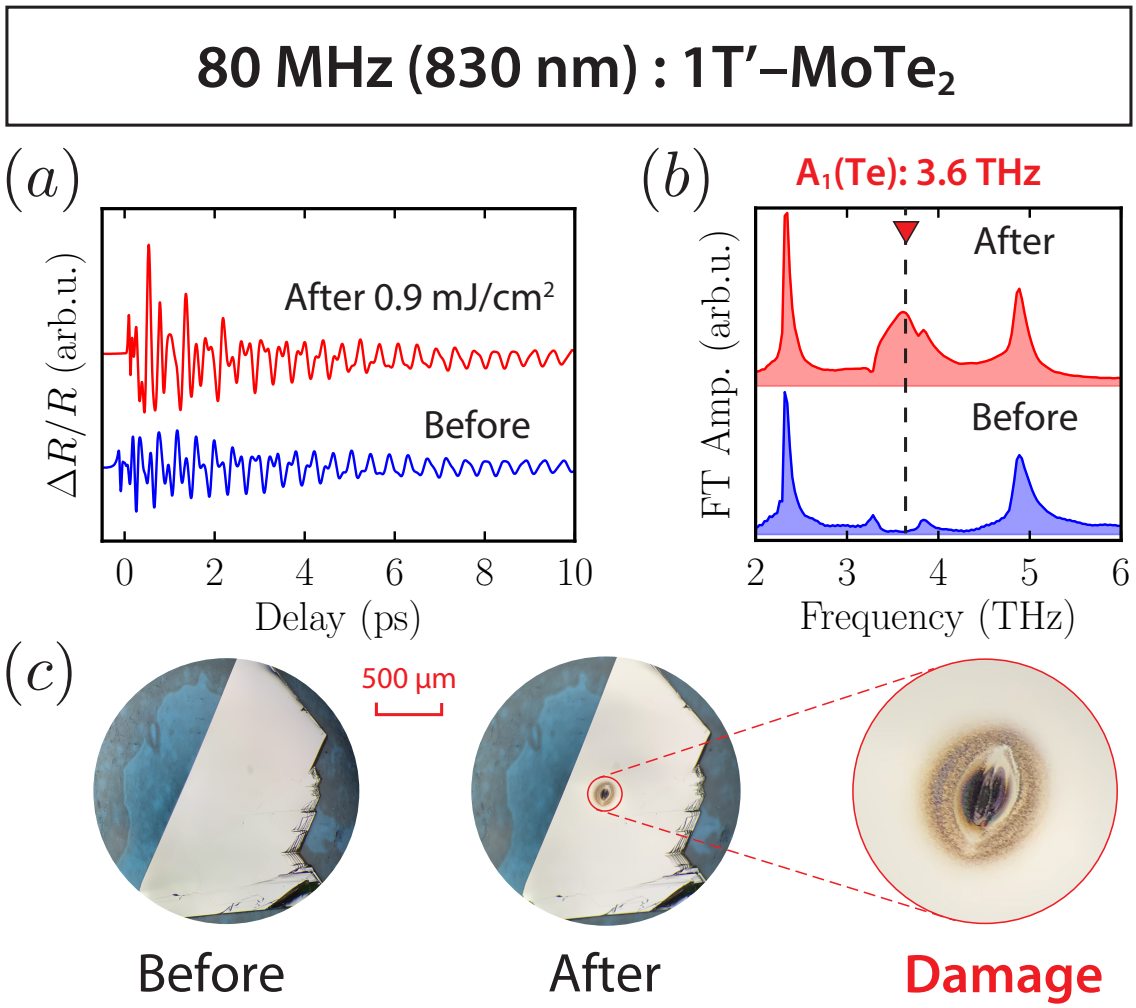

Figure 4.3: 80-MHz Experiment for 1T'−$MoTe_2$ before and after the damage-threshold irradiation of $F = 0.9$ mJ/cm^2. (a) Experimental coherent phonon signal subtracted from time-domain $\Delta R/R$ data before and after sample damage. (b) FT spectra of (a) (c) Optical microscope image of the sample surface before and after sample damage.

First, we show the coherent phonon signals before and after surface damage due to the use of the 80-MHz pulsed laser with $\lambda = 830$ nm. To analyze the oscillatory components of the time-domain signals, we subtracted a background signal derived from electronic response using the bi-exponential function. The damage-threshold pump fluence for both the 2H− and $1T' - MoTe_2$ samples was found to be about $F_{\mathrm{th(MHz)}} = 0.9$ mJ/cm^2 for the 80-MHz measurements so that the pump fluence used was set to 0.3 mJ/cm^2, a value much lower than $F_{\mathrm{th(MHz)}}$. Figures 4.2 and 4.3 show the coherent

phonon signals, and Fourier transformed (FT) phonon spectra observed in 2H− and $1T' - MoTe_2$ before and after sample damage. Before laser irradiation, coherent phonon oscillations from both samples are visible for time ranges longer than 25 ps, indicating that the scattering terms, such as electron-phonon and phonon-phonon interaction, are quite small, as expected based on the characteristic low dimensional structure of TMDCs. From the FT spectra of the coherent phonon signals, we found one A_{1g} mode (5.1 THz) for $2H - MoTe_2$ and four A_g modes (2.3 THz, 3.3 THz, 3.9 THz, and 4.9 THz) for $1T' - MoTe_2$, which are in good agreement with the previous reports of Raman and coherent phonon measurements on the 2H and 1T' phases [148, 149, 150, 151, 152, 54, 138]. It is noted that since we carried out the experiment using an isotropic reflection geometry for coherent phonon detection, anisotropic lattice vibration modes, such as E modes, are expected to be challenging to detect in our measurements. After laser irradiation, we observed that a new vibrational mode at 3.6 THz (≈ 120 cm^{-1}) appeared for both samples, accompanied by ablation-like permanent damage patterns in the form of a black discoloring in optical contrast as can be seen in Figs. 4.2(c) and 4.2(d). The emergent mode at 3.6 THz is considered to be the A_1 mode of tellurium (Te) [117, 153, 154, 155, 118] due to tellurium segregation from the $MoTe_2$ samples as a result of surface melting induced by heat-accumulation effects of high repetitive pulsed laser irradiation. The Te segregation observed to date in coherent phonon spectra appearing at 3.6 THz has been occasionally observed in other telluride compounds, such as $Ge_2Sb_2Te_5$ [156], Sb_2Te_3 [157, 158], CdTe [159], ZnTe [160] as well as static-measurement studies on $MoTe_2$ [143]. On the other hand, additional phonon modes related to the different structural phases were not observed after the laser irradiation: the 2H–to–1T' and 1T'–to–2H phase transitions were not observed. Notably, the 2H phase has an intrinsic vibrational mode at 3.6 THz manifested as the E_{1g} mode [148, 149, 161] and Te also has an E^1 mode at 4.2 THz [162, 163]. However, as mentioned above, our detection scheme is, in principle, insensitive to anisotropic lattice vibrations, so the scenario of Te segregation is the most plausible mechanism to describe our results. For these reasons, no structural phase transitions and Te segregation with permanent

sample damage was observed for both 2H– and 1T′–$MoTe_2$ samples at < 1 mJ/cm^2 irradiation with the use of the high repetition 80-MHz pulsed laser. It should be noted that the appearance of a 3.6-THz peak has been frequently reported in previous studies and is considered evidence of a phase transition from 2H to 1T' phases. However, many of these peaks likely arise due to Te segregation.[28, 139, 140] Therefore, when discussing the structural phase transition toward the 1T' phase based on the appearance of the 3.6-THz peak, it is necessary to carefully check whether other peaks derived from the 1T' phase are also present.

4.4 100-kHz Excitation

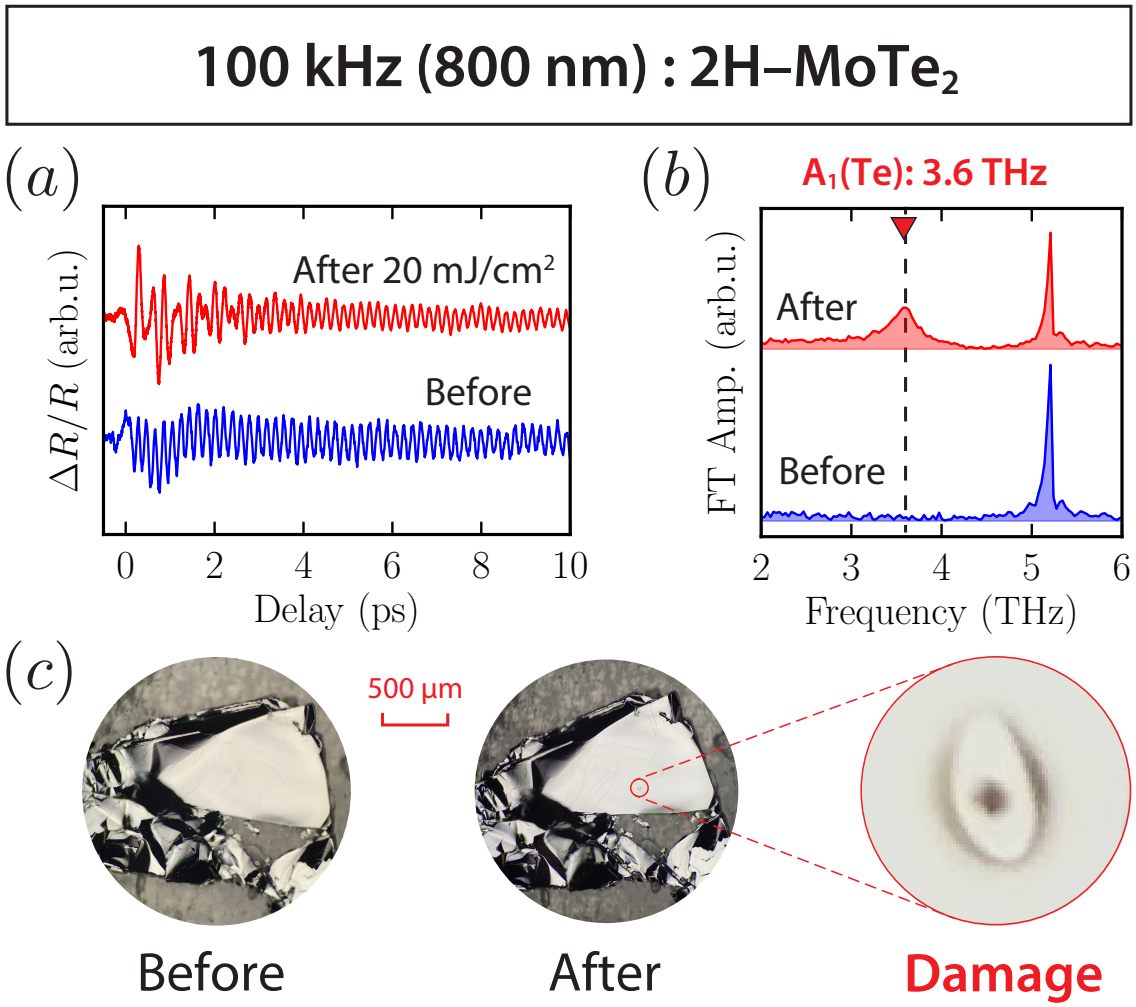

Figure 4.4: 100-kHz Experiment for $2H - MoTe_2$ before and after the damage-threshold irradiation of $F = 20$ mJ/cm^2. (a) Experimental coherent phonon signal subtracted from time-domain $\Delta R/R$ data before and after sample damage. (b) FT spectra of (a) (c) Optical microscope image of the sample surface before and after sample damage.

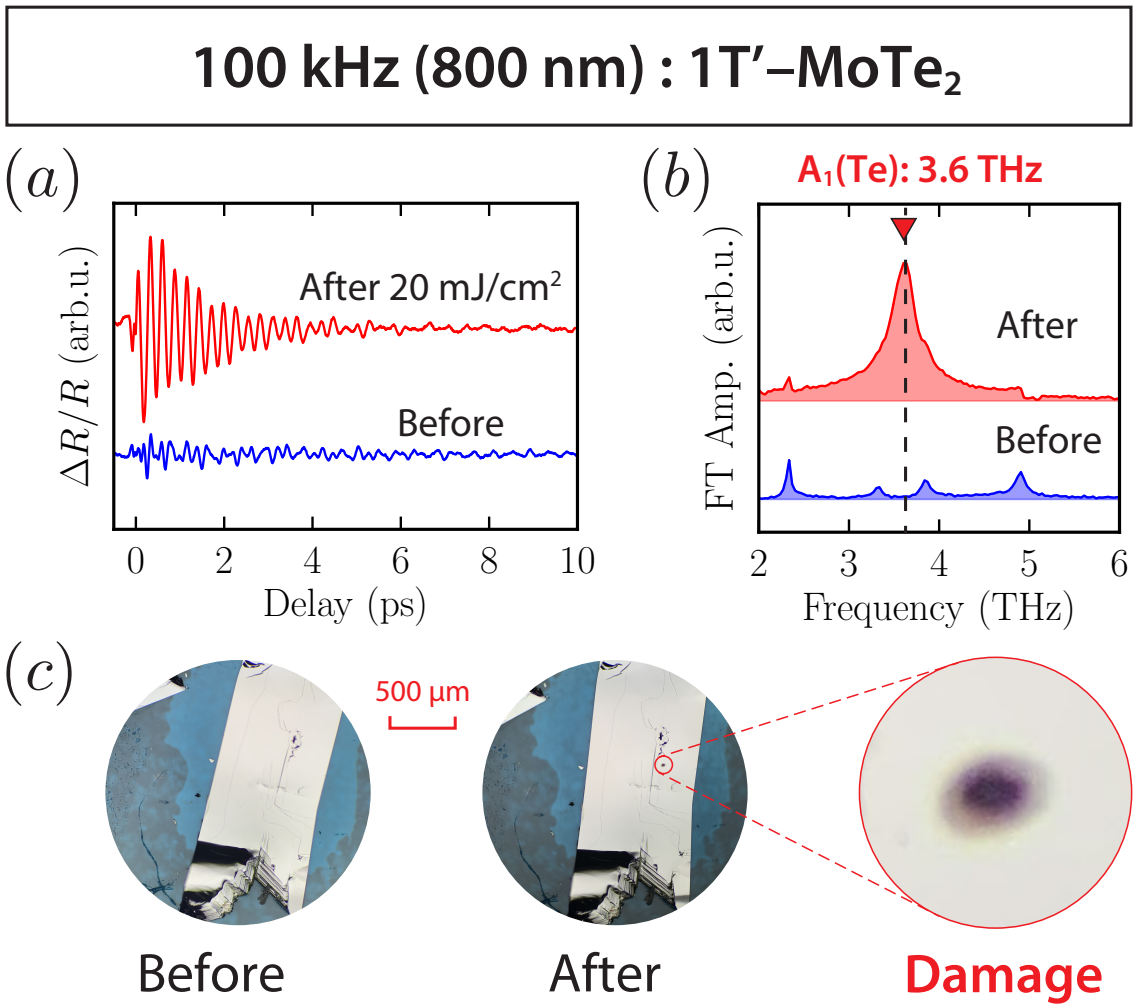

Figure 4.5: 100-kHz Experiment for 1T'−$MoTe_2$ before and after the damage-threshold irradiation of $F = 20$ mJ/cm^2. (a) Experimental coherent phonon signal subtracted from time-domain $\Delta R/R$ data before and after sample damage. (b) FT spectra of (a) (c) Optical microscope image of the sample surface before and after sample damage.

Second, we examined the effects of the low repetition 100-kHz pulsed laser with $\lambda = 800$ nm. The damage-threshold fluence $F_{\text{th(kHz)}}$ for both 2H− and 1T′ − $MoTe_2$ samples was found to be between 10 to 20 mJ/cm^2 for the 100-kHz measurements, which is surprisingly about ten times larger than the threshold for the high repetition 80-MHz measurements, $F_{\text{th(MHz)}} < F_{\text{th(kHz)}}$. This observation is considered to be a result of the reduced heat accumulation effects due to the reduced repetition rate. The pump fluence used for the coherent phonon measurements was 1 mJ/cm^2, a value much

lower than the threshold $F_{\mathrm{th(kHz)}}$, while the pump fluence leading to sample damage was 20 mJ/cm^2. Before laser irradiation, the coherent phonon oscillations and the associated FT phonon spectra for both samples were similar to those of the 80-MHz experiments, as seen in Figs. 4.4 and 4.5. After laser irradiation, although the spectral details are slightly different from those for the case of the 80-MHz experiments, the A_{1g} mode of Te segregation (3.6 THz) appears along with permanent damage patterns. As shown in Figs. 4.4(c) and 4.5(c), no additional phonon modes related to the structural phases in both samples were observed, . These results suggest that even when using low- and high-excitation pulsed lasers, Te segregation is inevitable, and light-induced structural phase transitions between 2H and 1T' phases are hard to realize under the current experimental conditions.

4.5 Surface-Damage Characterization

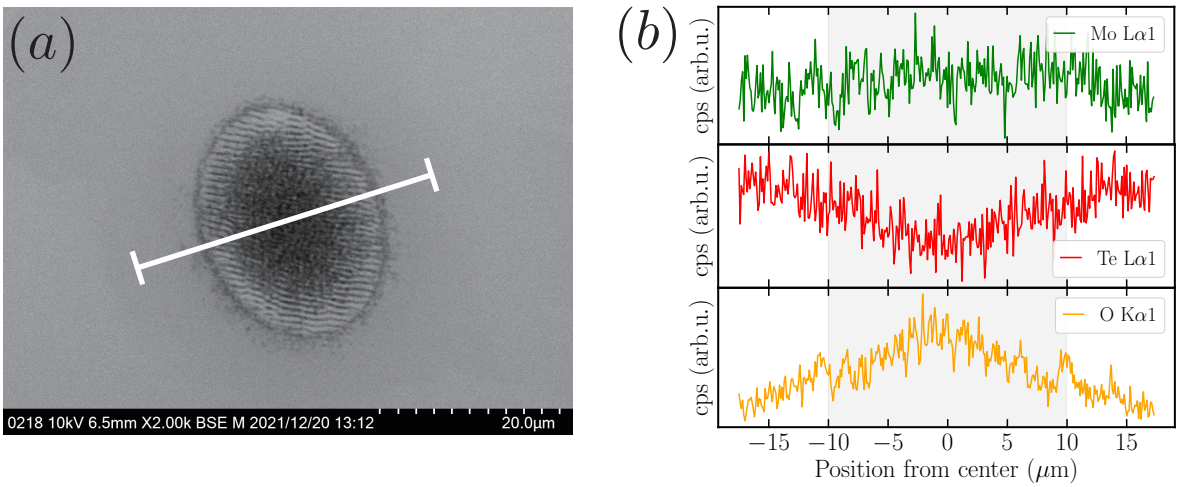

Figure 4.6: (a) The image of sample surface damage after laser irradiation above the damage threshold taken by scanning electron microscopy (SEM). (b) Spatial line scan of local chemical composition (Mo, Te, and O) on the damaged region, as shown in (a), taken by energy dispersive X-ray spectroscopy (EDX).

As discussed above, Te segregation is considered to be strongly promoted by photo-thermal effects due to heat accumulation, as can be seen in the observed differences

in the effects with the pulsed laser repetition rate. Since the samples we used in the measurement were exposed to air, the sample is thought to be oxidized due to laser irradiation, leading to the formation of other compounds. A recent investigation has revealed that molybdenum oxides such as MoO_{3-x} are formed on the surface of $MoTe_2$ due to elevated temperature [144]. We also confirmed oxide formation in the ablation-like damaged region using scanning electron microscopy and energy-dispersive X-ray spectroscopy (SEM-EDX) measurements. Figure 4.6(a) shows a SEM image of the damaged area, where a rippled pattern can be observed. This pattern may be Laser-induced periodic surface structures (LIPSS) resulting from ablation.[164] Figure 4.6(b) presents a spatial line scan of the chemical composition in the damaged area conducted by the EDX measurement. The results indicate that the composition of Mo remains unchanged while Te decreases and O increases. This suggests oxidation of the sample and the isolation of Te. The unchanged composition of Mo implies the formation of Mo oxides, which is consistent with results from previous research. As in the case here, the remaining Te atoms segregate to form Te-rich regions in the presence of surface oxidation, forming MoO_{3-x} by laser irradiation. To avoid surface oxidation and Te segregation, oxidation prevention countermeasures such as surface protection or high vacuum conditions are required to further investigate and control potential light-induced phase transitions among the polymorphs of $MoTe_2$.

4.6 Photon-Energy Dependence

Table 4.1: Absorption coefficients of the 2H phase (α_{2H}) and the 1T' phase ($\alpha_{1T'}$) for 800 nm (1.55 eV), 700 nm (1.78 eV), 600 nm(2.06 eV) calculated using DFT simulations.

	800 nm (1.55 eV)	700 nm (1.78 eV)	600 nm (2.06 eV)
α_{2H}	2.3×10^7 (m^{-1})	2.5×10^7 (m^{-1})	4.2×10^7 (m^{-1})
$\alpha_{1T'}$	2.3×10^7 (m^{-1})	2.8×10^7 (m^{-1})	3.6×10^7 (m^{-1})

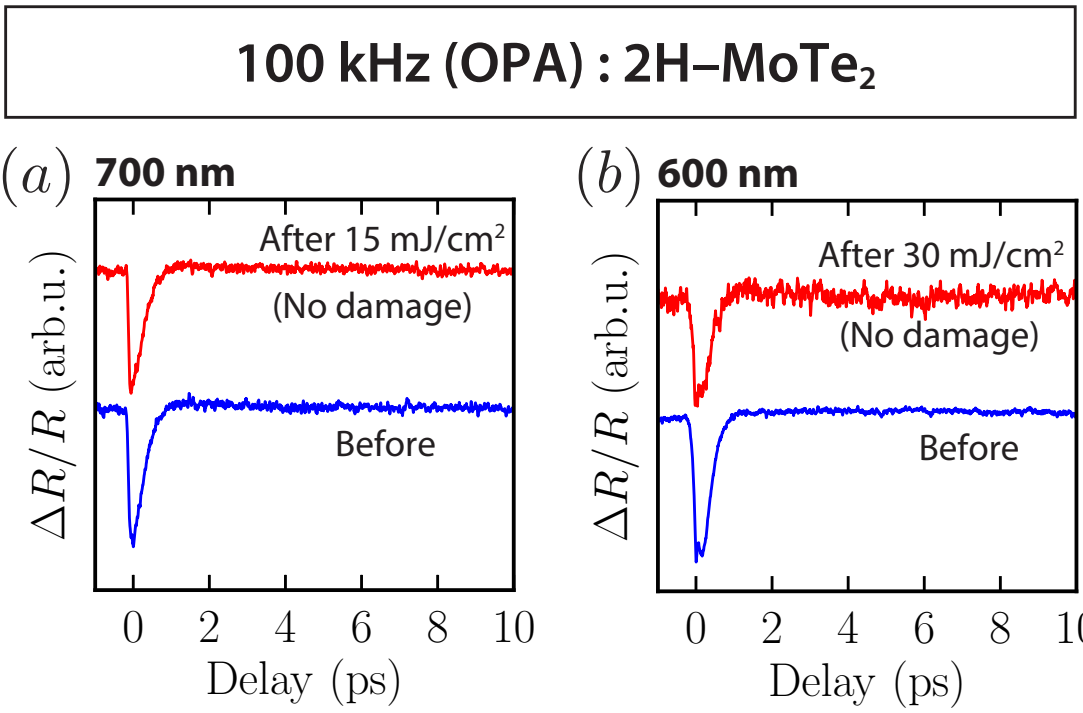

Figure 4.7: Photon-energy-dependence degenerate pump-probe measurements on $2H - MoTe_2$ with an OPA with variations of wavelength (photon energy) at (a) 700 nm (1.78 eV) light and (b) 600 nm (2.06 eV) light.

From another perspective, using different wavelengths may also play an essential role in light-induced phase transitions because higher photon energies may exceed the energy barrier of the free energy landscape [49]. According to a theoretical study, the use of the critical photon energy of 633 nm (= 1.96 eV) with dense electronic excitation can lower the potential barrier between the monolayer 2H and 1T' phases, which is thought to be also applicable to the bulk crystals.

To test for the effects of the photon energy, we performed reflectivity change measurements using light with central maximums of 700 nm (= 1.78 eV) and 600 nm (= 2.06 eV) generated using an OPA. Fig. 4.7 (a) and (b) show the $\Delta R/R$ signals of $2H - MoTe_2$ before and after laser irradiation with a fluence of 15 mJ/cm^2 for 700 nm, and 30 mJ/cm^2 for 600-nm, which are the maximum output for each wavelength for the OPA. Even with such high fluences, no surface damage was seen in the surface optical images for the 2H and 1T$'$ phases. In this experiment, coherent phonons in

the samples were invisible in $\Delta R/R$ signals except for the initial electronic response due to the pulse broadening of the OPA light compared with the 800-nm measurements or the wavelength dependence of coherent-phonon responses [165]. Although, due to the absence of coherent phonons, we cannot evaluate the structural dynamics under photon energies greater than 1.96 eV (λ = 633 nm), which is predicted to be a critical value for monolayer 2H-to-1T' phase transition [51], the time-domain $\Delta R/R$ signals from the 600-nm measurement show little change before and after 30 mJ/cm^2 irradiation, a value about twice as significant as the damage threshold for 800-nm irradiation. In addition to the repetition rate, the wavelength (photon energy) of the light source is possibly related to the presence of surface damage or the absence of Te segregation on the $MoTe_2$ samples. In general, the absorption coefficient can explain the photon-energy dependence of ablation since changes in optical absorption directly contribute to photo-thermal or heat-accumulation effects. The absorption coefficients α for 1.55 eV, 1.78 eV, and 2.06 eV photon energies calculated using DFT simulations are listed in Table 4.1. In both phases, we found the value of the absorption coefficient of 2.06 eV was more significant than that of 1.55 eV, suggesting photo-thermal effects should be more significant at 2.06 eV than 1.55 eV. However, it is inconsistent with our observation that the Te segregation is suppressed for the photon energy of 2.06 eV, which is more significant than 1.55 eV. This indicates that the photo-thermal effect induced by optical absorption cannot explain the suppression of Te segregation for light with energies under 2.06 eV. Therefore, a systematic study of the structural dynamics of $MoTe_2$ systems dependent on the photon energy with much higher intensities and much shorter pulse width is required in the future.

4.7 Conclusion

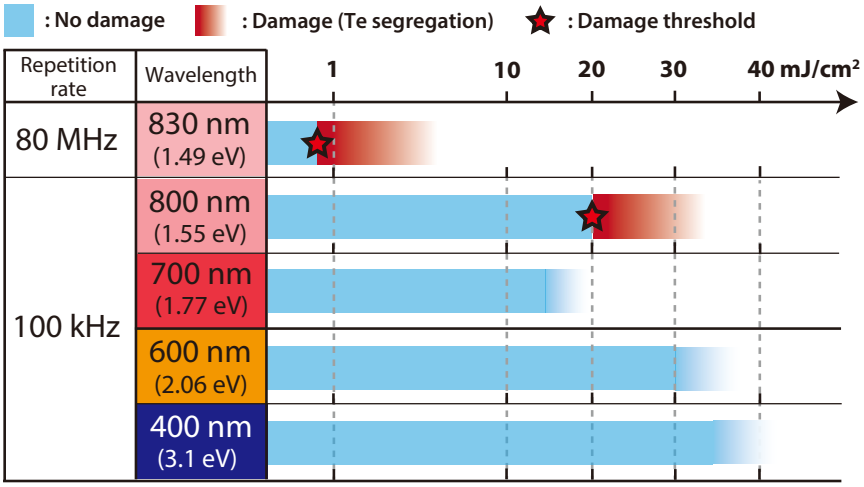

Figure 4.8: A schematic table summarizing the damage-threshold study on repetition rates and laser wavelength.

Figure 4.8 shows a schematic table summarizing the relationship of the damage thresholds and Te segregation for $MoTe_2$ to the repetition rates and laser wavelength.

We have investigated the structural changes induced by high-intensity femtosecond pulsed light above the sample-damage threshold. Reflective pump-probe coherent-phonon spectroscopy was carried out using two types of femtosecond pulsed lasers, a high repetitive 80-MHz with $\lambda = 830$ nm and a low repetitive 100-kHz light source with a wavelength range of $\lambda = 800$, 700, 600, and 400 nm, revealed that Te segregated on the surface of both phases leading to the observation of the A_1(Te) mode at 3.6 THz ($\approx$ 120 cm^{-1}). In addition, ablation-like patterns were observed in the optical contrast, which is considered to be a consequence of the heat-accumulation effects that depend on the repetition rate. However, when using higher photon-energy excitation, the sample damage was significantly suppressed, indicating that Te segregation is also likely related to the laser wavelength. Our results indicate that even using femtosecond pulsed light sources, Te segregation makes it difficult to realize the light-induced struc-

tural phase transitions between the 2H and 1T' phases. We suggest alternative sample structures to eliminate surface oxidation, such as oxidation prevention layers, and using high vacuum or selective photon energies may efficiently suppress Te segregation and realize the light-induced structural phase transitions.

Chapter 5

Ultrafast Interlayer Shear Phonon Dynamics in $1T' - MoTe_2$

Interlayer shear phonons in TMDs can change the symmetry of the crystal structure. This phenomenon is especially significant in the case of $MoTe_2$ and WTe_2, where the motion of shear phonons is crucial in the topological phase transition between the semimetal 1T' phase and the Weyl semimetal T_d phase. This chapter presents the coherent phonon dynamics of $1T' - MoTe_2$ at room temperature. This chapter explores the coherent phonon dynamics of $1T' - MoTe_2$ at room temperature, revealing the existence of the interlayer shear phonon mode, where the phonon mode is infrared active in the 1T' phase at room temperature, but Raman active in the low temperature T_d phase (< 250 K). This suggests that electronic excitation transiently induces an intermediate state between the 1T' and T_d phases.

The descriptions in this chapter are based on the research found in **T. Fukuda**, *et al. Appl. Phys. Lett.* **116**, 093103 (2020). [138]

5.1 Motivation and Introduction

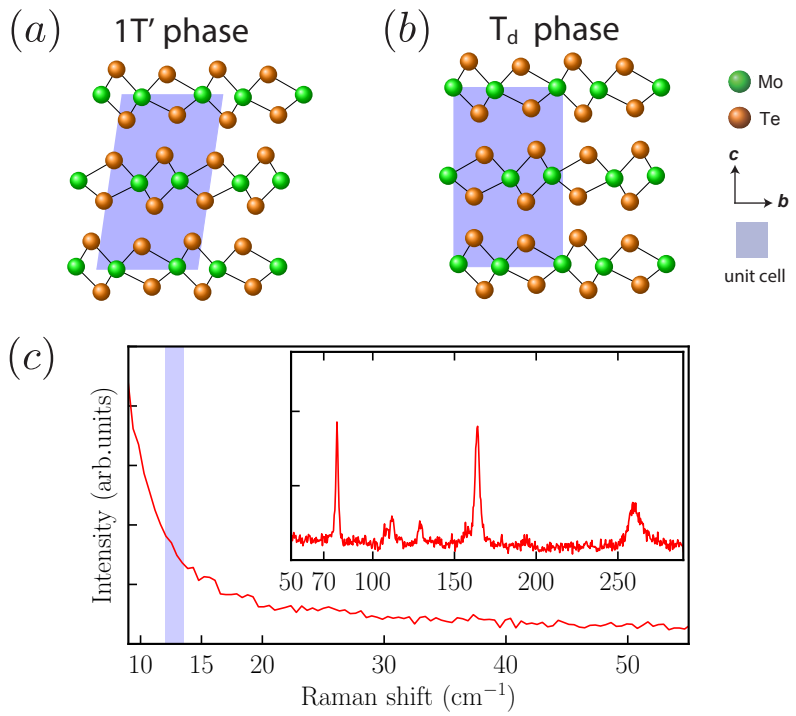

Figure 5.1: (a) Lattice structure of a 1T'−$MoTe_2$ crystal. (b) Lattice structure of a $T_d - MoTe_2$ crystal. (c) Raman spectrum of a 1T'−$MoTe_2$ bulk crystal sample, measured at room temperature ($\sim$ 300 K).

Recent interest in transition metal dichalcogenides (TMDCs) has dramatically increased owing to the variety of unusual properties stemming from the existence of two-dimensional van der Waals (vdW) structures, such as graphene. [12, 13, 14] One of the reasons that drives research in TMDCs is that they intrinsically possess a wide variety of possible crystal and electronic structures depending on a large number of accessible chemical combinations between metal (Mo, W, $\cdots$) and chalcogen (S, Se, Te) atoms, as well as the accessibility of other phases by low energy photon excitation. [49] These versatile properties can be useful for further understanding of the fundamental properties of topological materials as well as the advancement of high-performance and functional electronic, optoelectronic, and quantum devices [166, 16, 167], particularly the next generation of

strain-engineered phase-change materials [142] or phase patterning technology driven by light.[28] Within the TMDC family, $MoTe_2$ has attracted considerable attention because of its rich structural and electronic phases. $MoTe_2$ has three possible structural phases: the trigonal prismatic 2H semiconducting phase (the most stable at room temperature: RT), the centrosymmetric monoclinic 1T' semimetal phase (metastable at RT), and the lattice symmetry breaking orthorhombic T_d semimetal phase (stable below 250 K). Among these phases, the 1T' and T_d structures are similar, except for distortions along the $a-$ or $b-$axes as shown in Fig. 5.1(a) and (b). $MoTe_2$ is also known for being a candidate topological phase material such as a topological insulator (TI) or a Weyl semimetal (WSM) due to the breaking of lattice inversion symmetry by specific layer configurations. First-principle calculations and observations of Fermi arcs in lattice symmetry breaking orthorhombic T_d-MoTe_2 and similar structure, T_d-WTe_2, have led to the establishment and confirmation of the theory of Type-II WSMs with intriguing carrier transport properties with unusually long lifetimes. [32, 33, 34, 35, 168]

Some groups have recently observed the ultrafast dynamics of coherent phonons and lattice symmetry switching between the 1T' and T_d phases, corresponding to a phase transition from the WSM to the normal semimetal phases. Sie *et al.* induced shear displacements using THz pump pulses in the T_d phase of WTe_2, which was monitored by ultrafast electron diffraction.[53] On the other hand, Zhang *et al.* observed a similar phenomenon using optical pump-probe reflectivity measurements from extremely low temperature 4K to near RT [54], corresponding to the low-temperature T_d phase. However, the related coherent phonons at RT of the 1T'$-MoTe_2$ phase have not been well investigated. Therefore, it remains elusive if photoexcitation of the high temperature 1T' phase induces a phase transition in $MoTe_2$. It is essential to gain insight into the photoexcited state at RT and even higher temperatures in TMDCs because of potential device applications in general temperature conditions.

5.2 Experimental Methods

Optical pump-probe measurements were carried out using a Ti:Sapphire oscillator operated at 80 MHz, which provided near-infrared optical pulses with a pulse duration of $\leq$ 30 fs and a central wavelength of 830 nm (with a corresponding photon energy of $\hbar\omega \sim 1.5$ eV). It should be noted that the continuous heating effect by the 80 MHz repetition laser is negligibly small, as demonstrated by the phonon spectra shown below exhibiting the almost identical peak positions as those of previous Raman studies on bulk 1T'$-MoTe_2$. The average fluence of the pump beam was varied from $F = 170$ to 680 μJ/cm^2. The upper limit of fluence (680 μJ/cm^2) was set to prevent surface damage. The $s-$polarized pump and the $p-$polarized probe beams were co-focused onto the sample to a spot diameter of $\approx$ 16 μm with incident angles of about 5° and 15° for the sample normal, respectively. (See Section 2.3 for detail set up) The optical penetration depth at 830 nm was estimated to be 50 nm from the complex dielectric function calculated by density functional theory (DFT) simulations. The delay between the pump and probe pulses was scanned up to 30 ps [169] by an oscillating retroreflector operated at 9.5 Hz. The transient reflectivity change ($\Delta R/R$) was recorded as a function of pump-probe time delay. The measurements were performed in air at RT. The figures used in this article were generated using Matplotlib.[147]

The sample used was a small flake of a 1T'$-MoTe_2$ single crystal with the $c-$axis of the crystal corresponding to the sample normal. The 1T'$-MoTe_2$ bulk crystal was prepared by the chemical vapor transport (CVT) method.[146] Figure 5.1(c) shows Raman measurements of the 1T'$-MoTe_2$ bulk crystal used in this study. Several A_g modes were observed below 300 cm^{-1} = 9 THz, correponding to previous literatures.[150, 151] The crystal thickness was $\geq$ 500 μm and strain and/or confinement effects were negligible.[170] In addition, Raman measurements on our 1T'$-MoTe_2$ sample, as shown in Fig. 5.1(c) indicated no peak at 13 cm^{-1}(= 0.39 THz) and thus confirming that our sample at RT does not include the T_d phase.

5.3 Results and Discussions

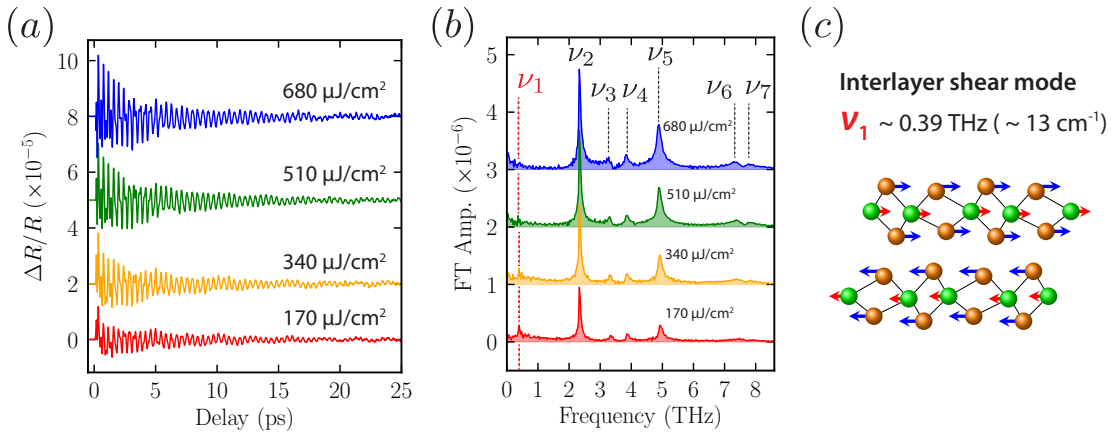

Figure 5.2: (a) Fluence dependence of coherent phonon signal observed in the time-domain reflectivity changes $\Delta R/R$ of 1T'−$MoTe_2$. (b) Fourier transform (FT) spectra of (a). (c) Schematic motion of interlayer shear phonon mode (ν_1 = 0.39 THz) observed in the FT spectra (b).

Figure 5.2(a) shows the $\Delta R/R$ signals measured for the 1T'−$MoTe_2$ phase with sub-picosecond time resolution for a variety of pump fluences ranging from 170 to 680 μJ/cm^2. Coherent phonon oscillations can be observed up to $\sim$ 25 ps time delay at RT. The oscillations are not simply sinusoidal, suggesting the existence of multiple phonon modes driven by charge-density fluctuations, which are traditionally described by resonant impulsive stimulated Raman scattering (ISRS) [67] or by a displacive excitation of coherent phonons (DECP) mechanism.[65] Under the condition that an opaque sample absorbs the pump photon, the driving force can be described by the Raman tensor, which includes both the resonant ISRS and DECP mechanisms. In the following section, we will briefly introduce the DECP mechanism. DECP theory describes that the change in initial phonon coordinate $Q_0'(t)$ is proportional to the photoexcited carrier density $n(t)$:

$$Q_0'(t) = \kappa n(t), . \tag{3.21}$$

Considering the relation $\Delta R(t)/R \propto Q_0$, the time evolution of phonon amplitude of coherent phonon generated by the DECP process should follow the dynamics of photoexcited carrier density $n(t)$.

Figure 5.2(b) shows the Fourier transformed (FT) spectra of the time domain coherent phonon signals for 1T'$-MoTe_2$ obtained for different pump fluences. According to the FT spectra, it can be seen that a total of seven different phonon modes can be observed in the $\Delta R/R$ data. Each phonon frequency has been labeled $\nu_1 \sim \nu_7$ from the lowest to the highest frequency. In detail, ν_1 = 0.39 THz, ν_2 = 2.34 THz, ν_3 = 3.34 THz, ν_4 = 3.88 THz, ν_5 = 4.94 THz, ν_6 = 7.48 THz and ν_7 = 7.90 THz. In particular, $\nu_2 \sim \nu_7$ modes, which are observed by the present optical pump-probe method, are consistent with the Raman spectra of the 1T' phase at RT, as reported recently by various groups [150, 151, 171, 152] and our Raman measurements in Fig. 5.1(c).

The low frequency ν_1 mode is, however, absent in the Raman spectra of the 1T' phase at RT, but is characteristic of the T_d phase, which is a low-temperature phase (< 250 K) of $MoTe_2$. Note that ν_1 can be assigned to the A_1 mode in the T_d phase or as the B_u mode in the 1T' phase, while the $\nu_2 \sim \nu_7$ phonon modes can be assigned as the A_1 modes in the T_d phase or as the A_g mode in the 1T' phase, according to previous reports.[150, 151, 152] Observing an infrared-active B_u phonon mode in pump-probe measurements based on resonant ISRS or DECP processes is generally difficult. [67, 65] In our experiments, this implies that the low frequency ν_1 mode cannot be the B_u mode of the 1T' phase. Thus, the low frequency ν_1 phonon observed in the present study is assigned to the A_1 mode originating from the T_d phase, as discussed below.

The low frequency ν_1 mode can be considered to be an interlayer shear vibration mode[54, 53], a mode that is a key to lattice symmetry switching [150, 151] as schematically drown in Fig. 5.2(c). It can also be seen that the asymmetric shape of the FT amplitude around ν_4 at low excitation density, as shown in Fig. 5.2(b) at $F \leq 340$ μJ/cm^2, implies the existence of splitting of a phonon mode (131 cm^{-1} = 3.93 THz), which is also characteristic of the T_d phase. Thus, the fact that the low frequency ν_1

mode was observed even at RT suggests the possibility of a transient structural transition to the T_d phase or a mixture of the two competing 1T' and T_d phases upon photoexcitation. In the present study, it was also noted that the 2H phase does not play a role in the structural phase transition.

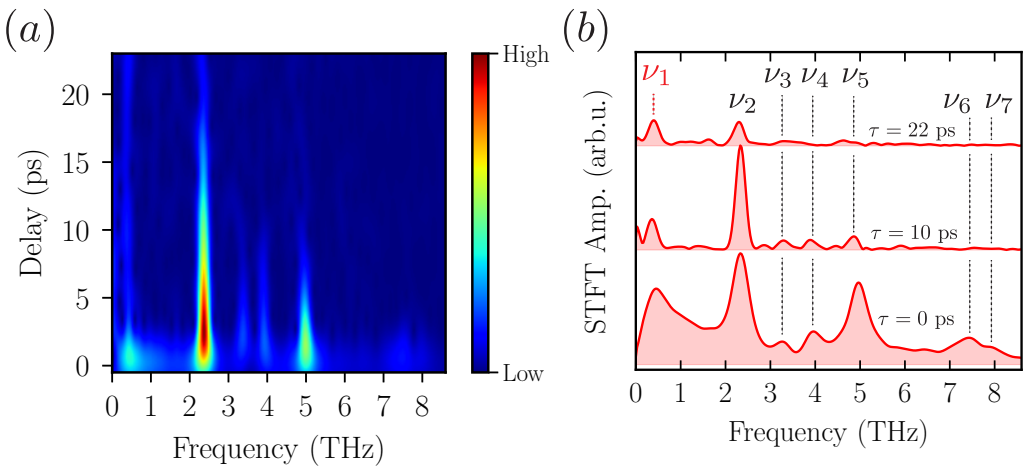

Figure 5.3: (a) A time-frequency-domain spectrogram of Fig. 5.2 at $F = 170\ \mu J/cm^2$ obtained by Short-time Fourier transform (STFT) analysis. (b) Sliced STFT spectra of (a) at $\tau = 0,\ 10,$ and 22 ps.

Figure 5.3(a) shows a short-time Fourier transform (STFT) spectrogram [172] for $F = 170\ \mu J/cm^2$, a time-frequency-domain representation of Fig. 5.2(a). (See also Chapter 2) Here, the FWHM of the Gaussian window function was set as 2.0 ps to eliminate any artifacts due to edge effects while allowing the detection of the low ($<$ 0.5 THz) frequency ν_1 mode. The dominant optical phonon modes and the ν_1 mode can be seen, and they decay with dramatically different time constants. In particular, the lifetimes of the $\nu_3 \sim \nu_7$ modes were found to decay within several picoseconds, a typical behavior of coherent phonons. However, the ν_1 and ν_2 modes persisted beyond $\approx$ 22 ps up to the limit of the time delay of the measurement. To explore this in more detail, we performed a fit of the time-domain data for $F = 170\ \mu J/cm^2$ shown in Fig.

5.2(c) using damped oscillations with the three dominant frequencies ν_1, ν_2 and ν_5:

$$\frac{\Delta R(t)}{R} = \sum_{i=1,2,5} \xi_i e^{-\frac{t}{\tau_i}} \cos(2\pi\nu_i t + \varphi_i), \tag{5.1}$$

where ξ_i is the amplitude, τ_i is the relaxation time, ν_i is the frequency and φ_i is the initial phase of the CP. The fit indicates $\tau_1 = 21.7 \pm 1.4$ ps, $\tau_2 = 9.8 \pm 0.04$ ps and $\tau_5 = 3.7 \pm 0.1$ ps. The ν_1 mode exhibits an even much longer lifetime than that of the ν_2 and ν_5 modes. It is noted that these relaxation times only weakly depend on the pump fluence, and therefore, we will not discuss this effect here. The fit also indicates $\varphi_1 = 27 \pm 2^\circ$, $\varphi_2 = 90 \pm 1^\circ$, and $\varphi_5 = 96 \pm 1^\circ$. Considering the value of φ_1 obtained above, the initial phase of the ν_1 mode is found to be cosine-like, while the other modes, φ_2 and φ_5 ($\approx \pi/2$), exhibits sine-like behavior. It can also be seen that the shear vibration mode (ν_1) exhibits a larger amplitude than that observed in static spectra (Fig. 5.2(b)) just after the excitation by the pump pulse ($\tau = 0$ ps) as seen in Fig. 5.3(b).

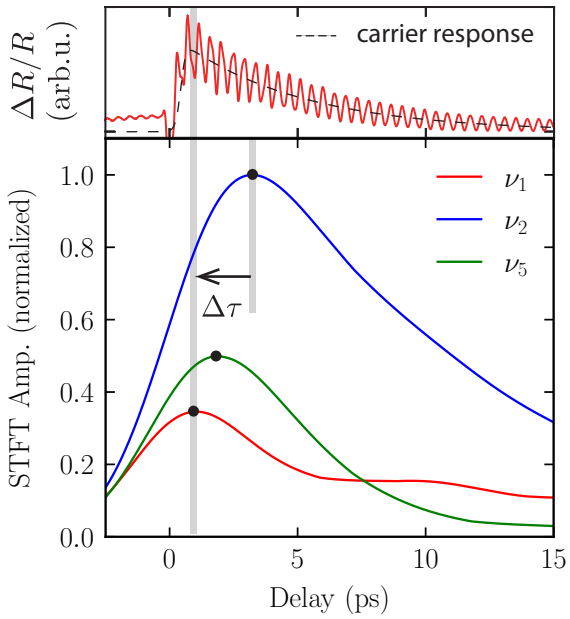

Figure 5.4: (a) $\Delta R/R$ signal including carrier relaxation and the phonon oscillations of the 1T' phase at $F = 170$ μJ/cm^2. The dashed line represents the carrier response in the signal. (b) Time evolution of the STFT amplitudes for ν_1, ν_2, and ν_5 modes as a function of the time delay. The vertical dashed lines represent the peak positions. Δt represents the time lag between the ν_1 and ν_2 modes.

Figure 5.4 shows the time evolution of the peak amplitude for the three dominant modes ν_1, ν_2, and ν_5, shown in Fig. 5.3(a). According to Fig. 5.4(b), the rise time of the amplitude of the ν_1 mode is the fastest among all the vibrational modes (this is also the case for the other optical modes, although the data is not shown) just after excitation. It was also found that the rise of the ν_1 mode coincides with that of the photoexcited carrier dynamics shown in Fig. 5.4(a) by Eq. (3.21). In addition to the results in Fig. 5.4, the fact that the ν_1 mode exhibits displacive behavior (cosine-like), while the other modes exhibit impulsive behavior (sine-like) indicates the ν_1 mode strongly couples with the photogenerated carriers. It is excited preferentially over all the phonon modes. Thus, under low excitation density (170 μJ/cm^2) in which the lattice temperature rise is negligibly small, photoexcited carriers exert a step function electrostrictive force on the lattice driving the coherent ν_1 mode, which induces the

lattice symmetry of 1T' phase to partially change toward T_d phase.

Based on the relationship between the carrier (electron) relaxation time and the initial phase of the coherent phonons for simple semimetals (i.e., $\tan\varphi = \Gamma/\Omega$, where Γ is the reciprocal of carrier relaxation time and $\Omega = 2\pi\nu$) [65, 109], Fig. 5.4 also suggests a different relaxation time as the driving force of three dominant phonon modes. That is, the shorter the carrier relaxation time τ_{el}, the stronger the impulsive behavior (sine-like). The observation that the displacive-like ν_1 mode strongly couples with photoexcited carriers indicates a longer relaxation time on the order of several picoseconds (See Fig. 5.4(a)), consistent with the relationship discussed. On the other hand, the other modes exhibit impulsive behavior (sine-like), and therefore, the carrier relaxation time for the driving force coupled with these modes would be short-lived. However, more experimental and theoretical work is required to fully understand the different carrier dynamics in TMDC systems.

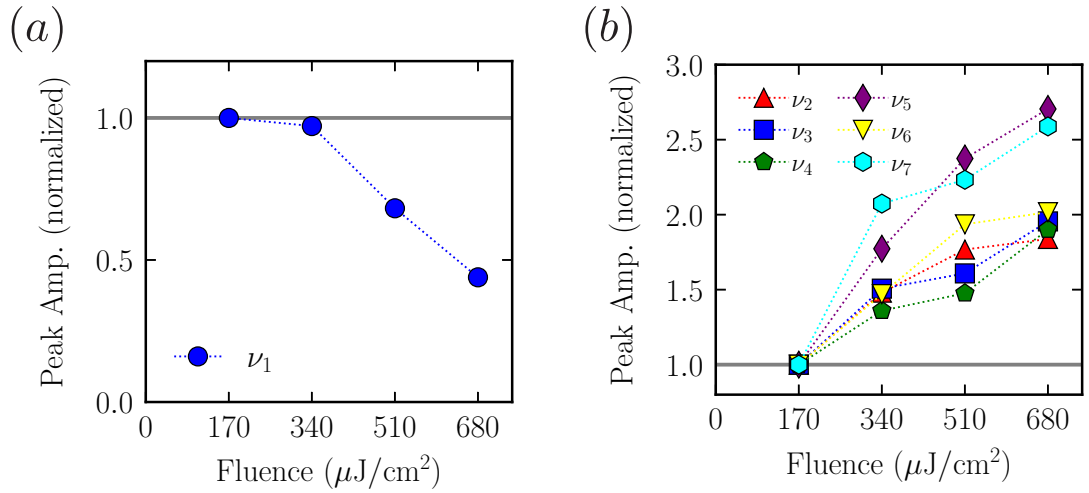

Figure 5.5: Fluence dependence of peak amplitudes normalized by each of the values for $F = 170$ μJ/cm^2 obtained from the FT spectra displayed in Fig. 5.2(b). (a) displays that of ν_1. (b) displays those from ν_1 to ν_7.

Figure 5.5 shows the peak amplitudes versus the pump fluence obtained from Fig. 5.2(b), being plotted for the low frequency ν_1 mode in Fig. 5.5(a) and for the other optical modes in Fig. 5.5(b). First, for the $\nu_2 \sim \nu_7$ cases, Fig. 5.5(b) shows that the peak

intensities (amplitudes) almost linearly increase with increasing pump fluence. This phenomenon can be understood as a characteristic property of coherent phonons, as observed for conventional semiconductors and metals.[70, 173, 174] In contrast, the peak intensity of the ν_1 mode surprisingly decreased with increasing pump fluence, as seen in Fig. 5.5(a). This behavior was opposite to that of the characteristic coherent phonon modes $\nu_2 \sim \nu_7$, suggesting that the ν_1 mode is sensitive to the lattice temperature (T_l) [150, 151], as very recently reported by Ref. [54]. Although the amplitude near time zero (ξ_1) increases with excitation fluence, the lattice temperature rise promotes faster dephasing of the coherent phonons, resulting in the decrease of FT amplitude as shown in Fig. 5.5(a).[175, 176]

Comparing the measurements taken at ultra-low temperature (T = 4 K) [54] and our present measurements at RT, the pump fluence dependence of the T_l is expected to be significantly different. In fact, the maximum pump fluence used by Zhang *et al.* was up to $\approx$ 5 mJ/cm^2, while in the current experiments was only 680 μJ/cm^2, a fluence value one order less. Thus, the rise of T_l in the current study is also expected to be one order of magnitude less than in the former study. According to two-temperature model (TTM) calculations [177], the maximum increase in the T_l in the 1T'$-$$MoTe_2$ bulk crystal surface can be estimated to be from 305 K to 321 K for pump fluences 170 to 680 μJ/cm^2, where the initial temperature was set as T_l = 300 K. This TTM calculation result shows the pump pulse irradiation results in a rise of $\Delta T_l \approx$ 20 K at the sample surface. Although the phase transition between the 1T' and T_d phases has been believed to occur at 250 K, our data strongly suggest that the low frequency ν_1 phonon in the T_d phase appears upon photoexcitation even at RT. A possible mechanism for the light-induced structural phase transition from 1T' to T_d phases is the transient displacement of the nuclear equilibrium position of the ν_1 mode, which is induced and stabilized by electron doping via photoexcitation, as has been recently proposed by Kim *et al* .[178] The pump-induced temperature rise (ΔT_l) may partly contribute to the decrease in the peak amplitude [Fig. 5.5(a)] since higher temperature will destroy the T_d phase.[178]

Finally, we summarize the time evolution of the observed structural phase transition between 1T' and T_d phases, as depicted in Fig. 5.6. Initially, the ground state structure is in the 1T' phase at room temperature before the arrival of the pulse. Upon the arrival of a pump pulse, it generates photoexcited carriers, leading to transient electronic doping in a photoexcited state. This transient carrier doping effect drives the lattice inversion symmetry of the crystal structure from the 1T' to T_d phases or induces an intermediate structure between these two phases in a displacive manner. Consequently, the interlayer shear phonon can be detected in the coherent phonon signal, which is only observable in the T_d phase. After sufficient time has passed, the structure gradually returns to the ground state 1T' phase as the photoexcited carriers relax.

The transient phase transition between the normal semimetal 1T' and the WSM T_d phases observed in the sub-picosecond time domain is expected to be a critical phenomenon in controlling the process of the creation and annihilation of Weyl fermions. It may allow the development of ultrafast phase switching device applications at RT.

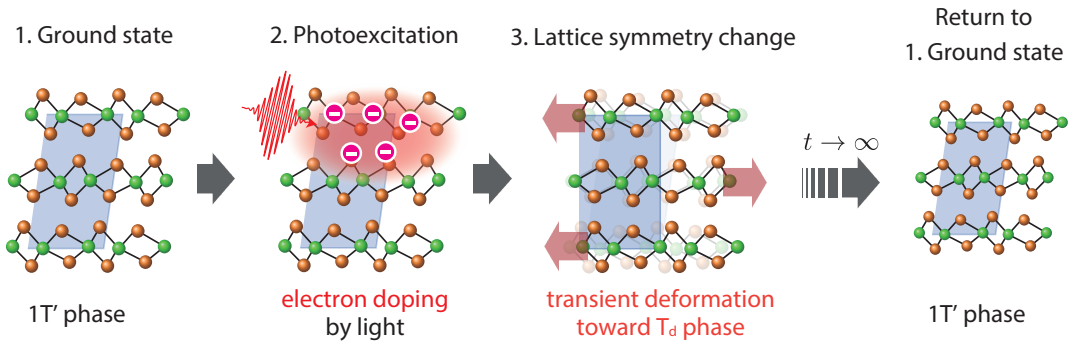

Figure 5.6: Schematic diagram of the physical processes, describing the phenomena observed in this study.

5.4 Conclusions

In conclusion, we observed a long lifetime low-frequency shear phonon in the 1T'$-MoTe_2$ phase even at RT using pump-probe spectroscopy, which was thought to be present in only the T_d phase below 250 K. The observed behavior implies the existence of a tran-

sient phase transition from the normal semimetal 1T' phase to the Type-II WSM T_d phase or a mixture between both phases in the ultrafast sub-picosecond time domain. The STFT analysis revealed that the amplitude of the shear phonon, which is considered to result in lattice symmetry breaking in the bulk crystal, is primarily induced just after excitation, caused by a resonant ISRS or DECP mechanism. High fluence laser irradiation leads the shear phonon mode to decrease in amplitude due to a lattice temperature rise of $\approx$ 20 K as calculated by a TTM analysis. This study on ultrafast dynamics in the 1T' phase agrees with previously reported lattice symmetry switching between the normal semimetal to the WSM phase, even at RT. Also, it suggests a new technique to unveil the sub-picosecond time domain creation and annihilation of Weyl fermions and their thermal dependence, which is expected to lead to new device applications using topological phase switching.

Chapter 6

Coherent Optical Response Driven by Non-Equilibrium Electrons and Phonons in Layered 2H − $MoTe_2$

Layered transition-metal dichalcogenides (TMDs) are model systems to explore ultrafast many-body interactions and various nonlinear optical phenomena. For the application of TMD-based optoelectronic devices capable of ultrafast response, it is essential to understand how characteristic electron-hole and electron-phonon couplings modify ultrafast electronic and optical properties under photoexcitation. Here, we investigate subpicosecond optical responses of layered semiconductor 2H − $MoTe_2$ in the presence of an electron–hole (e–h) plasma and a long-lived coherent phonon. Transient reflectivity measurements depending on photon energy reveal that the optical response for short-time delays (< 1 ps) was significantly modified by band-gap renormalization and state filling due to the presence of the e–h plasma. Furthermore, octave, sum, and difference phonon frequencies transiently appeared for the early time delays (< 2 ps). The emergent multiple phonon frequencies can be described as higher-order optical modulations due to deformation-potential electron-phonon coupling under resonant photoexcitation conditions. This work provides comprehensive insights into fundamental physics and the application of the non-equilibrium quasiparticle generations on TMDs under time-periodic phonon driving forces.

The descriptions in this chapter are based on the research found in **T. Fukuda**, *et al. APL Mater.* **12** 021102 (2024).[179]

6.1 Motivation and Introduction

Coherent light-matter interactions give rise to exotic non-equilibrium electronic and structural properties of matter, inaccessible under thermal equilibrium or static stimuli conditions. With the development of high-intensity ultrashort pulse light sources and pump-probe methodologies, a variety of light-induced phenomena: quasiparticle generations [180, 181], field-driven dressed states [182, 183], structural phase transitions [184, 173, 185], and high-harmonic generations [186, 187] have been discovered, leading to the hot topic in the research field of optical and material sciences. The ultrafast response of non-equilibrium electronic and structural phases is expected to be utilized in the development of next-generation optoelectronics capable of operating in the terahertz (THz) regime, such as optical switching and memory devices.

As well as lightwave driving and photoexcited charges, coherently excited lattice motion in time and space, here referred to as coherent phonons, plays an essential role in the formation of non-equilibrium phenomena. The excitation of coherent Raman-active optical phonons has been described by the following processes: impulsive stimulated Raman scattering (ISRS) [58, 111] and displacive excitation of coherent phonons (DECP)[65, 68], describing indirect phonon excitations under electronic off-resonant and resonant conditions, respectively; ionic Raman scattering (IRS) [92] and sum-frequency excitation (SFE) [95], describing direct excitation of phonons in the absence of electrons. Due to the presence of electron-phonon interactions and significant lattice deformations, coherent phonons strongly modulate the electronic and optical properties of solids in a time-periodic manner, inducing temporal optical response and lattice symmetry changes that can alter electronic or magnetic orders on sub-picosecond time scales.[114, 188, 53, 119, 189, 126] Therefore, it is essential to further explore the mechanics of phonon-driven non-equilibrium properties of matter for a fundamental

understanding as well as applications.

Two-dimensional layered transition-metal dichalcogenides (TMDs) are attractive systems for the exploration of unique non-equilibrium physics due to the enhancement of electron-hole and electron-phonon interactions in each atomic layer. To date, ultrafast studies of TMDs have revealed valley-selective excitations [24, 36, 190], strongly binding excitons [26], exciton-Mott transitions into electron-hole (e–h) plasmas [47], and saturable absorption effects [191, 192] depending on the photoexcitation conditions. Furthermore, characteristic van-der-Waals (vdW) lattice structures give rise to the presence of long-lived coherent phonons [193, 138], exciton-phonon interactions[194, 195], THz emission[196], light-induced charge-density-wave order [197, 198, 199], and lattice symmetry switching of topological properties via an interlayer shear displacement.[53, 54] Although remarkable light-induced phenomena have been demonstrated in TMDs, the interplay between electrons and the lattice remains elusive. This is because, in general, coherent quasiparticle states based on many-body interactions build up within sub-picosecond time scales .[180, 181] These extremely short time scales make it difficult to investigate in detail. Nevertheless, gaining insight into the non-equilibrium dynamics of electrons and coherent phonons is of great importance for exploring novel functionalities of TMDs and further understanding ultrafast quasiparticle physics.

In this paper, we investigate the ultrafast quasiparticle dynamics of electrons and phonons in a layered TMD semiconductor $2\mathrm{H}-\mathrm{MoTe_2}$ with sub-picosecond time resolutions. Using transient reflectivity change measurements under resonant conditions, we capture an extremely long-lived coherent phonon and the associated optical response just after photoexcitation (< 2 ps), a period dominated by photoexcited e–h plasmas and multiple phonon frequency generation. The study of the photon-energy dependence clarified that the initial optical response can be well described in terms of resonant energy shifts or modulations driven by electron–hole and electron–phonon couplings.

6.2 Experimental Methods

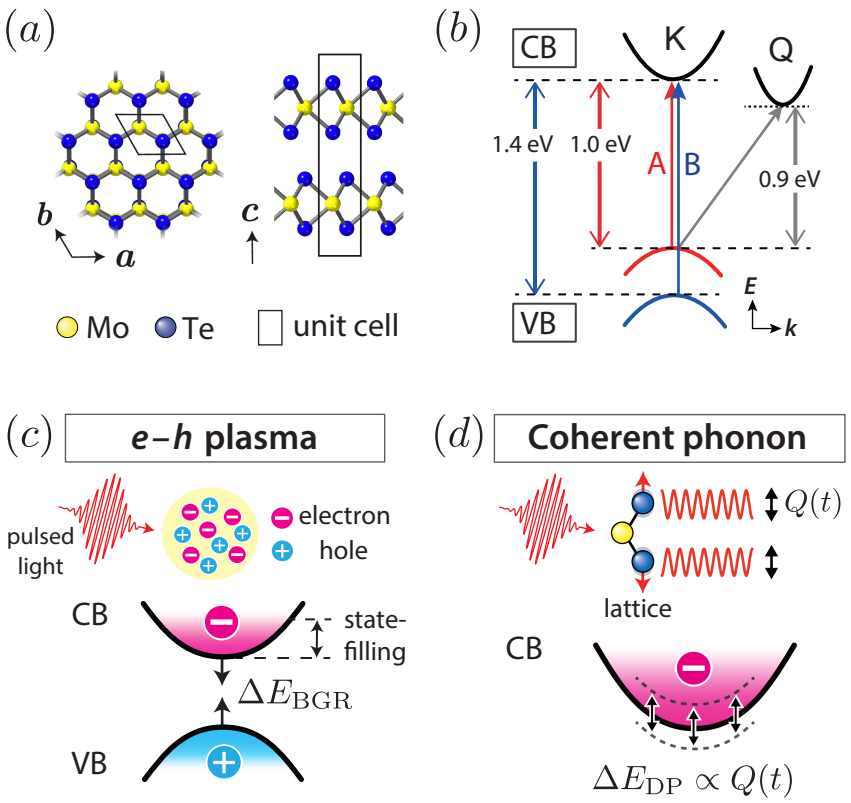

Figure 6.1: (a) Lattice structure of a $2H-MoTe_2$ crystal. (b) Schematic of the band structure of the bulk $2H-MoTe_2$ with indirect (from K to Q valleys) and direct band gaps (A-gap and B-gap) at the K valley. The lower panels show schematic pictures of electron energy modulations in the presence of e–h plasma (c) and coherent phonon (d) generated by ultrashort pulsed light. The CB and VB denote conduction and valence bands, respectively. The ΔE_{BGR} represents band-gap renormalization (BGR) effects. $Q(t)$ is an atomic displacement by a coherent phonon. ΔE_{DP} represents an electronic band energy modulation via a deformation-potential (DP) electron-phonon interaction proportional to $Q(t)$.

$2H-MoTe_2$ has a hexagonal structure that is stacked along the c-axis via VdW interactions [Fig. 6.1(a)], with an indirect band-gap (≈ 0.9 eV) and two direct transitions: the A-gap (≈ 1.0 eV) and the B-gap (≈ 1.4 eV) at the K point [Fig. 6.1(b)].[200] A $2H-MoTe_2$ bulk single crystal, commercially available from *2D semiconductors*, was prepared by a flux zone technique with the $c-$axis of the crystal corresponding to the

sample normal. (See further sample characterizations by Raman and spectroscopic ellipsometry measurements in Supplementary section 6.11.) The thickness of the bulk crystal was about 100 μm. The optical penetration depth at 830 nm was estimated to be around 50 nm from the complex dielectric function calculated by density-functional theory (DFT) simulations. (See also Supplementary section 6.11.) Reflection-type optical pump-probe measurements were conducted using a near-infrared Ti:Sapphire light source with a repetition rate of 80 MHz under ambient conditions. A central wavelength of 830 nm (1.49 eV) was used for high-time resolution measurements with a pulse duration of $\sim$ 30 fs. Photon-energy dependence measurements were conducted using tunable central wavelengths from 820 nm (1.51 eV) to 880 nm (1.41 eV) with a pulse duration of $\sim$ 60 fs. The photon energy used in this study is nearly resonant with the B-gap (1.40 eV) of $2\mathrm{H}-\mathrm{MoTe_2}$. The s–polarized pump and the p–polarized probe beams with the degenerate wavelength were co$-$focused onto the sample to a spot radius of $\approx$ 16 μm with incident angles of about 5° and 15° from the sample normal, respectively. The delay time t between the pump and probe pulses was scanned up to 30 ps by an oscillating retroreflector operated at 9.5 Hz. (See further information for pump-probe set-up in Chapter 2.)

The incident pump fluence F used was in the range of several hundreds of $\mu\mathrm{J/cm^2}$, corresponding to an estimated absorption density $n_{\mathrm{ex}} \sim 10^{19}$ $\mathrm{cm^{-3}}$, a value far above the general Mott density $n_{\mathrm{Mott}} \lesssim 10^{18}$ $\mathrm{cm^{-3}}$.[201, 202, 203] (See also Supplementary section 6.11.) Therefore, an optical excitation nearly resonant with the B-gap introduced a photoexcited e–h plasma in the conduction bands at the K-point, which is off-resonant with the A-gap. The upper limit of fluence ($F = 855$ $\mu\mathrm{J/cm^2}$) was set to prevent surface damage or tellurium segregation in the $2\mathrm{H}-\mathrm{MoTe_2}$ sample under the use of a high-repetition 80-MHz light source.[134]

6.3 Photoexcited Electronic and Optical Properties in a Semiconductor

In a semiconductor, two physical processes, e–h plasmas and coherent phonons, can contribute to changes in electronic and optical properties, such as the band structures and transient optical response. The optical response is the change in the intensity $I(t)$ of reflection or transmission probe light from media for each pump-probe delay time t, corresponding to the time variation of the optical susceptibility $\chi(t)$: i.e., $\Delta I/I_0 \sim \Delta\chi/\chi_0$, where I_0 and χ_0 are the $I(t)$ and $\chi(t)$ before photoexcitation, respectively; $\Delta I = I(t) - I_0$ and $\Delta\chi = \chi(t) - \chi_0$. In the present study, we observed the optical response induced by photoexcited electrons and coherent phonons through transient reflectivity changes $\Delta R/R$ $(= \Delta I/I_0)$.

When e–h plasmas are generated by a pump pulse above the Mott density, band-gap renormalization (BGR) by the screening of Coulomb interactions leads to shrinkage of the band gap (ΔE_{BGR}) between the valence and conduction bands, and state filling effects contribute to Pauli blocking or optical bleaching under dense electronic excitation conditions [Fig. 6.1(c)].[202, 47, 204] These effects give rise to significant changes in the optical response with a resonant photo-energy probe pulse.

When coherent phonons are generated by a pump pulse, the energies of Bloch electrons are temporally modulated via electron-phonon interactions, such as the deformation-potential (DP) or Fröhlich interactions. In general, the resonant energy modulations via the DP interaction (ΔE_{DP}) proportional to the coherent atomic displacement $Q(t)$ induce a temporal change in optical properties [Fig. 6.1(d)].[205, 206, 76, 207, 208] The optical susceptibility modulation induced by lattice vibrations is well known to be described by the following expression[112], as also present in Chapter 3 :

$$\chi(\omega; Q) = \chi_0(\omega) + \sum_n \frac{1}{n!} \left(\frac{\partial^n \chi}{\partial Q^n} \right)_{Q=0} Q^n(t), \tag{3.47}$$

where $\chi_0(\omega)$ is the optical susceptibility in the absence of interactions and $\partial^n\chi/\partial Q^n$ denotes the n-th order Raman tensor associated with DP interactions. $\chi(\omega;Q)$ is dominated by a time-domain oscillation proportional to $Q(t)$, but can also show higher-order oscillations when the coefficients of $\partial^n\chi/\partial Q^n$ have large values. It should be noted that we cannot observe the coherent phonon directly because our laser photon energy is $\hbar\omega \sim 1.5$ eV, far from the phonon energy range of only several tens to hundreds meV.

6.4 Time-Domain Reflectivity Change

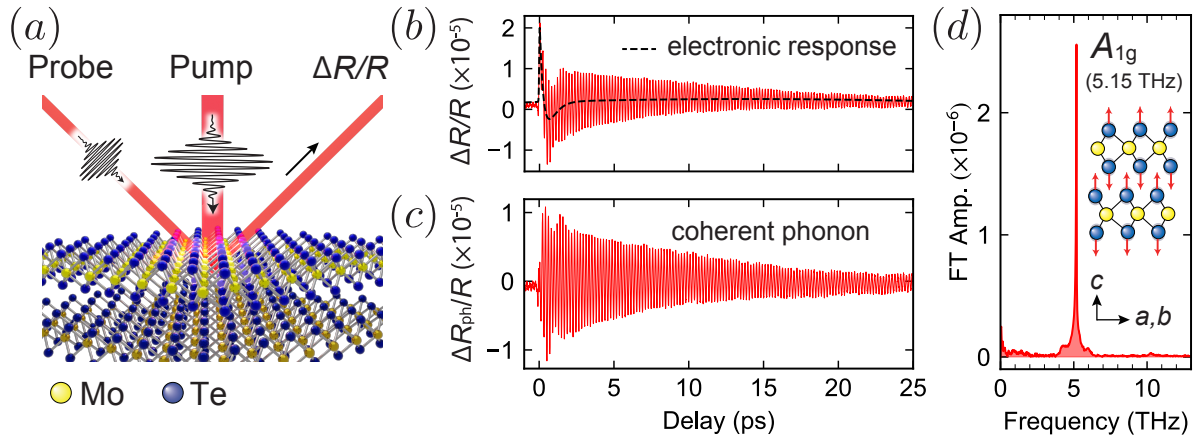

Figure 6.2: (a) Schematic of the reflective-type pump-probe setup for bulk $2\mathrm{H}-\mathrm{MoTe_2}$. (b) A $\Delta R/R$ signal in $2\mathrm{H}-\mathrm{MoTe_2}$ for an incident fluence of $F = 513$ $\mu\mathrm{J/cm^2}$. The dashed line represents the electronic response. (c) Coherent phonon signal ($\Delta R_{\mathrm{ph}}/R$) after subtracting the electronic response. (d) The FT spectrum of the coherent phonon signal. A peak in the spectrum is assigned to the A_{1g} mode.

We carried out reflection-type pump-probe spectroscopy for a $2\mathrm{H}-\mathrm{MoTe_2}$ bulk crystal [Figure.6.2(a)]. The observed time-domain transient reflectivity change $\Delta R/R$ in Fig. 6.2(b) shows a transient response of the photoexcited e–h plasmas and a coherent phonon oscillation. After the subtraction of the electronic response and nonlinear artifacts using a biexponential decaying function, the coherent phonon oscillation $\Delta R_{\mathrm{ph}}/R$ part was extracted, as shown in Fig. 6.2(c). A clear coherent oscillation emerges at the arrival of the pump pulse and persists for longer than 25 ps, accompanying the

narrow bandwidth of the A_{1g} mode ($\nu_A \approx 5.15$ THz) as shown in the Fourier transform (FT) spectrum of Fig. 6.2(d). In the present study, DECP is the dominant generation mechanism for the observed coherent phonon near time delay = 0.0 ps since the photon energy used is always located above the B-gap (~ 1.40 eV).[65, 68] Under the presence of photoexcited carriers, the electron–phonon interaction should play an essential role in the decay of coherent phonons in addition to other phonon scattering mechanisms, such as phonon-phonon, phonon-impurity, and phonon-defect scattering. [106, 107, 108] Nevertheless, the observed long-lived A_{1g} mode suggests that the contributions of the related scattering terms are expected to be small, leading to an electron–lattice system that undergoes nearly time-periodic conditions for early time delays: e.g., within 2 ps. The following sections discuss the time- and photon-energy-domain behavior of the electronic response and coherent oscillations.

6.5 The Initial Time-Delay Optical Response

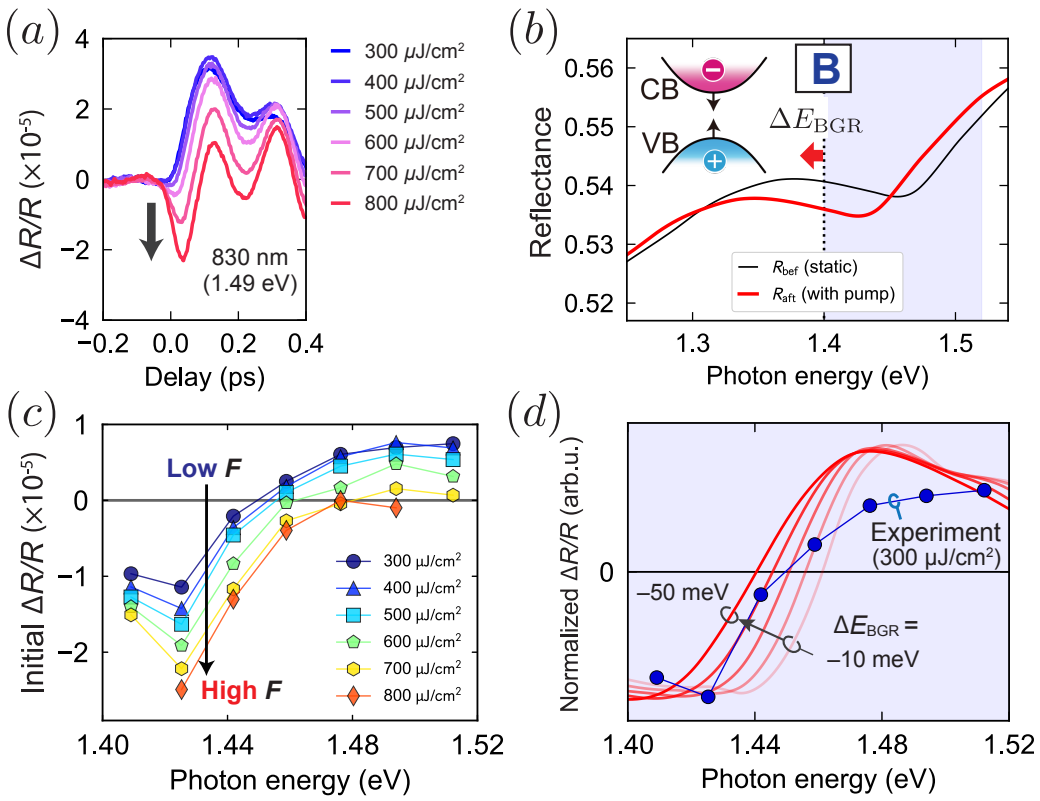

Figure 6.3: (a) Fluence-dependent $\Delta R/R$ signals before subtracting electronic response observed for 830 nm (1.49 eV) displayed around 0 ps. (b) Fluence and photon-energy dependence of the initial $\Delta R/R$ signals. (c) The static reflectance spectrum R around the B-gap (1.4 eV) and the simulated reflectance spectrum upon photoexcitation around the B-gap, taking into account the spectrum redshift ΔE_{BGR}. The reflectance is based on the complex refractive index experimentally obtained by the previous study.[209] (d) Comparison between the initial $\Delta R/R$ at 300 μJ/cm^2 and differential curves of the simulated reflectance produced by the energy redshift of $\Delta E_{\mathrm{BGR}} = -10$ meV to -50 meV, focused onto the blue-shaded area of (c).

Figure. 6.3(a) shows the $\Delta R/R$ signals observed for early time delays from -0.2 to 0.4 ps for different excitation fluences before subtracting the electronic response. The $\Delta R/R$ around the delay = 0.0 ps is dominated by the photoexcited electron system, exhibiting inversion from positive to negative values with increasing excitation density. To gain insights into the flipping phenomena, we investigated the fluence and the

photon-energy dependence of the initial $\Delta R/R$ signals as displayed in Fig. 6.3(b). (See detailed information for the photon-energy dependent measurement in Supplementary section 6.11.) The result shows a monotonic increase in the range from 1.41 to 1.51 eV in a manner similar to the previous study.[210] In addition, the $\Delta R/R$ spectra over the entire photon energy range decrease with increasing pump fluence, resulting in the $\Delta R/R$ signal flipping from positive to negative values between 830 nm (1.49 eV) to 850 nm (1.46 eV).

The observed optical bleaching of the reflectivity change in Fig. 6.3(b) results from state-filling effects in the presence of the *e–h* plasma as expected for semiconductors with a photoexcitation density in excess of the Mott density.[211] Similar bleaching features have been observed in other materials around the resonant photon energy.[47, 212] It should be noted that the observed optical bleaching is irrelevant to a possible light-induced 2H-to-1T' structural phase transition [49, 50, 51, 52], because the coherent phonon spectra in $2H - MoTe_2$ show no drastic changes with pump fluence. Therefore, the lattice symmetry of $2H - MoTe_2$ remains unchanged for photoexcitation $< 900\ \mu J/cm^2$ in our measurements.[114, 213, 134]

Furthermore, we found that the observed photon-energy dependence of the $\Delta R/R$ spectra at low pump fluence can be well simulated by assuming band-gap renormalization (BGR) in the presence of an *e–h* plasma. The *e–h* plasma reduces the single-particle energy via the screening of the Coulomb interaction, resulting in a band-gap shrinkage ΔE_{BGR} to the same extent as the intrinsic exciton binding energy E_b.[214, 202, 47] For bulk $2H - MoTe_2$, ΔE_{BGR} is assumed to be in the range of several tens of meV since E_b was estimated to be $\approx$ 70 meV based upon a *GW* first principle calculation .[215] To evaluate the BGR effect, we simulated the normalized curves $\Delta R/R = (R_{\mathrm{aft}} - R_{\mathrm{bef}})/R_{\mathrm{bef}}$, where R_{bef} is the static reflectance derived from experimental optical constants taken from the previous report by Li, *et al.* [209] (See also Supplementary section 6.11) and R_{aft} is the photoexcited reflectance calculated by introducing the ΔE_{BGR} to R_{bef}, as shown in Fig. 6.3(c). Fig. 6.3(d) shows that a normalized experimental $\Delta R/R$ spectrum taken using an incident fluence of 300 $\mu J/cm^2$ is well reproduced by a

series of normalized simulated $\Delta R/R$ spectra when the fact that $\Delta E_{\mathrm{BGR}} = -10$ meV to -50 meV are taken into account. The discrepancies between the data and the simulations around 1.48 eV may result from a negative offset induced by optical bleaching effects in the experimental data. Since the value of ΔE_{BGR} is the same order of magnitude as E_b, the photon-energy dependence of $\Delta R/R$ in our study can be explained by the BGR effect in the presence of an e–h plasma, as well as the state filling effect discussed above. To exactly simulate the $\Delta R/R$ spectra and understand the contribution of the BGR and state-filling effect at high excitation densities, it is necessary to perform first-principle calculations, including many-body effects, which are out of scope in the present study.

6.6 A Time-frequency-Domain Analysis

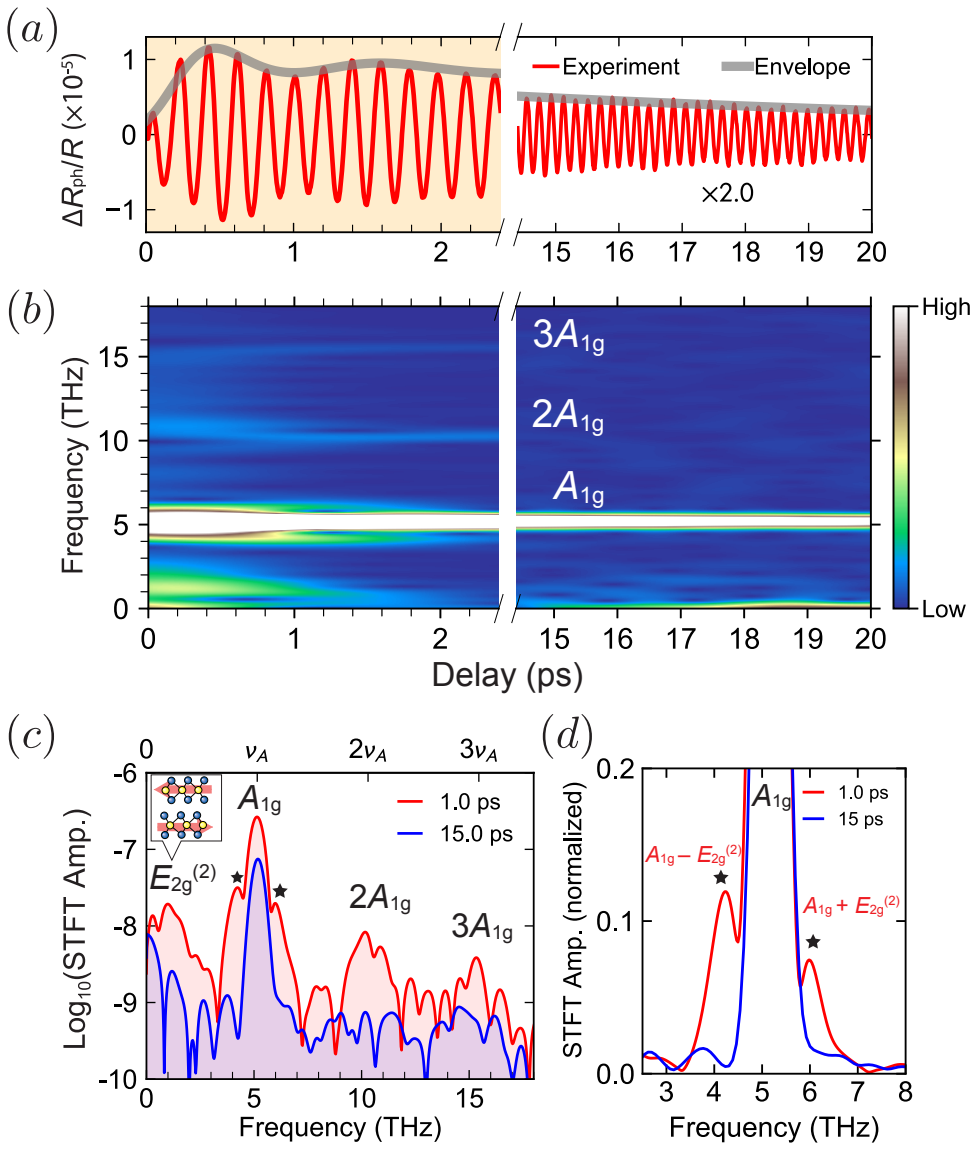

Figure 6.4: (a) $\Delta R_{\rm ph}/R$ on $F = 627$ μJ/cm^2 and an amplitude envelope function. The left and right parts show the early ($0 \sim 2.5$ ps) and the later ($15 \sim 20$ ps) time regions, respectively. (b) STFT spectrogram of $\Delta R_{\rm ph}/R$ displayed in (a). (c) Sliced STFT spectra obtained at 1.0 and 15 ps. The upper ticks represent overtones of the A_{1g} mode. The star-shaped markers remark satellite peaks around the A_{1g} mode, $A_{1g} \pm E_{2g}^{(2)}$ modes. The inset shows the interlayer shear motion of the $E_{2g}^{(2)}$ mode. (d) Horizontally enlarged sliced STFT spectra at 1.0 and 15.0 ps around 5 THz normalized by the peak intensity of the A_{1g} mode. The $A_{1g} \pm E_{2g}^{(2)}$ modes only present in the early time delay.

We discuss the time-frequency dynamics of the coherent phonon signal $\Delta R_{\rm ph}/R$ on $2H-MoTe_2$ to figure out transient coherent electron–phonon interactions for early time delays just after photoexcitation in the presence of the e–h plasma. Figure. 6.4(a) displays $\Delta R_{\rm ph}/R$ for early (< 2.5 ps) and later time delays. Although the time-domain signal is mainly dominated by the simple damped harmonic oscillation of the A_{1g} mode, a beating oscillation can be seen for early time delays. This amplitude beating implies the existence of other phonon modes.

We employed a short-time Fourier transform (STFT) analysis for the $\Delta R_{\rm ph}/R$ signal, as shown in Fig. 6.4(b). (For detailed information on the STFT method, see Chapter 2) The time-frequency-domain spectrogram shows that additional frequencies transiently appear evenly spaced for early time delays, while only the A_{1g} mode can be seen for later time delays. Fig. 6.4(c) shows the two STFT spectra sliced from 1.0 ps and 15 ps, respectively. In the STFT spectrum for a 1.0-ps time delay, overtones of the A_{1g} mode up to the 3rd-order: $2A_{1g}$ ($2\nu_A \approx 10.3$ THz) and $3A_{1g}$ ($3\nu_A \approx 15.4$ THz) modes are visible. In addition, we found a zone-center interlayer shear $E_{2g}^{(2)}$ mode around $\nu_E = 0.8 \pm 0.2$ (THz) in the low frequency region.[216, 149, 161] Furthermore, there are two satellite peaks besides the A_{1g} mode (5.15 THz) at ≈ 4.3 THz and 6.0 THz, as shown in Fig 6.4(d). The frequency interval between the A_{1g} mode and the satellite peaks is ≈ 0.8 THz, which is in good agreement with ν_E. The formation of sideband peaks indicates that the $E_{2g}^{(2)}$ phonon leads to an amplitude modulation of the reflectivity oscillation of the ν_A frequency: i.e., $\cos\nu_E t \cdot \cos\nu_A t \propto \cos(\nu_A+\nu_E)t + \cos(\nu_A-\nu_E)t$. Therefore, the observed satellite peaks around the A_{1g} mode are considered to be the sum and difference frequencies of the A_{1g} and $E_{2g}^{(2)}$ phonon modes: $A_{1g} \pm E_{2g}^{(2)}$.

The following processes have conventionally dictated the couplings of the optical phonon frequencies: anharmonic nonlinear phonon coupling under large phonon displacement [172, 217, 218, 219], higher-order resonant Raman processes [220, 221, 222, 223] or refractive index modulation induced by coherent phonons [224, 169, 225] under the harmonic approximation with a small phonon displacement. In the present study, considering the observed multiple phonon frequencies appear even for the smallest pump

fluence (57 μJ/cm^2) with small oscillatory amplitude, the contribution of anharmonic phonon-phonon coupling can be ruled out. Therefore, there is expected to be no direct phonon-phonon coupling between the A_{1g} and $E_{2g}^{(2)}$ modes. Since we observe the optical response via electronic energy band modulations under near-resonant conditions, the observed multiple phonon frequencies are likely to be explained by the optical-phonon-induced refractive index modulations or higher-order Raman process in the presence of electron-phonon couplings. Here, the out-of-plane A_{1g} mode, which dominantly contributes to the time-domain oscillation, is a non-polar phonon. [226] In addition, the $E_{2g}^{(2)}$ mode is also considered to be a non-polar phonon since the motion of the interlayer shear lattice vibration does not induce a charge separation or a macroscopic electric field. Therefore, the contribution of Fröhlich interactions can be ruled out, and only the DP interactions are considered here.

6.7 Dephasing Dynamics among Photoexcited Electrons, A Fundamental Phonon, and Multiple Phonon Modes

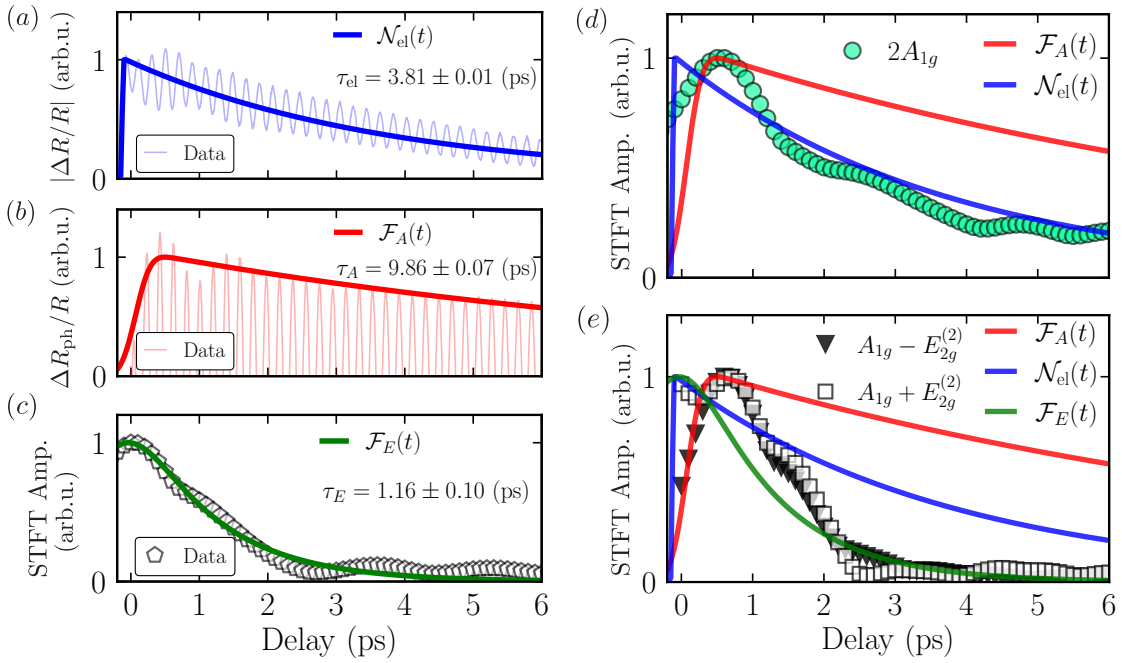

Figure 6.5: (a) Normalized hot-electron thermalization dynamics $\mathcal{N}_{\rm el}(t)$ obtained from the largest-bandwidth $\Delta R/R$ measurement ($F = 627$ μJ/cm^2) and from a fitting analysis using a single exponential decay. (b) Normalized amplitude dephasing dynamics of the A_{1g} mode $\mathcal{F}_A(t)$ obtained from a fitting analysis using a damped oscillation. (c) Normalized amplitude dephasing dynamics of the $E^{(2)}_{2g}$ mode $\mathcal{F}_E(t)$ obtained from the STFT amplitude around 0.8 THz and from a fitting analysis using a single exponential decay. (d) Comparison of the dephasing dynamics of the $2A_{1g}$ mode with $\mathcal{N}_{\rm el}(t)$ and $\mathcal{F}_A(t)$. The exponential decaying constant of $2A_{1g}$ mode indicates $\tau_{2A} = 3.20 \pm 0.11$ ps. (e) Comparison of the dephasing dynamics of $A_{1g} \pm E^{(2)}_{2g}$ modes with $\mathcal{N}_{\rm el}(t)$, $\mathcal{F}_A(t)$, and $\mathcal{F}_E(t)$. The exponential decaying constant of $A_{1g} \pm E^{(2)}_{2g}$ modes indicate $\tau_{A\pm E} = 0.87 \pm 0.04$ ps.

Here, we discuss the relationship of dephasing dynamics among the e-h plasmas, A_1g, $2A_{1g}$ and $A_{1g} \pm E^{(2)}_{2g}$ modes. We extracted the electronic thermalization dynamics $\mathcal{N}_{\rm el}(t)$, the amplitude-decay dynamics of the A_{1g} mode $\mathcal{F}_A(t)$ and the $E^{(2)}_{2g}$ mode $\mathcal{F}_E(t)$

from the time-domain data, as shown in Figure 6.5(a)-(c). The $\mathcal{N}_{\rm el}(t)$, $\mathcal{F}_A(t)$, and $\mathcal{F}_E(t)$ were obtained using a fitting function consisting of a single exponential decay from the largest-bandwidth $\Delta R/R$ measurement, from the $\Delta R_{\rm ph}/R$ signal, and from the peak-area intensity around 0.8 THz in the STFT spectrogram, respectively. The decay time constants of $\mathcal{N}_{\rm el}(t)$, $\mathcal{F}_A(t)$ and $\mathcal{F}_E(t)$ can be estimated from the fit to be $\tau_{\rm el} = 3.81 \pm 0.01$ ps, $\tau_A = 9.86 \pm 0.07$ ps and $\tau_E = 1.16 \pm 0.10$ ps, respectively, where $\tau_E < \tau_{\rm el} < \tau_A$ is satisfied. Since the value of $\tau_{\rm el}$ obtained from $\mathcal{N}_{\rm el}(t)$ is of the same order as earlier reports [137, 227, 228], the non-equilibrium population distribution of photoexcited electrons (e-h plasma) is expected to be thermalized by incoherent electron–phonon scattering toward the conduction-band minima at the K point, and toward the Q valleys. The oscillation cycles of the phonon driving during the dephasing time constants are estimated to be $\nu_A\tau_A = 50.4 \pm 0.8$ for the A_{1g} mode and $\nu_E\tau_E = 0.92 \pm 0.23$ for the $E_{2g}^{(2)}$ mode. In light of the $\nu_A\tau_A \gg \nu_E\tau_E$, the A_{1g} mode is the main time-periodic driving force in the present electron-phonon coupled system.

First, we compare dephasing dynamics of the $2A_{1g}$ mode with $\mathcal{N}_{\rm el}(t)$ and $\mathcal{F}_A(t)$, as shown in Fig. 6.5(d). The dephasing time constant of the $2A_{1g}$ mode is estimated to be $\tau_{2A} = 3.20 \pm 0.11$ ps that is close to $\tau_{\rm el}$ rather than τ_A. This indicates that the dephasing of the $2A_{1g}$ mode is dominated by electronic thermalization $\mathcal{N}_{\rm el}(t)$. Second, we compare the $A_{1g} \pm E_{2g}^{(2)}$ modes with $\mathcal{N}_{\rm el}(t)$, $\mathcal{F}_A(t)$, and $\mathcal{F}_E(t)$, as shown in Fig. 6.5(e). Both $A_{1g} \pm E_{2g}^{(2)}$ modes show the same relaxation dynamics, whose dephasing time constant is estimated to be $\tau_{A\pm E} = 0.87 \pm 0.04$ ps, which is in good agreement with $\tau_{{\rm el}-E} \approx 0.89$ ps derived from the relationship of the combined scattering rate $\tau_{{\rm el}-E}^{-1} = \tau_{\rm el}^{-1} + \tau_E^{-1}$. This result indicates that the dephasing of the $A_{1g} \pm E_{2g}^{(2)}$ modes is dominated by electronic thermalization $\mathcal{N}_{\rm el}(t)$ and the dephasing of the $E_{2g}^{(2)}$ mode, $\mathcal{F}_E(t)$, suggesting the existence of the coupling between the photoexcited carriers and the $E_{2g}^{(2)}$ mode. Interestingly, when the amplitude reaches the maximum value, the rise time of both the $2A_{1g}$ and $A_{1g} \pm E_{2g}^{(2)}$ modes, coincides with that of $\mathcal{F}_A(t)$. This is strong evidence that the long-lifetime A_{1g} mode plays a pivotal role in producing the multiple phonon frequencies. It is noted that the A_{1g} mode is unlikely to contribute to

the dephasing of the multiple phonon frequencies since the A_{1g} mode does not lose its coherence during the early time delay.

6.8 Multiple Phonon Frequencies Depending on Photon Energy

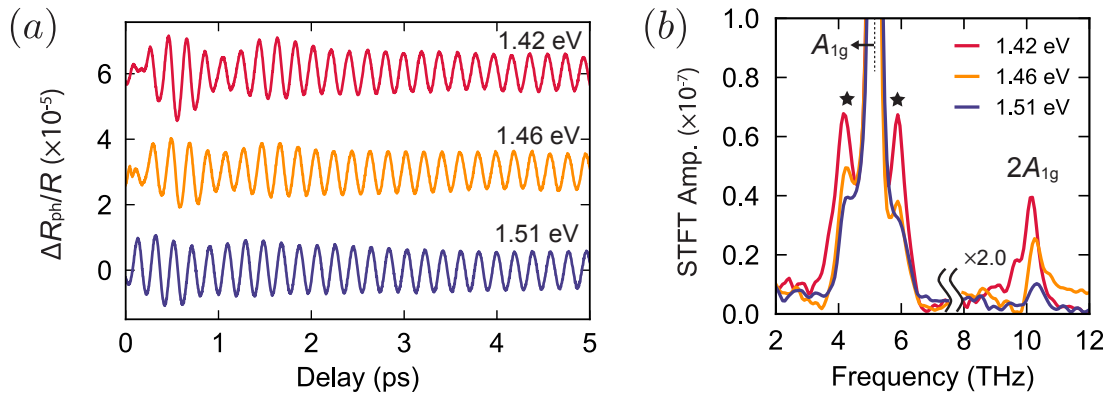

Figure 6.6: (a) Photon-energy-dependence $\Delta R_{\mathrm{ph}}/R$ signals for $\hbar\omega = 1.42, 1.46$, and 1.51 eV. (b) Sliced STFT spectra at 1.0 ps of coherent phonon signals measured at various photon energies, 1.42, 1.46, and 1.51 eV. The star-shaped markers represent the $A_{1g} \pm E_{2g}^{(2)}$ modes.

To further understand the optical properties of the higher-order frequency modes, we investigated the photon-energy dependence of the time-domain coherent oscillation $\Delta R_{\mathrm{ph}}/R$ from 1.41 to 1.51 eV. Note that we do not argue the $3A_{1g}$ mode here since we cannot observe the $3A_{1g}$ mode in photon-energy dependent measurements because of the broader pulse duration ($\sim$ 60 fs), compared to the measurement shown in Fig. 6.4 using a shorter pulse duration ($\sim$ 30 fs). Figure. 6.6(a) shows the sliced STFT spectra of $\Delta R_{\mathrm{ph}}/R$ for early time delays (1.0 ps) with various photon energies. These spectra show significant changes in the oscillatory amplitudes $2A_{1g}$ and $A_{1g} \pm E_{2g}$ modes depending on photon energy. i.e., those higher-order frequency modes were enhanced near the B-gap resonance (1.4 eV) but decreased under off-resonance conditions (1.5 eV).

Figs. 6.7(a) and (b) show the normalized peak intensities of the fundamental A_{1g} mode and the higher-order frequency modes ($2A_{1g}$ and $A_{1g} \pm E_{2g}^{(2)}$) extracted from the STFT spectra at 1.0 ps for photon energies ranging from 1.41 to 1.51 eV, respectively. The intensity reduction of the fundamental A_{1g} mode around 1.4 eV is considered to be a characteristic behavior of optically detected coherent phonon under resonance conditions[73, 207] The higher-order $2A_{1g}$ and $A_{1g} \pm E_{2g}^{(2)}$ modes indicate a significant enhancement in intensity near the B-gap (1.4 eV) resonance, as shown in Fig 6.7(b). Notably, the intensity reduction of the higher-order frequency modes was more significant than that of the A_{1g} mode when the photon energy was varied toward off-resonance. Therefore, the observation of the higher-order frequency modes is strongly triggered under optical resonance conditions.

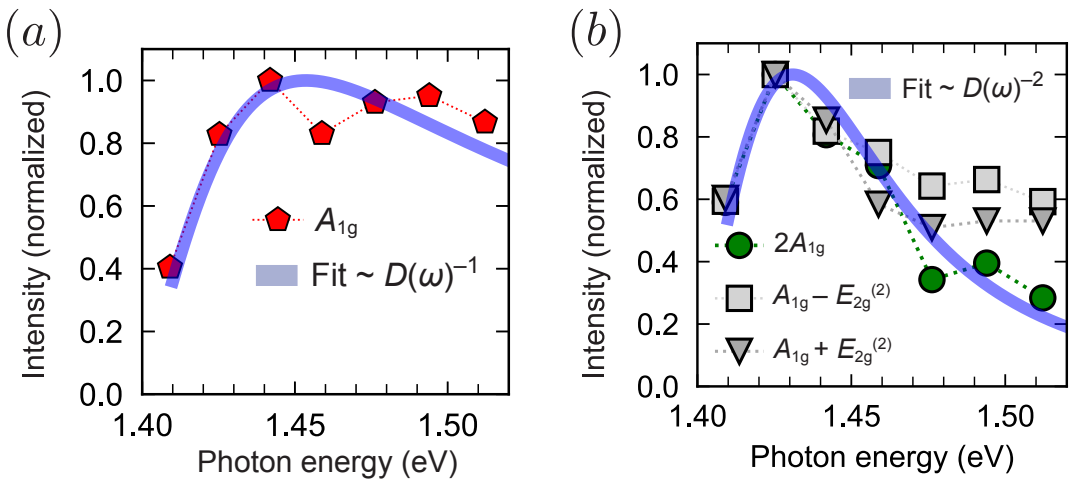

Figure 6.7: Photon-energy dependence on the normalized peak intensity of the A_{1g} mode (a) and the multiple phonon frequencies (b), respectively. The thick lines in (a) and (b) represent the fit based on $D(\omega)^{-1}$ for the A_{1g} mode, and $D(\omega)^{-2}$ for the multiple phonon frequencies.

6.9 Probe Intensity Modulations Induced by A Phonon-Driven Electronic State

The enhancement of higher-order phonon frequencies under near resonance conditions has been seen in previous reports for both coherent phonon [224, 169] and Raman

measurements [221, 223], where the generation mechanism is explained by a second-order Raman process or optical-phonon-induced refractive index modulation via the DP interactions. To further explain the observed photon-energy dependence, we introduce a simple two-level model of the valence and conduction bands at the K-point in the presence of electron-phonon coupling. Here, we assume the coherent-phonon coupled time-periodic Hamiltonian $H(t) = \hat{H}_0 + H_\Omega(t)$, where $\hat{H}_0$ is a two-level electron system: i.e., valence and conduction bands, $H_\Omega(t) = -\hat{h}Q(t)$ is electron-phonon coupling term under a coherent phonon driving force, $\hat{h}$ is associated with the diagonal DP electron-phonon coupling matrix, $Q(t) = Q_0 \cos(\Omega_{\rm ph}t + \varphi)$ is a phonon displacement, Q_0 is a phonon amplitude, $\Omega_{\rm ph}(= 2\pi/T)$ is a phonon frequency, and φ is an oscillatory phase.[112, 128, 229] In this case, we, in particular, consider the phonon amplitude of the A_{1g} mode: i.e., $\Omega_{\rm ph} = 2\pi\nu_{A_{1g}}$. Under a weak resonance optical probe pulse, the complex optical susceptibility without a phonon driving force $Q(t) = 0$ is given by the well-known formalism: the complex optical susceptibility can be represented by the following expression[230]:

$$\chi_0(\omega) = \frac{|P_{\rm cv}|^2}{\epsilon_0}\frac{1}{\hbar(\omega - \omega_{\rm cv}) + i\Gamma}\left(= \frac{|P_{\rm cv}|^2}{\epsilon_0 D(\omega)}\right) \tag{6.1}$$

, where $|P_{\rm cv}|$ is the interband dipole moment, ϵ_0 is the vacuum permittivity, $D(\omega) = \hbar(\omega - \omega_{\rm cv}) + i\Gamma$, $\hbar$ is Dirac's constant, $\hbar\omega$ is the photon energy, $\hbar\omega_{\rm cv}$ is the resonant energy, and Γ is the electronic linewidth. In the presence of coherent lattice vibration, the interband resonant energy can be modulated by the deformation-potential electron-phonon interaction $\Delta E_{\rm DP}$ proportional to the atomic displacement $Q(t)$: $\Delta E_{\rm DP} = -h_0 Q(t)$ and $\hbar\omega_{\rm cv}(t) = \hbar\omega_{\rm cv} - \Delta E_{\rm DP}$, where h_0 is associated with diagonal deformation-potential electron-phonon coupling matrix. Therefore, a coherent-phonon coupled optical susceptibility $\chi(\omega; Q(t))$ can be represented by semi-classical treatment as follows .

$$\chi(\omega; Q(t)) = \frac{|P_{\rm cv}|^2}{\epsilon_0}\frac{1}{\hbar(\omega - \omega_{\rm cv}(t)) + i\Gamma} = \frac{|P_{\rm cv}|^2}{\epsilon_0}\frac{1}{\hbar(\omega - [\omega_{\rm cv} - \Delta\omega_{\rm DP}(t)]) + i\Gamma}, \tag{6.2}$$

where $\Delta\omega_{\mathrm{DP}} = \Delta E_{\mathrm{DP}}(t)/\hbar$.Since an amplitude of phonon-induced electronic energy modulation $h_0 Q_0$ (typically < 10 meV with a sub-picometer atomic displacement of Q_0 induced by sub-mJ/cm^2 photoexcitation [122, 207, 208, 231]) is assumed to be sufficiently smaller than electronic linewidth Γ ($2\Gamma \sim 100$ meV for $2\mathrm{H}-\mathrm{MoTe}_2$ [200]), $|\hbar(\omega-\omega_{\mathrm{cv}})+i\Gamma| > h_0 Q_0$ is satisfied under the resonant conditions, $\omega \sim \omega_{\mathrm{cv}}$. Based on the relationship, the higher-order expansion by $Q(t)$ is valid for the $\chi(\omega; Q(t))$.

$$\chi(\omega; Q(t)) \approx \chi_0(\omega)\left(1+\left[\frac{h_0 Q(t)}{\hbar(\omega-\omega_{\mathrm{cv}})+i\Gamma}\right]+\left[\frac{h_0 Q(t)}{\hbar(\omega-\omega_{\mathrm{cv}})+i\Gamma}\right]^2+\cdots\right) \tag{6.3}$$

The final expression of time-varying optical susceptibility $\chi(\omega, t)$ is obtained by rearranging the Eq. (6.3) formula:

$$\chi(\omega,t) \sim \chi_0(\omega)\sum_{l(>0)}\xi_l(\omega)\cos l\Omega_{\mathrm{ph}}t,\ \xi_l(\omega)=\left[\frac{h_0 Q_0}{\hbar(\omega-\omega_{\mathrm{cv}})+i\Gamma}\right]^l+O\left((h_0 Q_0)^{l+2}\right). \tag{6.4}$$

Since the $h_0 Q_0$ is small, the higher-order term $O\left((h_0 Q_0)^{l+2}\right)$ can be neglected. The probe intensity change $\Delta I/I_0$ is assumed to be as follows.

$$\frac{\Delta I}{I_0} \sim \frac{\Delta\chi}{\chi_0} = \frac{\chi(\omega,t)-\chi_0(\omega)}{\chi_0(\omega)} \tag{6.5}$$

Finally, Using Eqs.(6.1), (6.4) and (6.5), the probe intensity change by a coherent phonon under resonant conditions is represented as follows.

$$\frac{\Delta I(\omega,t)}{I_0} \sim \left[\frac{h_0 Q_0}{D(\omega)}\right]\cos\Omega_{\mathrm{ph}}t+\left[\frac{h_0 Q_0}{D(\omega)}\right]^2\cos 2\Omega_{\mathrm{ph}}t+\cdots, \tag{6.6}$$

where $D(\omega) = \hbar(\omega-\omega_{\mathrm{cv}})+i\Gamma$ and the case of $\varphi = 0$ is considered for simplicity. It should be note that the expansion to higher-order modulations is carried out in a similar way as Eq. (3.47).

According to Eq. (6.6), the amplitude of first-order oscillation is proportional to $D(\omega)^{-1}$, and that of second-order oscillation is proportional to $D(\omega)^{-2}$. Therefore, the

$D(\omega)^{-1}$ and $D(\omega)^{-2}$ are relevant to first- and second-order Raman processes, respectively. The fits based on $D(\omega)^{-1}$ and $D(\omega)^{-2}$ reasonably reproduce the photon-energy dependence of the amplitude of the A_{1g} mode and multiple phonon modes by assuming the B-gap resonance energy $\hbar\omega_{\rm cv} = 1.40$ eV, as shown in Fig. 6.7. Here, the absolute values of the real part of $D(\omega)^{-1}$ and imaginary part of $D(\omega)^{-2}$ were used as fit functions to simulate the energy dependence having an anti-resonance dip around 1.40 eV. The value of the fit parameter $2\Gamma = 106.4$ meV matches well with the order of the previously reported FWHM of the electronic linewidth at the B-gap. [200] According to the discussions above, the observation of multiple phonon frequencies results from the specific enhancement of the higher-order Raman process under resonant conditions derived from a two-level time-periodic electronic system modulated by coherent phonons.

It is worth noting that our result can also be associated with a Floquet-phonon description.[232] Floquet state is a non-equilibrium steady state driven by temporal bosonic fields with a frequency Ω, such as photons and phonons, forming dressed states around the original energy level by integer multiples of $\hbar\Omega$. [182, 183, 233, 229] When a resonant optical probe is used, optical radiations from the dressed states give rise to higher-order frequencies of driving fields in time-domain optical responses or Raman scattering spectra. [233, 229, 223] This interpretation is also applicable to the present study because we argue the generation of the higher-order phonon frequencies in the presence of a time-periodic electron-phonon coupling system under optical-phonon fields with long coherence times: i.e., $H(t) = \hat{H}_0 + H_\Omega(t) = H(t+T)$. Therefore, 2H $-$ $MoTe_2$ or related TMD materials are expected to be ideal systems to study non-equilibrium Floquet dynamics and time-crystal-like electronic phases driven by coherent phonon fields. Further investigations using time-resolved angle-resolved photoemission spectroscopy, scanning tunneling microscopy with high-time resolutions, and advanced theoretical studies are expected to clarify ultrafast momentum and localized dynamics of non-equilibrium phonon-driven phenomena in the future.[234, 235, 236, 237, 231]

6.10 Conclusion

In conclusion, we have experimentally investigated time-domain optical response in the presence of non-equilibrium quasiparticle states of an e–h plasma and coherent phonons in a layered semiconductor $2H - MoTe_2$ using reflective pump-probe spectroscopy under near-resonant photoexcitation conditions. The time-resolved reflectivity change signal ($\Delta R/R$) simultaneously captured the transient generation of electron–hole and electron–phonon interactions for early time delays. The photon-energy dependence of the initial-time response of $\Delta R/R$ and its bleaching with the increase of pump fluence is attributed to the BGR and state-filling effects by photoexcited e–h plasmas. In addition to a long-lived coherent A_{1g} optical phonon, the emergent multiple frequencies of the optical phonons: overtones, sum and difference frequencies between the A_{1g} and $E^{(2)}_{2g}$ modes are found to emerge within sub-picosecond time scales by a time-frequency-domain analysis. Photon-energy dependence measurements demonstrated that multiple phonon frequencies are strongly enhanced when the resonant photon energy is used. The enhancement of the multiple phonon frequencies under resonance conditions can be dictated by the higher-order optical response as a result of resonance energy modulations between the valence and conduction bands induced by the DP electron–phonon interaction in the presence of the coherent A_{1g} mode. Our findings pave the way for a comprehensive description of coherent optical response driven by a photoexcited electron-phonon system and provide access to the ultrafast switching of electronic band structures dressed by a long-lived periodic lattice vibration or the device applications for atomically thin ultrafast electro–phononic modulators.

6.11 Supplementary

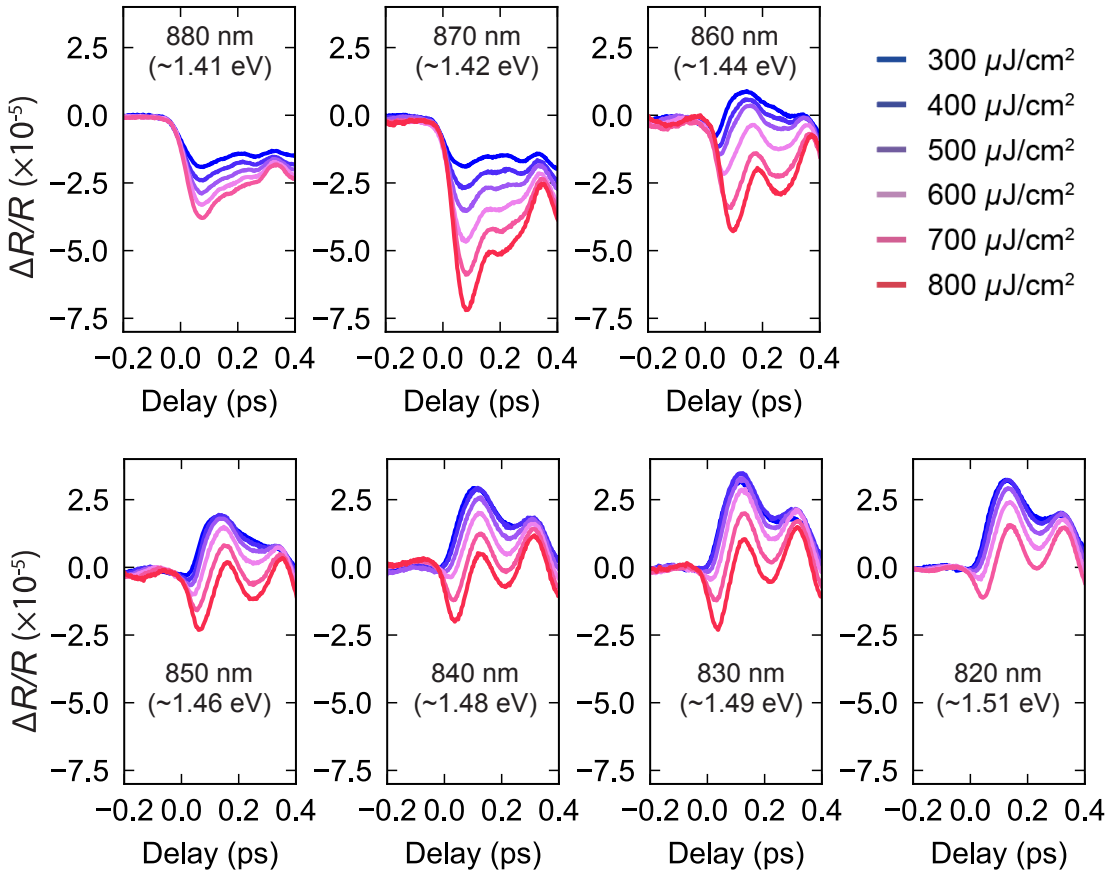

Figure 6.8: A dataset of wavelength- and fluence-dependence measurements that are used for Figs. 6.3 and 6.7. The $\Delta R/R$ data in the wavelength range from 820 nm to 880 nm and in the fluence range from 300 μJ/cm^2 to 800 μJ/cm^2 are displayed.

Transient Reflectivity Measurement Depending on Photon Energy: The central wavelength (photon energy) was varied by the sweeping of an iris in the laser cavity, allowing for a wavelength-dependent measurement from 820 nm (1.52 eV) to 880 nm (1.41 eV) to clarify the behavior of the initial $\Delta R/R$ signal of the sample (see Fig. 2.3 in Chapter. 2). It should be noted that, when applying the wavelength tunability in our laser system, the performance of time-resolution and signal-to-noise ratio decreases due to the pulse-width broadening ($\sim$ 60 fs). Figure.6.8 shows the $\Delta R/R$

data of the wavelength- and fluence-dependence measurements with band-pass filtering of 300 Hz $\sim$ 300 kHz. The dataset in the wavelength range from 820 nm to 880 nm and in the fluence range from 300 μJ/cm^2 to 800 μJ/cm^2 was used for Figs 3 and 5 in the main text to discuss the physics underlying the initial optical responses around zero-time delay and higher-order phonon frequencies.

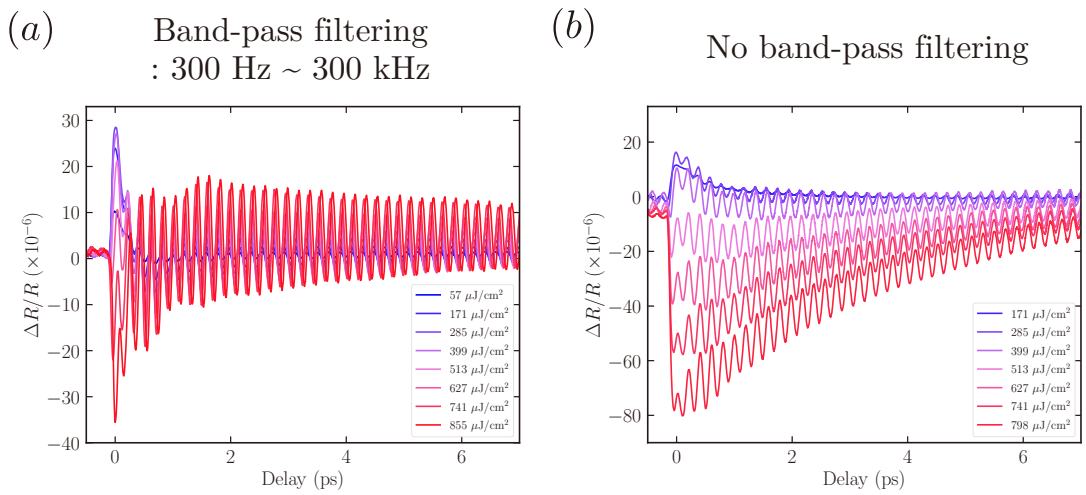

Figure 6.9: A series of $\Delta R/R$ data taken from $2H-MoTe_2$ at 830 nm with band-pass filtering using (a) the bandwidth of 300 Hz $\sim$ 300 kHz and (b) no band-pass filtering (the largest bandwidth).

The Effects of Band-Pass Filtering: In this study, we have usually used band-pass filtering with the bandwidth of 300 Hz $\sim$ 300 kHz in the electronic circuits to detect and get oscillatory data of initial electronic response and the following coherent phonon signal with high signal-to-noise ratio, as shown in Fig. 6.9(a). In the fast-scan method we used, the optical path of the pump beam was modulated at $\approx$ 10 Hz by a delay shaker. The photocurrent signal obtained from the sample was amplified by a current-to-voltage preamplifier and then integrated into a digital oscilloscope. The use of a bandpass filter in the preamplifier eliminates the 10-Hz contributions and the corresponding higher-order harmonic terms induced by the shaker. Without the use of a bandpass filter in the preamplifier, the magnitude and relaxation time constant

of the electronic response can indeed be accurately evaluated. However, this unfiltered condition presents a strong disadvantage: a significant increase in the background noise, leading to longer integration times ($\sim$ 20 minutes per time-domain data), which in turn increases the risk of permanent sample damage during the measurement. For these reasons, measurements performed without using a filter are not usually a practical way to obtain the optical response. In contrast, under filtered conditions with the wide bandwidth filter (e.g., 300 Hz 300 kHz) used in our study, we can acquire data with a high signal-to-noise ratio using a shorter integration time ($\sim$ 3 minutes per time-domain data). Furthermore, applying a wide-bandwidth band-pass filter is unlikely to contribute to significant changes in the magnitude of the electronic response in the time-domain data despite some variations. Therefore, the results presented in this paper are uniformly discussed based on experiments with the above filter conditions ranging from 300 Hz to 300 kHz.

On the other hand, we measured time-domain data without a filter at specific wavelengths and fluences to accurately determine and compare the relaxation time constants of electronic responses, as shown in Fig. 6.9(b).

As shown in Fig. 6.10, we have confirmed that the decaying time of electronic (electron-hole plasma) population dynamics indicates almost constant (3 $\sim$ 4 ps) in the range of fluence (500 $\sim$ 800 μJ/cm^2) and the wavelength (830 nm and 870 nm), that the order of the values (a few picoseconds) are almost consistent with previous reports.[137] This fact shows that the decay time of electronic population dynamics may not be drastically changed by the pump fluence we used and the wavelength in the range from 830 nm to 870 nm.

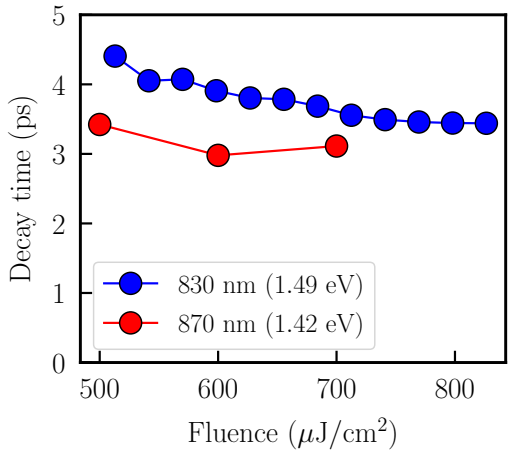

Figure 6.10: Fluence-dependence decay constant of electronic dynamics extracted from $\Delta R/R$ of the wavelength 830 nm and 870 nm.

It should be noted that we present three different types of datasets here: (1) high time-resolution measurement (pulse duration $\sim$ 30 fs, wavelength $\sim$ 830 nm fixed, band-pass filtered) for the investigation of multiple-phonon generation up to higher order, as shown in Fig. 6.9(a); (2) wavelength-dependence measurement (pulse duration $\sim$ 60 fs, wavelength 820 $\sim$ 880 nm variable, band-pass filtered) for the comprehensive investigation of the initial $\Delta R/R$ signals in the early time delays, as shown in Fig. 6.8; (3) unfiltered measurement (pulse duration $\sim$ 30 fs, wavelength $\sim$ 830 nm fixed, unfiltered) for the estimation of relaxation constant of electronic response, as shown in Fig. 6.9(b). In every dataset, the reversal of positive and negative values in early-time $\Delta R/R$ signals has been consistently observed. However, one can see that the transition points between positive and negative values differ slightly between datasets. This is because the transition point in our measurements is sensitive to various experimental factors, including the sample's condition and laser parameters: wavelength, bandwidth, and focusing condition. Since each dataset was acquired on different days, the variations of experimental parameters likely contribute to the observed variations in the transition point. To eliminate those variations depending on experiments, we evaluate the behavior of initial optical responses only based on the dataset (2), as displayed in Fig. 6.8, in the main text Figs. 6.3 and 6.7.

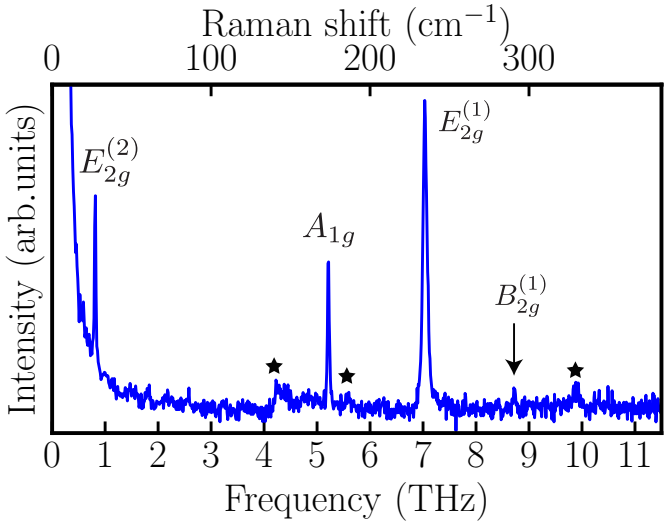

Figure 6.11: Raman spectrum of $2H - MoTe_2$ bulk crystal.

Sample Characterization by Raman Spectroscopy: To characterize the sample, we carried out the Raman measurement using a system (Renishaw InVia Reflex) with 532-nm continuous-wave (CW) laser excitation and with Eclipse notch filter, which enables the measurement up to extremely low Raman shift 10 cm^{-1} region. The observed static phonon spectrum of our $2H - MoTe_2$ sample is shown in Fig. 6.11. We found the pronounced first-order Raman modes: $E_{2g}^{(2)}$ (27 cm^{-1} = 0.81 THz), A_{1g} (174 cm^{-1} = 5.22 THz), and $E_{2g}^{(1)}$ (234 cm^{-1} = 7.02 THz) except for E_{1g} (120 cm^{-1} = 3.6 THz) mode.[148, 149, 238, 161, 137] We have also observed small peaks of pronounced double resonance Raman modes arising from the combination of $M-$point phonons: 141 cm^{-1} (4.22 THz), 185 cm^{-1} (5.55 THz) and 329 cm^{-1} (9.87 THz) which are assigned as 2TA(M), $E_{2g}^{(1)}$(M) − TA(M), and $2A_{1g}$(M) or $E_{2g}^{(1)}$(M) + TA(M), respectively, in previous Raman studies.[238, 161] In the present study based on the pump-probe method, the contribution of double resonance modes at the M-point (direct gap of > 1.7 eV) can be safely excluded because the near-infrared ~ 1.5 eV pump pulse cannot excite electrons from the valence to the conduction bands at the M-point.

Optical Constants of 2H-$MoTe_2$ from Experiments and a Calculation In the main text, we demonstrated the simulation of reflectivity changes $\Delta R/R$ using an experimental reflectance R data based on previously reported optical constants of $2H - MoTe_2$ by Li, *et al.* [209] to explain the observed inversion feature of reflectivity changes $\Delta R/R$ near-zero time delay around or above B-gap by introducing a band-gap renormalization (BGR). We certified that the analysis based on the spectroscopic data from a different $2H - MoTe_2$ sample is expected to be valid even in our $2H - MoTe_2$ sample according to an additional spectroscopic measurement for our sample and a DFT simulation whose results were in good agreement with the previously reported spectroscopic data.

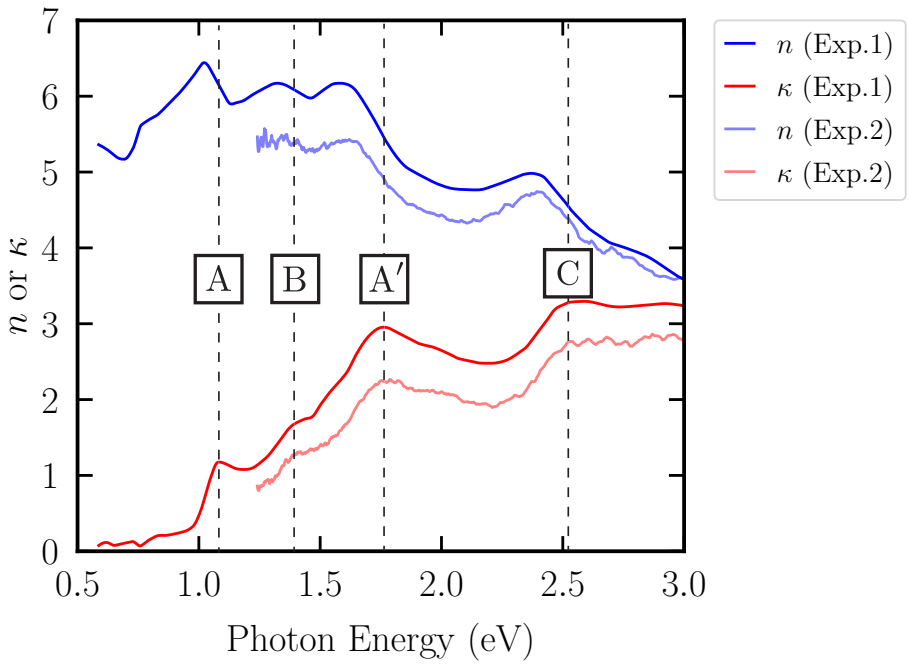

Figure 6.12: Comparison of the experimentally obtained optical constants of $2H - MoTe_2$ between the previously reported spectroscopic result by Li, *et al.* [209] (Exp.1) and our spectroscopic result by ellipsometry measurement (Exp.2).

Spectroscopic Ellipsometry Measurements: we compare the experimentally obtained complex refractive indices $\tilde{n} = n + i\kappa$, where n is the refractive index and κ is

the optical extinction index, between those of Li, *et al.* [209] and our spectroscopic ellipsometry measurement. Our spectroscopic measurement was performed using a J. A. Woollam M-2000U Ellipsometer with UV-to-NIR spectral range ($\lambda = 250 \sim 1000$ nm or photon energy $E = 1.24 \sim 4.96$ eV) and the probe light focused onto the $2H - MoTe_2$ sample with spot radius ≈ 3 mm and angle of incident AOI $= 45°$. We assigned the previously reported spectroscopic result by Li, *et al.* using an Ellipsometer with spectral range ($\lambda = 300 \sim 2100$ nm or photon energy $E = 0.59 \sim 4.13$ eV) and AOI $= 70°$ as Exp.1, and our result as Exp.2 for comparison displayed in Fig. 6.12. The previously reported spectroscopic data (Exp.1) clearly shows optical transition energies of A-, B-, A'- and C-gaps ($E \approx 1.1,\ 1.4,\ 1.7$ and 2.5 eV).[209, 200] Our spectroscopic data (Exp.2) reasonably reproduces the spectral feature of the previously reported Exp.1, that the B-, A'-, and C-gaps positions of Exp.2 are in good agreement with those of Exp.1. Based on the comparison above, the optical properties of $2H - MoTe_2$ samples we used and Li, *et al.* used are considered to be almost the same, although the values of n and κ are slightly different for each other. The smooth optical spectrum of Exp.1 is preferred to calculate reflectance spectra and simulate $\Delta R/R$ upon photoexcitation where the BGR-induced band-gap shrinkage was taken into account instead of our spectroscopic data with poor signal-to-noise ratio around the B-gap.

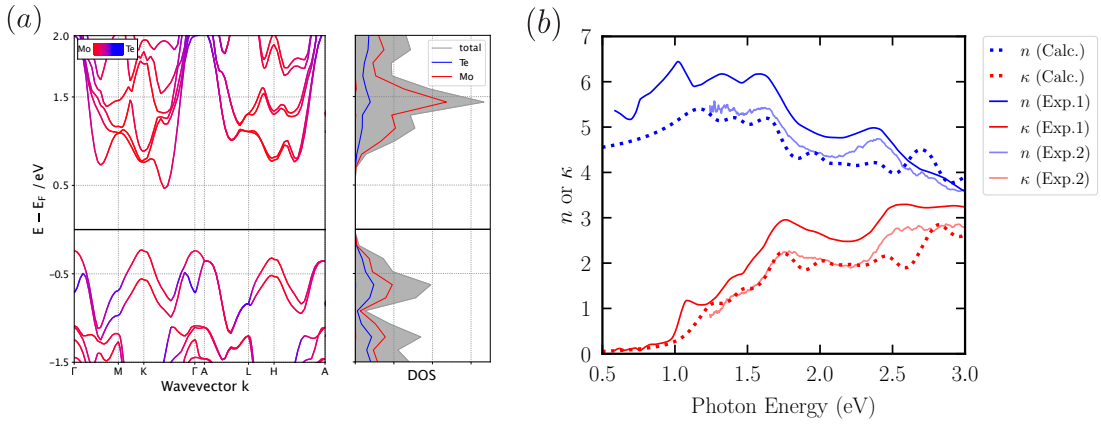

Figure 6.13: (a)The band structure of bulk $2H - MoTe_2$ calculated by the DFT simulation. (b) The experimental and calculated complex refractive indices.

A Calculation by Density-Functional Theory (DFT): The electronic structure of the bulk $2H - MoTe_2$ (Fig. 6.13(a)) was generated using the plane-wave density-functional theory program VASP 6.[239] Projector augmented waves were used as the basis.[240] The generalized gradient approximation (GGA) of Perdew-Burke-Ernzerhof (PBE) was used.[241] A value of 400 eV was used for the energy cutoff based on a convergence study that yielded a tolerance of 1 meV in total energy. An $8 \times 8 \times 2$ Monkhorst-Pack grid was used for Brillouin zone integration. Spin-orbit coupling was enabled. The band dispersion plots were drawn using the pymatgen library .[242]

Fig. 6.13(b) shows the comparison among experimental (Exp.1 and Exp.2) and Calculated (Calc.) optical constants n and κ. The n and κ calculated by the DFT simulation also reasonably well reproduce the spectral feature of the experimental results, while the optical transition energies of A- and B-gaps were overestimated to be 1.25 eV and 1.47 eV, respectively, in the calculation. Nevertheless, the calculated spectroscopic result is comparable with the experimental spectroscopic results.

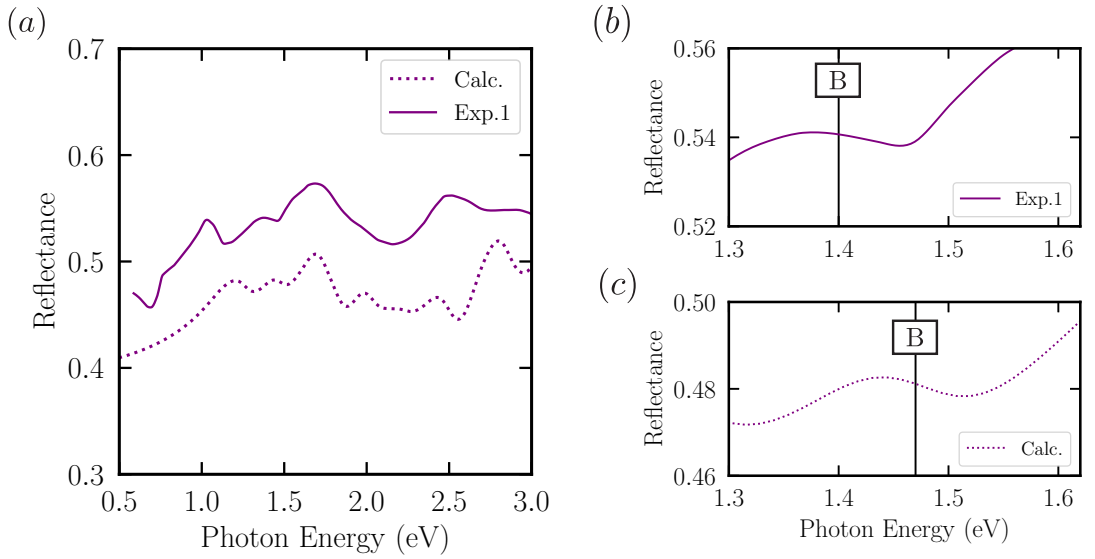

Figure 6.14: Comparison of the experimental [209] (Exp.1) and calculation (Calc.) reflectance R. (a) Comparison of the reflectance spectra between the experiment (Exp.1) and the calculation (Calc.) in the spectral range from 0.5 eV to 3.0 eV. (b) The enlarged view around B-gap (= 1.40 eV) of the experimental (Exp.1) reflectance spectrum. (c) The enlarged view around B-gap (= 1.47 eV) of the calculated reflectance spectrum.

Reflectance Spectra: the reflectance spectra around were compared around the B-gap between the experimental spectroscopic data (Exp.1) and the DFT calculation (Calc). Reflectance R was calculated using the following equation:

$$R = \left|\frac{\tilde{n}-1}{\tilde{n}+1}\right|^2 = \left|\frac{n+i\kappa-1}{n+i\kappa+1}\right|^2 = \frac{(n-1)^2+\kappa^2}{(n+1)^2+\kappa^2} \tag{6.7}$$

by substituting complex refractive indices obtained by the experiment or calculation. Fig. 6.14(a) shows the reflectance spectra obtained by Exp.1 and Calc. with a spectral range from 0.5 eV to 3.0 eV. In the spectral region < 2.0 eV, the reflectance curves by the experiment and the calculation show the same behavior. Fig. 6.14(b) and (c) present the enlarged view of the experimental and calculated reflectance spectrum around the B-gap (1.40 eV and 1.47 eV). Both reflectance curves around the B-gap show the same spectral appearance, enabling us to analyze the BGR effect embedded in our initial $\Delta R/R$ spectrum. As mentioned in the previous section, it should be noted that the B-gap energy obtained by the calculation is overestimated to the extent of ≈ 0.07 eV for the experimental result.

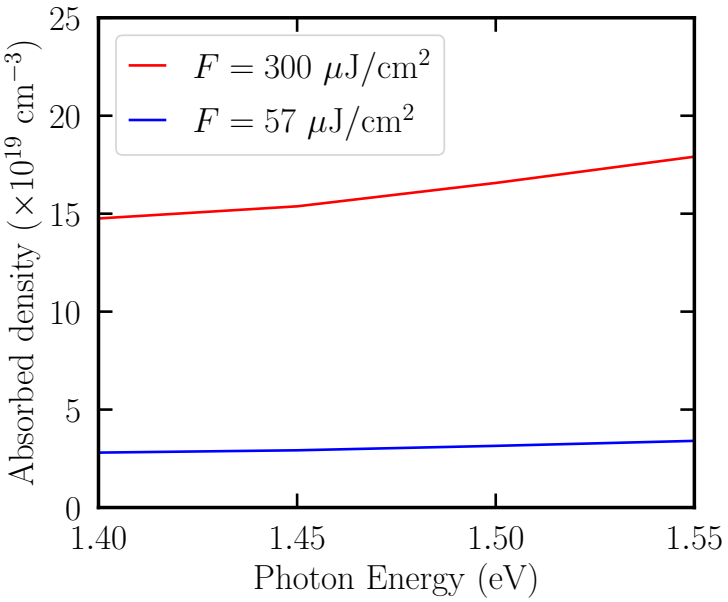

Figure 6.15: Photon-energy dependence of absorbed density calculated by the incident laser fluence ($F = 57$ and 300 μJ/cm^2) and the reflectivity curve of 2H $-$ $MoTe_2$.

Estimation of the Absorbed Density: The absorbed density n_{exc} is generally estimated using following equations:

$$n_{\text{exc}}(\text{cm}^{-3}) \approx \frac{(1-R)F}{\hbar\omega} \cdot \frac{1}{x_p} \tag{6.8}$$

, where $\hbar\omega$ (J) is the photon energy, R is reflectance at the photon energy given in the following Fig. 6.14, F (J/cm^2) is the incident laser fluence, and x_p cm is the penetration depth at the photon energy. Based on the equations above, we calculated the 3D absorbed density in the range of 1.4 to 1.55 eV for the incident laser fluence $F = 57$ and 300 (μJ/cm^2), as shown in Fig. 6.15. The calculation shows that the absorbed density is almost constant in the photon-energy range used in our study. Its orders of magnitude are $\geq 10^{19}$ cm^{-3} being larger than the general Mott density of $\leq 10^{18}$ cm^{-3}. This is because the reflection coefficients and penetration depths in the range of $1.4 \sim 1.5$ eV are almost identical around $R \sim 0.5$ and $x_p \sim 50$ nm.

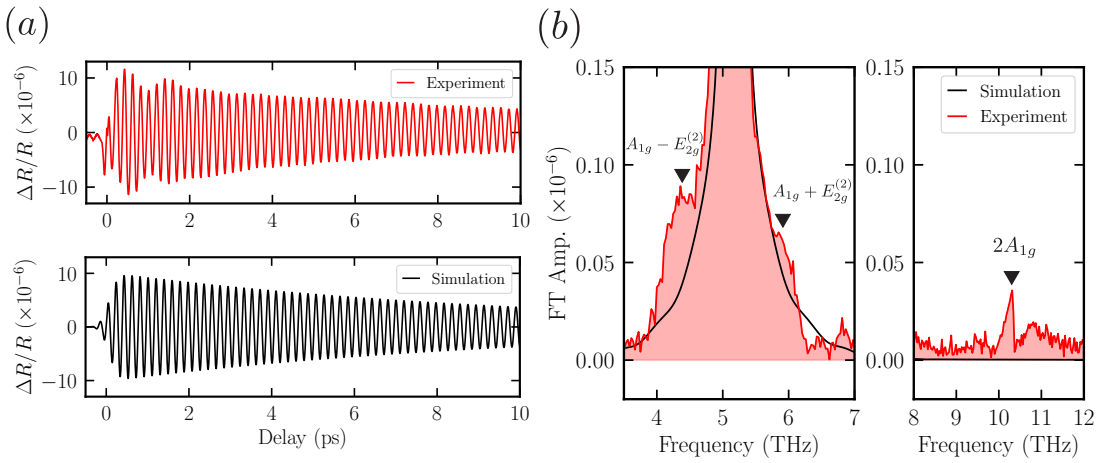

Figure 6.16: (a) Experimental ($F = 627$ μJ/cm^2) and simulated coherent phonon oscillations of the A_{1g} mode ($\nu_A \approx 5.15$ THz). (b) Comparison of the FT spectra from experiment and simulation around 5 THz. (c) Comparison of the FT spectra between the experiment and simulation around 10 THz.

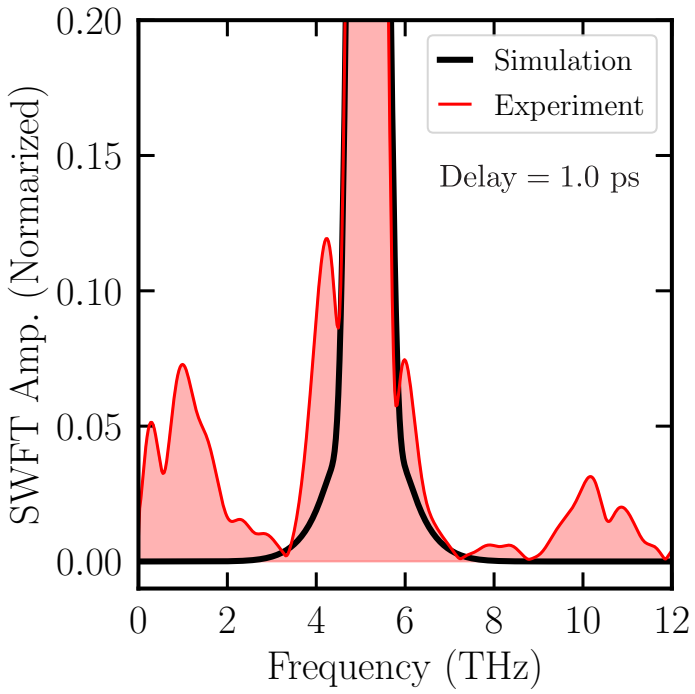

Figure 6.17: A comparison of the STFT spectra between experimental and simulated data for a 1.0 ps time delay.

Examination of the Ripple-Structure Formation Effects in the Fourier Transform and STFT Analyses: To examine the ripple artifacts due to the FT, we compared the FT spectra between the experiment and a simulation of the A_{1g} mode ($\nu_A \approx 5.15$ THz), as shown in Fig. 6.16. The simulated oscillation Fig. 6.16(a) was obtained fitting using a single damped oscillator. In the resulting FT spectra, the sum and difference frequency modes ($A_{1g} \pm E_{2g}$ and $2A_{1g}$) did not appear in the simulated oscillation, while they were present in the FT of the experimental results (Fig. 6.16(b)). Furthermore, we also compared the SWFT spectra at 1 ps in the same way and found the same results as those generated from the FT spectra (Fig. 6.17). These observations underscore that the appearance of combination modes is not an artifact associated with the Fourier transform process.

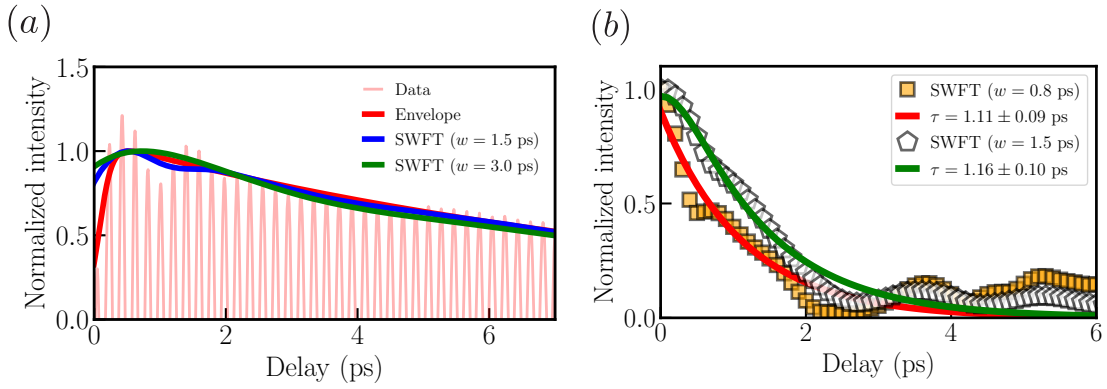

Figure 6.18: (a) A comparison of the envelope of coherent phonon signal (the A_{1g} mode) with the decaying curves obtained by the STFT analysis using window widths of $w = 1.5$ and 3.0 ps. (b) A comparison of the decaying curves of the $E_{2g}^{(2)}$ mode obtained by the STFT analysis using window widths of $w = 0.8$ and 1.5 ps.

Evaluation of Dephasing Dynamics of Time-Domain Oscillation in the STFT spectrogram: We assume that the obtained reflectivity change signal is to be a damped oscillation, $\Delta R(t)/R = y_0 e^{i(\Omega + i\gamma)t}$, where the y_0 is a constant, the $\gamma(= 1/\tau_{dec})$ is the decaying rate and time constant respectively, and the Ω is the oscillatory frequency,

substituting into the Eq. (2.10) of the STFT analysis, as was described in Chapter. 2:

$$
\begin{aligned}
I(\omega,\tau) &\propto \left| \int_{-\infty}^{\infty} dt\ e^{-\frac{(t-\tau)^2}{\sigma^2}} \cdot y_0 e^{i(\Omega+i\gamma)t} \cdot e^{-i\omega t} \right| \\
&= y_0 \left| \int_{-\infty}^{\infty} dt\ e^{-\frac{\left[t-\left(\tau-\frac{i(\omega-\Omega-i\gamma)\sigma^2}{2}\right)\right]^2 + i(\omega-\Omega-i\gamma)\sigma^2\tau + \frac{(\omega-\Omega-i\gamma)^2}{4}\sigma^4}{\sigma^2}} \right| \\
&= y_0 \underbrace{\left| e^{-i(\omega-\Omega-i\gamma)\tau} \right|}_{e^{-\gamma\tau}} \cdot \underbrace{\left| e^{\frac{(\omega-\Omega-i\gamma)}{4}\sigma^2} \right|}_{e^{-\frac{(\omega-\Omega)^2}{(2/\sigma)^2}} \cdot\ e^{-\frac{\gamma^2\sigma^2}{4}}} \cdot \underbrace{\left| \int_{-\infty}^{\infty} dt\ e^{-\frac{\left[t-\left(\tau-\frac{i(\omega-\Omega-i\gamma)\sigma^2}{2}\right)\right]^2}{\sigma^2}} \right|}_{\sqrt{\pi}\sigma} \\
\therefore \quad I(\omega,\tau) &\propto e^{-\frac{(\omega-\Omega)^2}{(2/\sigma)^2}} \cdot\ e^{-\gamma\tau}. \qquad (6.9)
\end{aligned}
$$

The Eq. (6.9) indicates that the damped oscillatory signal shows the Gaussian shape of the peak around the frequency Ω and that peak intensity decreases in the actual decaying rate γ in the STFT spectrogram, suggesting that the decaying rate obtained from STFT analysis is independent on the window width σ.

In the case of our oscillatory data, it is not simply the single-damped oscillatory function but also includes the step-function-like contribution near zero-time delay. Although the convolution effect of the step-function-like contribution in the STFT analysis results in the small shift of the rise time of the maximum value near zero-time delay, it is unlikely to affect the decaying time constant, as shown in the following discussion.

We practically compare the window-width dependence ($w = 1.5$ and 3.0 ps) of the A_{1g} decaying curve obtained by the STFT analysis with the envelope of A_{1g} amplitude obtained by the fitting, as shown in Fig. 6.9(a). Even when a broad window width $w = 3.0$ ps that is two times larger than $w = 1.5$ ps was used, the decaying curves of the STFT analysis fairly well reproduced the original amplitude envelope function regardless of the window widths.

We also compare the decay dynamics for the short-lifetime $E_{2g}^{(2)}$ mode using two different window-width ($w = 0.8$ and 1.5 ps), as shown in Fig. 6.9(b). Although the decay curve or the rise time of $w = 1.5$ ps slightly shifts toward later time delay

compared to that of $w = 0.8$ ps, both the decay time constants are almost identical each other, obtained by a single exponential fitting function ($f(t) = \Theta(t) \cdot e^{-\frac{t-t_0}{\tau_{\rm dec}}}$, where the $\Theta(t)$ is a Heaviside step function, the t_0 is a rise time of the decaying curves, the $\tau_{\rm dec}$ is a decay time constant).

As discussed above, it is unlikely to drastically change the decaying time constant even in the presence of the step-function-like part. Therefore, we can reasonably discuss and compare the decay time constants for even the small amplitude modes, such as the observed multiple phonon modes obtained from the STFT analysis.

Chapter 7

Ultrafast Structural Dynamics of 2H − $MoTe_2$ Under High-Density Excitation Conditions

In the previous chapter, the nature of the optical response due to the interaction between electrons and phonons under weak photoexcitation conditions was clarified. On the other hand, to explore the possibility of the expected photo-induced structural phase transition, it is necessary to investigate under stronger excitation conditions. As described in Chapter 6, under photoexcitation conditions, not only structural changes but also various effects of electronic excitation and nonlinear optical phenomena are involved. Considering this, it is extremely important, both fundamentally and practically, to experimentally investigate how the excited electronic states affect structural changes. In this chapter, we examined the impact of high-density photoexcitation on the electronic states and crystal structure of $MoTe_2$ under various excitation levels at a wavelength of 400 nm using ultrafast time-resolved electron diffraction and transient reflection measurements. We also verified whether a phase transition from semiconductor to semimetal is possible under light excitation conditions below the damage threshold.

The descriptions in this chapter are based on the research found in **T. Fukuda**, *et al. J. Phys. Chem.* **127**, 13149-13156 (2023).[191]

7.1 Motivation and Introduction

Two-dimensional transition-metal dichalcogenides (TMDs) manifest a diversity of electronic phases—including semiconducting, semimetal, superconducting, and topologically nontrivial states—determined by their chemical compositions, structural configurations, and stacking sequences, extending from monolayer formations to bulk or artificially engineered stacks.[22, 243, 141, 35, 167, 15] The pronounced confinement of the Coulomb potential within each atomic layer remarkably enhances electron-hole and electron-phonon interactions, potentially giving rise to exotic quantum many-body phenomena, such as the emergence of strongly binding excitons, exciton complexes states, and charge-density-wave states.[26, 244, 245] Furthermore, light-matter interactions in TMDs facilitate valley-selective electronic excitation, high-harmonic generation, Mott transitions from excitons to electron-hole plasmas, and structural phase transitions, depending on the excitation levels.[24, 36, 246, 47, 28, 53] These unique fundamental electronic and optical properties of TMDs, which exhibit significant degrees of freedom, show promise for developing next-generation atomically thin electronic, spintronic, and optoelectronic applications. [16] They also play a pivotal role in advancing fundamental quantum computing research. In ultrafast studies, the electron and structural dynamics under intense photoexcitation conditions are particularly intriguing, offering insights for potential applications in TMD-based saturable absorbers, nano-lasers, and phase-change memories. [47, 247, 248, 249, 31]

$MoTe_2$, a representative TMD, displays remarkable electronic and structural properties under dense electronic excitation conditions. It has three structural polymorphs: the 2H (semiconductor), 1T' (semimetal), and T_d (type-II Weyl semimetal) phases. [141, 35] The 2H and 1T' phases are stable and metastable at room temperature, respectively, while the T_d phase is a low-temperature (< 250 K) phase of the 1T'. Ultrafast transient spectroscopic measurements have illustrated the structural phase transition between the 1T' and T_d phases, including the emergence of an intermediate T^* phase.[54, 138, 250] Moreover, theoretical calculations have predicted the 2H-to-

1T' phase transition, involving a transient metallic $2H^*$ phase under several percent of valence electrons excitation. [49, 50, 51, 52] Therefore, it is crucial to investigate the structural dynamics of $2H - MoTe_2$ by the experiment, in the presence of photoexcited dense electron-hole plasma.[204] However, few experimental studies have been demonstrated under intense electronic excitation conditions since photothermal and heat-accumulation effects lead to permanent ablation and tellurium segregation to the $2H - MoTe_2$ sample.[134] Thus, a comprehensive study of the light-induced structural dynamics of $MoTe_2$, without sample damage, is needed. In this study, we investigate the light-induced structural dynamics of $2H - MoTe_2$ across various excitation levels, employing an excitation wavelength of 400 nm through ultrafast time-resolved electron diffraction and coherent phonon spectroscopy by transient reflectivity measurements. Our findings indicate that both saturable absorption and damage induction manifest at relatively low photoexcitation levels, complicating the phase transition process under conditions of femtosecond and near-UV photoexcitation.

7.2 Experimental Methods

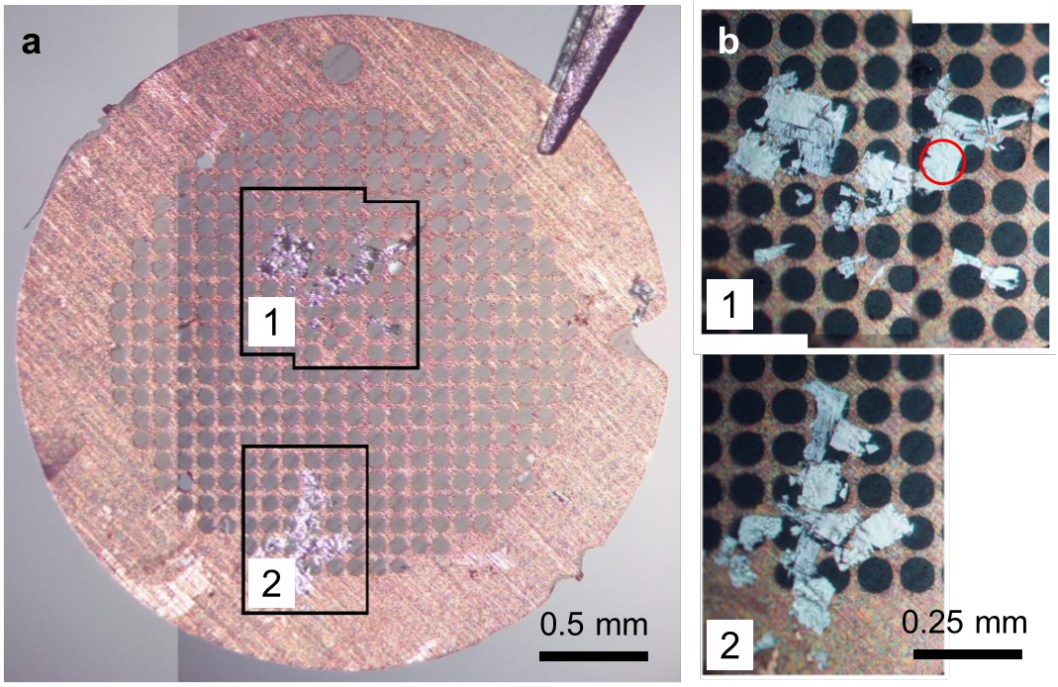

Figure 7.1: (a) Micrograph of the ultrathin $2H - MoTe_2$ samples on a transmission electron microscopy grid. (b) Enlarged views of positions 1 and 2 in (a). Time-resolved electron diffraction measurements were performed at position 1. The red circle indicates the electron beam diameter (100 μm).

The bulk $2H - MoTe_2$ crystal employed in this study was sourced from HQ Graphene, Netherlands. For ultrafast transient reflection measurements, a bulk sample was utilized. Typically, samples with thickness below 100 nm are preferred for ultrafast time-resolved electron diffraction measurements. In this case, the samples were sliced to a thickness of 40 nm using an ultra-microtome (EM UC6, Leica Microsystems GmbH). Sliced ultrathin samples were used for static transmission measurements and ultrafast time-resolved electron diffraction measurements.

As shown in Fig. 7.1, the sample was mounted on a grid designed explicitly for transmission electron microscopy (TEM). To ascertain the presence of nonlinear optical effects in the ultrathin $2H - MoTe_2$ sample, we conducted measurements of its static

transmission at various photoexcitation levels, reaching up to 20 mJ/cm^2 in an ambient air environment. Near-ultraviolet (near-UV) light, with a wavelength of 400 nm, was precisely focused onto the $2H - MoTe_2$ sample placed on the TEM grid, which had a diameter of approximately $\sim$ 63 μm. We quantified the relative intensities of the incident and transmitted and reflected light from the sample using a power meter.

Ultrafast time-resolved electron diffraction measurements were conducted on an ultrathin $2H - MoTe_2$ film of 40 nm thickness, employing a pump wavelength of 400 nm in a vacuum environment. Detailed descriptions of the experimental assembly for these measurements can be found in Fig. 2.10(b) (Chapter 2) or ref [251]. The pump-beam diameter was set at 360 μm, and the fluence ranged between 2 $\sim$ 16 mJ/cm^2. The probe electron pulse, with an approximate duration of 1 ps, was accelerated at a voltage of 75 kV, and the diameter of the electron beam was maintained at 100 μm.

Ultrafast transient reflectivity measurements were carried out on a bulk $2H - MoTe_2$ sample, utilizing a pump wavelength of 400 nm and a probe wavelength of 800 nm, under ambient conditions. Detailed information regarding the optical layout for these measurements is provided in Chapter 2, Figs. 2.7 and 2.8. The 400 nm pump pulse was efficiently generated via SHG from a β-BBO crystal under phase-matching conditions. The spot diameter of the pump and probe light is estimated to be $\sim$ 20 μm. The sample used in the reflection measurement was a bulk $2H - MoTe_2$ sample with a thickness of $\sim$ 100 μm.

7.3 Static Transmission Under High-Density Excitations

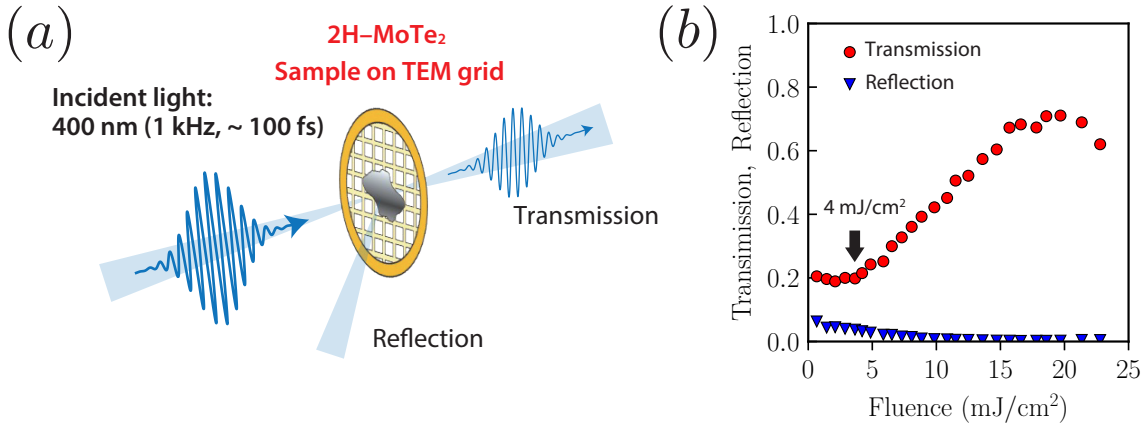

Figure 7.2: (a) Schematic configuration of static transmission and reflection measurement. (b) Static transmission and reflection of an ultrathin $2H - MoTe_2$ sample. Saturable absorption occurs at an incident fluence of $F = 4$ mJ/cm^2, as indicated by the red arrow. The sample was ablated above an incident fluence of $F = 15$ mJ/cm^2.

$2H - MoTe_2$ possesses an indirect band gap of $\sim$ 0.9 eV and two direct band gaps of $\sim$ 1.0 eV (A-gap) and $\sim$ 1.4 eV (B-gap) at the K valley.[200] The 400 nm (3.1 eV) excitation photons can excite electrons across almost all momenta in the band structure.[252] Initially, the static transmission and reflection measurements were conducted in a fluence range up to about 20 mJ/cm^2, as shown in Fig. 7.2(a). Figure 7.2(b) illustrates the transmission of near-UV light as a function of incident fluence. The transmission remained constant for incident fluences of $0 \sim 4$ mJ/cm^2; however, it linearly increases for fluences exceeding 4 mJ/cm^2 due to saturable absorption. An incident fluence of 4 mJ/cm^2 at a wavelength of 400 nm leads to $\sim$ 0.4 % excitation of the valence electrons, assuming an absorptivity of $\sim$ 50 %, a unit cell volume of 74.9 Å^3, and 18 valence electrons in the unit cell. The small ablation started from an incident fluence of 15 mJ/cm^2 in air. Note that a single pulse of 15 mJ/cm^2 does not cause damage. It took several minutes to detect the static transmission with 1 kHz optical

pulses, suggesting that roughly 100,000 pulses at a fluence of 15 mJ/cm^2 are required to induce minor ablation. Above a fluence of 20 mJ/cm^2, a single pulse can ablate the sample due to air breakdown. Moreover, due to the significant scattering induced by the ripple structure created by the microtome knife, the static reflectivity exhibited a much lower value than the transmission. Notably, the reflectivity decreases to zero for fluences exceeding 4 mJ/cm^2, attributable to saturable absorption.

7.4 Ultrafast Electron Diffraction Measurements

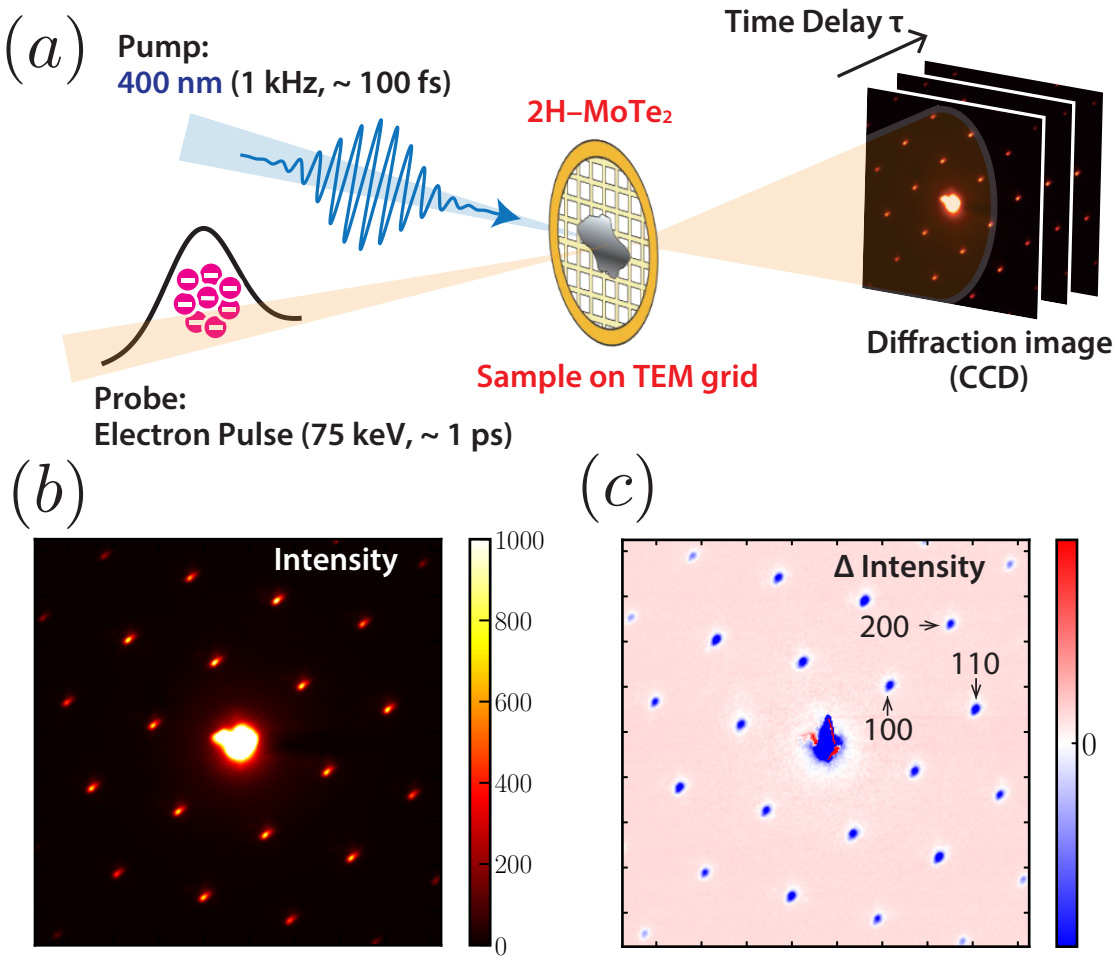

Figure 7.3: (a) Schematic configuration of ultrafast electron diffraction (UED) measurement. (b) and (c) Electron diffraction and its differential images (after 100 ps) at an incident fluence of $F = 8$ mJ/cm^2 from an ultrathin $2H - MoTe_2$ sample, respectively. Six-symmetric diffraction spots from the {100}, {110}, and {200} planes are indicated.

We conducted ultrafast time-resolved electron diffraction measurements on an ultrathin $2H - MoTe_2$ sample, as depicted in Figure 7.3(a). Ultrafast time-resolved electron diffraction measurements are pivotal in exploring the photoinduced structural dynamics of TMDs.[253, 254, 127, 255] In our setup, the electron pulse was oriented perpendicular to the ab-plane of the $2H - MoTe_2$ sample. The resulting electron diffraction pattern

from the sample, as illustrated in Figure 7.3(b), prominently displays six symmetric diffraction spots corresponding to the {100}, {110}, and {200} planes. Figure 7.3(c) presents the differential electron diffraction patterns after photoexcitation ($\sim$ 100 ps), where a notable decrease in the diffraction intensities from the lower order is observed, and an even larger decrease from higher orders. These decreases in diffraction intensity are attributed to the reduction in the Debye-Waller factor, indicative of a temperature increase. Typically, electronic excitation occurs immediately after photoexcitation ($<$ 100 fs). This is followed by electron-electron and electron-phonon scatterings, which induce non-thermal atomic displacements within a timeframe ranging from subpicosecond to a few picoseconds. The electron-lattice system attains thermalization after several to 10 ps, involving phonon-phonon scattering – the energy transfer from high-frequency optical phonon modes to low-frequency acoustic phonon modes. The temperature rise due to laser irradiation ($3 \sim 4$ mJ/cm^2) was calculated to be in the range of $220 \sim 300$ K, using the density, specific heat, and absorptivity of 400 nm light for $2H - MoTe_2$. The Debye-Waller factor using atomic bond length and force constant values derived from the bulk modulus of $MoTe_2$ was estimated in Supplementary section 7.8. The changes in diffraction intensity due to the Debye-Waller factor were estimated to be around $4 \sim 5$ % for the 100 diffraction and $10 \sim 13$ % for the 110 diffraction. While the change in the 100 diffraction was slightly underestimated, that in the 110 diffraction was close to our estimation.

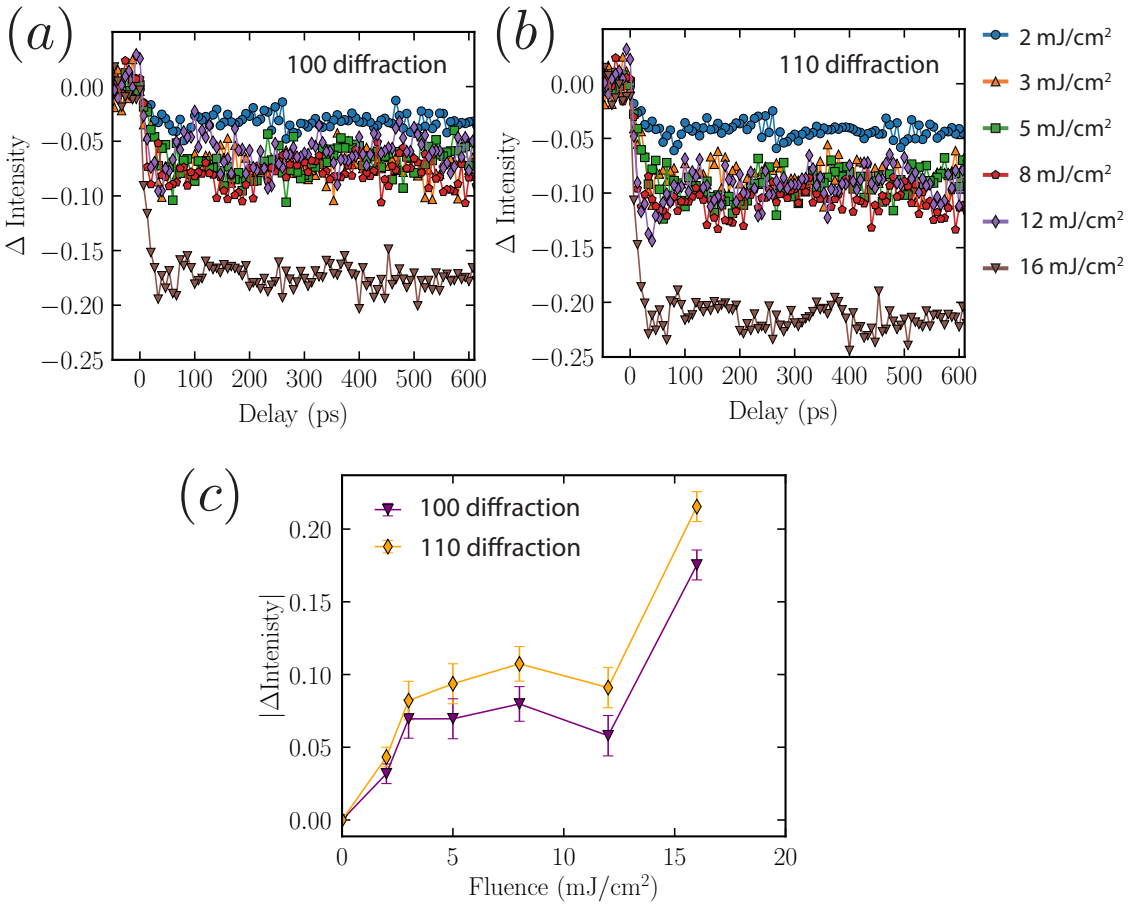

Figure 7.4: (a) and (b) Temporal variation in the diffraction intensity changes from the 100 and 110 planes in the fluence range $F = 1 \sim 16$ mJ/cm^2. (c) Fluence-dependence plots of diffraction intensity changes with the data of (a) and (b) being averaged over the time-delay range after 100 ps. The figure shows linearly increasing ($F = 0 \sim 3$ mJ/cm^2), plateau ($F = 3 \sim 12$ mJ/cm^2), and reviving up ($F > 12$ mJ/cm^2) regions.

The temporal evolution of the diffraction intensities from the {100} and {110} planes, under various excitation levels, is depicted in Figs. 7.4(a) and (b), respectively. The decrease in diffraction intensity ~ 100 ps as a function of incident laser fluence is comprehensively summarized in Fig. 7.4(c). Notably, the intensity linearly decreases below an incident fluence of 3 mJ/cm^2. This suggests that all absorbed photons is converted into thermal vibrational energy within this fluence range. The observed declines in diffraction intensities exhibit a plateau region when the incident fluence is in the range of $F = 3 \sim 12$ mJ/cm^2. This plateau can be attributed to saturable absorption,

as previously discussed. It is observed that for excitation intensities resulting in greater than approximately ~ 0.4 % excitation of the valence electrons, $2H - MoTe_2$ does not absorb additional light. However, at a relatively high incident fluence (16 mJ/cm^2), the system absorbs more light, which could be explained by multiphoton absorption. par

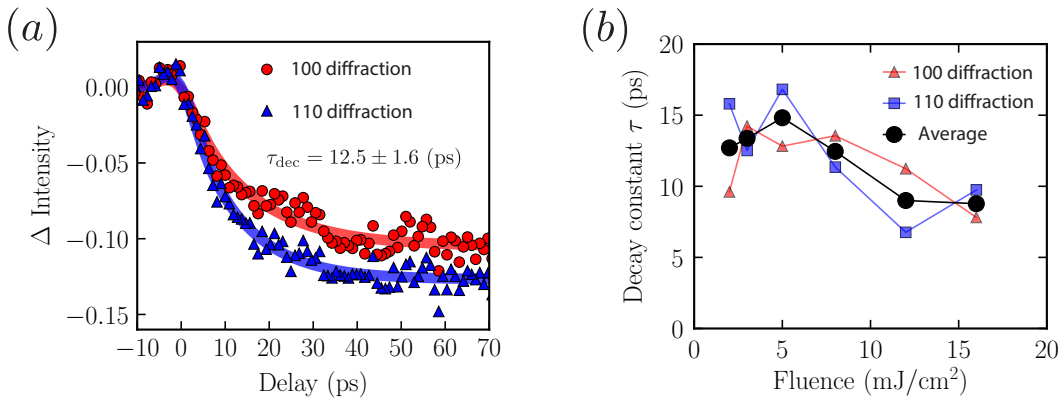

Figure 7.5: (a) Fast dynamics of electron diffraction from {100} and {110} planes at an incident fluence of $F = 8$ mJ/cm^2. Exponential decay with a time constant of 12.5 ps is observed, corresponding to photo-thermal effect via electron-lattice thermalization process. (b) Fluence dependence of the decay constant.

A marked decrease in diffraction intensities following photoexcitation is observed within an approximate timescale of ~ 10 ps, as illustrated in Fig. 7.5(a). This duration aligns with the typical manifestation timeframe for photo-thermal effects. Fig. 7.5(b) presents the decay constants of changes in the 100 and 110 diffraction patterns as a function of incident fluence. Notably, the decay time appears to accelerate in the multi-photon absorption regime. The decay constants in the single-photon and multi-photon absorption regimes are quantified as 13 ± 2 and 8 ± 2 ps, respectively. Such a change is likely attributable to increased phonon-phonon scattering under conditions of dense electronic excitation. [256] With an increase in absorbed fluence, particularly in the multi-photon absorption regime near the ablation threshold in this study, an elevation in lattice temperature is anticipated due to electron-phonon scattering. Subsequently, this increase in lattice temperature enhances phonon-phonon scattering, leading to a quicker lattice thermalization. As a result, the decay time of diffraction intensity is

observed to quicken with an increase in incident fluence.

In the air experiment, as depicted in Fig. 7.2, the $2H - MoTe_2$ sample underwent ablation at an incident fluence of approximately 15 mJ/cm^2. In contrast, under vacuum conditions, the sample exhibited greater robustness, showing damage only above a fluence of 20 mJ/cm^2 and complete ablation at 30 mJ/cm^2). This difference suggests that surface oxidation-assisted photoexcitation or the emergence of air plasma under high electric fields might induce surface damage in air experiments, lowering the damage threshold. The peripheral region of the photo-induced damage was examined using TEM. Notably, the TEM image of this region under vacuum conditions revealed a marble-like structure. The diffraction pattern obtained from this marble structure, which resembles polycrystalline tellurium, suggests that extreme near-UV photoexcitation leads to tellurium segregation. This segregation implies that laser ablation may occur when the segregated tellurium serves as an absorption center.

7.5 Transient Reflection Measurements

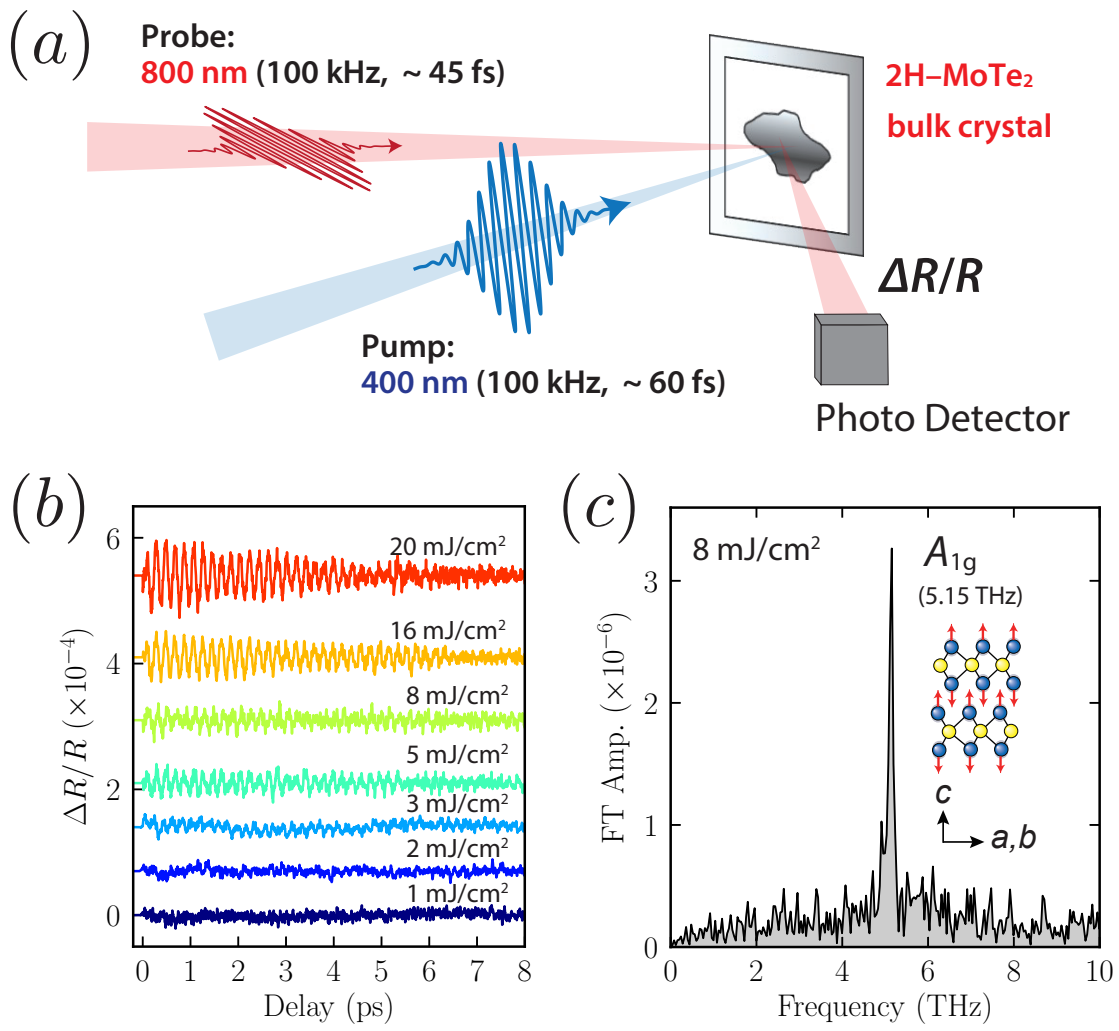

Figure 7.6: (a) Schematic configuration of transient reflectivity measurement. The 400 nm (3.1 eV) and 800 nm (1.55 eV) light were used for the pump and probe light, respectively. (b) Fluence dependent coherent phonon signals extracted from reflectivity changes ($\Delta R/R$). (c) A FT spectrum of a coherent phonon signal for $F = 8$ mJ/cm^2. The inset displays the lattice vibration motion of the A_{1g} mode.

Ultrafast time-resolved electron diffraction effectively measures thermal atomic motions within the ab-plane of $2H - MoTe_2$. However, a complementary method is required to fully understand atomic motions along the c-axis. We addressed this by focusing

on the coherent phonon dynamics of the out-of-plane A_{1g} lattice vibration mode in $2H - MoTe_2$, as measured by transient reflectivity measurements (Fig. 7.6(a)), following the discussion in the previous Chapter 6. Coherent phonon signals at various excitation levels, illustrated in Fig. 7.6(b), were extracted from the observed reflectivity changes ($\Delta R/R$) after electronic background subtraction. The oscillation at a frequency of ~ 5.1 THz corresponds to the A_{1g} phonon mode of $2H - MoTe_2$, as confirmed by the Fourier Transform (FT) spectrum in Fig. 7.6(c).[134, 149] The generation of observed coherent phonons can be described by models such as displacive excitation of coherent phonons (DECP) or resonant impulsive stimulated Raman scattering (ISRS). [65, 68] According to these models, electronic excitation by an ultrashort pulse results in displaced quasi-equilibrium atomic coordination, thereby generating fully symmetric A_{1g} coherent lattice vibrations. It is noteworthy that the 400 nm (3.1 eV) pump used in this study significantly exceeds the direct A-gap energy of (~ 1.0 eV), potentially leading to electronic excitation from valence to conduction bands. Should structural phase transitions or lattice symmetry changes occur upon photoexcitation, these would alter the frequency spectra of coherent phonons. [114, 173] However, no additional coherent phonon modes were observed beyond the A_{1g} mode after photoexcitation, even under incident fluences up to 30 mJ/cm^2. This suggests that no significant structural phase transitions or lattice symmetry changes toward other phases occurred under these conditions. Notably, the surface damage and tellurium segregation reported in a previous study were not evident in the present $\Delta R/R$ signals approaching 30 mJ/cm^2 irradiation. [134] This can be attributed to the greater robustness of the bulk sample compared to the ultrathin sample used in ultrafast electron diffraction measurements.

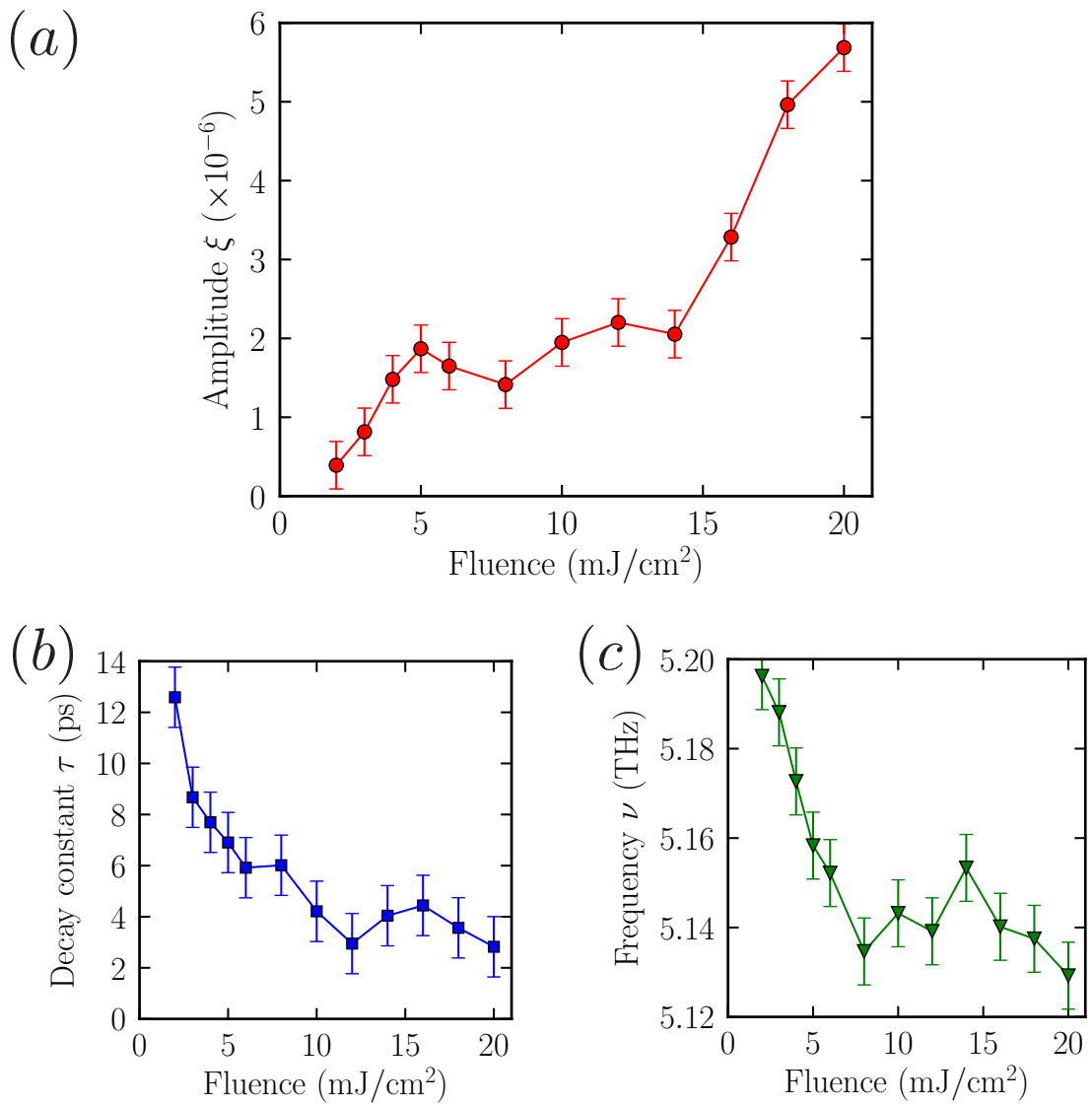

Figure 7.7: Parameters derived from the time-domain fitting employing a damped harmonic oscillation include: (a) the amplitude, (b) the frequency, and (c) the dephasing time constant of coherent oscillation.

We performed time-domain fitting of coherent phonons using a simple damped harmonic oscillation function:

$$y(t) = \theta(t - \tau_r) \cdot \xi \exp\left(\frac{t - \tau_r}{\tau}\right) \cos(2\pi\nu t + \varphi), \tag{7.1}$$

where $\theta(t)$ is a step-like error function:

$$\theta(t) = \frac{\text{erf}\left(\frac{t}{\tau_s}\right) + 1}{2}, \tag{7.2}$$

The dependency of the A_{1g} coherent phonon amplitude on the incident fluence is concisely summarized in Fig. 7.7(a). We observed that the amplitude increases linearly for incident fluences below 4 mJ/cm^2, reaches a plateau between 4 and 15 mJ/cm^2, and then rises again for fluences exceeding 15 mJ/cm^2. This trend, as shown in Fig. 7.7(a), reproduces the observations in Fig. 7.4(c) from ultrafast time-resolved electron diffraction measurements. According to the DECP model [65], the amplitude of the observed coherent phonon is expected to increase linearly with the density of photoexcited electrons (See Eq. (3.21)). Hence, the plateau observed in the coherent phonon amplitude alongside the increasing incident pump fluence implies a saturation in electronic excitation. Specifically, in our study, the phonon amplitude was proportional to the incident pump fluence at relatively low excitations. However, it became constant for fluence exceeding approximately 0.4 % excitation of the valence electrons, indicative of saturable absorption. At exceedingly high excitation levels, multi-photon absorption may become predominant, increasing phonon amplitude with higher incident fluence.

Figures 7.7(b) and (c) illustrate the fluence dependence of the decay constant τ and the A_{1g} frequency ν, as determined from time-domain fitting. Both parameters exhibit a similar linear decrease up to 5 $\sim$ 10 mJ/cm^2 and then enter a saturation phase beyond 5 mJ/cm^2. The decrease in τ suggests the presence of electron-phonon scattering depending on the absorbed density.[69] Conversely, the redshift in ν is attributable to a softening of the crystal bonds due to increased photoexcited carrier density [117] or the influence of anharmonic lattice potential.[70] Such saturation behaviors in τ and ν under high-density excitation regimes have been commonly observed in semimetals like Bi under near-damage threshold photoexcitation conditions.[69] The exact physical mechanism behind this nonlinear behavior remains unclear at this point. We hypothesize

that saturable absorption could suppress changes in τ and ν under high-density excitation scenarios. Further investigation into this phenomenon, possibly through studies on other materials, is essential for future clarification.

7.6 Discussions

As observed through ultrafast transient reflection measurements, the fluence dependence of the coherent phonon vibration along the c-axis aligns with the thermal vibration within the ab-plane revealed by ultrafast time-resolved electron diffraction measurements. Ultrafast time-resolved electron diffraction elucidates the isotropic heating (vibration), while transient reflection measurements highlight the non-thermal coherent A_{1g} lattice vibration. This heat generation stems from enhanced electron-phonon and phonon-phonon scatterings instigated by electronic excitation. Conversely, the electronic excitation induces the coherent lattice vibration. The underlying physics inferred from these two sets of observations suggests a linear correlation between the degree of electronic excitation and the induction of these vibrational effects, consistent with absorption effects. The occurrence of saturable absorption at an incident pump fluence of approximately 4 mJ/cm^2 (corresponding to $\sim$ 0.4% electronic excitation), coupled with sample damage in the high fluence regime, indicates the challenges in achieving electronic excitation of a significant proportion of valence electrons solely through photoexcitation with an ultrashort pulsed laser. Such extensive excitation is necessary for the 2H-to-1T' phase transition, as suggested by theoretical calculations. [49, 50, 51, 52] Additional strategies are required to realize the structural phase transition further. These include the preparation of a sample encapsulated by hexagonal boron nitride (h-BN)[257], employing terahertz (THz) pulses, and implementing single-shot measurement techniques.[258]

7.7 Conclusions

In this study, we conducted a comprehensive investigation of the light-induced structural dynamics of $2H - MoTe_2$ under various excitation levels, employing a wavelength of 400 nm, using ultrafast time-resolved electron diffraction and transient reflection measurements. Our findings reveal a consistent relationship between the fluence dependences of the vibration observed by both methods regarding absorption effects. Notably, the amplitudes of non-thermal or fully thermalized phonons are found to be linearly correlated with the input photoenergy at relatively low incident fluences, reaching up to $3 \sim 4$ mJ/cm^2. Above an excitation level of approximately 0.4% of the valence electrons (4 mJ/cm^2), the amplitude becomes constant, indicating the onset of the saturable absorption effect. At extremely high excitation levels (above 15 mJ/cm^2), an increase in the amplitude of the phonon was observed, which may be attributed to multi-photon absorption. Furthermore, we note that photoexcitation at very high fluences ($\sim$ 30 mJ/cm^2) results in permanent damage to the sample due to tellurium segregation.

Throughout our experiments, we did not observe an structural phase transition from the 2H phase to different phases, such as $2H^*$ and 1T' phases. This suggests that further investigations under varied photoexcitation conditions (wavelength or pulse duration) and thermal management strategies is required to truly realize the structural phase transitions. Characterizations of ultrafast localized electronic and structural dynamics, such as time-resolved scanning tunneling microscopy [259, 236], would be effective for a deeper understanding for the mechanism of the structural deformations in transition-metal dichalcogenide (TMD) materials. The insights gained from this study are expected to be crucial in advancing the applicability and understanding of the fundamental optical properties of photodevices based on TMD materials.

Instead of the expected structural phase transitions in the $2H - MoTe_2$, this study clearly shows that the coherent and incoherent(thermal) phonon responses linearly depend on the excited carrier density in the range from linear absorption regime to

nonlinear absorption regime, such as saturable absorption and multiphoton absorption. This suggests that information on the excited carrier density can be extracted by evaluating phonon behaviors. Extending this idea, we also conducted ultrafast electron diffraction measurements with double-optical-pulse excitation under a saturable absorption regime.[192] This technique visualizes relaxation dynamics of saturable absorption (Pauli-block) effects as a consequence of electronic momentum scattering in the conduction band, whose decay constant was estimated to be around 120 fs close to the pulse width used. In the future work, semiconductor TMDs are expected to be utilized as an atomically-thin saturable absorber in pulsed laser oscillator and a model system to explore nonlinear physics and the momentum scattering phenomena under high-density excitation regime by advanced instruments, such as tr-ARPES.

7.8 Supplementary

7.8.1 Calculation of Debye-Waller Factor

The temperature increase of the sample is estimated with the incident fluence, absorptivity, specific heat, and density. The absorptivity of a 40-nm-thick $MoTe_2$ is estimated to be 50.8 %. [18] The specific heat and density of $MoTe_2$ are 0.218 $J/g \cdot K$ and 7.78 g/cm^3, respectively.[260] Thus, the temperature increase with the incident fluence of $3-4$ mJ/cm^2 is estimated to be 220–300 K. The Debye–Waller factor can be expressed as a function of the mean square displacement (U_j) as follows:

$$D_j(\boldsymbol{K}) = \exp(-8\pi^2|\boldsymbol{K}|^2 U_j) \tag{7.3}$$

The isotropic thermal displacement (U) can be calculated using the coefficient of linear contraction (ρ), which is derived from the bulk modulus [261], and the atomic distance ($d_A = 2.68$Å) with the following equation [262]:

$$U = \frac{k_B T}{d_A \rho} \tag{7.4}$$

where k_B and T are the Boltzmann constant and lattice temperature, respectively. Taking into account the room temperature of $\sim$ 300 K, the temperature rise of approximately 220–300 K corresponded to decreases in the electron diffraction intensity of 4–5 % and 10–13 % of their original values for the {100} and {110} reflections.

7.8.2 Electron Diffraction Images toward Laser Ablation

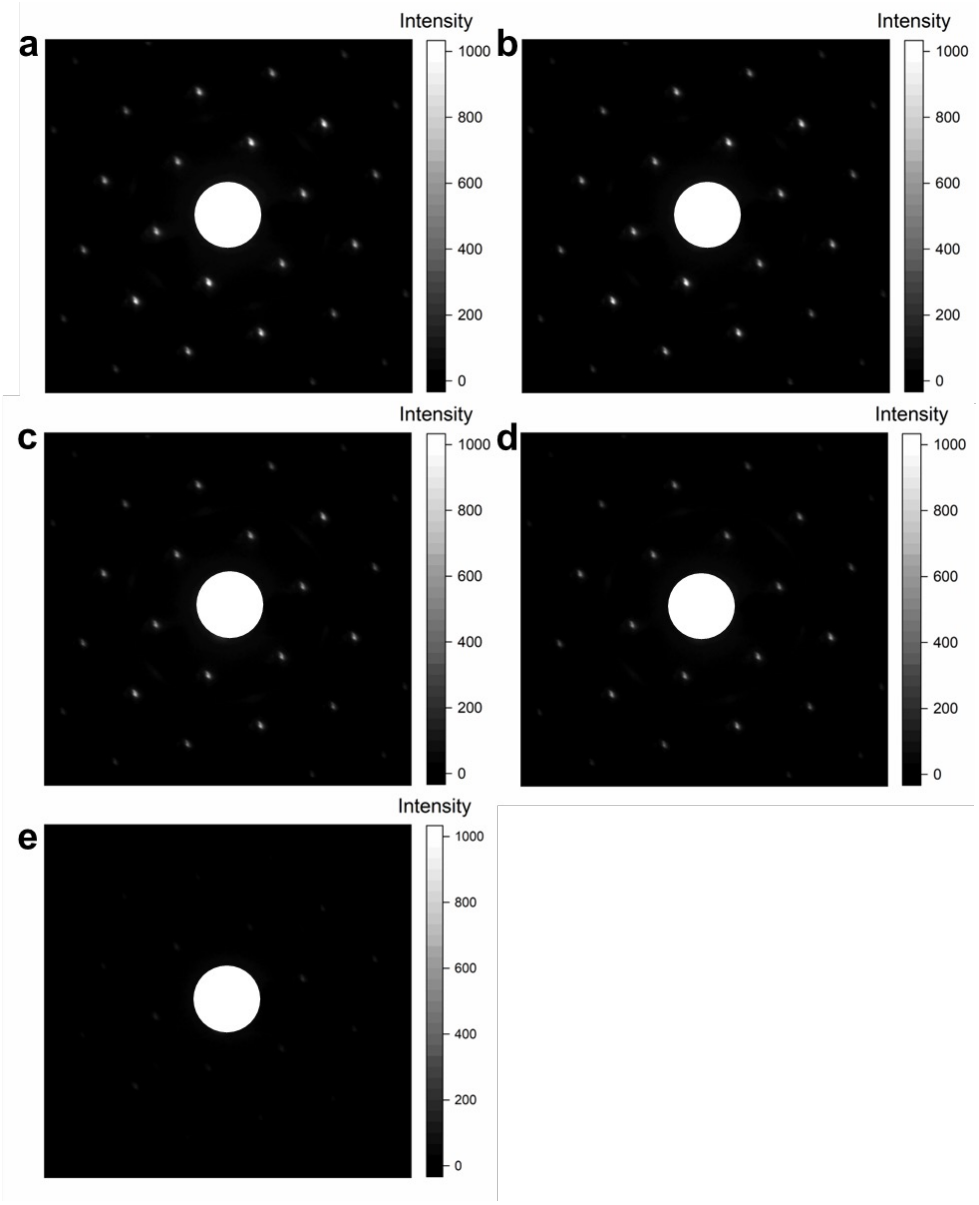

Figure 7.8: Electron diffraction pattern from the $2H - MoTe_2$ sample after 1000-shot-laser irradiation at (a) 20, (b) 24, (c) 26, (d) 28, and (e) 30 mJ/cm^2. The sample was gradually damaged above an intensity of 20 mJ/cm^2, and it was completely ablated at 30 mJ/cm^2.

7.8.3 Characterization of Damage Region

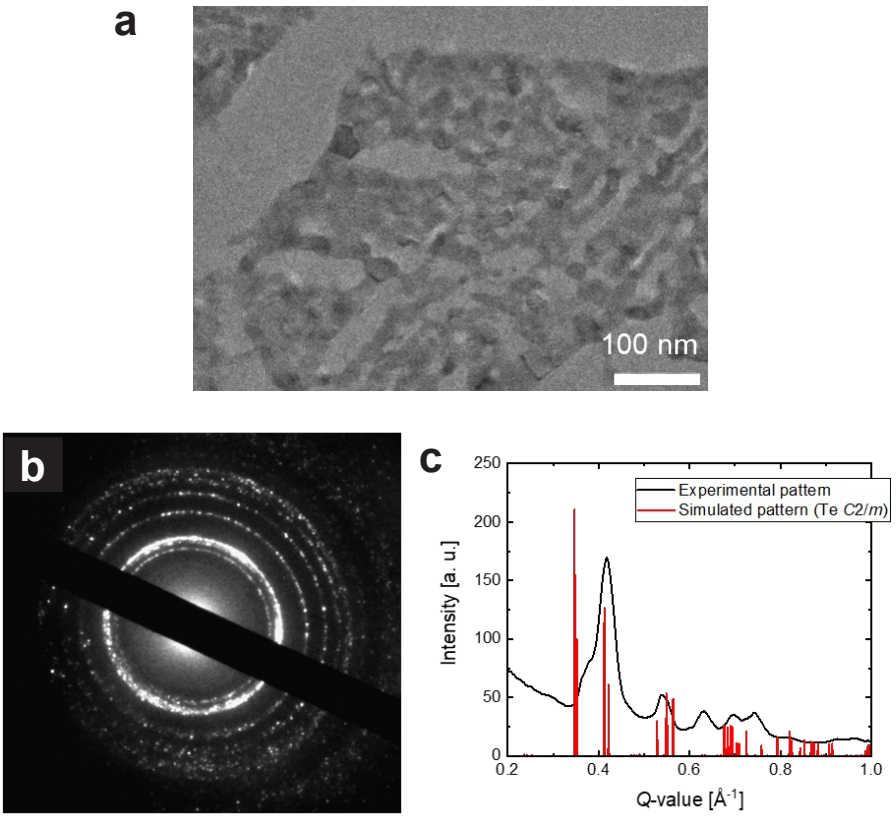

Figure 7.9: (a)Transmission electron microscopy image of the peripheral region of photo-induced damage. The experiment was performed using JEM-2100 (JEOL Ltd.) at an electron acceleration voltage of 200 kV. (b) Electron diffraction image obtained from the region shown in Fig. 7.8. (c) Comparison of the experimental diffraction pattern and the simulated pattern from the tellurium polycrystal in the space group of *C2/m* (No. 12).[263]

Chapter 8

Summary and Future Outlook

8.1 Summary and Conclusion

This dissertation explores the impact of various degrees of freedom within the phonon system, such as structural changes and electron-phonon interactions, on the formation of non-equilibrium physical states in the photoexcited state of a polymorphic layered $MoTe_2$. These studies that presented here shed new light on the ultrafast optoelectronic phenomena of TMDs and highlight the significance of electron-lattice interactions, a topic that has been largely overlooked. These findings pave the way for future exploration of novel non-equilibrium states driven by electron-lattice interactions and for manipulating material properties through coherent phonons.

In Chapter 4, the study reveals that no structural phase transition between the 2H- and 1T'-$MoTe_2$ phases was observed in the damaged region following light irradiation above the damage threshold. Instead, tellurium segregation was detected, coinciding with the presence of 3.6-THz coherent phonon oscillation in the time-domain signal. It was also determined that the repetition rates and photon energy influence the damage threshold of the incident pump fluence.

In Chapter 5, the study observed a low-frequency coherent shear phonon mode, with

a frequency of 0.39 THz, in 1T'$-MoTe_2$ bulk crystal under ambient conditions. This mode is Raman "Inactive" in the 1T' phase but becomes Raman "Active" in the T_d phase. The findings suggest that photoexcited carriers, followed by displacively forced interlayer shear motion, transiently stabilize an intermediate state between the 1T' and T_d phases.

In Chapter 6, the research demonstrates the observation of an extremely long-lived coherent A_{1g} phonon in the layered semiconductor $2H - MoTe_2$. The study utilized fluence- and wavelength-dependent reflectivity change measurements to detect characteristic modifications in the $\Delta R/R$ spectra during early time delays (< 2 ps). These ultrafast optical modulations are attributed to coherent quasiparticle states induced by electron-hole and electron-phonon interactions in the presence of electron-hole plasmas and the generation of overtones, sum, and difference frequencies of the A_{1g} and $E_{2g}^{(2)}$ phonons.

In Chapter 7, complementary time-resolved methods, coherent phonon spectroscopy, and ultrafast electron diffraction measurement were performed for evaluating structural dynamics of $2H - MoTe_2$ under 400-nm photoexcitation and high-density excitation density ($1 \sim 30$ mJ/cm^2) below the damage threshold. Consequently, from both measurements, we found a saturable absorption effect by which the lattice is irresponsible from ~ 4 mJ/cm^2 (~ 0.4 % electronic excitation) due to the system incapable of absorbing photons. This fact indicates that it is quite challenging to realize the structural phase transition from the 2H phase into a transient 2H* phase or the 1T' phase by simple optical excitation, which requires several percent of electronic excitation predicted by theoretical studies.

Finally, this dissertation provides comprehensive experimental insights into the influence of electronic excitation on both transient and permanent structural changes in $MoTe_2$ polymorphs and, in turn, examines how characteristic long-lived coherent phonons alter the electronic and optical properties of the two-dimensional materials under various femtosecond-laser conditions, such as wavelength, repetition rate, pulse width, and excitation density, using complementary time-domain measurement

methods. Although the expected structural phase transition from semiconductor to semimetal in $MoTe_2$ was not achieved, this work represents a pioneering effort in understanding the long-lived optical phonon properties of $MoTe_2$, as well as other TMD compounds. Consequently, this dissertation contributes to a universal physical understanding of phonon responses during saturable absorption under high-density photoexcitation and phonon-driven non-equilibrium states.

8.2 Future Outlook

8.2.1 Light-Induced Manipulation of Structural Polymorphism

I have been studying structural phase transition in $MoTe_2$, and unfortunately, I could not achieve the desired photo-induced transition from the 2H to the 1T' phase. However, recent studies have suggested that using hBN-encapsulated $2H - MoTe_2$ samples could facilitate such transitions.[257] To achieve this, careful sample design is necessary to reduce surface oxidation and prevent the evaporation of Te. Anisotropic atomic movement on a two-dimensional plane is also required to achieve the desired result. For this, excitation by the polarized electric field along the in-plane atomic direction in the wavelength range from THz to the mid-infrared light is essential. A recent study has also suggested that electric-field enhancement is effective through patterning gold antenna structures around the sample periphery.[258] Despite the ongoing exploration of the semiconductor-to-semimetal phase transition in $MoTe_2$, I believe that significant progress will soon be made.

8.2.2 Exploration of Phonon-Driven Non-Equilibrium State

Further research is essential to advancing our understanding of non-equilibrium states caused by coherent optical phonon fields. During my doctoral studies, I focused on the relationship between coherent phonons and electronic states and how they affect optical constants. This connection has given rise to new non-equilibrium quasiparti-

cle states, such as valley-selective phonoritons that emerge from interactions among valleys, photons, excitons, and phonons in TMDs. The energy dispersion relations of these quasiparticles can be revealed through time-resolved angle-resolved photoelectron spectroscopy (ARPES) with high energy resolution.[264] Investigating how coherent phonons can alter material properties at a fundamental level is crucial for developing future device applications that utilize coherent phonons, such as phononic modulators.

8.2.3 Development of THz Optoelectronics using Ultrafast Phenomena

In device technology, utilizing ultrafast physical phenomena is a significant challenge for the future. Since the 1980s, researchers have been exploring the ultrafast dynamics of electrons, lattices, and quasiparticles in the femtosecond time domain. However, this research has primarily remained within the realm of fundamental research for approximately 40 years. However, to support the advancements of our rapidly evolving information society, it is essential to harness these ultrafast phenomena for THz frequency-driven optical devices. Recently, researchers have developed techniques for sampling and detecting photo-induced current pulses generated on-chip with picosecond time resolution.[265, 266, 267, 268, 269, 270] Notably, light-induced anomalous Hall currents, triggered by driven Floquet topological states, have been observed in on-chip graphene devices.[269] Investigating how non-equilibrium states of materials, including coherent phonons, contribute to current generation and electron transport under photoexcitation is expected to be directly relevant to developing future device applications operating at THz frequencies.

References

[1] Einstein, A. (1917) Zur quantentheorie der strahlung. Phys. Zeit. **18**, 121.

[2] Schawlow, A. L & Townes, C. H. (1958) Infrared and Optical Masers. Phys. Rev. **112**, 1940–1949.

[3] Sanders, J. H. (1959) Optical Maser Design. Phys. Rev. Lett. **3**, 86–87.

[4] Maiman, T. H. (1960) Stimulated Optical Radiation in Ruby. Nature **187**, 493–494.

[5] Fork, R. L, Brito Cruz, C. H, Becker, P. C, & Shank, C. V. (1987) Compression of optical pulses to six femtoseconds by using cubic phase compensation. Opt. Lett. **12**, 483–485.

[6] Strickland, D & Mourou, G. (1985) Compression of amplified chirped optical pulses. Opt. Commun. **55**, 447–449.

[7] Paul, P. M, Toma, E. S, Breger, P, Mullot, G, Augé, F, Balcou, P, Muller, H. G, & Agostini, P. (2001) Observation of a train of attosecond pulses from high harmonic generation. Science **292**, 1689–1692.

[8] Hentschel, M, Kienberger, R, Spielmann, C, Reider, G. A, Milosevic, N, Brabec, T, Corkum, P, Heinzmann, U, Drescher, M, & Krausz, F. (2001) Attosecond metrology. Nature **414**, 509–513.

[9] Salcedo, J. R, Siegman, A. E, Dlott, D. D, & Fayer, M. D. (1978) Dynamics of Energy Transport in Molecular Crystals: The Picosecond Transient-Grating Method. Phys. Rev. Lett. **41**, 131–134.

[10] Nelson, K, Dlott, D, & Fayer, M. (1979) Excited state dynamics in pure molecular crystals: perylene and the excimer problem. Chem. Phys. Lett. **64**, 88–93.

[11] Zewail, A. H. (2000) Femtochemistry: Atomic-Scale Dynamics of the Chemical Bond. J. Phys. Chem. A **104**, 5660–5694.

[12] Novoselov, K. S, Geim, A. K, Morozov, S. V, Jiang, D, Zhang, Y, Dubonos, S. V, Grigorieva, I. V, & Firsov, A. A. (2004) Electric field effect in atomically thin carbon films. Science **306**, 666–669.

[13] Novoselov, K. S, Geim, A. K, Morozov, S, Jiang, D, Katsnelson, M, Grigorieva, I, Dubonos, S, & Firsov, A. A. (2005) Two-dimensional gas of massless dirac fermions in graphene. Nature **438**, 197.

[14] Geim, A. K. (2009) Graphene: status and prospects. Science **324**, 1530–1534.

[15] Cao, Y, Fatemi, V, Fang, S, Watanabe, K, Taniguchi, T, Kaxiras, E, & Jarillo-Herrero, P. (2018) Unconventional superconductivity in magic-angle graphene superlattices. Nature **556**, 43–50.

[16] Wang, Q. H, Kalantar-Zadeh, K, Kis, A, Coleman, J. N, & Strano, M. S. (2012) Electronics and optoelectronics of two-dimensional transition metal dichalcogenides. Nat. Nanotechnol. **7**, 699.

[17] Wilson, J & Yoffe, A. (1969) The transition metal dichalcogenides discussion and interpretation of the observed optical, electrical and structural properties. Adv. Phys. **18**, 193–335.

[18] Beal, A. R & Hughes, H. P. (1979) Kramers-Kronig analysis of the reflectivity spectra of $2H - MoS_2$, $2H - MoSe_2$ and $2H - MoTe_2$. J. Phys. C: Solid State Phys. **12**, 881.

[19] Sugai, S, Murase, K, Uchida, S, & Tanaka, S. (1980) Raman studies of lattice dynamics in $1T - TiSe_2$. Solid State Commun. **35**, 433–436.

[20] Wieting, T, Grisel, A, & Lévy, F. (1980) Interlayer bonding and localized charge in $MoSe_2$ and $\alpha - MoTe_2$. Physica B+C **99**, 337–342.

[21] Sugai, S & Ueda, T. (1982) High-pressure Raman spectroscopy in the layered materials $2H - MoS_2$, $2H - MoSe_2$, and $2H - MoTe_2$. Phys. Rev. B **26**, 6554–6558.

[22] Mak, K. F, Lee, C, Hone, J, Shan, J, & Heinz, T. F. (2010) Atomically Thin MoS_2: A New Direct-Gap Semiconductor. Phys. Rev. Lett. **105**, 136805.

[23] Xiao, D, Liu, G.-B, Feng, W, Xu, X, & Yao, W. (2012) Coupled Spin and Valley Physics in Monolayers of MoS_2 and Other Group-VI Dichalcogenides. Phys. Rev. Lett. **108**, 196802.

[24] Mak, K. F, He, K, Shan, J, & Heinz, T. F. (2012) Control of valley polarization in monolayer MoS_2 by optical helicity. Nat. Nanotechnol. **7**, 494–498.

[25] Mak, K. F & Shan, J. (2016) Photonics and optoelectronics of 2D semiconductor transition metal dichalcogenides. Nat. Photonics **10**, 216–226.

[26] Chernikov, A, Berkelbach, T. C, Hill, H. M, Rigosi, A, Li, Y, Aslan, B, Reichman, D. R, Hybertsen, M. S, & Heinz, T. F. (2014) Exciton Binding Energy and Nonhydrogenic Rydberg Series in Monolayer WS_2. Phys. Rev. Lett. **113**, 076802.

[27] He, K, Kumar, N, Zhao, L, Wang, Z, Mak, K. F, Zhao, H, & Shan, J. (2014) Tightly Bound Excitons in Monolayer WSe_2. Phys. Rev. Lett. **113**, 026803.

[28] Cho, S, Kim, S, Kim, J. H, Zhao, J, Seok, J, Keum, D. H, Baik, J, Choe, D.-H, Chang, K. J, Suenaga, K, Kim, S. W, Lee, Y. H, & Yang, H. (2015) Phase patterning for ohmic homojunction contact in $MoTe_2$. Science **349**, 625–628.

[29] Song, S, Keum, D. H, Cho, S, Perello, D, Kim, Y, & Lee, Y. H. (2016) Room Temperature Semiconductor–Metal Transition of $MoTe_2$ Thin Films Engineered by Strain. Nano Lett. **16**, 188–193.

[30] Wang, Y, Xiao, J, Zhu, H, Li, Y, Alsaid, Y, Fong, K. Y, Zhou, Y, Wang, S, Shi, W, Wang, Y, et al. (2017) Structural phase transition in monolayer $MoTe_2$ driven by electrostatic doping. Nature **550**, 487–491.

[31] Zhang, F, Zhang, H, Krylyuk, S, Milligan, C. A, Zhu, Y, Zemlyanov, D. Y, Bendersky, L. A, Burton, B. P, Davydov, A. V, & Appenzeller, J. (2019) Electric-field induced structural transition in vertical $MoTe_2$- and $Mo_{1-x}W_xTe_2$-based resistive memories. Nat. Mater. **18**, 55–61.

[32] Soluyanov, A. A, Gresch, D, Wang, Z, Wu, Q, Troyer, M, Dai, X, & Bernevig, B. A. (2015) Type-II Weyl semimetals. Nature **527**, 495.

[33] Sun, Y, Wu, S.-C, Ali, M. N, Felser, C, & Yan, B. (2015) Prediction of Weyl semimetal in orthorhombic $MoTe_2$. Phys. Rev. B **92**, 161107.

[34] Huang, L, McCormick, T. M, Ochi, M, Zhao, Z, Suzuki, M.-T, Arita, R, Wu, Y, Mou, D, Cao, H, Yan, J, Trivedi, N, & Kaminski, A. (2016) Spectroscopic evidence for a type II Weyl semimetallic state in $MoTe_2$. Nat. Mater. **15**, 1155.

[35] Deng, K, Wan, G, Deng, P, Zhang, K, Ding, S, Wang, E, Yan, M, Huang, H, Zhang, H, Xu, Z, Denlinger, J, Fedorov, A, Yang, H, Duan, W, Yao, H, Wu, Y, Fan, S, Zhang, H, Chen, X, & Zhou, S. (2016) Experimental observation of topological fermi arcs in type-II Weyl semimetal $MoTe_2$. Nat. Phys. **12**, 1105.

[36] Sie, E. J, McIver, J. W, Lee, Y.-H, Fu, L, Kong, J, & Gedik, N. (2015) Valley-selective optical Stark effect in monolayer WS_2. Nat. Mater. **14**, 290–294.

[37] Sie, E. J, Frenzel, A. J, Lee, Y.-H, Kong, J, & Gedik, N. (2015) Intervalley biexcitons and many-body effects in monolayer MoS_2. Phys. Rev. B **92**, 125417.

[38] Sie, E. J, Lui, C. H, Lee, Y.-H, Kong, J, & Gedik, N. (2016) Observation of intervalley biexcitonic optical Stark effect in monolayer WS_2. Nano Lett. **16**, 7421–7426.

[39] Sie, E. J, Lui, C. H, Lee, Y.-H, Fu, L, Kong, J, & Gedik, N. (2017) Large, valley-exclusive bloch-siegert shift in monolayer WS_2. Science **355**, 1066–1069.

[40] Arora, A, Drüppel, M, Schmidt, R, Deilmann, T, Schneider, R, Molas, M. R, Marauhn, P, Michaelis de Vasconcellos, S, Potemski, M, Rohlfing, M, & Bratschitsch, R. (2017) Interlayer excitons in a bulk van der Waals semiconductor. Nat. Commun. **8**, 1–6.

[41] Kunstmann, J, Mooshammer, F, Nagler, P, Chaves, A, Stein, F, Paradiso, N, Plechinger, G, Strunk, C, Schüller, C, Seifert, G, Reichman, D. R, & Korn, T. (2018) Momentum-space indirect interlayer excitons in transition-metal dichalcogenide van der Waals heterostructures. Nat. Phys. **14**, 801–805.

[42] Merkl, P, Mooshammer, F, Steinleitner, P, Girnghuber, A, Lin, K.-Q, Nagler, P, Holler, J, Schüller, C, Lupton, J. M, Korn, T, Ovesen, S, Brem, S, Malic, E, & Huber, R. (2019) Ultrafast transition between exciton phases in van der Waals heterostructures. Nat. Mater. **18**, 691–696.

[43] Wallauer, R, Perea-Causin, R, Münster, L, Zajusch, S, Brem, S, Güdde, J, Tanimura, K, Lin, K.-Q, Huber, R, Malic, E, & Höfer, U. (2021) Momentum-Resolved Observation of Exciton Formation Dynamics in Monolayer WS_2. Nano Lett. **21**, 5867–5873.

[44] Madéo, J, Man, M. K. L, Sahoo, C, Campbell, M, Pareek, V, Wong, E. L, Al-Mahboob, A, Chan, N. S, Karmakar, A, Mariserla, B. M. K, Li, X, Heinz, T. F, Cao, T, & Dani, K. M. (2020) Directly visualizing the momentum-forbidden dark excitons and their dynamics in atomically thin semiconductors. Science **370**, 1199–1204.

[45] Schmitt, D, Bange, J. P, Bennecke, W, AlMutairi, A, Meneghini, G, Watanabe, K, Taniguchi, T, Steil, D, Luke, D. R, Weitz, R. T, Steil, S, Jansen, G. S. M, Brem, S, Malic, E, Hofmann, S, Reutzel, M, & Mathias, S. (2022) Formation of moiré interlayer excitons in space and time. Nature **608**, 499–503.

[46] Karni, O, Barré, E, Pareek, V, Georgaras, J. D, Man, M. K. L, Sahoo, C, Bacon, D. R, Zhu, X, Ribeiro, H. B, O'Beirne, A. L, Hu, J, Al-Mahboob, A, Abdelrasoul, M. M. M, Chan, N. S, Karmakar, A, Winchester, A. J, Kim, B, Watanabe, K, Taniguchi, T, Barmak, K, Madéo, J, Da Jornada, F. H, Heinz, T. F, & Dani, K. M. (2022) Structure of the moiré exciton captured by imaging its electron and hole. Nature **603**, 247–252.

[47] Chernikov, A, Ruppert, C, Hill, H. M, Rigosi, A. F, & Heinz, T. F. (2015) Population inversion and giant bandgap renormalization in atomically thin WS_2 layers. Nat. Photonics **9**, 466–470.

[48] Pogna, E. A. A, Marsili, M, De Fazio, D, Dal Conte, S, Manzoni, C, Sangalli, D, Yoon, D, Lombardo, A, Ferrari, A. C, Marini, A, Cerullo, G, & Prezzi, D. (2016) Photo-Induced Bandgap Renormalization Governs the Ultrafast Response of Single-Layer MoS_2. ACS Nano **10**, 1182–1188.

[49] Kolobov, A. V, Fons, P, & Tominaga, J. (2016) Electronic excitation-induced semiconductor-to-metal transition in monolayer $MoTe_2$. Phys. Rev. B. **94**, 094114.

[50] Krishnamoorthy, A, Bassman, L, Kalia, R. K, Nakano, A, Shimojo, F, & Vashishta, P. (2018) Semiconductor–metal structural phase transformation in $MoTe_2$ monolayers by electronic excitation. Nanoscale **10**, 2742–2747.

[51] Peng, B, Zhang, H, Chen, W, Hou, B, Qiu, Z.-J, Shao, H, Zhu, H, Monserrat, B, Fu, D, Weng, H, & Soukoulis, C. M. (2020) Sub-picosecond photo-induced displacive phase transition in two-dimensional $MoTe_2$. npj 2D Mater. Appl. **4**, 14.

[52] Guan, M.-X, Liu, X.-B, Chen, D.-Q, Li, X.-Y, Qi, Y.-P, Yang, Q, You, P.-W, & Meng, S. (2022) Optical Control of Multistage Phase Transition via Phonon Coupling in $MoTe_2$. Phys. Rev. Lett. **128**, 015702.

[53] Sie, E. J, Nyby, C. M, Pemmaraju, C. D, Park, S. J, Shen, X, Yang, J, Hoffmann, M. C, Ofori-Okai, B. K, Li, R, Reid, A. H, Weathersby, S, Mannebach, E, Finney, N, Rhodes, D, Chanet, D, Antony, A, Balicas, L, Hone, J, Devereaux, T. P, Heinz, T. F, Wang, X, & Lindenberg, A. M. (2019) An ultrafast symmetry switch in a Weyl semimetal. Nature **565**, 61.

[54] Zhang, M. Y, Wang, Z. X, Li, Y. N, Shi, L. Y, Wu, D, Lin, T, Zhang, S. J, Liu, Y. Q, Liu, Q. M, Wang, J, Dong, T, & Wang, N. L. (2019) Light-Induced Subpicosecond Lattice Symmetry Switch in $MoTe_2$. Phys. Rev. X **9**, 021036.

[55] Bron, W. E, Kuhl, J, & Rhee, B. K. (1986) Picosecond-laser-induced transient dynamics of phonons in GaP and ZnSe. Phys. Rev. B **34**, 6961–6971.

[56] Nelson, K. A & Fayer, M. D. (1980) Laser induced phonons: A probe of intermolecular interactions in molecular solids. J. Chem. Phys. **72**, 5202–5218.

[57] Nelson, K. A, Lutz, D. R, Fayer, M. D, & Madison, L. (1981) Laser-induced phonon spectroscopy. Optical generation of ultrasonic waves and investigation of electronic excited-state interactions in solids. Phys. Rev. B **24**, 3261–3275.

[58] De Silvestri, S, Fujimoto, J, Ippen, E, Gamble Jr, E. B, Williams, L. R, & Nelson, K. A. (1985) Femtosecond time-resolved measurements of optic phonon dephasing by impulsive stimulated Raman scattering in α-perylene crystal from 20 to 300 K. Chem. Phys. Lett. **116**, 146–152.

[59] Yan, Y & Nelson, K. A. (1987) Impulsive stimulated light scattering. I. General theory. J. Chem. Phys. **87**, 6240–6256.

[60] Yan, Y & Nelson, K. A. (1987) Impulsive stimulated light scattering. II. Comparison to frequency-domain light-scattering spectroscopy. J. Chem. Phys. **87**, 6257–6265.

[61] Cho, G. C, Kütt, W, & Kurz, H. (1990) Subpicosecond time-resolved coherent-phonon oscillations in GaAs. Phys. Rev. Lett. **65**, 764–766.

[62] Pfeifer, T, Dekorsy, T, Kütt, W, & Kurz, H. (1992) Generation mechanism for coherent LO phonons in surface-space-charge fields of III-V-compounds. Appl. Phys. A **55**, 482–488.

[63] Dekorsy, T, Pfeifer, T, Kütt, W, & Kurz, H. (1993) Subpicosecond carrier transport in GaAs surface-space-charge fields. Phys. Rev. B **47**, 3842–3849.

[64] Cheng, T. K, Vidal, J, Zeiger, H. J, Dresselhaus, G, Dresselhaus, M. S, & Ippen, E. P. (1991) Mechanism for displacive excitation of coherent phonons in Sb, Bi, Te, and Ti_2O_3. Appl. Phys. Lett. **59**, 1923–1925.

[65] Zeiger, H. J, Vidal, J, Cheng, T. K, Ippen, E. P, Dresselhaus, G, & Dresselhaus, M. S. (1992) Theory for displacive excitation of coherent phonons. Phys. Rev. B **45**, 768.

[66] Kuznetsov, A. V & Stanton, C. J. (1994) Theory of Coherent Phonon Oscillations in Semiconductors. Phys. Rev. Lett. **73**, 3243–3246.

[67] Garrett, G, Albrecht, T, Whitaker, J, & Merlin, R. (1996) Coherent THz phonons driven by light pulses and the Sb problem: what is the mechanism? Phys. Rev. Lett. **77**, 3661.

[68] Stevens, T. E, Kuhl, J, & Merlin, R. (2002) Coherent phonon generation and the two stimulated Raman tensors. Phys. Rev. B **65**, 144304.

[69] DeCamp, M. F, Reis, D. A, Bucksbaum, P. H, & Merlin, R. (2001) Dynamics and coherent control of high-amplitude optical phonons in bismuth. Phys. Rev. B **64**, 092301.

[70] Hase, M, Kitajima, M, Nakashima, S.-i, & Mizoguchi, K. (2002) Dynamics of coherent anharmonic phonons in bismuth using high density photoexcitation. Phys. Rev. Lett. **88**, 067401.

[71] Fritz, D. M, Reis, D. A, Adams, B, Akre, R. A, Arthur, J, Blome, C, Bucksbaum, P. H, Cavalieri, A. L, Engemann, S, Fahy, S, Falcone, R. W, Fuoss, P. H, Gaffney, K. J, George, M. J, Hajdu, J, Hertlein, M. P, Hillyard, P. B, Horn-von Hoegen, M, Kammler, M, Kaspar, J, Kienberger, R, Krejcik, P, Lee, S. H, Lindenberg, A. M, McFarland, B, Meyer, D, Montagne, T, Murray, E. D, Nelson, A. J, Nicoul, M, Pahl, R, Rudati, J, Schlarb, H, Siddons, D. P, Sokolowski-Tinten, K, Tschentscher, T, Von Der Linde, D, & Hastings, J. B. (2007) Ultrafast Bond Softening in Bismuth: Mapping a Solid's Interatomic Potential with X-rays. Science **315**, 633–636.

[72] Hase, M, Miyamoto, Y, & Tominaga, J. (2009) Ultrafast dephasing of coherent optical phonons in atomically controlled $GeTe/Sb_2Te_3$ superlattices. Phys. Rev. B **79**, 174112.

[73] Lim, Y.-S, Yee, K.-J, Kim, J.-H, Haroz, E. H, Shaver, J, Kono, J, Doorn, S. K, Hauge, R. H, & Smalley, R. E. (2006) Coherent lattice vibrations in single-walled carbon nanotubes. Nano Lett. **6**, 2696–2700.

[74] Kato, K, Ishioka, K, Kitajima, M, Tang, J, Saito, R, & Petek, H. (2008) Coherent Phonon Anisotropy in Aligned Single-Walled Carbon Nanotubes. Nano Lett. **8**, 3102–3108.

[75] Makino, K, Hirano, A, Shiraki, K, Maeda, Y, & Hase, M. (2009) Ultrafast vibrational motion of carbon nanotubes in different pH environments. Phys. Rev. B **80**, 245428.

[76] Lüer, L, Gadermaier, C, Crochet, J, Hertel, T, Brida, D, & Lanzani, G. (2009) Coherent Phonon Dynamics in Semiconducting Carbon Nanotubes: A Quantitative Study of Electron-Phonon Coupling. Phys. Rev. Lett. **102**, 127401.

[77] Ishioka, K, Hase, M, Kitajima, M, Wirtz, L, Rubio, A, & Petek, H. (2008) Ultrafast electron-phonon decoupling in graphite. Phys. Rev. B **77**, 121402.

[78] Ishioka, K, Hase, M, Kitajima, M, & Petek, H. (2006) Coherent optical phonons in diamond. Applied Physics Letters **89**, 231916.

[79] Weiner, A. M, Leaird, D. E, Wiederrecht, G. P, & Nelson, K. A. (1990) Femtosecond Pulse Sequences Used for Optical Manipulation of Molecular Motion. Science **247**, 1317–1319.

[80] Hase, M, Mizoguchi, K, Harima, H, Nakashima, S, Tani, M, Sakai, K, & Hangyo, M. (1996) Optical control of coherent optical phonons in bismuth films. Appl. Phys. Lett. **69**, 2474–2476.

[81] Makino, K, Tominaga, J, & Hase, M. (2011) Ultrafast optical manipulation of atomic arrangements in chalcogenide alloy memory materials. Opt. Express **19**, 1260.

[82] Misochko, O. V, Ishioka, K, Hase, M, & Kitajima, M. (2006) Fully symmetric and doubly degenerate coherent phonons in semimetals at low temperature and high excitation: similarities and differences. J. Phys.: Condens. Matter **18**, 10571.

[83] Ishioka, K, Kitajima, M, & Misochko, O. V. (2008) Coherent a_{1g} and e_g phonons of antimony. J. Appl. Phys. **103**, 123505.

[84] Kuznetsov, A. V & Stanton, C. J. (1995) Coherent phonon oscillations in GaAs. Phys. Rev. B **51**, 7555–7565.

[85] Cho, G. C, Dekorsy, T, Bakker, H. J, Hövel, R, & Kurz, H. (1996) Generation and Relaxation of Coherent Majority Plasmons. Phys. Rev. Lett. **77**, 4062–4065.

[86] Vallée, F, Ganikhanov, F, & Bogani, F. (1997) Dephasing of LO-phonon–plasmon hybrid modes in n-type GaAs. Phys. Rev. B **56**, 13141.

[87] Hase, M, Nakashima, S.-i, Mizoguchi, K, Harima, H, & Sakai, K. (1999) Ultrafast decay of coherent plasmon-phonon coupled modes in highly doped GaAs. Phys. Rev. B **60**, 16526–16530.

[88] Hu, J, Misochko, O. V, Goto, A, & Nakamura, K. G. (2012) Delayed formation of coherent LO phonon-plasmon coupled modes in n- and p-type GaAs measured using a femtosecond coherent control technique. Phys. Rev. B **86**, 235145.

[89] Bakker, H. J, Hunsche, S, & Kurz, H. (1998) Coherent phonon polaritons as probes of anharmonic phonons in ferroelectrics. Rev. Mod. Phys. **70**, 523–536.

[90] Lu, R, Ishioka, K, Misochko, O. V, Hase, M, & Kitajima, M. (2005) Amplitude beating of coherent phonon in graphite under high intensity photo-excitation. Surface Science **593**, 116–121.

[91] Misochko, O. V, Hase, M, Ishioka, K, & Kitajima, M. (2004) Observation of an Amplitude Collapse and Revival of Chirped Coherent Phonons in Bismuth. Phys. Rev. Lett. **92**, 197401.

[92] Först, M, Manzoni, C, Kaiser, S, Tomioka, Y, Tokura, Y, Merlin, R, & Cavalleri, A. (2011) Nonlinear phononics as an ultrafast route to lattice control. Nat. Phys. **7**, 854–856.

[93] Shinohara, Y, Yabana, K, Kawashita, Y, Iwata, J.-I, Otobe, T, & Bertsch, G. F. (2010) Coherent phonon generation in time-dependent density functional theory. Phys. Rev. B **82**, 155110.

[94] Shinohara, Y, Sato, S. A, Yabana, K, Iwata, J.-I, Otobe, T, & Bertsch, G. F. (2012) Nonadiabatic generation of coherent phonons. J. Chem. Phys. **137**, 22A527.

[95] Maehrlein, S, Paarmann, A, Wolf, M, & Kampfrath, T. (2017) Terahertz Sum-Frequency Excitation of a Raman-Active Phonon. Phys. Rev. Lett. **119**, 127402.

[96] Dhar, L, Rogers, J. A, & Nelson, K. A. (1994) Time-resolved vibrational spectroscopy in the impulsive limit. Chem. Rev. **94**, 157–193.

[97] Merlin, R. (1997) Generating coherent THz phonons with light pulses. Sol. Stat. Commun. **102**, 207–220.

[98] Kutt, W. A, Albrecht, W, & Kurz, H. (1992) Generation of Coherent Phonons in Condensed Media. IEEE J. Quantum Electon. **28**, 2434–2444.

[99] Dekorsy, T, Cho, G. C, & Kurz, H. (2000) in Light Scattering in Solids VIII, eds. Cardona, M & Güntherodt, G. (Springer Berlin Heidelberg, Berlin, Heidelberg) Vol. 76, pp. 169–209.

[100] Först, M & Dekorsy, T. (2007) in Coherent Vibrational Dynamics, eds. Lanzani, G, Cerullo, G, & De Silvestri, S. (CRC Press), 1st edition, pp. 145–188.

[101] Ishioka, K & Misochko, O. V. (2010) in Progress in Ultrafast Intense Laser Science, eds. Yamanouchi, K, Giulietti, A, & Ledingham, K. (Springer Berlin Heidelberg, Berlin, Heidelberg) Vol. 98, pp. 47–63.

[102] Hase, M & Kitajima, M. (2010) Interaction of coherent phonons with defects and elementary excitations. J. Phys.: Condens. Matter **22**, 073201.

[103] Subedi, A. (2021) Light-control of materials via nonlinear phononics. Comp. Rendus. Phys. **22**, 161–184.

[104] Mankowsky, R, Först, M, & Cavalleri, A. (2016) Non-equilibrium control of complex solids by nonlinear phononics. Rep. Prog. Phys. **79**, 064503.

[105] Caruso, F & Zacharias, M. (2023) Quantum theory of light-driven coherent lattice dynamics. Phys. Rev. B **107**, 054102.

[106] Hase, M, Ishioka, K, Kitajima, M, Ushida, K, & Hishita, S. (2000) Dephasing of coherent phonons by lattice defects in bismuth films. Appl. Phys. Lett. **76**, 1258–1260.

[107] Ichikawa, T, Saito, Y, & Hase, M. (2020) The effect of ion irradiation on dephasing of coherent optical phonons in GaP. AIP Adv. **10**, 105117.

[108] Komori, Y, Saito, Y, Fons, P, & Hase, M. (2021) Ultrafast scattering dynamics of coherent phonons in $Bi_{1-x}Sb_x$ in the Weyl semimetal phase. New J. Phys. **23**, 023034.

[109] Li, J. J, Chen, J, Reis, D. A, Fahy, S, & Merlin, R. (2013) Optical probing of ultrafast electronic decay in bi and Sb with slow phonons. Phys. Rev. Lett. **110**, 047401.

[110] Fu, Z & Yamaguchi, M. (2016) Coherent Excitation of Optical Phonons in GaAs by Broadband Terahertz Pulses. Sci. Rep. **6**, 38264.

[111] Uchida, K, Nagai, K, Yoshikawa, N, & Tanaka, K. (2020) Inherent limit to coherent phonon generation under nonresonant light-field driving. Phys. Rev. B **101**, 094301.

[112] Peter, Y & Cardona, M. (2010) Fundamentals of semiconductors: physics and materials properties. (Springer Science & Business Media).

[113] Riffe, D. M & Sabbah, A. J. (2007) Coherent excitation of the optic phonon in Si: Transiently stimulated Raman scattering with a finite-lifetime electronic excitation. Phys. Rev. B **76**, 085207.

[114] Wall, S, Wegkamp, D, Foglia, L, Appavoo, K, Nag, J, Haglund, R, Stähler, J, & Wolf, M. (2012) Ultrafast changes in lattice symmetry probed by coherent phonons. Nat. Commun. **3**, 721.

[115] Ning, H, Mehio, O, Lian, C, Li, X, Zoghlin, E, Zhou, P, Cheng, B, Wilson, S. D, Wong, B. M, & Hsieh, D. (2022) Light-induced Weyl semiconductor-to-metal transition mediated by Peierls instability. Phys. Rev. B **106**, 205118.

[116] Ning, H, Mehio, O, Li, X, Buchhold, M, Driesse, M, Zhao, H, Cao, G, & Hsieh, D. (2023) A coherent phonon-induced hidden quadrupolar ordered state in Ca_2RuO_4. Nat. Commun. **14**, 8258.

[117] Hunsche, S, Wienecke, K, Dekorsy, T, & Kurz, H. (1995) Impulsive softening of coherent phonons in tellurium. Phys. Rev. Lett. **75**, 1815.

[118] Kamaraju, N, Kumar, S, Anija, M, & Sood, A. (2010) Large-amplitude chirped coherent phonons in tellurium mediated by ultrafast photoexcited carrier diffusion. Phys. Rev. B **82**, 195202.

[119] Afanasiev, D, Hortensius, J. R, Ivanov, B. A, Sasani, A, Bousquet, E, Blanter, Y. M, Mikhaylovskiy, R. V, Kimel, A. V, & Caviglia, A. D. (2021) Ultrafast control of magnetic interactions via light-driven phonons. Nat. Mater. **20**, 607–611.

[120] Giorgianni, F, Udina, M, Cea, T, Paris, E, Caputo, M, Radovic, M, Boie, L, Sakai, J, Schneider, C. W, & Johnson, S. L. (2022) Terahertz displacive excitation of a coherent Raman-active phonon in V_2O_3. Commun. Phys. **5**, 103.

[121] Juraschek, D. M & Maehrlein, S. F. (2018) Sum-frequency ionic Raman scattering. Phys. Rev. B **97**, 174302.

[122] Soranzio, D, Peressi, M, Cava, R. J, Parmigiani, F, & Cilento, F. (2019) Ultrafast broadband optical spectroscopy for quantifying subpicometric coherent atomic displacements in WTe_2. Phys. Rev. Res. **1**, 032033.

[123] Tani, M, Fukasawa, R, Abe, H, Matsuura, S, Sakai, K, & Nakashima, S. (1998) Terahertz radiation from coherent phonons excited in semiconductors. J. Appl. Phys. **83**, 2473–2477.

[124] Takeda, R, Kida, N, Sotome, M, Matsui, Y, & Okamoto, H. (2014) Circularly polarized narrowband terahertz radiation from a eulytite oxide by a pair of femtosecond laser pulses. Phys. Rev. A **89**, 033832.

[125] Sotome, M, Kida, N, Takeda, R, & Okamoto, H. (2014) Terahertz radiation induced by coherent phonon generation via impulsive stimulated Raman scattering in paratellurite. Phys. Rev. A **90**, 033842.

[126] Luo, L, Cheng, D, Song, B, Wang, L.-L, Vaswani, C, Lozano, P. M, Gu, G, Huang, C, Kim, R. H. J, Liu, Z, Park, J.-M, Yao, Y, Ho, K, Perakis, I. E, Li, Q, & Wang, J. (2021) A light-induced phononic symmetry switch and giant dissipationless topological photocurrent in $ZrTe_5$. Nat. Mater. **20**, 329–334.

[127] Qi, Y, Guan, M, Zahn, D, Vasileiadis, T, Seiler, H, Windsor, Y. W, Zhao, H, Meng, S, & Ernstorfer, R. (2022) Traversing Double-Well Potential Energy Surfaces: Photoinduced Concurrent Intralayer and Interlayer Structural Transitions in XTe_2 (X = Mo, W). ACS Nano **16**, 11124–11135.

[128] De Giovannini, U, Hübener, H, Sato, S. A, & Rubio, A. (2020) Direct Measurement of Electron-Phonon Coupling with Time-Resolved ARPES. Phys. Rev. Lett. **125**, 136401.

[129] Monney, C, Puppin, M, Nicholson, C. W, Hoesch, M, Chapman, R. T, Springate, E, Berger, H, Magrez, A, Cacho, C, Ernstorfer, R, & Wolf, M. (2016) Revealing the role of electrons and phonons in the ultrafast recovery of charge density wave correlations in $1T - TiSe_2$. Phys. Rev. B **94**, 165165.

[130] Gerber, S, Yang, S.-L, Zhu, D, Soifer, H, Sobota, J. A, Rebec, S, Lee, J. J, Jia, T, Moritz, B, Jia, C, Gauthier, A, Li, Y, Leuenberger, D, Zhang, Y, Chaix, L, Li, W, Jang, H, Lee, J.-S, Yi, M, Dakovski, G. L, Song, S, Glownia, J. M, Nelson, S, Kim, K. W, Chuang, Y.-D, Hussain, Z, Moore, R. G, Devereaux, T. P, Lee, W.-S, Kirchmann, P. S, & Shen, Z.-X. (2017) Femtosecond electron-phonon lock-in by photoemission and x-ray free-electron laser. Science **357**, 71–75.

[131] Yang, S.-L, Sobota, J, He, Y, Leuenberger, D, Soifer, H, Eisaki, H, Kirchmann, P, & Shen, Z.-X. (2019) Mode-Selective Coupling of Coherent Phonons to the Bi2212 Electronic Band Structure. Phys. Rev. Lett. **122**, 176403.

[132] Sakamoto, S, Gauthier, N, Kirchmann, P. S, Sobota, J. A, & Shen, Z.-X. (2022) Connection between coherent phonons and electron-phonon coupling in Sb (111). Phys. Rev. B **105**, L161107.

[133] Liu, S, Hammud, A, Hamada, I, Wolf, M, Müller, M, & Kumagai, T. (2022) Nanoscale coherent phonon spectroscopy. Sci. Adv. **8**, eabq5682.

[134] Fukuda, T, Kaburauchi, R, Saito, Y, Makino, K, Fons, P, Ueno, K, & Hase, M. (2022) Photo-induced Tellurium Segregation in $MoTe_2$. Phys. Status Solidi RRL. **16**, 2100633.

[135] Mannebach, E. M, Nyby, C, Ernst, F, Zhou, Y, Tolsma, J, Li, Y, Sher, M.-J, Tung, I.-C, Zhou, H, Zhang, Q, et al. (2017) Dynamic optical tuning of interlayer interactions in the transition metal dichalcogenides. Nano Lett. **17**, 7761–7766.

[136] Zong, A, Shen, X, Kogar, A, Ye, L, Marks, C, Chowdhury, D, Rohwer, T, Freelon, B, Weathersby, S, Li, R, Ji, Y, Checkelsky, J, Wang, X, & Gedik, N. (2018) Ultrafast manipulation of mirror domain walls in a charge density wave. Sci. Adv. **4**, eaau5501.

[137] Krishnamoorthy, A, Lin, M.-F, Zhang, X, Weninger, C, Ma, R, Britz, A, Tiwary, C. S, Kochat, V, Apte, A, Yang, J, Park, S, Li, R, Shen, X, Wang, X, Kalia, R, Nakano, A, Shimojo, F, Fritz, D, Bergmann, U, Ajayan, P, & Vashishta, P. (2019) Optical control of non-equilibrium phonon dynamics. Nano Lett. **19**, 4981–4989.

[138] Fukuda, T, Makino, K, Saito, Y, Fons, P, Kolobov, A. V, Ueno, K, & Hase, M. (2020) Ultrafast dynamics of the low frequency shear phonon in $1T' - MoTe_2$. Appl. Phys. Lett. **116**, 093103.

[139] Tan, Y, Luo, F, Zhu, M, Xu, X, Ye, Y, Li, B, Wang, G, Luo, W, Zheng, X, Wu, N, Yu, Y, Qin, S, & Zhang, X.-A. (2018) Controllable 2H-to-1T' phase transition in few-layer $MoTe_2$. Nanoscale **10**, 19964–19971.

[140] Kang, S, Won, D, Yang, H, Lin, C.-H, Ku, C.-S, Chiang, C.-Y, Kim, S, & Cho, S. (2021) Phase-controllable laser thinning in $MoTe_2$. Appl. Surf. Sci. p. 150282.

[141] Keum, D. H, Cho, S, Kim, J. H, Choe, D.-H, Sung, H.-J, Kan, M, Kang, H, Hwang, J.-Y, Kim, S. W, Yang, H, Chang, K. J, & Lee, Y. H. (2015) Bandgap opening in few-layered monoclinic $MoTe_2$. Nat. Phys. **11**, 482–486.

[142] Song, S, Keum, D. H, Cho, S, Perello, D, Kim, Y, & Lee, Y. H. (2015) Room temperature semiconductor–metal transition of $MoTe_2$ thin films engineered by strain. Nano Lett. **16**, 188–193.

[143] Sakanashi, K, Ouchi, H, Kamiya, K, Krüger, P, Miyamoto, K, Omatsu, T, Ueno, K, Watanabe, K, Taniguchi, T, Bird, J. P, & Aoki, N. (2020) Investigation of laser-induced-metal phase of $MoTe_2$ and its contact property via scanning gate microscopy. Nanotechnology **31**, 205205.

[144] Ueno, K & Fukushima, K. (2015) Changes in structure and chemical composition of $\alpha - MoTe_2$ and $\beta - MoTe_2$ during heating in vacuum conditions. Appl. Phys. Exp. **8**, 095201.

[145] Sundaram, S & Mazur, E. (2002) Inducing and probing non-thermal transitions in semiconductors using femtosecond laser pulses. Nat. Mater. **1**, 217–224.

[146] Ueno, K. (2015) Introduction to the growth of bulk single crystals of two-dimensional transition-metal dichalcogenides. J. Phys. Soc. Jpn. **84**, 121015.

[147] Hunter, J. D. (2007) Matplotlib: A 2D graphics environment. Computing in Science & Engineering **9**, 90–95.

[148] Sugai, S & Ueda, T. (1982) High-pressure raman spectroscopy in the layered materials $2H - MoS_2$, $2H - MoSe_2$, and $2H - MoTe_2$. Phys. Rev. B **26**, 6554.

[149] Froehlicher, G, Lorchat, E, Fernique, F, Joshi, C, Molina-Sánchez, A, Wirtz, L, & Berciaud, S. (2015) Unified description of the optical phonon modes in n-layer $MoTe_2$. Nano Lett. **15**, 6481–6489.

[150] Chen, S.-Y, Goldstein, T, Venkataraman, D, Ramasubramaniam, A, & Yan, J. (2016) Activation of new raman modes by inversion symmetry breaking in type II Weyl semimetal candidate $T' - MoTe_2$. Nano Lett. **16**, 5852–5860.

[151] Zhang, K, Bao, C, Gu, Q, Ren, X, Zhang, H, Deng, K, Wu, Y, Li, Y, Feng, J, & Zhou, S. (2016) Raman signatures of inversion symmetry breaking and structural phase transition in type−II Weyl semimetal $MoTe_2$. Nat. Commun. **7**, 13552.

[152] Ma, X, Guo, P, Yi, C, Yu, Q, Zhang, A, Ji, J, Tian, Y, Jin, F, Wang, Y, Liu, K, Xia, T, Shi, Y, & Zhang, Q. (2016) Raman scattering in the transition-metal dichalcogenides of $1T' - MoTe_2$, $T_d - MoTe_2$, and $T_d - WTe_2$. Phys. Rev. B. **94**, 214105.

[153] Hunsche, S, Wienecke, K, & Kurz, H. (1996) Details of coherent phonon motion in tellurium. Appl. Phys. A **62**, 499–502.

[154] Roeser, C, Kandyla, M, Mendioroz, A, & Mazur, E. (2004) Optical control of coherent lattice vibrations in tellurium. Phys. Rev. B **70**, 212302.

[155] Misochko, O, Lebedev, M, Schäfer, H, & Dekorsy, T. (2007) Coherent a_1 phonons in te studied with tailored femtosecond pulses. J. Phys. Condens. Matter **19**, 406220.

[156] Miller, T. A, Rudé, M, Pruneri, V, & Wall, S. (2016) Ultrafast optical response of the amorphous and crystalline states of the phase change material $Ge_2Sb_2Te_5$. Phys. Rev. B **94**, 024301.

[157] Li, Y, Stoica, V. A, Endicott, L, Wang, G, Uher, C, & Clarke, R. (2010) Coherent optical phonon spectroscopy studies of femtosecond-laser modified Sb_2Te_3 films. Appl. Phys. Lett. **97**, 171908.

[158] Norimatsu, K, Hada, M, Yamamoto, S, Sasagawa, T, Kitajima, M, Kayanuma, Y, & Nakamura, K. G. (2015) Dynamics of all the Raman-active coherent phonons in Sb_2Te_3 revealed via transient reflectivity. J. Appl. Phys, **117**, 143102.

[159] Ishioka, K, Kitajima, M, Irisawa, J, Hironaka, Y, Ushida, K, & Nakamura, K. G. (2006) Amplitude saturation of coherent phonon excited by field screening in cdte. Jpn. J. Appl. Phys. **45**, 9111.

[160] Shimada, T, Kamaraju, N, Frischkorn, C, Wolf, M, & Kampfrath, T. (2014) Indication of te segregation in laser-irradiated znte observed by in situ coherent-phonon spectroscopy. Appl. Phys. Lett. **105**, 111908.

[161] Caramazza, S, Collina, A, Stellino, E, Ripanti, F, Dore, P, & Postorino, P. (2018) First-and second-order Raman scattering from $MoTe_2$ single crystal. Eur. Phys. J. B **91**, 35.

[162] Pine, A. S & Dresselhaus, G. (1971) Raman spectra and lattice dynamics of tellurium. Phys. Rev. B **4**, 356–371.

[163] Du, Y, Qiu, G, Wang, Y, Si, M, Xu, X, Wu, W, & Ye, P. D. (2017) One-dimensional van der waals material tellurium: Raman spectroscopy under strain and magneto-transport. Nano Lett. **17**, 3965–3973.

[164] Bonse, J, Krüger, J, Höhm, S, & Rosenfeld, A. (2012) Femtosecond laser-induced periodic surface structures. J. Laser Appl. **24**, 042006.

[165] Sato, K, Tahara, K, Minami, Y, Katayama, I, Kitajima, M, Kawai, H, Yanagi, K, & Takeda, J. (2014) Resonance enhancement of first-and second-order coherent phonons in metallic single-walled carbon nanotubes. Phys. Rev. B **90**, 235435.

[166] Unuchek, D, Ciarrocchi, A, Avsar, A, Watanabe, K, Taniguchi, T, & Kis, A. (2018) Room-temperature electrical control of exciton flux in a van der waals heterostructure. Nature **560**, 340.

[167] Chhowalla, M, Shin, H. S, Eda, G, Li, L.-J, Loh, K. P, & Zhang, H. (2013) The chemistry of two-dimensional layered transition metal dichalcogenide nanosheets. Nat. Chem. **5**, 263.

[168] Crepaldi, A, Autès, G, Gatti, G, Roth, S, Sterzi, A, Manzoni, G, Zacchigna, M, Cacho, C, Chapman, R, Springate, E, Seddon, E. A, Bugnon, P, Magrez, H, Berger, H, Vobornik, I, Kalläne, M, Quer, A, Rossnagel, K, Parmigiani, F, Yazyev, O. V, & Grioni, M. (2017) Enhanced ultrafast relaxation rate in the Weyl semimetal phase of $MoTe_2$ measured by time-and angle-resolved photoelectron spectroscopy. Phys. Rev. B **96**, 241408.

[169] Hase, M, Katsuragawa, M, Constantinescu, A. M, & Petek, H. (2012) Frequency comb generation at terahertz frequencies by coherent phonon excitation in silicon. Nat. Photonics **6**, 243.

[170] He, R, Zhong, S, Kim, H. H, Ye, G, Ye, Z, Winford, L, McHaffie, D, Rilak, I, Chen, F, Luo, X, Sun, Y, & Tsen, A. W. (2018) Dimensionality-driven orthorhombic $MoTe_2$ at room temperature. Phys. Rev. B **97**, 041410.

[171] Lai, J, Liu, X, Ma, J, Wang, Q, Zhang, K, Ren, X, Liu, Y, Gu, Q, Zhuo, X, Lu, W, Wu, Y, Li, Y, Feng, J, Zhou, S, Chen, J.-H, & Sun, D. (2018) Anisotropic Broadband Photoresponse of Layered Type-II Weyl Semimetal $MoTe_2$. Adv. Mater. **30**, 1707152.

[172] Gambetta, A, Manzoni, C, Menna, E, Meneghetti, M, Cerullo, G, Lanzani, G, Tretiak, S, Piryatinski, A, Saxena, A, Martin, R. L, & R, B. A. (2006) Real-time observation of nonlinear coherent phonon dynamics in single-walled carbon nanotubes. Nat. Phys. **2**, 515.

[173] Hase, M, Fons, P, Mitrofanov, K, Kolobov, A. V, & Tominaga, J. (2015) Femtosecond structural transformation of phase-change materials far from equilibrium monitored by coherent phonons. Nat. Commun. **6**, 8367.

[174] Flock, J, Dekorsy, T, & Misochko, O. V. (2014) Coherent lattice dynamics of the topological insulator Bi_2Te_3 probed by ultrafast spectroscopy. Appl. Phys. Lett. **105**, 011902.

[175] He, B, Zhang, C, Zhu, W, Li, Y, Liu, S, Zhu, X, Wu, X, Wang, X, Wen, H.-h, & Xiao, M. (2016) Coherent optical phonon oscillation and possible electronic softening in WTe_2 crystals. Sci. Rep. **6**, 30487.

[176] Hase, M, Mizoguchi, K, Harima, H, Nakashima, S.-i, & Sakai, K. (1998) Dynamics of coherent phonons in bismuth generated by ultrashort laser pulses. Phys. Rev. B **58**, 5448–5452.

[177] Hohlfeld, J, Wellershoff, S.-S, Güdde, J, Conrad, U, Jähnke, V, & Matthias, E. (2000) Electron and lattice dynamics following optical excitation of metals. Chem. Phys. **251**, 237–258.

[178] Kim, H.-J, Kang, S.-H, Hamada, I, & Son, Y.-W. (2017) Origins of the structural phase transitions in $MoTe_2$ and WTe_2. Phys. Rev. B **95**, 180101.

[179] Fukuda, T, Makino, K, Saito, Y, Fons, P, Ando, A, Mori, T, Ishikawa, R, Ueno, K, Afalla, J, & Hase, M. (2024) Coherent optical response driven by non-equilibrium electron–phonon dynamics in a layered transition-metal dichalcogenide. APL Mater. **12**, 021102.

[180] Huber, R, Tauser, F, Brodschelm, A, Bichler, M, Abstreiter, G, & Leitenstorfer, A. (2001) How many-particle interactions develop after ultrafast excitation of an electron–hole plasma. Nature **414**, 286–289.

[181] Hase, M, Kitajima, M, Constantinescu, A. M, & Petek, H. (2003) The birth of a quasiparticle in silicon observed in time–frequency space. Nature **426**, 51–54.

[182] Wang, Y, Steinberg, H, Jarillo-Herrero, P, & Gedik, N. (2013) Observation of Floquet-Bloch states on the surface of a topological insulator. Science **342**, 453–457.

[183] Ito, S, Schüler, M, Meierhofer, M, Schlauderer, S, Freudenstein, J, Reimann, J, Afanasiev, D, Kokh, K. A, Tereshchenko, O. E, Güdde, J, Sentef, M. A, Höfer, U, & Huber, R. (2023) Build-up and dephasing of Floquet–Bloch bands on subcycle timescales. Nature **616**, 696–701.

[184] Cavalleri, A, Tóth, C, Siders, C. W, Squier, J, Ráksi, F, Forget, P, & Kieffer, J. (2001) Femtosecond structural dynamics in VO_2 during an ultrafast solid-solid phase transition. Phys. Rev. Lett. **87**, 237401.

[185] Kogar, A, Zong, A, Dolgirev, P. E, Shen, X, Straquadine, J, Bie, Y.-Q, Wang, X, Rohwer, T, Tung, I.-C, Yang, Y, Li, R, Yang, J, Weathersby, S, Park, S, Kozina, M. E, Sie, E. J, Wen, H, Jarillo-Herrero, P, Fisher, I. R, Wang, X, & Gedik, N. (2020) Light-induced charge density wave in $LaTe_3$. Nat. Phys. **16**, 159–163.

[186] Ghimire, S, DiChiara, A. D, Sistrunk, E, Agostini, P, DiMauro, L. F, & Reis, D. A. (2011) Observation of high-order harmonic generation in a bulk crystal. Nat. Phys. **7**, 138–141.

[187] Yoshikawa, N, Tamaya, T, & Tanaka, K. (2017) High-harmonic generation in graphene enhanced by elliptically polarized light excitation. Science **356**, 736–738.

[188] Juraschek, D. M & Spaldin, N. A. (2017) Sounding out optical phonons. Science **357**, 873–874.

[189] Stupakiewicz, A, Davies, C. S, Szerenos, K, Afanasiev, D, Rabinovich, K. S, Boris, A. V, Caviglia, A, Kimel, A. V, & Kirilyuk, A. (2021) Ultrafast phononic switching of magnetization. Nat. Phys. **17**, 489–492.

[190] LaMountain, T, Nelson, J, Lenferink, E. J, Amsterdam, S. H, Murthy, A. A, Zeng, H, Marks, T. J, Dravid, V. P, Hersam, M. C, & Stern, N. P. (2021) Valley-selective optical Stark effect of exciton-polaritons in a monolayer semiconductor. Nat. Commun. **12**, 4530.

[191] Fukuda, T, Ozaki, U, Jeong, S, Arashida, Y, En-ya, K, Yoshida, S, Fons, P. J, Fujita, J.-i, Ueno, K, Hase, M, & Hada, M. (2023) Photoinduced Structural Dynamics of $2H - MoTe_2$ Under Extremely High-Density Excitation Conditions. J. Phys. Chem. C **127**, 13149–13156.

[192] Iwasaki, Y, Fukuda, T, Noyama, G, Akei, M, Shigekawa, H, Fons, P. J, Hase, M, Arashida, Y, & Hada, M. (2023) Electronic intraband scattering in a transition-metal dichalcogenide observed by double-excitation ultrafast electron diffraction. Appl. Phys. Lett. **123**, 181901.

[193] Jeong, T. Y, Jin, B. M, Rhim, S. H, Debbichi, L, Park, J, Jang, Y. D, Lee, H. R, Chae, D.-H, Lee, D, Kim, Y.-H, Jung, S, & Yee, K. J. (2016) Coherent lattice vibrations in mono- and few-layer WSe_2. ACS Nano **10**, 5560–5566.

[194] Trovatello, C, Miranda, H. P, Molina-Sanchez, A, Borrego-Varillas, R, Manzoni, C, Moretti, L, Ganzer, L, Maiuri, M, Wang, J, Dumcenco, D, Kis, A, Wirtz, L, Marini, A, Soavi, G, Ferrari, A. C, Cerullo, G, Sangali, D, & Dal Conte, S. (2020) Strongly coupled coherent phonons in single-layer MoS_2. ACS nano **14**, 5700–5710.

[195] Li, Z, Peng, B, Lin, M.-L, Leng, Y.-C, Zhang, B, Pang, C, Tan, P.-H, Monserrat, B, & Chen, F. (2021) Phonon-assisted electronic states modulation of few-layer $PdSe_2$ at terahertz frequencies. npj 2D Mater. Appl. **5**, 87.

[196] Afalla, J, Muldera, J, Takamizawa, S, Fukuda, T, Ueno, K, Tani, M, & Hase, M. (2023) Terahertz emission from transient currents and coherent phonons in layered $MoSe_2$ and WSe_2. J. Appl. Phys. **133**, 165103.

[197] Yoshikawa, N, Suganuma, H, Matsuoka, H, Tanaka, Y, Hemme, P, Cazayous, M, Gallais, Y, Nakano, M, Iwasa, Y, & Shimano, R. (2021) Ultrafast switching to an insulating-like metastable state by amplitudon excitation of a charge density wave. Nat. Phys. **17**, 909–914.

[198] Cheng, Y, Zong, A, Li, J, Xia, W, Duan, S, Zhao, W, Li, Y, Qi, F, Wu, J, Zhao, L, Zhu, P, Zou, X, Jiang, T, Guo, Y, Yang, L, Qian, D, Zhang, W, Kogar, A, Zuerch, M. W, Xiang, D, & Zhang, J. (2022) Light-induced dimension crossover dictated by excitonic correlations. Nat. Commun. **13**, 963.

[199] Mizukoshi, Y, Fukuda, T, Komori, Y, Ishikawa, R, Ueno, K, & Hase, M. (2023) Ultrafast melting of charge-density wave fluctuations at room temperature in 1T-$TiSe_2$ monitored under non-equilibrium conditions. Appl. Phys. Lett. **122**, 243101.

[200] Ruppert, C, Aslan, O. B, & Heinz, T. F. (2014) Optical properties and band gap of single- and few-layer $MoTe_2$ crystals. Nano Lett. **14**, 6231–6236.

[201] Nojima, S. (1995) Dimensionality of exciton-state renormalization in highly excited semiconductors. Phys. Rev. B **51**, 11124–11127.

[202] Haug, H & Koch, S. W. (2009) Quantum theory of the optical and electronic properties of semiconductors. (World Scientific Publishing Company).

[203] Sie, E. J, Steinhoff, A, Gies, C, Lui, C. H, Ma, Q, Rösner, M, Schönhoff, G, Jahnke, F, Wehling, T. O, Lee, Y. H, Kong, J, Jarillo-Herrero, P, & Gedik, N. (2017) Observation of Exciton Redshift–Blueshift Crossover in Monolayer WS_2. Nano Lett. **17**, 4210–4216.

[204] Meckbach, L, Hader, J, Huttner, U, Neuhaus, J, Steiner, J. T, Stroucken, T, Moloney, J. V, & Koch, S. W. (2020) Ultrafast band-gap renormalization and build-up of optical gain in monolayer $MoTe_2$. Phys. Rev. B **101**, 075401.

[205] Cheng, T. K, Acioli, L. H, Vidal, J, Zeiger, H. J, Dresselhaus, G, Dresselhaus, M. S, & Ippen, E. P. (1993) Modulation of a semicondutor-to-semimetal transition at 7 THz via coherent lattice vibrations. Appl. Phys. Lett. **62**, 1901–1903.

[206] Kudryashov, S. I, Kandyla, M, Roeser, C. A. D, & Mazur, E. (2007) Intraband and interband optical deformation potentials in femtosecond-laser-excited $\alpha-$Te. Phys. Rev. B **75**, 085207.

[207] Mor, S, Gosetti, V, Molina-Sánchez, A, Sangalli, D, Achilli, S, Agekyan, V. F, Franceschini, P, Giannetti, C, Sangaletti, L, & Pagliara, S. (2021) Photoinduced modulation of the excitonic resonance via coupling with coherent phonons in a layered semiconductor. Phys. Rev. Res. **3**, 043175.

[208] Fu, J, Li, M, Solanki, A, Xu, Q, Lekina, Y, Ramesh, S, Shen, Z. X, & Sum, T. C. (2021) Electronic States Modulation by Coherent Optical Phonons in 2D Halide Perovskites. Adv. Mater. **33**, 2006233.

[209] Li, Y, Singh, A, Krylyuk, S, Davydov, A, & Jaramillo, R. (2019) Near-infrared photonic phase-change properties of transition metal ditellurides. (International Society for Optics and Photonics), Vol. 11085, p. 110850T.

[210] Perlangeli, M, Peli, S, Soranzio, D, Puntel, D, Parmigiani, F, & Cilento, F. (2020) Polarization-resolved broadband time-resolved optical spectroscopy for complex materials: application to the case of $MoTe_2$ polytypes. Opt. Exp. **28**, 8819–8829.

[211] Sokolowski-Tinten, K & von der Linde, D. (2000) Generation of dense electron-hole plasmas in silicon. Phys. Rev. B **61**, 2643.

[212] Guzelturk, B, Winkler, T, Van de Goor, T. W. J, Smith, M. D, Bourelle, S. A, Feldmann, S, Trigo, M, Teitelbaum, S. W, Steinrück, H.-G, de la Pena, G. A, Alonso-Mori, R, Zhu, D, Sato, T, Karunadasa, H. I, Toney, M. F, Deschler, F, & Lindenberg, A. M. (2021) Visualization of dynamic polaronic strain fields in hybrid lead halide perovskites. Nat. Mater. pp. 618–623.

[213] Bretscher, H. M, Andrich, P, Telang, P, Singh, A, Harnagea, L, Sood, A, & Rao, A. (2021) Ultrafast melting and recovery of collective order in the excitonic insulator Ta_2NiSe_5. Nat. Commun. **12**, 1699.

[214] Haug, H & Koch, S. W. (1989) Semiconductor laser theory with many-body effects. Phys. Rev. A **39**, 1887–1898.

[215] Komsa, H.-P & Krasheninnikov, A. V. (2012) Effects of confinement and environment on the electronic structure and exciton binding energy of MoS_2 from first principles. Phys. Rev. B **86**, 241201.

[216] Song, Q, Tan, Q, Zhang, X, Wu, J, Sheng, B, Wan, Y, Wang, X, Dai, L, & Tan, P. (2016) Physical origin of Davydov splitting and resonant Raman spectroscopy of Davydov components in multilayer $MoTe_2$. Phys. Rev. B **93**, 115409.

[217] von Hoegen, A, Mankowsky, R, Fechner, M, Först, M, & Cavalleri, A. (2018) Probing the interatomic potential of solids with strong-field nonlinear phononics. Nature **555**, 79–82.

[218] Zukerstein, M, Kozák, M, Trojánek, F, & Malỳ, P. (2018) Experimental observation of anharmonic effects in coherent phonon dynamics in diamond. Diamond Relat. Mater. **90**, 202–206.

[219] Yu, J, Han, Y, Wang, L, Xu, F, Zhang, H, Yu, Y, Wu, Q, & Hu, J. (2021) Visualizing Nonlinear Phononics in Layered $ReSe_2$. J. Phys. Chem. Lett. **12**, 5178–5184.

[220] Abdumalikov, A. A & Klochikhin, A. A. (1977) The double resonance in two-phonon Raman scattering. Phys. Stat. Sol. (b) **80**, 43–50.

[221] Calleja, J. M & Cardona, M. (1977) Resonant Raman scattering in ZnO. Phys. Rev. B **16**, 3753–3761.

[222] Sun, L, Yan, J, Zhan, D, Liu, L, Hu, H, Li, H, Tay, B. K, Kuo, J.-L, Huang, C.-C, Hewak, D. W, Lee, P. S, & Shen, Z. X. (2013) Spin-Orbit Splitting in Single-Layer MoS_2 Revealed by Triply Resonant Raman Scattering. Phys. Rev. Lett. **111**, 126801.

[223] Jin, W, Kim, H. H, Ye, Z, Ye, G, Rojas, L, Luo, X, Yang, B, Yin, F, Horng, J. S. A, Tian, S, Fu, Y, Xu, G, Deng, H, Lei, H, Tsen, A. W, Sun, K, He, R, & Zhao, L. (2020) Observation of the polaronic character of excitons in a two-dimensional semiconducting magnet CrI_3. Nat. Commun. **11**, 4780.

[224] Ishioka, K, Petek, H, Kaydashev, V. E, Kaidashev, E. M, & Misochko, O. V. (2010) Coherent optical phonons of ZnO under near resonant photoexcitation. J. Phys. Condens. Matter **22**, 465803.

[225] Bae, S, Matsumoto, K, Raebiger, H, Shudo, K.-i, Kim, Y.-H, Handegård, Ø. S, Nagao, T, Kitajima, M, Sakai, Y, Zhang, X, Vajtai, R, Ajayan, P, Kono, J, Takeda, J, & Katayama, I. (2022) K-point longitudinal acoustic phonons are responsible for ultrafast intervalley scattering in monolayer $MoSe_2$. Nat. Commun. **13**, 4279.

[226] Miller, B, Lindlau, J, Bommert, M, Neumann, A, Yamaguchi, H, Holleitner, A, Högele, A, & Wurstbauer, U. (2019) Tuning the Fröhlich exciton-phonon scattering in monolayer MoS_2. Nat. Commun. **10**, 807.

[227] Li, L, Lin, M.-F, Zhang, X, Britz, A, Krishnamoorthy, A, Ma, R, Kalia, R. K, Nakano, A, Vashishta, P, Ajayan, P, Hoffmann, M. C, Fritz, D. M, Bergmann, U, & Prezhdo, O. V. (2019) Phonon-Suppressed Auger Scattering of Charge Carriers in Defective Two-Dimensional Transition Metal Dichalcogenides. Nano Lett. **19**, 6078–6086.

[228] Chi, Z, Chen, H, Zhao, Q, & Weng, Y.-X. (2019) Ultrafast carrier and phonon dynamics in few-layer $2H - MoTe_2$. J. Chem. Phys. **151**, 114704.

[229] Sono, N, Otaki, T, Kitao, T, Yamakawa, T, Sakai, D, Morimoto, T, Miyamoto, T, & Okamoto, H. (2022) Phonon-dressed states in an organic Mott insulator. Commun. Phys. **5**, 72.

[230] Boyd, R. W. (2020) Nonlinear optics. (Academic press).

[231] Liu, X.-B, Hu, S.-Q, Chen, D, Guan, M, Chen, Q, & Meng, S. (2022) Calibrating out-of-equilibrium electron–phonon couplings in photoexcited MoS_2. Nano Lett. **22**, 4800–4806.

[232] Hübener, H, De Giovannini, U, & Rubio, A. (2018) Phonon driven Floquet matter. Nano Lett. **18**, 1535–1542.

[233] Uchida, K, Otobe, T, Mochizuki, T, Kim, C, Yoshita, M, Akiyama, H, Pfeiffer, L. N, West, K. W, Tanaka, K, & Hirori, H. (2016) Subcycle optical response caused by a terahertz dressed state with phase-locked wave functions. Phys. Rev. Lett. **117**, 277402.

[234] Hein, P, Jauernik, S, Erk, H, Yang, L, Qi, Y, Sun, Y, Felser, C, & Bauer, M. (2020) Mode-resolved reciprocal space mapping of electron-phonon interaction in the Weyl semimetal candidate $T_d - WTe_2$. Nat. Commun. **11**, 2613.

[235] Ren, Q, Suzuki, T, Kanai, T, Itatani, J, Shin, S, & Okazaki, K. (2023) Phase-resolved frequency-domain analysis of the photoemission spectra for photoexcited $1T - TaS_2$ in the Mott insulating charge density wave state. Appl. Phys. Lett. **122**, 221902.

[236] Arashida, Y, Mogi, H, Ishikawa, M, Igarashi, I, Hatanaka, A, Umeda, N, Peng, J, Yoshida, S, Takeuchi, O, & Shigekawa, H. (2022) Subcycle Mid-Infrared Electric-Field-Driven Scanning Tunneling Microscopy with a Time Resolution Higher Than 30 fs. ACS Photonics **9**, 3156–3164.

[237] De Giovannini, U, Sato, S. A, Hübener, H, & Rubio, A. (2022) First-principles modelling for time-resolved ARPES under different pump–probe conditions. J. Electron Spectros. Relat. Phenomena **254**, 147152.

[238] Guo, H, Yang, T, Yamamoto, M, Zhou, L, Ishikawa, R, Ueno, K, Tsukagoshi, K, Zhang, Z, Dresselhaus, M. S, & Saito, R. (2015) Double resonance Raman modes in monolayer and few-layer $MoTe_2$. Phys. Rev. B **91**, 205415.

[239] Kresse, G & Hafner, J. (1994) Ab initio molecular-dynamics simulation of the liquid-metal–amorphous-semiconductor transition in germanium. Phys. Rev. B **49**, 14251–14269.

[240] Blöchl, P. E. (1994) Projector augmented-wave method. Phys. Rev. B **50**, 17953–17979.

[241] Perdew, J. P, Burke, K, & Ernzerhof, M. (1996) Generalized gradient approximation made simple. Phys. Rev. Lett. **77**, 3865–3868.

[242] Ong, S. P, Richards, W. D, Jain, A, Hautier, G, Kocher, M, Cholia, S, Gunter, D, Chevrier, V. L, Persson, K. A, & Ceder, G. (2013) Python materials genomics (pymatgen): A robust, open-source python library for materials analysis. Comp. Mater. Sci. **68**, 314–319.

[243] Dawson, W. G & Bullett, D. W. (1987) Electronic structure and crystallography of $MoTe_2$ and WTe_2. J. Phys. C: Sol. Stat. Phys. **20**, 6159.

[244] You, Y, Zhang, X.-X, Berkelbach, T. C, Hybertsen, M. S, Reichman, D. R, & Heinz, T. F. (2015) Observation of biexcitons in monolayer WSe_2. Nat. Phys. **11**, 477–481.

[245] Sugawara, K, Nakata, Y, Shimizu, R, Han, P, Hitosugi, T, Sato, T, & Takahashi, T. (2016) Unconventional Charge-Density-Wave Transition in Monolayer $1T - TiSe_2$. ACS Nano **10**, 1341–1345.

[246] Yoshikawa, N, Nagai, K, Uchida, K, Takaguchi, Y, Sasaki, S, Miyata, Y, & Tanaka, K. (2019) Interband resonant high-harmonic generation by valley polarized electron–hole pairs. Nat. Commun. **10**, 3709.

[247] Han, X, Wang, X, Huang, T, & Yan, X. (2021) The versatile device with $MoTe_2$ mode-locker for ultrafast optics application. Opt. Laser Technol. **135**, 106692.

[248] Gies, C & Steinhoff, A. (2021) Atomically Thin van der Waals Semiconductors—A Theoretical Perspective. Laser Photonics Rev. **15**, 2000482.

[249] Erben, D, Steinhoff, A, Lorke, M, & Jahnke, F. (2022) Optical nonlinearities in the excited carrier density of atomically thin transition metal dichalcogenides. Phys. Rev. B **106**, 045409.

[250] Cheng, M, Zhong, S, Rivas, N, Dekker, T, Petruk, A. A, Gicala, P, Pichugin, K, Chen, F, Luo, X, Sun, Y, Tsen, A. W, & Sciaini, G. (2022) Persistent Photogenerated State Attained by Femtosecond Laser Irradiation of Thin $T_d - MoTe_2$. J. Phys. Chem. C **126**, 13840–13846.

[251] Hada, M, Yamaguchi, D, Ishikawa, T, Sawa, T, Tsuruta, K, Ishikawa, K, Koshihara, S.-y, Hayashi, Y, & Kato, T. (2019) Ultrafast isomerization-induced cooperative motions to higher molecular orientation in smectic liquid-crystalline azobenzene molecules. Nat. Commun. **10**, 4159.

[252] Böker, T, Severin, R, Müller, A, Janowitz, C, Manzke, R, Voß, D, Krüger, P, Mazur, A, & Pollmann, J. (2001) Band structure of MoS_2 , $MoSe_2$, and $\alpha-MoTe_2$: Angle-resolved photoelectron spectroscopy and *ab initio* calculations. Phys. Rev. B **64**, 235305.

[253] Mannebach, E. M, Li, R, Duerloo, K.-A, Nyby, C, Zalden, P, Vecchione, T, Ernst, F, Reid, A. H, Chase, T, Shen, X, Weathersby, S, Hast, C, Hettel, R, Coffee, R, Hartmann, N, Fry, A. R, Yu, Y, Cao, L, Heinz, T. F, Reed, E. J, Dürr, H. A, Wang, X, & Lindenberg, A. M. (2015) Dynamic Structural Response and Deformations of Monolayer MoS_2 Visualized by Femtosecond Electron Diffraction. Nano Lett. **15**, 6889–6895.

[254] Lin, M.-F, Kochat, V, Krishnamoorthy, A, Bassman Oftelie, L, Weninger, C, Zheng, Q, Zhang, X, Apte, A, Tiwary, C. S, Shen, X, Li, R, Kalia, R, Ajayan, P, Nakano, A, Vashishta, P, Shimojo, F, Wang, X, Fritz, D. M, & Bergmann, U. (2017) Ultrafast non-radiative dynamics of atomically thin $MoSe_2$. Nat. Commun. **8**, 1745.

[255] Hu, J, Xiang, Y, Ferrari, B. M, Scalise, E, & Vanacore, G. M. (2023) Indirect Exciton–Phonon Dynamics in $MoSe_2$ Revealed by Ultrafast Electron Diffraction. Adv. Funct. Mater. **33**, 2206395.

[256] Hu, J, Vanacore, G. M, Cepellotti, A, Marzari, N, & Zewail, A. H. (2016) Rippling ultrafast dynamics of suspended 2D monolayers, graphene. Proc. Natl. Acad. Sci. U.S.A. **113**.

[257] Ryu, H, Lee, Y, Jeong, J. H, Lee, Y, Cheon, Y, Watanabe, K, Taniguchi, T, Kim, K, Cheong, H, Lee, C, & Lee, G. (2023) Laser-Induced Phase Transition and Patterning of hBN-Encapsulated $MoTe_2$. Small **19**, 2205224.

[258] Shi, J, Bie, Y.-Q, Zong, A, Fang, S, Chen, W, Han, J, Cao, Z, Zhang, Y, Taniguchi, T, Watanabe, K, Fu, X, Bulović, V, Kaxiras, E, Baldini, E, Jarillo-Herrero, P, & Nelson, K. A. (2023) Intrinsic 1T' phase induced in atomically thin $2H - MoTe_2$ by a single terahertz pulse. Nat. Commun. **14**, 5905.

[259] Yoshida, S, Hirori, H, Tachizaki, T, Yoshioka, K, Arashida, Y, Wang, Z.-H, Sanari, Y, Takeuchi, O, Kanemitsu, Y, & Shigekawa, H. (2019) Subcycle Transient Scanning Tunneling Spectroscopy with Visualization of Enhanced Terahertz Near Field. ACS Photonics **6**, 1356–1364.

[260] Kobayashi, A, Takano, Y, & Demura, S. (2022) Observation of the Specific Heat Jump in the Se-Substituted $MoTe_2$ Single Crystals. Materials **15**, 3782.

[261] Yang, L, Dai, L, Li, H, Hu, H, Liu, K, Pu, C, Hong, M, & Liu, P. (2019) Characterization of the pressure-induced phase transition of metallization for $MoTe_2$ under hydrostatic and non-hydrostatic conditions. AIP Adv. **9**, 065104.

[262] Hada, M, Norimatsu, K, Tanaka, S, Keskin, S, Tsuruta, T, Igarashi, K, Ishikawa, T, Kayanuma, Y, Miller, R. J. D, Onda, K, Sasagawa, T, Koshihara, S.-y, & Nakamura, K. G. (2016) Bandgap modulation in photoexcited topological insulator Bi_2Te_3 via atomic displacements. J. Chem. Phys. **145**, 024504.

[263] Masaharu, T, Takeshi, M, & Kiyofumi, N. (2002) X-ray structural analysis of the high-pressure phase III of tellurium. J. Phys.:Condens. Matter **14**, 10609.

[264] Latini, S, De Giovannini, U, Sie, E. J, Gedik, N, Hübener, H, & Rubio, A. (2021) Phonoritons as Hybridized Exciton-Photon-Phonon Excitations in a Monolayer $h-$BN Optical Cavity. Phys. Rev. Lett. **126**, 227401.

[265] Krökel, D, Grischkowsky, D, & Ketchen, M. B. (1989) Subpicosecond electrical pulse generation using photoconductive switches with long carrier lifetimes. Appl. Phys. Lett. **54**, 1046–1047.

[266] Prechtel, L, Song, L, Schuh, D, Ajayan, P, Wegscheider, W, & Holleitner, A. W. (2012) Time-resolved ultrafast photocurrents and terahertz generation in freely suspended graphene. Nat. Commun. **3**, 646.

[267] Kastl, C, Karnetzky, C, Karl, H, & Holleitner, A. W. (2015) Ultrafast helicity control of surface currents in topological insulators with near-unity fidelity. Nat. Commun. **6**, 6617.

[268] Island, J. O, Kissin, P, Schalch, J, Cui, X, Ul Haque, S. R, Potts, A, Taniguchi, T, Watanabe, K, Averitt, R. D, & Young, A. F. (2020) On-chip terahertz modulation and emission with integrated graphene junctions. Appl. Phys. Lett. **116**, 161104.

[269] McIver, J. W, Schulte, B, Stein, F.-U, Matsuyama, T, Jotzu, G, Meier, G, & Cavalleri, A. (2020) Light-induced anomalous Hall effect in graphene. Nat. Phys. **16**, 38–41.

[270] Yoshioka, K, Wakamura, T, Hashisaka, M, Watanabe, K, Taniguchi, T, & Kumada, N. (2022) Ultrafast intrinsic optical-to-electrical conversion dynamics in a graphene photodetector. Nat. Photon. **16**, 718–723.